Physics of Atomic Nuclei, Vol. 67, No. 6, 2004, pp. 1065–1075. From Yadernaya Fizika, Vol. 67, No. 6, 2004, pp. 1093–1103.

NEUTRINO PHYSICS AND ASTROPHYSICS

Status of the Sudbury Neutrino Observatory*

I. T. Lawson**
(for the SNO Collaboration)

Department of Physics, University of Guelph, Guelph, Canada

Received November 4, 2003

Abstract—Solar neutrinos from the decay of ^{8}B have been detected at the Sudbury Neutrino Observatory via the charged-current (CC) and neutral-current (NC) reactions on deuterium and by the elastic scattering (ES) of electrons. The CC reaction is sensitive exclusively to electron neutrinos, the NC reaction is sensitive to all neutrino species, and the ES reaction also has a small sensitivity to muon and tau neutrinos. These measurements provided strong evidence that neutrinos change flavor as they propagate from the center of the Sun to the Earth at the 5.3σ level. It will also be shown that a global solar neutrino analysis of matter-enhanced neutrino oscillations of two active flavors strongly favors the large mixing angle solution.

1. INTRODUCTION

For more than 30 years, solar neutrino experiments [1–6] observed fewer neutrinos than what were predicted by the detailed models of the Sun [7, 8]. Table 1 shows the observed solar neutrino fluxes for these experiments. As observed, the experimental results are less than the theoretical expectations, even though each experiment probes different aspects of the solar neutrino energy spectrum, and have an energy dependence on the observed solar neutrino flux. Figure 1 shows the energy spectra for the different reactions in the Sun which produce electron neutrinos. One explanation of this neutrino flux deficit would be the transformation of the Sun's electron neutrinos into another flavor while traveling to the Earth.

The Sudbury Neutrino Observatory (SNO) is an imaging water Čerenkov detector that was constructed to resolve this solar neutrino anomaly. It can make simultaneous measurements of the electron-type neutrino (ν_e) flux from the ^{8}B decay in the Sun and the flux of all active neutrino flavors through the following three reactions:

$$\nu_e + d \to p + p + e^- \text{ (CC)},$$
$$\nu_x + d \to p + n + \nu_x \text{ (NC)},$$
$$\nu_x + e^- \to \nu_x + e^- \text{ (ES)}.$$

The charged-current (CC) reaction on the deuteron is sensitive only to ν_e, and the neutral-current (NC) reaction has equal sensitivity to all active neutrino flavors ($\nu_x, x = e, \mu, \tau$). The elastic scattering (ES) reaction is sensitive to all active flavors, but with a reduced sensitivity to ν_μ and ν_τ. Each of these interactions is detected by the SNO detector when one or more electrons produced during the reaction emit Čerenkov light. The CC reaction produces an electron with an energy highly correlated with that of the neutrino and is sensitive to the energy spectrum of ν_e and hence to deviations from the parent spectrum. The NC reaction is detected after the neutron is absorbed by the deuterium, giving a 6.25-MeV photon. The photon subsequently Compton scatters, imparting enough energy to electrons to create Čerenkov light.

A comparison of the solar neutrino flux inferred from the reaction rates of these three interaction channels under the assumption of no oscillations can provide evidence for flavor-changing neutrino oscillations. If ν_e from the Sun transform into another active flavor, then the solar neutrino flux deduced from the CC reaction rate, $\Phi^{\mathrm{CC}}(\nu_e)$, must be less than those deduced from the ES or NC reaction rate, such that $\Phi^{\mathrm{CC}}(\nu_e) < \Phi^{\mathrm{ES}}(\nu_x)$ or $\Phi^{\mathrm{CC}}(\nu_e) < \Phi^{\mathrm{NC}}(\nu_x)$.

The solar neutrino physics analysis program is designed to exploit the unique NC capability of the SNO detector. Since the result of this NC measurement is a definitive statement on the oscillation of solar neutrinos, the SNO experiment intends to make three separate NC measurements of the total ^{8}B neutrino flux. The first NC measurement was made with a pure D_2O target; this phase is complete and the results are presented in [9]. The measured $\Phi^{\mathrm{CC}}(\nu_e)$ is significantly smaller than $\Phi^{\mathrm{NC}}(\nu_x)$; thus, it is inconsistent with the null hypothesis of a pure ν_e constituent in the solar neutrino flux. This indicates that ν_e emitted by

*This article was submitted by the author in English.

**e-mail: lawson@physics.uoguelph.ca

Table 1. A summary of the solar neutrino observations at different solar neutrino detectors (The neutrino production processes are shown in decreasing order of magnitude. The systematic and statistical uncertainties are added in quadrature for each experiment.)

Experiment	Measured flux	SSM flux [7]	Production process	References
Homestake	2.56 ± 0.23 SNU	$7.6^{+1.3}_{-1.1}$ SNU	^{8}B, ^{7}Be, *pp*, *pep*	[1]
SAGE	$70.8^{+6.5}_{-6.1}$ SNU	128^{+9}_{-7} SNU	*pp*, *pep*, ^{7}Be, ^{8}B	[3]
Gallex	$77.5^{+7.5}_{-7.8}$ SNU	128^{+9}_{-7} SNU	*pp*, *pep*, ^{7}Be, ^{8}B	[4]
GNO	$65.8^{+10.8}_{-10.3}$ SNU	128^{+9}_{-7} SNU	*pp*, *pep*, ^{7}Be, ^{8}B	[5]
Kamiokande	$(2.80 \pm 0.38) \times 10^6$ cm^{-2} s^{-1}	$5.05(1^{+0.20}_{-0.16}) \times 10^6$ cm^{-2} s^{-1}	^{8}B	[2]
Super-Kamiokande	$2.32^{+0.09}_{-0.08} \times 10^6$ cm^{-2} s^{-1}	$5.05(1^{+0.20}_{-0.16}) \times 10^6$ cm^{-2} s^{-1}	^{8}B	[6]

the Sun are transformed into the other active neutrino species (ν_μ and ν_τ) as they travel to the Earth. In addition, the results of the day–night asymmetry of the neutrino event rates are presented.

The second NC measurement will be made with NaCl added to the D_2O; this phase is under way and is expected to be completed in the fall of 2003. The advantages of this phase in measuring the total neutrino flux from the Sun will be briefly discussed. The third NC measurement will involve the installation of ^{3}He proportional counters into the D_2O volume [10]. In this configuration, the detection of the CC and NC signals are decoupled, and the covariance of the CC and NC signals that appear in the first two detector configurations is removed.

2. THE SNO DETECTOR

The SNO detector [11] is an imaging water Čerenkov detector located in the International Nickel Company's Creighton mine in Sudbury, Canada. The detector consists of a barrel-shaped cavity with a height of 34 m and a diameter of 22 m at a depth of 2092 m. Figure 2 shows a cross-sectional view of the SNO detector. It contains 1000 t of 99.92% isotopically pure D_2O contained inside a 12-m diameter acrylic sphere. The acrylic vessel (AV) is constructed out of 122 ultraviolet transmitting acrylic panels. A 17.8-m diameter stainless steel structure supports 9456 20-cm inward-facing photomultiplier tubes (PMTs). This sphere is surrounded by 7000 t of ultrapure H_2O contained in the cavity. The H_2O shields the detector from high-energy γ rays and neutrons originating from the PMTs and the cavity wall.

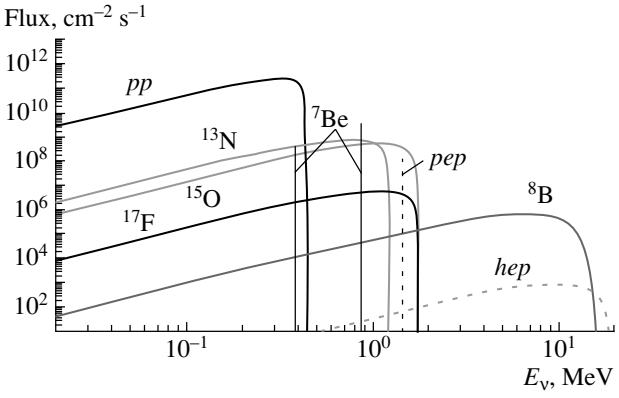

Fig. 1. The standard solar neutrino energy spectra for the different processes that produce ν_e in the Sun. The spectra are taken from [7] and references therein.

Physics event triggers are created in the detector when there are $\geq$18 PMTs exceeding a threshold of $\sim$0.25 photoelectrons within a coincidence time window of 93 ns. All the PMT hits registered in a $\sim$420-ns window after the start of the coincidence time window are recorded; this time window allows scattered and reflected Čerenkov photons to be included in the event. The mean noise rate of the PMTs is $\sim$500 Hz, which gives $\sim$2 noise PMT hits in the 420-ns window. The instantaneous trigger rate is about 15–20 Hz, of which 6–8 Hz are physics triggers. The remaining triggers are diagnostic triggers for monitoring the well-being of the detector. The trigger efficiency reaches 100% when the PMT multiplicity in the event window is $\geq$ 23. For every event trigger, the time and charge responses of each participating PMT are recorded.

3. SOLAR NEUTRINO ANALYSIS IN THE PURE D_2O PHASE

The data reported in this paper were recorded from November 2, 1999, to May 28, 2001, and give a live time of 306.4 d, 128.5 d during the day and 177.9 d during the night. The target media was pure D_2O throughout this period. In the following subsections, the analysis steps are discussed in more detail.

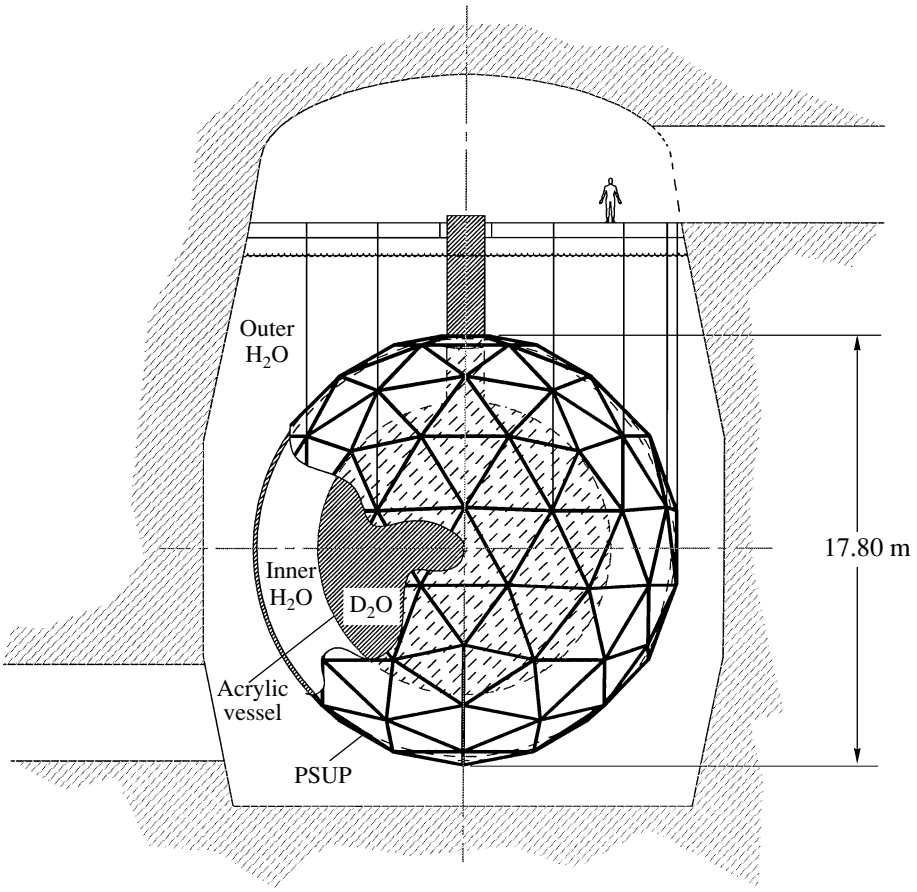

Fig. 2. A cross-sectional view of the SNO detector. The outer geodesic structure is the PMT support structure which surrounds the acrylic vessel.

3.1. Instrumental Background

The analysis began by removing the instrumental backgrounds from the data set. Electrical pickup or interference creates false PMT hits (N_{hits}) and electrical discharges in the PMTs or insulating materials may produce false light. These events have characteristic PMT time and charge distributions that are different from Čerenkov light, and are removed using cuts based on these distributions. Some instrumental backgrounds are localized near the water piping at the top of the detector. Veto PMTs were installed in this region to enhance the rejection efficiency of these non-Čerenkov events. Most of the observed electronic channel charges in the interference events are near the pedestal and are removed by a cut on the mean charge of the fired PMTs. Some of these electrical discharge or electronic interference background events have different event-to-event time correlations from physics events, and time correlation cuts are used to remove these events.

The efficiency and residual backgrounds of these instrumental background requirements are studied using a triggered ^{16}N 6.13-MeV γ-ray source [12] and a triggered ^{8}Li 13-MeV endpoint β source [13] deployed in the D_2O and H_2O volumes. Further tests of the N_{hits} dependence on the cuts are performed with an isotropic light source at various wavelengths. The efficiency on the physics data after the instrumental background cuts are applied, weighted over the fiducial volume, is measured to be $0.9966^{+0.0011}_{-0.0002}$. The residual instrumental background rejection contamination is less than 1%.

Further instrumental background rejection cuts are applied to the data once the events are reconstructed. These cuts test the hypothesis that each event has the properties of single-electron Čerenkov light. The reconstruction figure-of-merit cut tests for the consistency between the time and angular expectations for an event fitted to the location of the reconstructed vertex and that based on the properties of the Čerenkov light and the detector response.

The Čerenkov characteristics of each event are parametrized using the average opening angle between two hit PMTs (θ_{ij}), measured from the recon-

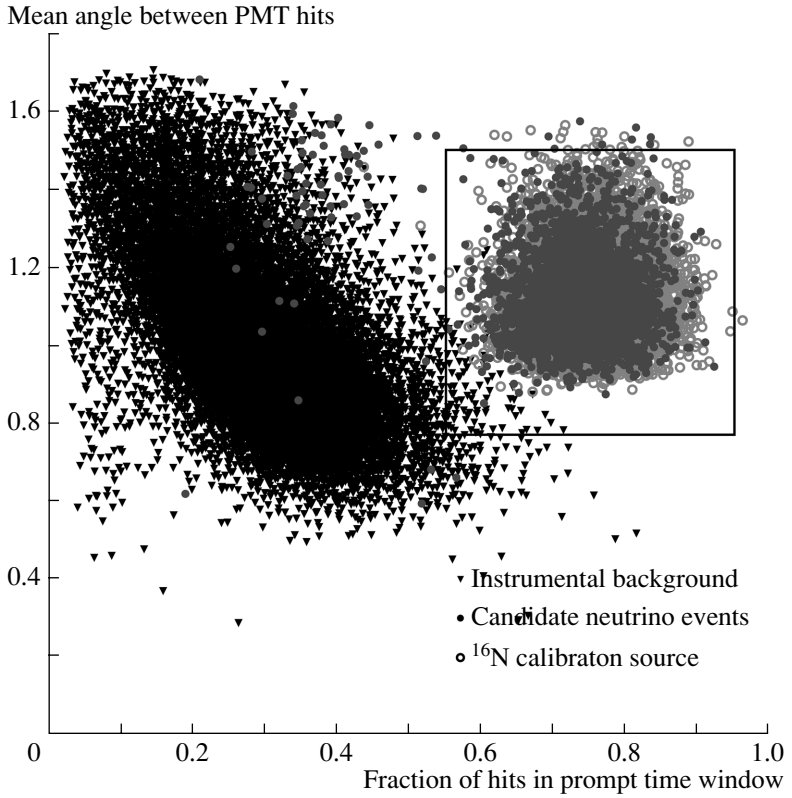

Fig. 3. Separation of instrumental backgrounds and Čerenkov light events using the mean angle between PMT hits and the fraction of hits in the prompt time window (ITR).

structed vertex, and the in-time ratio (ITR), which is the ratio of the number of hit PMTs within an asymmetric time window around the prompt light peak to the number of calibrated PMTs in the event. Figure 3 shows the correlations between θ_{ij} and ITR for instrumental backgrounds and neutrino candidate events.

The residual instrumental background contamination in the neutrino signal after the background cuts is estimated using a bifurcated analysis. For the same fiducial volume and energy thresholds, the instrumental background contamination is estimated to be less than 0.1% of the final neutrino candidate data set.

3.2. Event Reconstruction and Calibration

After passing the instrumental background cuts, all events with $N_{\text{hits}} \geq 30$ are reconstructed. The calibrated times and positions of the hit PMTs are used to reconstruct the vertex position and direction of the particle. Two different reconstruction algorithms were used; an event-by-event comparison shows good agreement between the data sets. The analysis described in this paper used a maximum likelihood technique which uses both the time and angular characteristics of Čerenkov light. Vertex reconstruction accuracy and resolution for electrons are measured using Compton electrons from the ^{16}N γ-ray source, and their energy dependence is verified by the ^{8}Li β source. Compton-scattered electrons from a 6.13-MeV γ ray are preferentially scattered in the forward direction relative to the incident γ-ray direction. At these energies, the vertex reconstruction resolution is 16 cm and the angular resolution is 26.7°.

The calibration of the PMT time and charge pedestals, slopes, offsets, charge vs. time dependences, and second-order rate dependences are performed using electronic pulsers and pulsed light sources. Optical calibrations are obtained using a near-isotropic source of pulsed laser light with variable intensity [14, 15]. The laser light source is deployed within the D_2O and H_2O. Optical parameters of different optical media in the detector are obtained [16]. The attenuation lengths in the D_2O and H_2O are found to be near the Rayleigh scattering limit.

The absolute energy scale and uncertainties are measured with the ^{16}N source deployed in the same regions as the laser source. The detector energy response to the photopeak of this source provides a

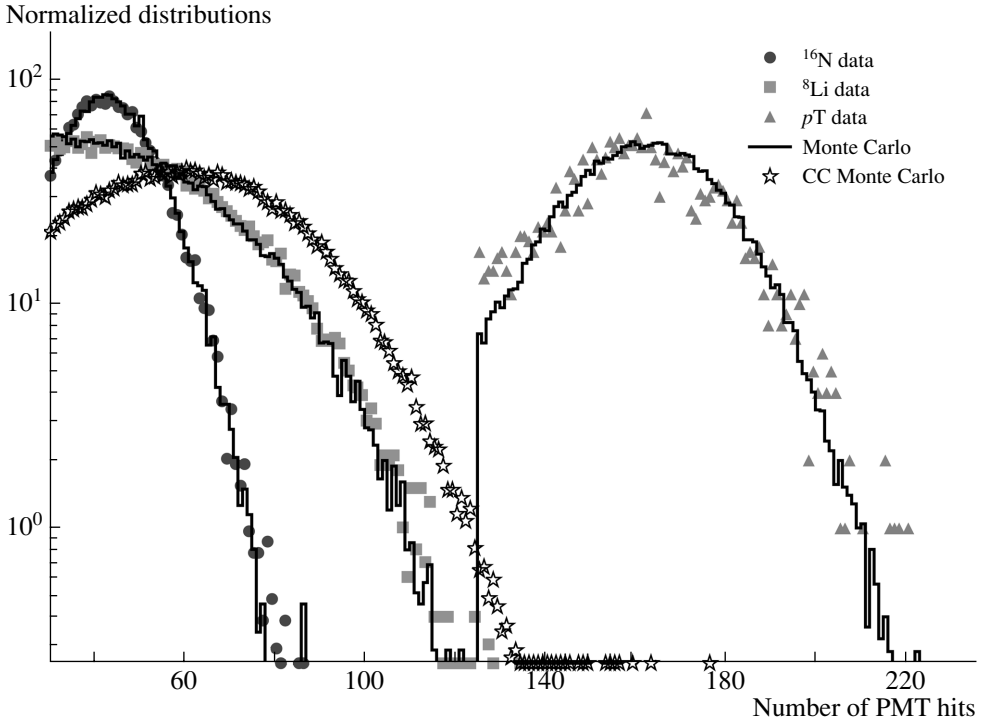

Fig. 4. Comparison of the Monte Carlo predicted responses to different calibrated sources.

normalization to the PMT photon collection efficiency used in the Monte Carlo and establishes the absolute energy calibration. A long-term stability study of the detector response to the ^{16}N source shows a linear drift of -1.3% per year; this drift correction is applied to the event-by-event energy estimator.

The resulting Monte Carlo is then used to make predictions for the energy response to different calibration sources. The pT source generates 19.8-MeV γ rays through the $^3\mathrm{H}(p,\gamma)^4\mathrm{He}$ reaction [17] and is used to check the linearity of the energy response beyond the endpoint of the ^{8}B neutrino energy spectrum. The ^{252}Cf fission source provides an extended distribution of 6.25-MeV γ rays from $d(n,\gamma)t$. Figure 4 shows a comparison of the Monte Carlo predictions and the detector responses to these sources. In addition, the neutron response and systematic uncertainty were calibrated with a ^{252}Cf source. The deduced efficiency for neutron captures on deuterium was $(29.9 \pm 1.1)\%$ for a uniform source of neutrons in the D_2O. The neutron detection efficiency within the fiducial volume and above the energy threshold was $(14.38 \pm 0.53)\%$.

The energy response estimator uses the same input parameters as the Monte Carlo. It assigns an effective kinetic energy T_{eff} to each event based upon its position, direction, and the number of N_{hits} within the prompt (unscattered) photon peak. For an electron of total energy E_e, the derived energy response is parametrized by a Gaussian:

$$R(E_{\mathrm{eff}}, E_e) = \frac{1}{\sqrt{2\pi}\sigma_E(E_e)} \times \exp\left[-\frac{1}{2}\left(\frac{E_{\mathrm{eff}} - E_e}{\sigma_E(E_e)}\right)^2\right],$$

where $E_{\mathrm{eff}} = T_{\mathrm{eff}} + m_e$, and the energy resolution is given by

$$\sigma_E(E_e) = -0.0684 + 0.331\sqrt{E_e - m_e} + 0.0425(E_e - m_e)\,[\mathrm{MeV}].$$

The systematic uncertainty on the energy calibration is $\pm 1.2\%$. Other energy related systematic uncertainties to the flux include the energy resolution and the energy scale linearity.

3.3. Physics Backgrounds

Physics background events can come from the $\beta\gamma$ decays of ^{208}Tl and ^{214}Bi, which are progeny of the natural Th and U chains. These $\beta\gamma$ radionuclei can emit γ rays with sufficient energy to generate free neutrons in the D_2O, from photodisintegration (pd) of the deuteron, and low-energy Čerenkov events. The free neutron from this breakup is indistinguishable

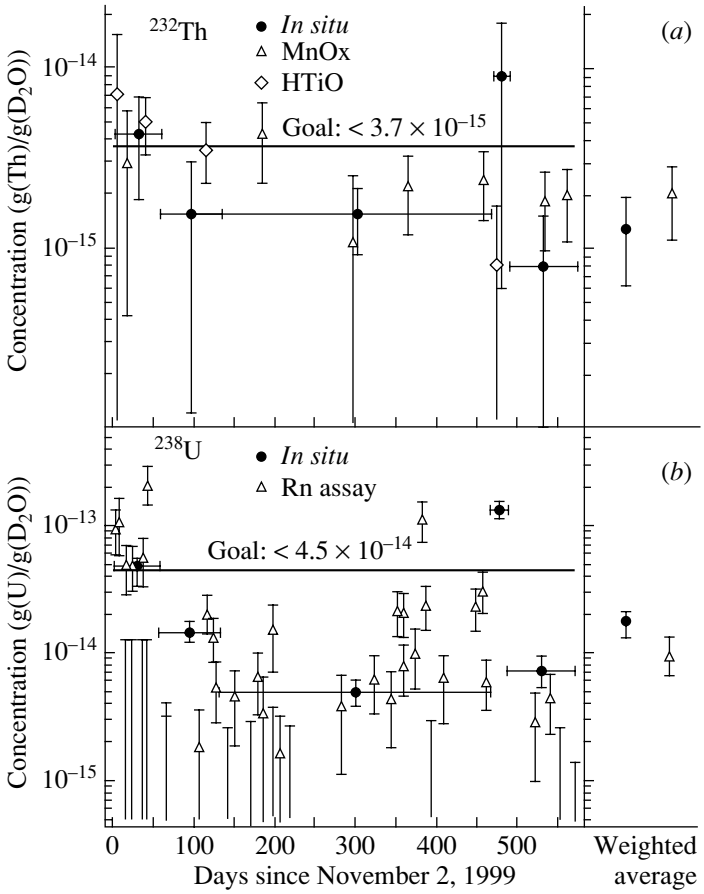

Fig. 5. Th (a) and U (b) backgrounds (equivalent equilibrium concentrations) in the D_2O deduced by in situ and ex situ techniques. The radiochemical assay results and the in situ Čerenkov signal determination of the backgrounds are shown on the left-hand side. The right-hand side shows the time-integrated averages.

from the NC signal. However, this neutron background can be subtracted from the total neutron signal in the detector if the internal radioactivity level of the detector is known. In this analysis, most of the Čerenkov signals from the $\beta\gamma$ decays are removed by the energy threshold and radius cut imposed. Internal radioactivity levels in the D_2O and H_2O are measured by regular low level ex situ radioassays of Th and U chain progeny. The light isotropy is used to provide an in situ monitoring of these backgrounds. Both techniques show that the Th and U radioactivity levels are either at or below the target level of one disintegration per day per ton of water. Figure 5 shows the Th and U backgrounds as mass fractions in g(Th)/g(D_2O) and g(U)/g(D_2O). Results from the ex situ and in situ methods are consistent. The pd backgrounds are shown in Table 2.

Low-energy background Čerenkov events in the signal region were studied using encapsulated sources of Th and U placed in the detector volume and by Monte Carlo calculations. Table 2 shows the number of background Čerenkov events due to the activity in the D_2O, AV, H_2O, and PMT array. Other sources of free neutrons in the D_2O include cosmic rays and atmospheric neutrinos.

3.4. Solar Neutrino Signal Extraction

The final data set contains 2928 events after the fiducial and energy cuts. The extended maximum likelihood method is used in extracting the CC, ES, and neutron (i.e., NC + background) events from the data set. Data distributions in $T_{\rm eff}$, $(R/R_{\rm AV})^3$, and $\cos\theta_\odot$ are simultaneously fit to the probability density functions generated from Monte Carlo simulations assuming no flavor transformation and the ^{8}B spectrum from Ortiz *et al.* [18]. The quantity $\cos\theta_\odot$ is the angle between the reconstructed direction of the event and the instantaneous direction from the Sun to the Earth (see Fig. 6). The extraction yields $1967.7^{+61.9}_{-60.9}$ CC events, $263.6^{+26.4}_{-25.6}$ ES events, and $576.5^{+49.5}_{-48.9}$ neutron events for $T_{\rm eff} \geq 5.00$ MeV and $R < 550$ cm, where the uncertainties are statistical. The dominant sources of systematic uncertainty in

Table 2. Neutron and Čerenkov background events

Background source	Events
D_2O pd	44^{+8}_{-9}
H_2O + AV pd	27 ± 8
Atmospheric ν and sub-Čerenkov threshold μ	4 ± 1
Fission	$\ll 1$
$^2H(\alpha, \alpha)\, pn$	2.0 ± 0.4
$^{17}O(\alpha, n)$	$\ll 1$
Terrestrial and reactor $\overline{\nu}$	1^{+3}_{-1}
External neutrons	$\ll 1$
Total neutron background	78 ± 12
D_2O Čerenkov	20^{+13}_{-6}
H_2O Čerenkov	3^{+4}_{-3}
AV Čerenkov	6^{+3}_{-6}
PMT Čerenkov	16^{+11}_{-8}
Total Čerenkov background	45^{+18}_{-12}

this signal extraction are the energy scale uncertainty and reconstruction accuracy (see Table 3 for the complete list of the systematic uncertainties).

The ^8B neutrino flux can be determined from normalizing the observed integrated event rate above the energy threshold. Assuming the ^8B spectrum from [18], the flux deduced from the CC, ES, and NC reactions are

$$\Phi^{\rm CC}_{\rm SNO}(\nu_e) = 1.76^{+0.06}_{-0.05}({\rm stat.})^{+0.09}_{-0.09}({\rm syst.}) \times 10^6\ {\rm cm}^{-2}{\rm s}^{-1},$$

$$\Phi^{\rm ES}_{\rm SNO}(\nu_x) = 2.39^{+0.24}_{-0.23}({\rm stat.})^{+0.12}_{-0.12}({\rm syst.}) \times 10^6\ {\rm cm}^{-2}{\rm s}^{-1},$$

$$\Phi^{\rm NC}_{\rm SNO}(\nu_x) = 5.09^{+0.44}_{-0.43}({\rm stat.})^{+0.46}_{-0.43}({\rm syst.}) \times 10^6\ {\rm cm}^{-2}{\rm s}^{-1}.$$

The CC and ES results reported here are consistent with earlier results [20]. The excess of the NC flux over the CC and ES fluxes implies that flavor transformations occur.

A simple change of variables resolves the data directly into electron (Φ_e) and nonelectron ($\Phi_{\mu\tau}$) components,

$$\Phi_e = 1.76^{+0.05}_{-0.05}({\rm stat.})^{+0.09}_{-0.09}({\rm syst.}),$$

$$\Phi_{\mu\tau} = 3.41^{+0.45}_{-0.45}({\rm stat.})^{+0.48}_{-0.45}({\rm syst.}),$$

Table 3. Systematic uncertainties (in percent) on the fluxes [the experimental uncertainty for ES (not shown) is $-4.8, +5.0\%$; *denotes CC vs. NC anticorrelation]

Error source	CC error	NS error	$\Phi_{\mu\tau}$ Uncertainties
Energy scale*	$-4.2, +4.3$	$-6.2, +6.1$	$-10.4, +10.3$
Energy resolution*	$-0.9, +0.0$	$-0.0, +4.4$	$-0.0, +6.8$
Energy nonlinearity*	± 0.1	± 0.4	± 0.6
Vertex resolution*	± 0.0	± 0.1	± 0.2
Vertex accuracy	$-2.8, +2.9$	± 1.8	± 1.4
Angular resolution	± 0.2	± 0.3	± 0.3
Internal source pd*	± 0.0	$-1.5, +1.6$	$-2.0, +2.2$
External source pd	± 0.1	± 1.0	± 1.4
D_2O Čerenkov*	$-0.1, +0.2$	$-2.6, +1.2$	$-3.7, +1.7$
H_2O Čerenkov	± 0.0	$-0.2, +0.4$	$-0.2, +0.6$
AV Čerenkov	± 0.0	$-0.2, +0.2$	$-0.3, +0.3$
PMT Čerenkov*	± 0.1	$-2.1, +1.6$	$-3.0, +2.2$
Neutron capture	± 0.0	$-4.0, +3.6$	$-5.8, +5.2$
Cut acceptance	$-0.2, +0.4$	$-0.2, +0.4$	$-0.2, +0.4$
Experimental uncertainties	$-5.2, +5.2$	$-8.5, +9.1$	$-13.2, +14.1$
Cross section [19]	± 1.8	± 1.3	± 1.4

assuming the standard ^8B shape. Combining the statistical and systematic uncertainties in quadrature, $\Phi_{\mu\tau}$ is $3.41^{+0.66}_{-0.64}$, which is 5.3σ above zero, providing strong evidence for flavor transformation consistent with neutrino oscillations [21, 22]. Figure 7 shows the flux of $\nu_{\mu\tau}$ versus the flux of ν_e deduced from the SNO data. The three bands represent the $\pm 1\sigma$ measurements of the CC, ES, and NC rates. The error ellipses represent the 68, 95, and 99% joint probability contours for Φ_e and $\Phi_{\mu\tau}$.

3.5. Day–Night Analysis

The measured night and day fluxes Φ_N and Φ_D were used to form the asymmetry ratio for each reaction: $\mathcal{A} = 2(\Phi_N - \Phi_D)/(\Phi_N + \Phi_D)$, where the active-only neutrino models predict $\mathcal{A} \neq 0$. Note that the ES reaction has additional contributions from $\nu_{\mu\tau}$ leading to a reduction in its sensitivity to ν_e asymmetries. The day and night energy spectra are shown in Fig. 8 and the results of the signal extraction are shown in Table 4. SNO's day and night energy spectra were used to produce MSW exclusion plots

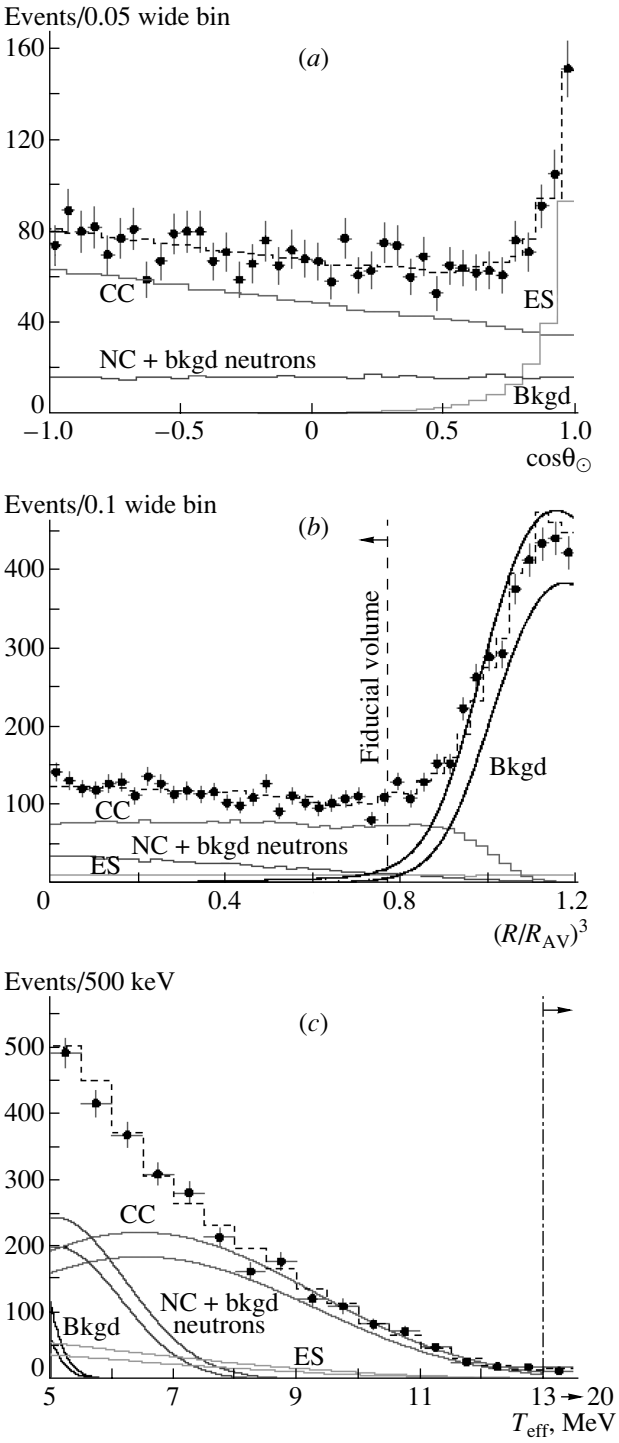

Fig. 6. (*a*) Distribution of $\cos\theta_\odot$ for $R < 550$ cm and $T_{\rm eff} > 5$ MeV. (*b*) Distribution of the volume-weighted radial variable $(R/R_{\rm AV})^3$. (*c*) Kinetic energy for $R < 550$ cm. Also shown are the Monte Carlo predictions for CC, ES, and NC + bkgd neutron events scaled to the fitted results and the calculated spectrum of Čerenkov background (Bkgd) events. The dashed lines represent the summed components, and the bands show the $\pm 1\sigma$ uncertainties.

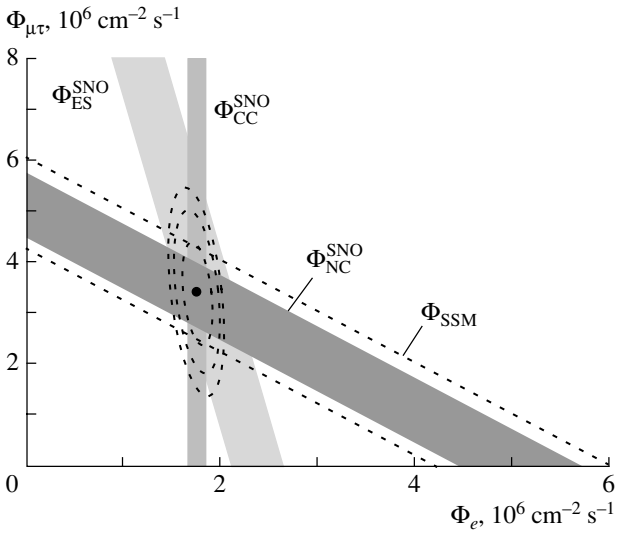

Fig. 7. Flux of ^{8}B solar neutrinos which are μ or τ flavor vs. flux of ν_e deduced from the three neutrino reactions in SNO. The diagonal bands show the total ^{8}B flux as predicted by the SSM [7] (dashed lines) and that measured with the NC reaction in SNO (shaded band). The intercepts of these bands with the axes represent the $\pm 1\sigma$ errors.

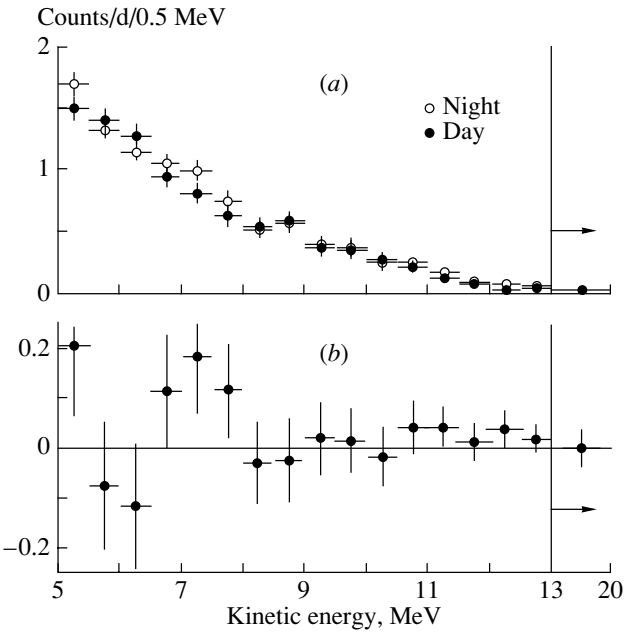

Fig. 8. (*a*) Energy spectra for day and night. All signals and backgrounds contribute. The final bin extends from 13.0 to 20.0 MeV. (*b*) Difference, night − day, between the spectra. The day rate was 9.23 ± 0.27 events/d, and the night rate was 9.79 ± 0.24 events/d.

and limits on neutrino-flavor-mixing parameters. MSW oscillation models between two active flavors were fitted to the data. For simplicity, only the energy spectra was used in the fit, and the radial and angular

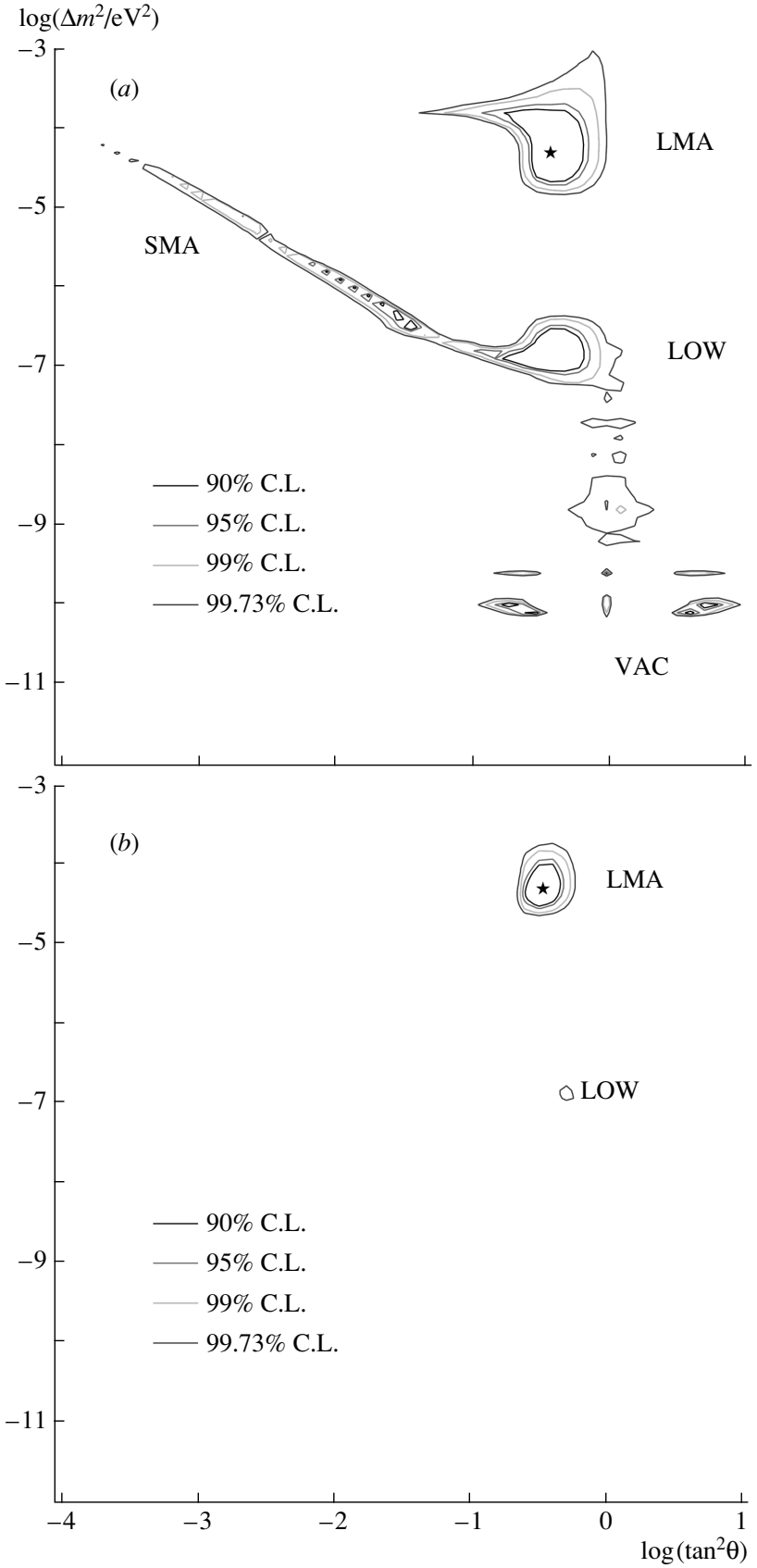

Fig. 9. Allowed regions of the MSW plane determined by a χ^2 fit to (*a*) SNO day and night energy spectra and (*b*) with additional experimental and solar model data.

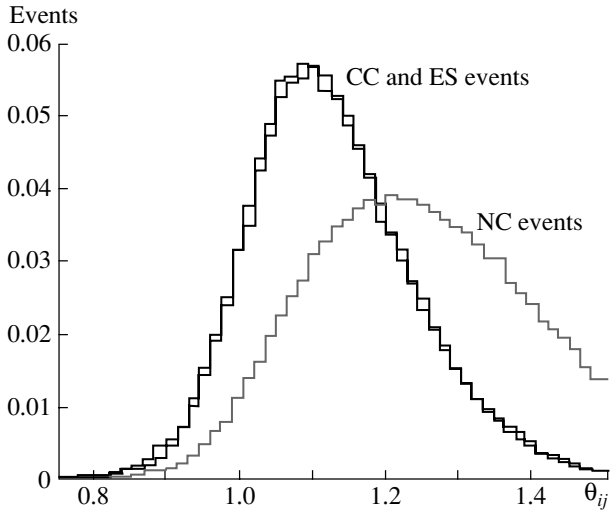

Fig. 10. Monte Carlo simulation of the mean pair angle (θ_{ij}) for CC and NC events in the salt phase of SNO.

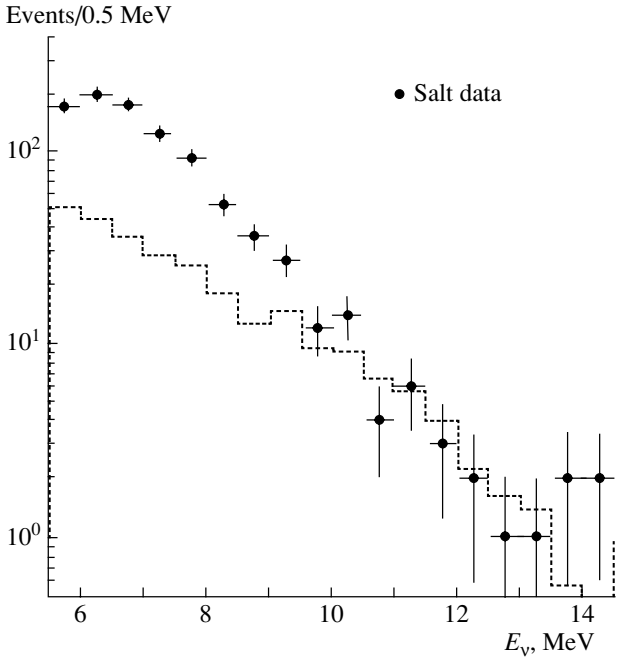

Fig. 11. Energy spectra for the salt phase of SNO compared to the pure D_2O phase. Note that extra neutron events have been added by the blindness process for the salt analysis.

information were omitted. This procedure preserves most of the ability to discriminate between oscillation solutions. A model was constructed for the expected number of counts in each energy bin by combining the neutrino spectrum, the survival probability, and the cross section with the SNO's response functions.

There are three free parameters in the fit: the total ^{8}B flux Φ_B, the difference Δm^2 between the squared masses of the two neutrino mass eigenstates, and the mixing angle θ. The flux of higher energy neutrinos from the solar *hep* reaction was fixed at 9.3×10^3 cm^{-2}s^{-1}. Figure 9*a* shows the allowed mixing parameter regions using only SNO data with no additional experimental constraints or inputs from solar models. By including flux information from the Cl and Ga experiments and the day and night spectra from the SK experiment, along with solar model predictions for the *pp*, *pep*, and ^{7}Be neutrino fluxes, the contours shown in Fig. 9*b* were produced. This global analysis strongly favors the large mixing angle (LMA) region and $\tan^2\theta < 1$. Recent results from KamLAND, which observes antineutrino oscillations from reactors, have confirmed these oscillation parameters [23].

4. SALT PHASE ANALYSIS PREVIEW

The second phase of the experiment started in June 2001, when 2 t of purified NaCl were added to the D_2O to enhance sensitivity to the detection of the NC reaction. The Cl has a large cross section for the capture of neutrons from the NC reaction and there are a number of γ produced after the capture, whose total energy is about 8.6 MeV.

It makes possible a separate measurement of CC and NC reactions through the use of pattern recognition of the two reactions. The NC events involving capture on Cl are much more isotropic (because of the emission of multiple low-energy γ rays) than the events from the CC reaction that produce a single electron with a characteristic Čerenkov cone of light. Figure 10 shows a Monte Carlo simulation of CC and NC events and shows the capability to separate CC and NC events. This variable will be used in addition to the previous variables, T_{eff}, $(R/R_{\text{AV}})^3$, and $\cos\theta_\odot$, to increase the separation power between CC and NC events. In addition, an independent measure of the NC flux will enable a better definition of the spectral shape for the CC reaction for spectral distortion.

The addition of NaCl raises the neutron detection efficiency for neutrons produced uniformly in the D_2O to about 40% when both capture efficiency and threshold are included. This is about 3 times the capture efficiency in pure D_2O. A preliminary energy spectrum for the salt phase compared to the pure D_2O phase is shown in Fig. 11. During the analysis of this phase, a blindness condition was imposed, where an unknown number of neutron events produced by muons interacting in the detector were added to the data set. Hence, the CC and NC ratio cannot be extracted from the data presented in this figure until the blindness criteria has been removed. However, the increased energy and efficiency for events associated

Table 4. The results of the signal extraction, assuming an undistorted ^{8}B spectrum

Signal	Φ_D, 10^6 cm^{-2} s^{-1}	Φ_N, 10^6 cm^{-2} s^{-1}	$\mathcal{A}$, %
CC	$1.62 \pm 0.08 \pm 0.08$	$1.87 \pm 0.07 \pm 0.10$	$+0.14 \pm 6.3^{+1.5}_{-1.4}$
ES	$2.64 \pm 0.37 \pm 0.12$	$2.22 \pm 0.30 \pm 0.12$	$-17.4 \pm 19.5^{+2.4}_{-2.2}$
NC	$5.69 \pm 0.66 \pm 0.44$	$4.63 \pm 0.57 \pm 0.44$	$-20.4 \pm 16.9^{+2.4}_{-2.5}$

with the capture on Cl can be observed, along with the increased isotropy compared to the data for the pure D_2O phase.

5. CONCLUSIONS

In conclusion, the results presented here give evidence that there is an active nonelectron flavor neutrino component in the solar neutrino flux. This is the first experimental determination of the total flux of active ^{8}B solar neutrinos, which is in good agreement with the solar model predictions. The analysis presented in this paper also showed the first direct measurement of the day–night asymmetries in the ν_e flux and the total neutrino flux. When combining the SNO results with those of other experiments in a global 2-ν flavor analysis of the MSW oscillation parameters, it was shown that the LMA solution is strongly favored.

The second phase of SNO began with the addition of NaCl to enhance the NC detection capability on May 28, 2001. The third phase of SNO will enable an extraction of the NC flux from an array of ^{3}He filled neutron detectors (NCDs) placed in the D_2O. These will detect neutrons from the NC reaction and the D_2O will detect neutrinos by the CC and ES reactions. This phase will provide a good opportunity to extract a spectral shape from the CC reaction, as well as provide a normalization for the neutron-capture contribution that remains.

ACKNOWLEDGMENTS

This research was supported by the Canadian organizations NSERC, Industry Canada, NRC, Northern Ontario Heritage Fund Corporation, INCO, AECL, and Ontario Power Generation; the US Department of Energy; and the UK PPARC.

We thank the SNO technical staff for their strong contributions.

REFERENCES

1. B. T. Cleveland *et al.*, Astrophys. J. **496**, 505 (1998).
2. K. S. Hirata *et al.*, Phys. Rev. Lett. **65**, 1297 (1990); Phys. Rev. D **44**, 2241 (1991); **45**, 2170(E) (1992); Y. Fukuda *et al.*, Phys. Rev. Lett. **77**, 1683 (1996).
3. J. N. Abdurashitov *et al.*, Zh. Éksp. Teor. Fiz. **122**, 211 (2002) [JETP **95**, 181 (2002)].
4. W. Hampel *et al.*, Phys. Lett. B **447**, 127 (1999).
5. M. Altmann *et al.*, Phys. Lett. B **490**, 16 (2000).
6. S. Fukuda *et al.*, Phys. Rev. Lett. **86**, 5651 (2001).
7. J. N. Bahcall, M. H. Pinosonneault, and S. Basu, Astrophys. J. **555**, 990 (2001).
8. A. S. Brun, S. Turck-Chièze, and J. P. Zahn, Astrophys. J. **525**, 1032 (1999); S. Turck-Chièze *et al.*, Astrophys. J. Lett. **555**, L69 (2001).
9. SNO Collab., Phys. Rev. Lett. **89**, 011301 (2002).
10. M. C. Browne *et al.*, IEEE Trans. Nucl. Sci. **46**, 873 (1999).
11. SNO Collab., Nucl. Instrum. Methods Phys. Res. A **449**, 172 (2000).
12. M. R. Dragowsky *et al.*, Nucl. Instrum. Methods Phys. Res. A **481**, 284 (2002).
13. N. Tagg *et al.*, Nucl. Instrum. Methods Phys. Res. A **489**, 178 (2002).
14. R. T. Ford, M. Sc. Thesis (Queens Univ., 1993).
15. R. T. Ford, PhD Thesis (Queen's Univ., 1998).
16. B. A. Mofat, PhD Thesis (Queen's Univ., 2001).
17. A. W. P. Poon *et al.*, Nucl. Instrum. Methods Phys. Res. A **452**, 115 (2000).
18. C. E. Ortiz *et al.*, Phys. Rev. Lett. **85**, 2909 (2000).
19. S. Nakamura, T. Sato, V. Gudkov, and K. Kubodera, Phys. Rev. C **63**, 034617 (2001); M. Butler, J.-W. Chen, and X. Kong, Phys. Rev. C **63**, 035501 (2001); G. 't Hooft, Phys. Lett. B **37B**, 195 (1971) [the M. Butler *et al.* cross section with $L_{1,A} = 5.6$ fm^3 is used].
20. SNO Collab., Phys. Rev. Lett. **87**, 071301 (2001).
21. Z. Maki, N. Nakagawa, and S. Sakata, Prog. Theor. Phys. **28**, 870 (1962).
22. V. Gribov and B. Pontecorvo, Phys. Lett. B **28B**, 293 (1969).
23. K. Eguchi *et al.*, Phys. Rev. Lett. **90**, 021802 (2003).

Physics of Atomic Nuclei, Vol. 67, No. 6, 2004, pp. 1076–1083. From Yadernaya Fizika, Vol. 67, No. 6, 2004, pp. 1104–1111.

NEUTRINO PHYSICS AND ASTROPHYSICS

Solar Neutrino Oscillation Parameters after KamLAND*

S. Goswami[**], **A. Bandyopadhyay**[1)], **and S. Choubey**[2)]

Harish-Chandra Research Institute, Chhatnag Road, Jhusi, India

Received November 17, 2003

Abstract—We explore the impact of the data from the KamLAND experiment in constraining neutrino mass and mixing angles involved in solar neutrino oscillations. In particular, we discuss the precision with which we can determine the mass squared difference $\Delta m^2_\odot$ and the mixing angle $\theta_\odot$ from combined solar and KamLAND data. We show that the precision with which $\Delta m^2_\odot$ can be determined improves drastically with the KamLAND data, but the sensitivity of KamLAND to the mixing angle is not as good. We study the effect of enhanced statistics in KamLAND as well as reduced systematics in improving the precision. We also show the effect of the SNO salt data in improving the precision. Finally, we discuss how a dedicated reactor experiment with a baseline of 70 km can improve the $\theta_\odot$ sensitivity by a large amount.

1. INTRODUCTION

Two very important results in the field of neutrino oscillations were announced in 2002. The first data from the neutral current (NC) events from the Sudbury Neutrino Observatory (SNO) experiment were announced in April 2002 [1]. Comparison of the NC event rates with the charged current (CC) event rates established the presence of a ν_μ/ν_τ component in the solar ν_e flux, reinforcing the fact that neutrino oscillation is responsible for the solar neutrino shortfall observed in the Homestake, SAGE, GALLEX/GNO, Kamiokande, and Super-Kamiokande experiments. The global analysis of solar neutrino data picked up the large mixing angle (LMA) MSW as the preferred solution [2]. The smoking-gun evidence came in December 2002 when the KamLAND experiment reported a distortion in the reactor antineutrino spectrum corresponding to the LMA parameters [3]. The induction of the KamLAND data into the global oscillation analysis resulted in splitting the allowed LMA zone into two parts (at 99% C.L.)—low-LMA lying around $\Delta m^2_\odot = 7.2 \times 10^{-5}$ eV^2, $\sin^2\theta_\odot = 0.3$ and high-LMA with $\Delta m^2_\odot = 1.5 \times 10^{-4}$ eV^2, $\sin^2\theta_\odot = 0.3$, respectively. The low-LMA solution was preferred statistically by the data [4]. The recently announced SNO data from the salt phase [5] has further disfavored high-LMA and it now appears at $>99.13\%$ C.L. [6]. Thus, the SNO and KamLAND results have heralded the birth of the precision era in the measurement of a solar neutrino oscillation parameter. In this article, we take a closer look at the precision with which we know the solar neutrino oscillation parameters at present and critically examine how precisely they can be measured with future data.

2. OSCILLATION PARAMETERS FROM SOLAR NEUTRINO DATA

In Fig. 1, we show the impact of the SNO NC data from the pure D_2O phase and the salt phase as well as combine the information from both phases on the oscillation parameters $\Delta m^2_\odot (\equiv \Delta m^2_{21})$ and $\sin^2\theta_\odot (\equiv \sin^2\theta_{12})$ from a two-flavor analysis. We include the total rates from the radiochemical experiments Cl and Ga (GALLEX, SAGE, and GNO combined) [7] and the 1496-day 44-bin SK Zenith angle spectrum data [8]. For the pure D_2O phase, we use the CC + ES (electron scattering) + NC spectrum data, whereas for the salt phase we use the published CC, ES, and NC rates [6]. The details of the analysis procedure can be found in [9]. Also shown superimposed on these curves are the isorates of the CC/NC ratio. We find the following:

The upper limit on $\Delta m^2_\odot$ tightens with increased statistics when the salt data is added to the data from the pure D_2O phase.

The upper limit on $\sin^2\theta_\odot$ tightens. For ^{8}B neutrinos undergoing adiabatic MSW transition in the sun, $R_{CC}/R_{NC} \sim \sin^2\theta_\odot$. The SNO salt data correspond

*This article was submitted by the authors in English.

[1)]Theory Group, Saha Institute of Nuclear Physics, 1/AF, Bidhannagar, Calcutta, India; e-mail: abhi@theory.saha.ernet.in

[2)]INFN, Sezione di Trieste and Scuola Internazionale Superiore di Studi Avanzati, Trieste, Italy; e-mail: sandhya@he.sissa.it

[**]e-mail: sruba@mri.ernet.in

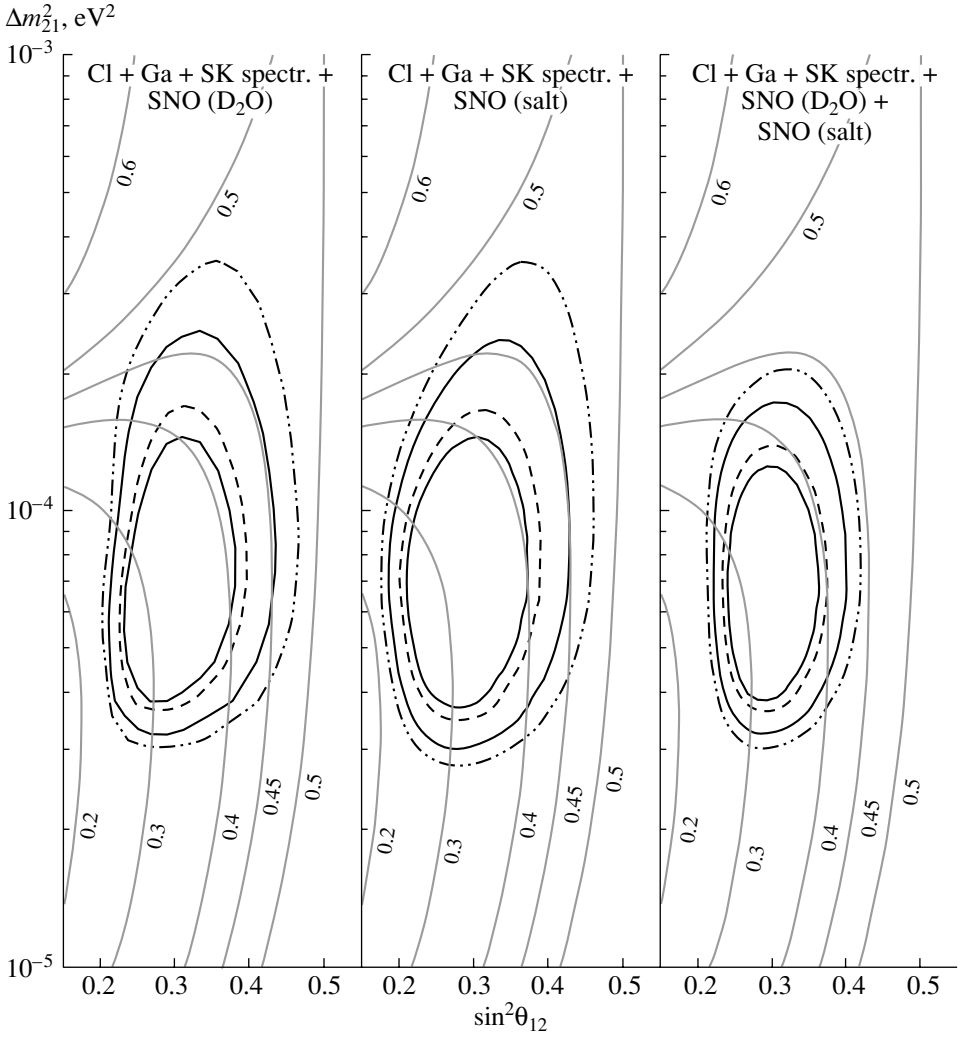

Fig. 1. The 90, 95, 99, and 99.73% C.L. allowed regions in the $\Delta m^2_{21} - \sin^2\theta_{12}$ plane from global χ^2 analysis of the data from solar neutrino experiments. We use $\Delta\chi^2$ values to plot the C.L. contours corresponding to a two-parameter fit. Also shown are the lines of constant CC/NC event rate ratio $R_{\mathrm{CC/NC}}$.

to a lower value of the CC/NC ratio, which results in a shift of $\sin^2\theta_\odot$ towards smaller values.

3. IMPACT OF KamLAND DATA ON OSCILLATION PARAMETERS

The KamLAND detector measures the reactor antineutrino spectrum from Japanese commercial nuclear reactors situated at a distance of 80–800 km. In this section, we present our results of a global two-generation χ^2 analysis of solar + KamLAND spectrum data. For details, we refer to our analysis in [4, 10].

Figure 2 shows the allowed regions obtained from global solar and 162 t yr KamLAND spectrum data. As is seen from the leftmost panel of Fig. 2, the inclusion of the KamLAND data breaks the allowed LMA region into two parts at 99% C.L. The low-LMA region is centered around a best-fit $\Delta m^2_\odot$ of 7.2×10^{-5} eV^2 and the high-LMA region is centered around 1.5×10^{-4} eV^2. At 3σ, the two regions merge. The low-LMA region is statistically preferred over the high-LMA region. With the addition of the SNO salt data, the high-LMA solution becomes disfavored at 99.13% C.L. In Table 1, we show the allowed ranges of $\Delta m^2_\odot$ and $\sin^2\theta_\odot$ from solar and combined solar + KamLAND analysis. We find that Δm^2_{21} is further constrained with the addition of the KamLAND data, but $\sin^2\theta_{12}$ is not constrained any further.

4. CLOSER LOOK AT KamLAND SENSITIVITY

In Table 2, we take a closer look at the sensitivity of the KamLAND experiment to the parameters Δm^2_{21}

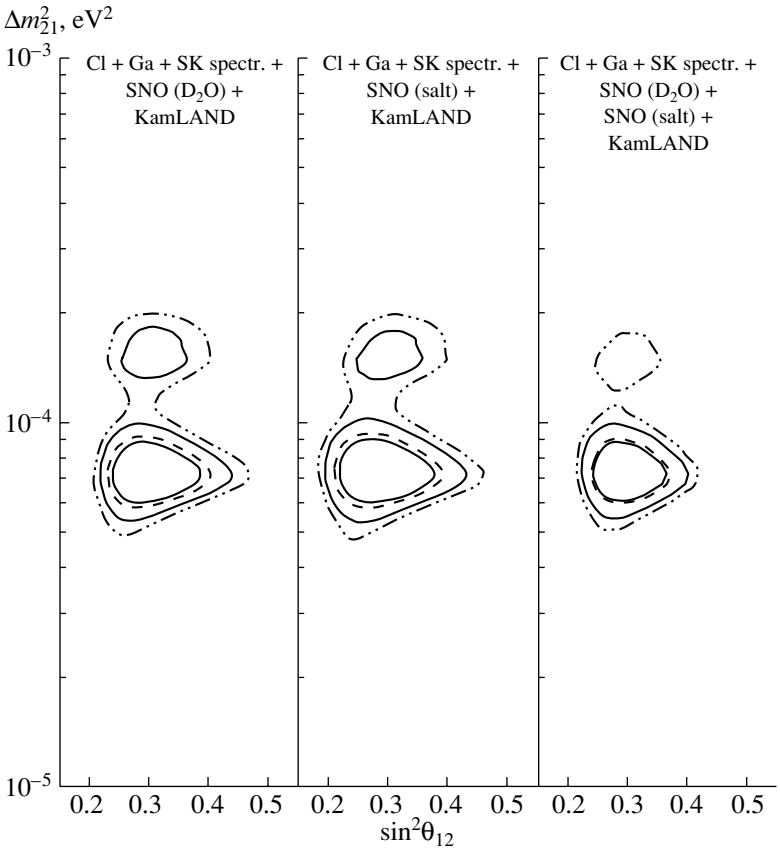

Fig. 2. The 90, 95, 99, and 99.73% C.L. allowed regions in the $\Delta m^2_{21}-\sin^2\theta_{12}$ plane from a global χ^2 analysis of solar and KamLAND data. We use the $\Delta\chi^2$ values corresponding to a two-parameter fit to plot the C.L. contours.

and $\sin^2\theta_{12}$ with the current as well as simulated future data and examine how far the sensitivity can improve with the future data. We define the percent spread in oscillation parameters (prm) as

$$\text{Spread} = \frac{\text{prm}_{\max} - \text{prm}_{\min}}{\text{prm}_{\max} + \text{prm}_{\min}} \times 100\% \qquad (1)$$

and determine this quantity for the current solar and KamLAND data as well as increase the KamLAND statistics. The current systematic error in KamLAND is 6.42% and the largest contribution comes from the uncertainty in fiducial volume. This is expected to improve with the calibration of the fiducial volume, and we use a 5% systematic error for 1 kt yr simulated KamLAND data and 3% systematic error for 3 kt yr simulated KamLAND data. The table reveals the tremendous sensitivity of KamLAND to Δm^2_{21}. The addition of the present KamLAND data improves the spread in Δm^2_{21} to 30% from 68% obtained with only solar data. With 1 kt yr KamLAND data, it improves to 10%, and if we increase the statistics to 3 kt yr, then the uncertainty in Δm^2_{21} reduces to 6%. However, the sensitivity of KamLAND to the parameter θ_{12} does not look as good. The addition of the current KamLAND data to the global solar analysis does not improve the spread in $\sin^2\theta_{12}$. With reduction of the systematic error to 5%, the spread with 1 kt yr statistics improves to 26%, and even with a very optimistic value of 3% for the systematic uncertainty and a substantial increase in statistics to 3 kt yr, the KamLAND data fails to constrain θ_{12} much better than the current solar neutrino experiments.

In Fig. 3, we compare the allowed areas computed with a spectrum simulated at $\Delta m^2_{21} = 7.2 \times 10^{-5}$ and 3.5×10^{-5} eV^2. We show limits for the current KamLAND systematic uncertainty of 6.42% and a very optimistic systematic uncertainty of just 2%. The percent spread in uncertainty for the spectrum simulated at 7.2×10^{-5} eV^2 with 6.42% systematic uncertainty is 37%, while for the 3.5×10^{-5} eV^2 case the spread is 25%. The effect of reducing the systematics to 2% results in the spread coming down to 32 and 19%, respectively [11]. We would like to mention that Fig. 3 uses the CC, NC, and ES rates from the D_2O and not the latest results from the salt phase. However, the purpose of this figure is to compare the

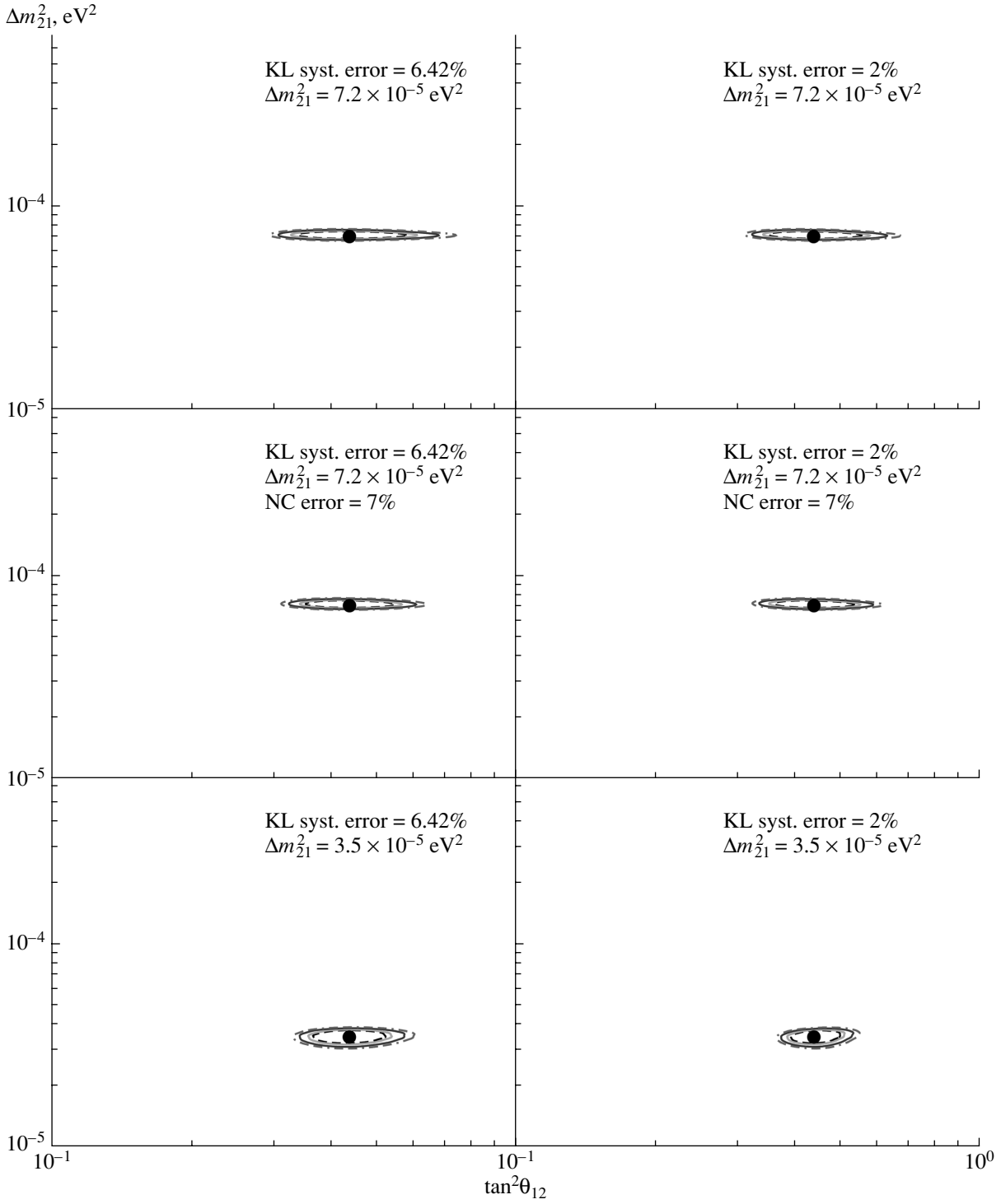

Fig. 3. The contours for the combined analysis using the solar and 3 kt yr simulated KamLAND spectrum. The first two rows of panels correspond to spectrum simulated at 7.2×10^{-5} eV^2, while the lowermost row of panels are for KamLAND data simulated at $\Delta m^2_{21} = 3.5 \times 10^{-5}$ eV^2.

spread in $\sin^2\theta_{12}$ obtained for the two different values of Δm^2_{21} and the use of the SNO salt phase data is not going to change the relative spreads significantly. We also present in the middle panel of Fig. 3 the allowed areas drawn using a 7% uncertainty in the NC rate. The uncertainty in the NC rate from the D_2O (salt) phase data is 12% (9%).

To trace the reason why the θ sensitivity is better

Table 1. The best-fit values of the solar neutrino oscillation parameters, obtained using different combinations of data sets (Shown also are the 99% C.L. allowed ranges of the parameters from the different analyses.)

Data set used	Best-fit parameters		99% C.L. allowed range	
	Δm^2_{21}, 10^{-5} eV^2	$\sin^2\theta_\odot$	Δm^2_{21}, 10^{-5} eV^2	$\sin^2\theta_\odot$
Cl + Ga + SK + D_2O	6.06	0.29	3.2–24.5	0.21–0.44
Cl + Ga + SK + salt	6.08	0.28	3.0–23.7	0.19–0.43
Cl + Ga + SK + D_2O + salt	6.06	0.29	3.2–17.2	0.22–0.40
Cl + Ga + SK + D_2O + KL	7.17	0.3	5.3–9.9	0.22–0.44
Cl + Ga + SK + D_2O + salt + KL	7.17	0.3	5.3–9.8	0.22–0.40

Table 2. The range of parameter values allowed at 99% C.L. and the corresponding spread

Data set used	99% C.L.			
	range of Δm^2_{21}, 10^{-5} eV^2	spread of Δm^2_{21}, %	range of $\sin^2\theta_{12}$	spread in $\sin^2\theta_{12}$, %
Only solar	3.2–17.0	68	0.22–0.40	29
Solar + 162 t yr KL	5.3–9.8	30	0.22–0.40	29
Solar + 1 kt yr KL	6.5–8.0	10	0.23–0.39	26
Solar + 3 kt yr KL	6.8–7.6	6	0.24–0.37	21

at 3.5×10^{-5} eV^2 in Fig. 4, we plot the probability vs. distance for energy fixed at 4 MeV. The figure shows that the average distance of ~150 km of KamLAND corresponds to a maximum in the probability for 7.2×10^{-5} eV^2, while at 3.5×10^{-5} eV^2 it corresponds to a minimum.

The relevant survival probability for KamLAND is given by the vacuum oscillation expression

$$P_{ee} = 1 - \sum_i \sin^2 2\theta_\odot \sin^2\left(\frac{\Delta m^2_{21} L_i}{4E}\right), \quad (2)$$

where L_i stands for the different reactor distances and

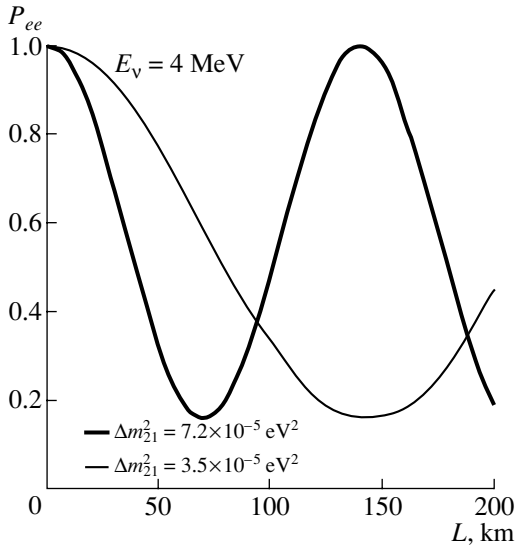

Fig. 4. The probability vs. distance for an average energy of 4 MeV for $\Delta m^2_{21} = 7.2 \times 10^{-5}$ and 3.5×10^{-5} eV^2.

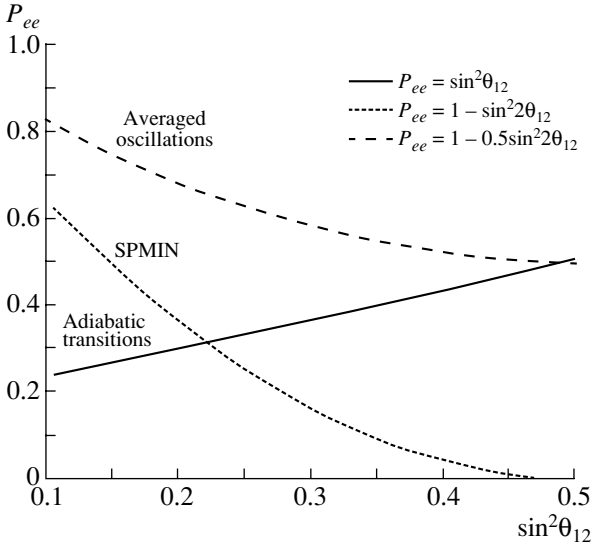

Fig. 5. The survival probability P_{ee} as a function of $\sin^2\theta_{12}$.

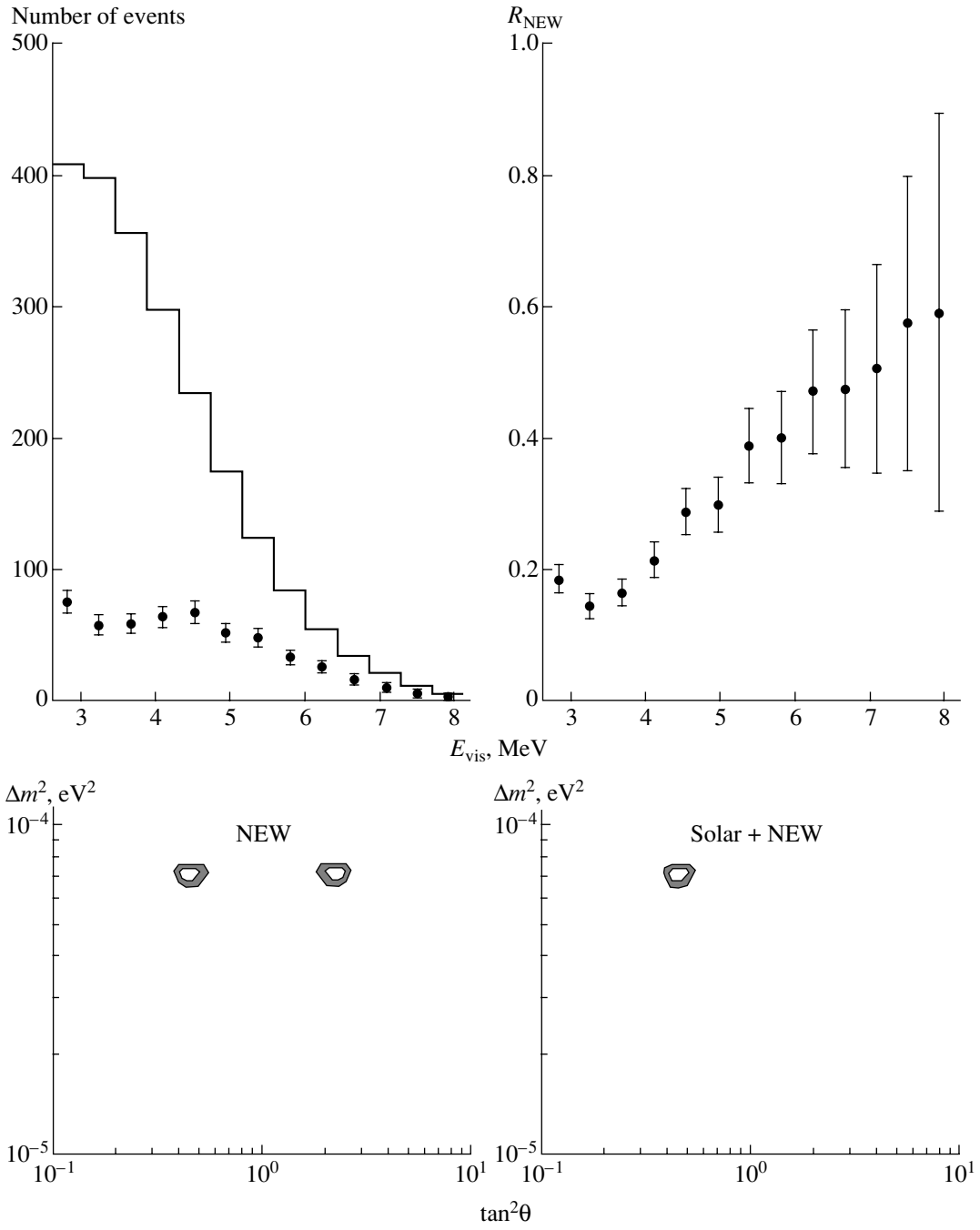

Fig. 6. The spectrum and allowed regions for a new reactor experiment with a source detector distance of 70 km.

one needs to do an averaging over these. Three limits can be distinguished:

$\sin^2(\Delta m^2_{21} L_i/4E) = 0$—we get a survival probability maximum (SPMAX);

$\sin^2(\Delta m^2_{21} L_i/4E) = 1$—we get a survival probability minimum (SPMIN);

$\sin^2(\Delta m^2_{21} L_i/4E) = 1/2$—we get averaged oscillation.

In the LMA region, the solar ^{8}B neutrinos undergo adiabatic MSW transition and the survival probability can be approximated as

$$P_{ee}(^8\mathrm{B}) \approx \sin^2\theta_\odot. \qquad (3)$$

In contrast, the low-energy *pp* neutrinos do not undergo any MSW resonance and the survival probability, is just the averaged oscillation probability in vacuum.

In Fig. 5, we plot the θ dependence of the adiabatic

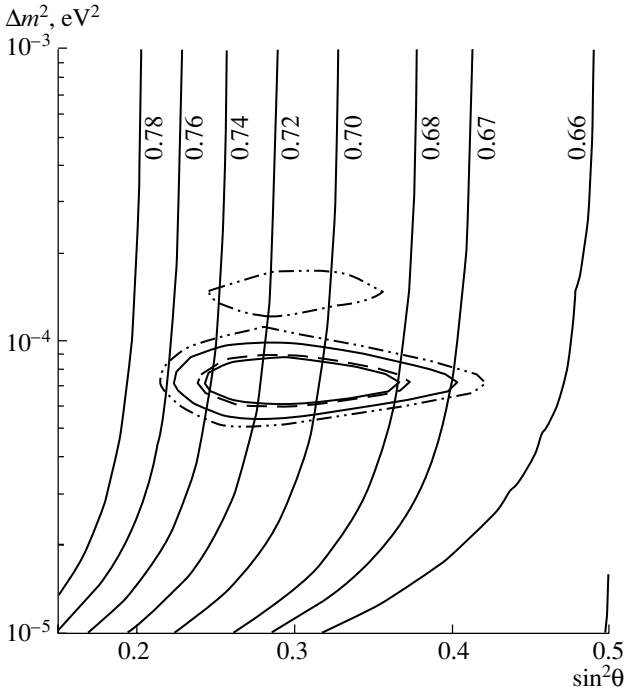

Fig. 7. The isorates for a *pp*-scattering experiment.

MSW probability, as well as the probability for the SPMIN and averaged oscillation case [11]. The figure shows that for large mixing angles close to maximal, the adiabatic case has the maximum sensitivity. For mixing angles not too close to maximal ($\sin^2\theta_\odot < 0.38$), P_{ee} for the SPMIN case has the sharpest dependence on the mixing angle and the $\theta_\odot$ sensitivity is maximal. Since the 99% C.L. allowed values of $\theta_\odot$ is within the range $0.22 < \sin^2\theta_\odot < 0.44$, SPMIN seems most promising for constraining θ_{12}. On the other hand, at SPMAX, the oscillatory term goes to zero and the θ_{12} sensitivity gets smothered. Since in the statistically significant region the KamLAND probability corresponds to an SPMAX for the best-fit value of 7.2×10^{-5} eV^2, the θ sensitivity of KamLAND is not as good as its Δm^2_{21} sensitivity. For this value of Δm^2_{21}, the SPMIN comes at 70 km.

5. A DEDICATED REACTOR EXPERIMENT FOR $\sin^2\theta_\odot$

We show in Fig. 6 the constraints on the mass and mixing parameters obtained using a "new" dedicated reactor experiment whose baseline is tuned to an oscillation SPMIN [11]. We use the antineutrino flux from a reactor a la the Kashiwazaki nuclear reactor in Japan with a power of about 25 GW. We assume an 80% efficiency for the reactor output and simulate the 3 kt yr data at the low-LMA best fit for a KamLAND-like detector placed 70 km from the reactor source and having systematic errors of only 2%. The top-left panel of Fig. 6 shows the simulated spectrum data. The histogram shows the expected spectrum for no oscillations. $E_{\rm vis}$ is the "visible" energy of the scattered electrons. The top-right panel gives the ratio of the simulated oscillations to the no-oscillation numbers. The sharp minimum around 3–4 MeV is clearly visible. The bottom-left panel gives the C.L. allowed areas obtained from this new reactor experiment data alone. With 3 kt yr statistics, we find a marked improvement in the $\theta_\odot$ bound with the 99% range $0.39 < \tan^2\theta_\odot < 0.52$ giving a spread of 14%. The "dark side" solution appearing in the bottom-left panel because of the $\theta_\odot$–$(\pi/2 - \theta_\odot)$ ambiguity in the vacuum oscillations probability is ruled out in the bottom-right panel by the solar neutrino data. Recently, sites of reactor neutrino experiments with a source reactor distance of 70 km have been discussed in [12]. Also in Japan, a new reactor complex SHIKA-2 at ~88 km (close to SPMIN) will start in 2006 (see, however, [13]).

6. OTHER FUTURE EXPERIMENTS

In Fig. 7, we show the lines of constant rate/SSM predicted in a generic LowNU electron scattering experiment sensitive to *pp* neutrinos [14]. At these low energies of neutrinos, the survival probability in the LMA zone is $\approx 1 - \sin^2(2\theta)/2$ and has almost no sensitivity to Δm^2_{21}. But the $\sin^2\theta_\odot$ sensitivity is quite good, and thus these experiments may have a fair chance to pin down the value of the mixing angle θ_{12}, if they can keep the errors low.

7. CONCLUSIONS

The KamLAND experiment has not only confirmed the LMA solution to the solar neutrino problem, but it has also narrowed down the allowed range of $\Delta m^2_\odot$ considerably owing to its sensitivity to the spectral distortion driven by this parameter. However, the $\theta_\odot$ sensitivity of KamLAND is not as good. A baseline is important to identify which parameters would be best determined. We discuss that an SPMIN in the vacuum oscillation probability is important for the determination of the mixing angle. For the current best-fit $\Delta m^2_\odot$ in the low-LMA region, SPMIN comes at a distance of 70 km. Note that, if high-LMA happens to be the true solution, contradicting the current trend from the solar neutrino data, then the SPMIN will correspond to a distance of 20 km [15]. We propose a dedicated 70-km baseline reactor experiment to measure $\theta_\odot$ down to ~10% accuracy. LowNU experiments could be important for precise determination of $\theta_\odot$ if the experimental errors are low.

ACKNOWLEDGMENTS

This talk is based on the work [11]. The updated analysis including the SNO salt results was done in collaboration with S.T. Petcov and D.P. Roy and we would like to acknowledge them. This work was supported in part by the Italian MIUR and INFN under "Fisica Astroparticellare" (S.C.).

REFERENCES

1. Q. R. Ahmad *et al.* (SNO Collab.), Phys. Rev. Lett. **89**, 011301 (2002); **89**, 011302 (2002).
2. A. Bandyopadhyay, S. Choubey, S. Goswami, and D. P. Roy, Phys. Lett. B **540**, 14 (2002).
3. K. Eguchi *et al.* (KamLAND Collab.), Phys. Rev. Lett. **90**, 021802 (2003).
4. A. Bandyopadhyay *et al.*, hep-ph/0212146.
5. S. N. Ahmed *et al.* (SNO Collab.), nucl-ex/0309004.
6. A. Bandyopadhyay *et al.*, hep-ph/0309174.
7. B. T. Cleveland *et al.*, Astrophys. J. **496**, 505 (1998); J. N. Abdurashitov *et al.* (SAGE Collab.), astro-ph/0204245; W. Hampel *et al.* (GALLEX Collab.), Phys. Lett. B **447**, 127 (1999); M. Altmann *et al.* (GNO Collab.), Phys. Lett. B **492**, 16 (2000); C. M. Cattadori, Nucl. Phys. B (Proc. Suppl.) **110**, 311 (2002).
8. S. Fukuda *et al.* (Super-Kamiokande Collab.), Phys. Lett. B **539**, 179 (2002).
9. S. Choubey, A. Bandyopadhyay, S. Goswami, and D. P. Roy, hep-ph/0209222.
10. A. Bandyopadhyay *et al.*, hep-ph/0211266.
11. A. Bandyopadhyay, S. Choubey, and S. Goswami, Phys. Rev. D **67**, 113011 (2003).
12. C. Bouchiat, hep-ph/0304253.
13. A. Bandyopadhyay, S. Choubey, S. Goswami, and S. T. Petcov, hep-ph/0309236.
14. For a discussion on LowNU experiments see, e.g., S. Schönert, *Talk Given at Neutrino 2002, Munich, Germany*, http://neutrino2002.ph.tum.de.
15. S. Choubey, S. T. Petcov, and M. Piai, hep-ph/0306017.

Physics of Atomic Nuclei, Vol. 67, No. 6, 2004, pp. 1084–1091. From Yadernaya Fizika, Vol. 67, No. 6, 2004, pp. 1112–1119.

NEUTRINO PHYSICS AND ASTROPHYSICS

Status and Prospects of the MINOS Experiment*

R. Saakyan**
(for the MINOS Collaboration)
University College London, London, United Kingdom
Received November 17, 2003

Abstract—The MINOS long-baseline neutrino oscillation experiment has completed the installation and commissioning of the Far Detector at the Soudan mine, while the construction of the Near Detector at the Fermi National Accelerator Laboratory is under way. We report on the current status of the experiment, the projected schedule, and its physics capabilities. © *2004 MAIK "Nauka/Interperiodica".*

1. INTRODUCTION

The Super-Kamiokande and SNO experiments have produced very strong evidence for nonzero neutrino mass by studying atmospheric and solar neutrinos [1, 2]. Recently, the KamLAND reactor antineutrino experiment has confirmed the existence of neutrino flavor oscillations and has set stringent limits on the neutrino mass-mixing mechanisms [3]. The evidence for the neutrino oscillations has shown the necessity of second-generation experiments using a well-controlled and understood neutrino source. The MINOS (Main Injector Neutrino Oscillation Search) experiment [4] is a long-baseline neutrino oscillation experiment utilizing a neutrino beam produced at FNAL and directed at a 5.4-kt detector (Far Detector) located 731 km away in the Soudan mine, northern Minnesota. A smaller 980-t detector (Near Detector) will measure the neutrino beam at the Fermilab site, where no effect from neutrino mixing is expected. Comparison between the two detectors will allow the measurement of the oscillation parameters with a high accuracy providing that their true values are within the region indicated by Super-Kamiokande [1].

2. NEUTRINO BEAM

The Main Injector is a high-intensity proton synchrotron which has the multiple purpose of producing the antiprotons for the Tevatron, preaccelerating the protons and antiprotons before their injection into the Tevatron, and providing an intense beam for fixed target experiments. The NuMI (Neutrinos at Main Injector) neutrino beam is obtained from the decay of pions and kaons produced in the interactions of 120-GeV protons with a carbon target. Single-turn extraction will be used with a pulse length of 10 μs. The secondary mesons will be focused by two parabolic horns and allowed to decay in a 675-m-long evacuated decay pipe. Combining this with the 50-m distance from the target to the start of the decay pipe gives a 725-m-long decay region for the beam line. The NuMI beam line provides an opportunity for adjusting the energy of the neutrino beam because the distance between the two horns can be changed by moving the second horn with respect to the first. By adjusting the horn positions and currents, one can select three different neutrino energy regimes: "low" ($\langle E_\nu \rangle \sim 3$ GeV), "medium" ($\langle E_\nu \rangle \sim 6$ GeV), and "high" ($\langle E_\nu \rangle \sim 15$ GeV). The energy spectrum of measured Far Detector charge-current (CC) neutrino events without oscillations for all three beam energy configurations is shown in Fig. 1. The current plan calls for using the low-energy beam. This is because of the relatively low central value of $\Delta m^2 = 0.0025$ eV^2, which is the current best fit value from Super-Kamiokande measurements [1]. This value is consistent with the less precise results from other atmospheric neutrino experiments and the current best value from the K2K experiment [5].

The initially anticipated proton flux was 4×10^{13} protons per pulse with a repetition rate of 1.9 s, which would give a total number of protons on target (p.o.t.) of 7.4×10^{20} over two years of data taking. The physics running with NuMI beam neutrinos will start in 2005 and the number of protons which can be realistically expected by this time is 2.5×10^{20} p.o.t. per year. Because high proton intensity is vitally important for the physics measurements targeted by the MINOS experiment, as well as for all accelerator-based neutrino experiments, the Collaboration has proposed a plan for a five-year run envisaging a

*This article was submitted by the author in English.
**e-mail: saakyan@hep.ucl.ac.uk

steady increase in the number of delivered protons starting early in 2005 [6]. Table 1 summarizes the proton request made to FNAL in [6]. 7.4×10^{20} p.o.t. combined with the low-energy configuration would yield about 5000 beam-related CC neutrino events in the Far Detector in the absence of oscillations. The statistics would be much higher in the high-energy beam configuration: about 30 000 ν_μCC events are expected in this case.

Substantial progress has been made in the NuMI beam line construction at FNAL. All the tunneling work was finished, and the decay pipe was installed and encased in concrete. In October 2003, the outfitting of the Target Hall was complete. The production of the beam line technical components is under way and on schedule. The NuMI beam line will be completed by December 2004. The first three months of 2005 will be used for low-intensity beam commissioning. The physics running with NuMI neutrinos is expected to start in April 2005.

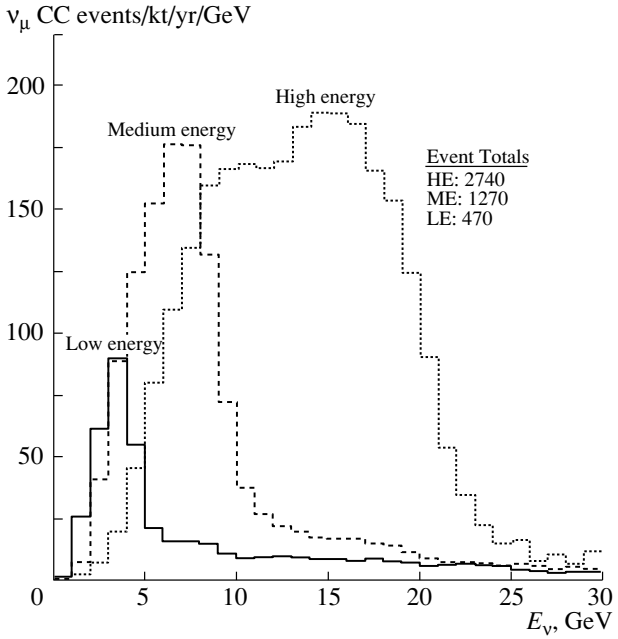

Fig. 1. Neutrino interaction spectra in the Far Detector predicted for three different focusing conditions corresponding to high-, medium-, and low-energy beam.

3. MINOS DETECTORS

The MINOS design includes two detectors: the Far Detector and the Near Detector. One can obtain an unbiased pattern of oscillations comparing the Near/Far neutrino rates and energy spectra. The detectors have been designed to be as similar as possible. They are iron/scintillator sampling calorimeters with identical longitudinal and transverse granularity and an average toroidal magnetic field of about 1.3 T. The 2.54-cm-thick iron plates are interleaved with scintillator planes composed of 4.1-cm-wide, 1.0-cm-thick strips. The strip orientation differs by 90° in successive planes so as to provide U and V coordinate measurements, Z being the number of the plane. The scintillator is commercially extruded polystyrene. A thin TiO_2 loaded layer has been coextruded on the outside to provide a reflective surface layer and a protective layer for handling. Each strip has a groove about 2 mm deep and 1.3 mm wide located in the center of one wide side. A green wavelength-shifting fiber, 1.2 mm in diameter, is glued into the groove. The light produced in the scintillator is trapped in the fiber, shifted in frequency, and delivered to the photomultipliers. Although the principal design of both detectors is very similar, there are differences reflecting the fact that experimental conditions at the near and far site are not identical.

3.1. Far Detector

The MINOS Far Detector is located in a specially excavated cavern in the Soudan mine 690 m below the surface. The detector is composed of 485 iron/scintillator octagonal modules giving a total mass of 5.4 kt. The detector is split up into two independent supermodules, each one toroidally magnetized by a current-carrying coil threaded through a hole through the center of the supermodule. A photograph of the MINOS detector in the Soudan mine is shown in Fig. 2. The scintillator strips in the Far Detector are read out from both ends. Clear fibers are used to transport the light from the green fibers to 16-pixel Hamamatsu M16 photomultiplier tubes. Each pixel is 4 × 4 mm and is coupled to eight fibers from eight different scintillator strips from the same plane but spaced about 1 m apart. Such multiplexing provides a substantial reduction in cost of the photomultipliers and readout electronics. The set of strips connected to a given pixel is different at the two ends, allowing one to "demultiplex" the event using the resulting pattern difference, i.e., to identify which strips were responsible for a particular event.

A detailed GEANT-based Monte Carlo simulation of the MINOS detector and experimental measurements with the MINOS Calibration Detector (see below) give an energy resolution σ/E of approximately $22\%/\sqrt{E}$ for electromagnetic showers

Table 1. Requested number of protons on target per year of MINOS running

Year	2005	2006	2007	2008	2009	Total
Protons $\times 10^{-20}$	2.5	3.8	5.0	6.5	7.2	25

Fig. 2. MINOS Far Detector in the Soudan mine (downstream part of the second supermodule).

and $55\%/\sqrt{E}$ for hadronic showers. The magnetic field allows measurement of the muon momentum by curvature (12% resolution for a 10-GeV muon) as well as by range for stopping muons ($\sim$6%).

The installation of the Far Detector was completed in July 2003. Both supermodules have been magnetized, commissioned, and taking atmospheric neutrino and cosmic muon data since summer 2003. It is worth noting that MINOS is the first large underground neutrino experiment using a magnetic field. Even though the statistical significance for the atmospheric neutrino measurement will be below that of Super-Kamiokande, MINOS will be able to measure the charge of the muons as well as the energy of through-going and partially contained events. Over a few months of data taking, the Far Detector observed a number of atmospheric neutrino events including a dozen upward-going muons generated by neutrino interactions with the rock under the detector. Figure 3 shows a $1/\beta$ distribution ($\beta = v/c$ is the speed of the muon) of the muons detected in the detector and reconstructed using developed tracking algorithms.

Table 2. Expected number of atmospheric neutrino and antineutrino events in 24 kt yr running of the Far Detector corresponding to oscillation parameters $\Delta m^2_{23} = 0.003\ \mathrm{eV}^2$, $\sin^2 2\theta_{23} = 1$

Reconstructed event types	Contained vertex with muon	Upgoing muon
Neutrino	440	280
Antineutrino	260	120

This measurement is possible thanks to a good timing resolution of the detector. The events corresponding to $\beta \approx -1$ are from the upward-going muons. In order to reduce the background coming from vertical muons entering the detector parallel to the planes and mimicking neutrino events, the MINOS scintillator modules were installed on top of the detector. The modules serve as a veto shield and allow the tagging of these muons.

MINOS will be the first experiment to compare directly atmospheric ν and $\tilde{\nu}$ oscillations, which may shed some light on CPT violation in the neutrino sector. Table 2 shows the expected number of events in 24 kt yr of running for neutrino and antineutrino interactions in the Far Detector provided that the oscillation parameters agree reasonably well with those predicted by Super-Kamiokande.

3.2. Near Detector

The Near Detector is functionally identical to the Far Detector, although its physical design has some different features due to the differences in characteristics of the neutrino beam at the two sites. Chiefly, these are much higher rates and a slightly lower average energy of the neutrino beam at the near site compared to the far site due to the effect of beam divergence. The detector has the same composition and modularity as the Far Detector and is composed of 282 "squashed" octagon planes giving a mass of 980 t. The detector is divided into two parts: 120-plane calorimeter consisting of "veto," "target," and "hadron spectrometer" regions and 162-plane muon spectrometer (Fig. 4). In the calorimeter section, four-fifths of the planes are partially instrumented around the beam fiducial region; every fifth plane is fully instrumented. Every fifth plane in the muon spectrometer section is fully instrumented. One-sided optical readout with no optical summing will be used. The fibers will be read out by Hamamatsu M64 tubes (64 2×2 mm pixels). The average magnetic field seen by a muon will be practically identical in both the Near Detector and the Far Detector. The Near Detector will be used to study the beam carefully, to measure ν_e contamination, and to understand the beam at the Far Detector site, which will substantially reduce the systematic uncertainty of the prediction. Outfitting of the Near Detector hall is underway and beneficial occupancy is expected in late January 2004. The Near Detector planes are completely fabricated and installation in the hall will start in February 2004 and will take eight months.

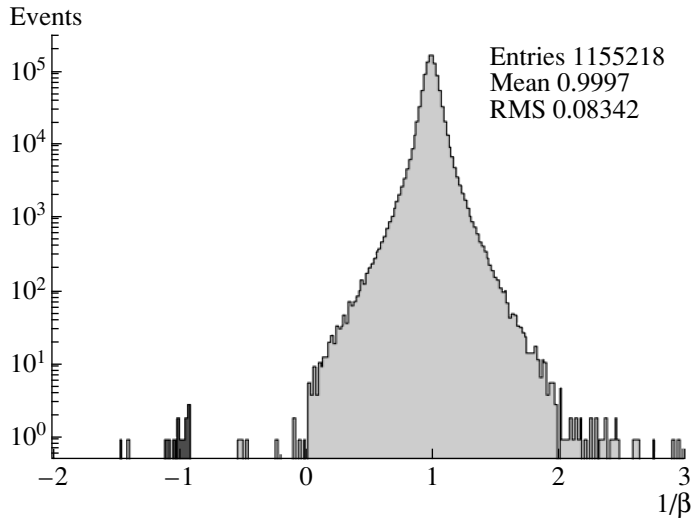

Fig. 3. $1/\beta$ distribution of upward- and downward-going muons observed in the MINOS Far Detector.

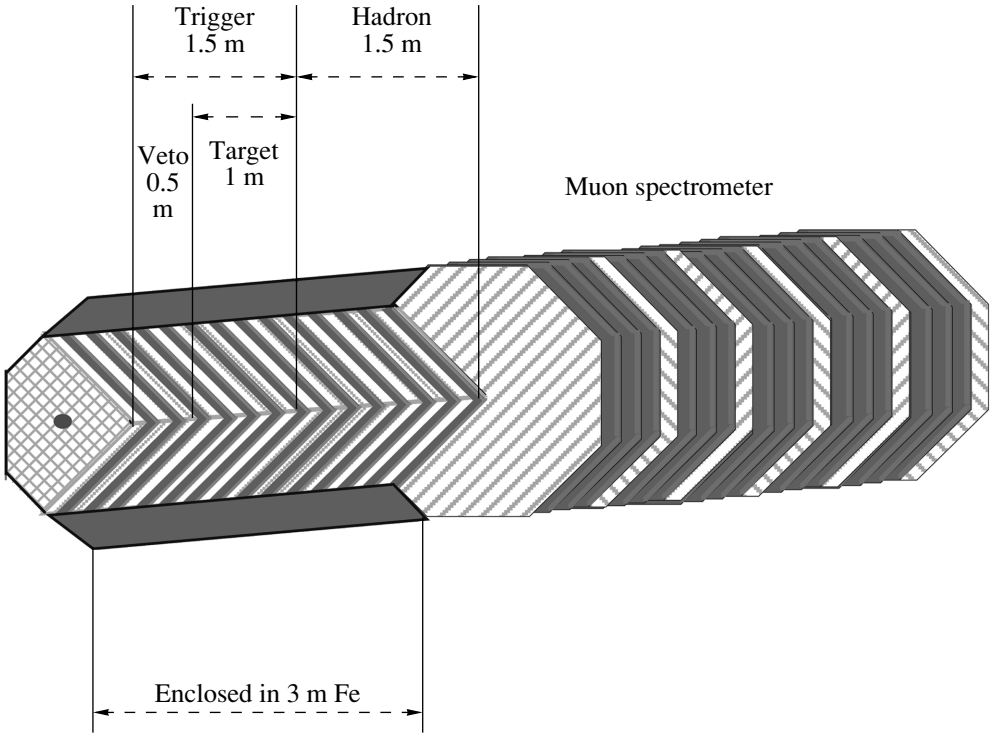

Fig. 4. Sketch of the MINOS Near Detector.

4. CALIBRATION

The two MINOS detectors must have a relative energy calibration of 2% in order to reduce systematic errors to less than the expected statistical errors on the oscillation parameters. This will be accomplished in several stages. Any nonlinearity in the readout, as well as any short-term changes in PMT gain, will be measured by injecting light from pulsed LEDs into the readout chain [7]. Cosmic-ray muons will be used to perform the strip-to-strip calibration and the relative calibration between the Near Detector and the Far Detector.

Finally, a comparison of the energy deposition by muons with that from electromagnetic and hadronic showers will be carried out with a smaller detector (the Calibration Detector) which is a replica of the MINOS detectors but with a more manageable size. At the time of writing (October 2003), the Calibration

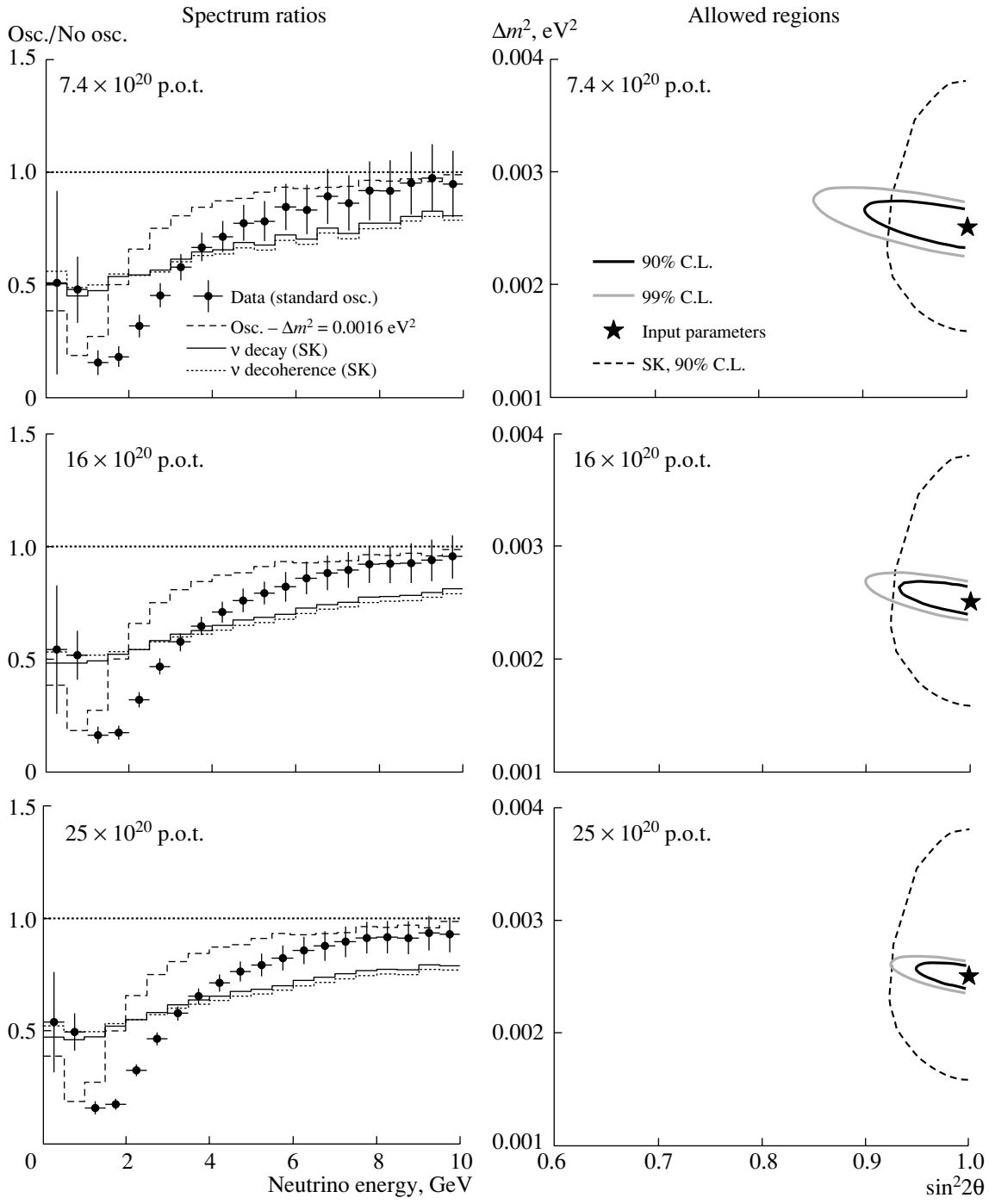

Fig. 5. Oscillation measurement for different number of p.o.t. which MINOS can make with the actual values of oscillation parameters $\Delta m^2_{23} = 0.0025$ eV^2 and $\sin^2 2\theta_{23} = 1$ (see text for details).

Detector has just finished its three-year program of data taking in the T11 and T7 test beams at CERN. The detector was exposed to a beam of electrons, pions, muons, and protons with momenta ranging from 0.4 to 10 GeV. It was equipped with both Far and Near Detector electronics in order to understand and to calibrate out the differences in the readout. An unprecedented amount of data was collected and a preliminary analysis has set the energy scale of the Far Detector for use in the energy reconstruction of atmospheric neutrino events. The energy resolution measured with the Calibration Detector confirmed the Monte Carlo expectations which are reported in

the Far Detector subsection. A more detailed data analysis of the collected data is under way.

5. PHYSICS GOALS AND SENSITIVITY

Large statistics and well-controlled systematics give MINOS powerful physics tools to study neutrino oscillation phenomena. The experiment will address the following issues:

An unambiguous demonstration of the oscillation mechanism through measurement of the energy distribution of ν_μCC events with $\nu_\mu \to \nu_\tau$ being the dominant mode. In this case, MINOS should see the disappearance in the ν_μCC sample without loss of neutral-current (NC) events and without appearance in the ν_e CC sample.

Precise measurement (at the roughly 10% level) of the oscillation parameters Δm^2 and $\sin^2 2\theta$ for the dominant $\nu_\mu \to \nu_\tau$ mode. The primary measurement for this is the comparison of rates and spectra of the CC events in the Far Detector and the Near Detector.

Measurement or improvement of the limit on the $\nu_\mu \to \nu_e$ oscillation mode. The ν_e CC appearance can be detected using topological criteria for electromagnetic shower identification.

Studying possible contributions from more exotic hypotheses such as neutrino decay [8], extra dimensions [9], or decoherence [10].

Below, we shall elaborate on some of these studies in more detail. The Collaboration has provided updated physics sensitivity curves according to the five-year MINOS run plan described above [6]. The sensitivity figures presented here are based on 7.4, 16, and 25×10^{20} total p.o.t.

$\nu_\mu \to \nu_\tau$. Neutrino oscillations will selectively deplete the ν_μ flux at certain energies. The highest energy at which maximal depletion occurs is dependent only on Δm^2, and the extent of the depletion is determined by $\sin^2 2\theta$. A measurement of the ν_μ CC energy spectrum in the Far Detector and its comparison with the unoscillated CC spectrum derived from the Near Detector will therefore yield the mixing parameters directly.

The selection of ν_μ CC events in MINOS depends primarily on identification of an event which contains a relatively clean and long track which is consistent with a muon. This is relatively straightforward at high energies, where most muons in such events travel sufficiently far to stand out clearly beyond the "shower region" of the interaction. At lower energies, more events are quasielastic and these events are generally easy to identify as CC events. However, at low energies, some NC events, where a single pion is produced or carries most of the momentum of the final state, can appear somewhat similar. Hence, it is important to use a realistic event simulation and pattern recognition algorithm to accurately predict the physics sensitivity from measurement of the low-energy neutrino events.

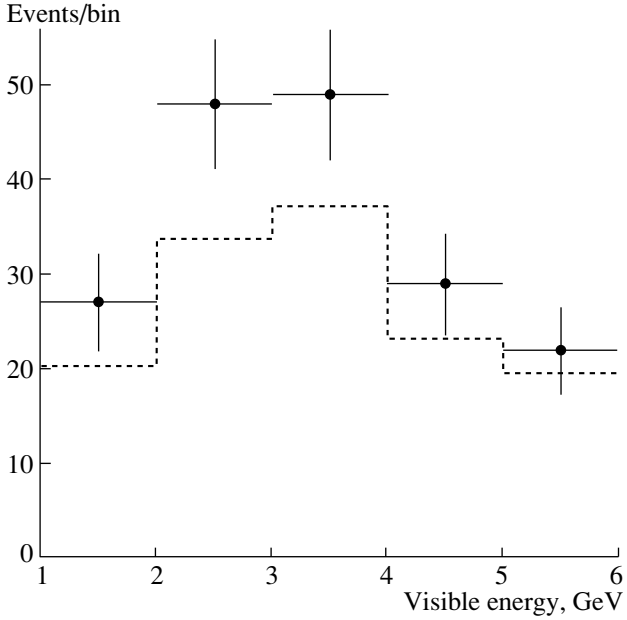

Fig. 6. Energy distribution of ν_e events in the MINOS Far Detector with $\Delta m^2_{23} = 0.0025$ eV^2, $\sin^2 2\theta_{13} = 0.067$ for $\nu_\mu \to \nu_e$ oscillations (data points with error bars) compared to the expected background with no $\nu_\mu \to \nu_e$ oscillations (dashed histogram).

For the analyses presented here, we have used events which have been fully simulated in the MINOS Far Detector using NeuGen and GEANT3.21 with Gheisha as the hadron interaction package. It includes a full simulation of the MINOS detector response. The latest version of our pattern recognition and track reconstruction software was used to identify whether events contain a muon track. The track reconstruction has been shown to be >90% efficient at identifying events which contain a muon with a momentum of at least 1 GeV/c. The probability of an NC event being misidentified as a CC event depends strongly on the apparent momentum of a muon. Preliminary estimates show that, below 1-GeV/c "muon" momentum, roughly half of the identified "CC" events are in fact NC background. Above 1 GeV/c, the background is less than 10%. Hence, it is important to understand this background at low energies and develop reliable background subtraction based on Near Detector measurements. A detailed analysis of the data obtained with the Calibration Detector will provide us with a measurement of how likely it is that charged pions can look like muons. In the results presented here, we have

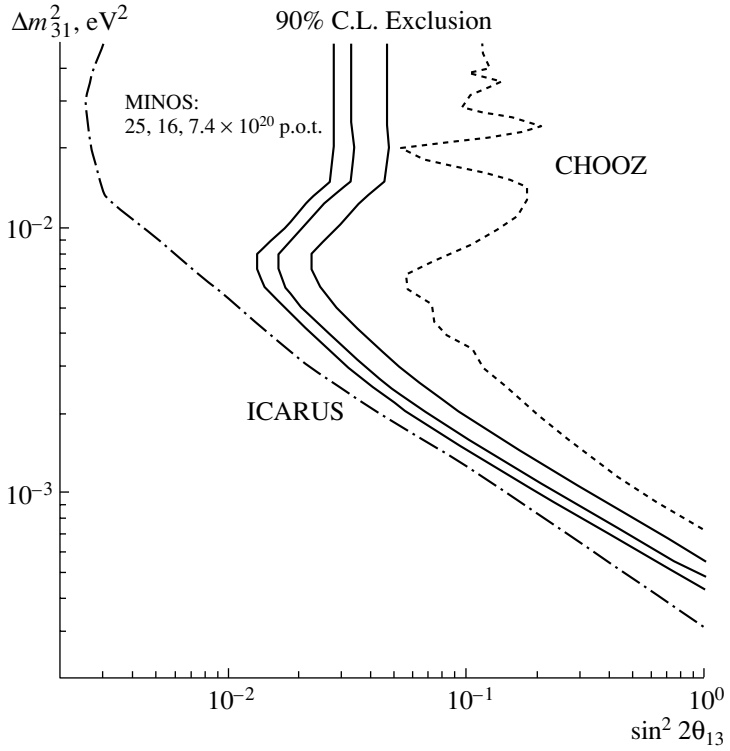

Fig. 7. 90% C.L. exclusion limits for $\nu_\mu \to \nu_e$ oscillations for MINOS with 7.4, 16, and 25×10^{20} p.o.t. The published limits of CHOOZ are also shown, as well as those expected for five years of running for 3-kt ICARUS.

made a conservative assumption of a 20% systematic uncertainty in the background subtraction of the NC events in the CC sample. Further, we have applied a 2% normalization uncertainty and an additional 2% bin-to-bin systematic uncertainty per 1 GeV bin on the ability to properly predict the unoscillated number of CC events at the Far Detector based on the Near Detector measurements. These uncertainties are estimated based on previous understanding of the beam and Near Detector analyses.

Once events are identified as containing a muon, the neutrino energy is calculated from the sum of the muon energy and the shower energy of the event. Figure 5 shows plots associated with measurements which MINOS can make with the actual values of the oscillation parameters being $\Delta m^2_{23} = 0.0025$ eV^2, $\sin^2 2\theta_{23} = 1$. There are three pairs of plots for a total of 7.4, 16, and 25×10^{20} p.o.t. The left plot in each pair shows the expected measured ratio of oscillated Far Detector data to the nonoscillation prediction, while the right plot shows the resulting C.L. regions on the measurement of the oscillation parameters. The energy distribution plots also show histograms for the expected ratio if Δm^2 were 0.0016 eV^2 instead or for neutrino decay or decoherence. The parameter space plots also show the current 90% C.L. measurement contours for Super-Kamiokande based on atmospheric neutrino measurements.

It is evident that MINOS will be able to demonstrate the oscillatory behavior definitively and will improve the measurement of Δm^2 by more than a factor of 5 over the current best measurement. For the highest level of protons, MINOS will be able to improve the measurement of $\sin^2 2\theta$ by about a factor of 2 and the measurement of Δm^2 by an order of magnitude.

$\nu_\mu \to \nu_e$. Recent results on solar and reactor neutrinos suggest a relatively large Δm^2_{sol} and mixing angle for those oscillations [2, 3]. This has heightened interest in such an admixture associated with the atmospheric Δm^2_{atm}. MINOS will improve on the best current limit by CHOOZ [11].

ν_e Interactions can be identified by the presence of an electromagnetic (EM) shower. The MINOS tracking calorimeters are able to identify such a shower using its typical characteristics such as shower compactness in both longitudinal and transverse dimensions and a large deposit of energy near the vertex. One background is the ν_e component in the beam ($\sim 0.6\%$). Additional, though probably the least important, background, comes from ν_τ CC events, where the produced τ^- decays to an electron. A somewhat more serious background is generated

by the NC events with a topology similar to a ν_e interaction. The most important backgrounds can be measured with the Near Detector and the corresponding uncertainty will be mainly due to statistical fluctuations in their predicted number in the Far Detector. The efficiencies of EM shower identification will be verified using the Calibration Detector data. The results presented here have been calculated using fully simulated and reconstructed Monte Carlo data. Two different methods of reconstruction and pattern recognition have been used to calculate the selection efficiency for true ν_e events and the probability of background. One method used a neural network, while the other used a likelihood analysis based on shower shape parameters and requiring identified events to have measured energies consistent with having oscillated from ν_μ in the main peak of the beam spectrum.

Figure 6 shows the number of ν_e selected events versus the observed energy in MINOS based on 25×10^{20} p.o.t. The figure shows a dashed histogram of the events expected with no $\nu_\mu \to \nu_e$ oscillation and points with error bars which result from an example of oscillation parameters for which MINOS can make a 3σ discovery, $\Delta m^2_{23} = 0.0025\ \mathrm{eV}^2$, $\sin^2 2\theta_{13} = 0.067$.

Figure 7 shows the 90% C.L. exclusion limits which MINOS will be able to make for the three scenarios with different numbers of protons. Also shown are the limits available from CHOOZ and expected sensitivity for a five-year run of ICARUS, whose data will become available only after MINOS.

It can be seen from the plots that MINOS will offer an improvement over the CHOOZ result by about a factor of 3 and, should $\sin^2 2\theta_{13}$ be not significantly less than 0.07, will discover $\nu_\mu \to \nu_e$ oscillations at a 3σ level.

6. CONCLUSION

MINOS has achieved an important milestone by completion of the installation of the Far Detector in the Soudan mine. It is taking atmospheric neutrino data and will be the first detector to compare atmospheric ν and $\tilde{\nu}$ oscillations directly. The construction of the Near Detector and the beam line at FNAL is well under way and will be completed by the end of 2004. The physics running with NuMI beam neutrinos will start in April 2005. With the expected investments in proton intensity at FNAL, MINOS will be able to provide the first ever high-precision measurement of the neutrino mixing parameters, $\Delta m^2_{23}, \theta_{23}$, and to improve the existing sensitivity to U_{e3}.

ACKNOWLEDGMENTS

Funding for MINOS has been provided by the US Department of Energy and by the UK Particle Physics and Astronomy Research Council.

REFERENCES

1. M. Shiozawa (Super-Kamiokande Collab.), in *Proceedings of the XX International Conference on Neutrino Physics and Astrophysics, Munich, Germany*, 2002.
2. Q. R. Ahmad *et al.* (SNO Collab.), Phys. Rev. Lett. **89**, 011302 (2002); S. N. Ahmed *et al.* (SNO Collab.), nucl-ex/0309004.
3. K. Eguchi *et al.* (KamLAND Collab.), Phys. Rev. Lett. **90**, 021802 (2003).
4. MINOS Technical Design Report, Fermilab (1998).
5. M. H. Ahn *et al.* (K2K Collab.), Phys. Rev. Lett. **90**, 041801 (2003).
6. The MINOS Collab., NuMI-930 (2003).
7. P. Adamson *et al.*, Nucl. Instrum. Methods Phys. Res. A **492**, 325 (2002).
8. S. Yanagisawa, Presented at *NOON'2003,* Kanazawa, Japan, Feb. 2003; http://www-sk.icrr.u-tokyo.ac.jp/noon2003/.
9. R. N. Mohapatra *et al.*, hep-ph/0006278; R. Barberi, P. Creminelli, and A. Strumia, hep-ph/0002199.
10. E. Lisi, A. Marrone, and D. Montanino, Phys. Rev. Lett. **85**, 1166 (2000); G. L. Fogli *et al.*, hep-ph/0303064.
11. M. Apollonio *et al.*, Phys. Lett. B **420**, 397 (1998); **466**, 415 (1999).

Physics of Atomic Nuclei, Vol. 67, No. 6, 2004, pp. 1092–1096. From Yadernaya Fizika, Vol. 67, No. 6, 2004, pp. 1120–1124.

NEUTRINO PHYSICS AND ASTROPHYSICS

The OPERA Experiment*

M. Dracos**
(on behalf of the OPERA Collaboration)

IReS, IN2P3-CNRS and Université Louis Pasteur, Strasbourg, France

Received November 17, 2003

Abstract—The OPERA (oscillation project with emulsion-tracking apparatus) experiment aims to observe an unambiguous $\nu_\mu \leftrightarrow \nu_\tau$ oscillation in the parameter region allowed by previous experiments. The OPERA detector will be installed in the underground Gran Sasso Laboratory, 732 km away from CERN, where the CNGS (CERN neutrino beam to Gran Sasso) ν_μ beam will be produced. The signature of the presence of ν_τ's in the ν_μ beam will be the detection of τ leptons produced by ν_τ interactions. Nuclear emulsions will be used for precise event reconstruction, while electronic detectors will be used for triggering.

1. INTRODUCTION

After the latest results of neutrino experiments, it is now well established that neutrinos oscillate. Most of these experiments observed the disappearance of one flavor but are not directly sensitive to the flavor of the oscillated neutrinos. "Appearance" long baseline experiments are now under construction concentrating their efforts on the observation of the $\nu_\mu \leftrightarrow \nu_\tau$ oscillation. These experiments are designed to be sensitive in the oscillation parameter region delimited mainly by the latest Super-Kamiokande [1] results on atmospheric neutrinos.

The OPERA [2] experiment will use the European Long Baseline CNGS [3] ν_μ beam and a "hybrid" detector to perform a direct observation of ν_τ's with a very low background.

2. DETECTION TECHNIQUE

In order to detect ν_τ's in the CNGS ν_μ beam, OPERA will detect τ leptons produced during these interactions. An unambiguous signature of the presence of τ's in the detector will be the precise detection of the τ decay topology. For that, OPERA will use lead foils as target and nuclear emulsions for charged track detection. This technique is able to give track reconstruction accuracy (better than a micron) needed to detect the τ decay point ("kink"), while allowing the coverage of large surfaces and a high target mass.

The detection principle is depicted in Fig. 1. The neutrinos interact with the 1 mm thick lead target plates, and the charged tracks are detected by the emulsion films (2 50 μm thick layers on both sides of a plastic foil). Two track segments of 15–20 visible grains are produced per particle. The spatial resolution is of the order of 0.5 μm while the angular resolution is about 5 mrad. The angular resolution must be as high as possible to avoid confusing particle multiple scattering and τ "kink." It has already been shown by the DONUT experiment [4] that this technique was well adapted for ν_τ detection.

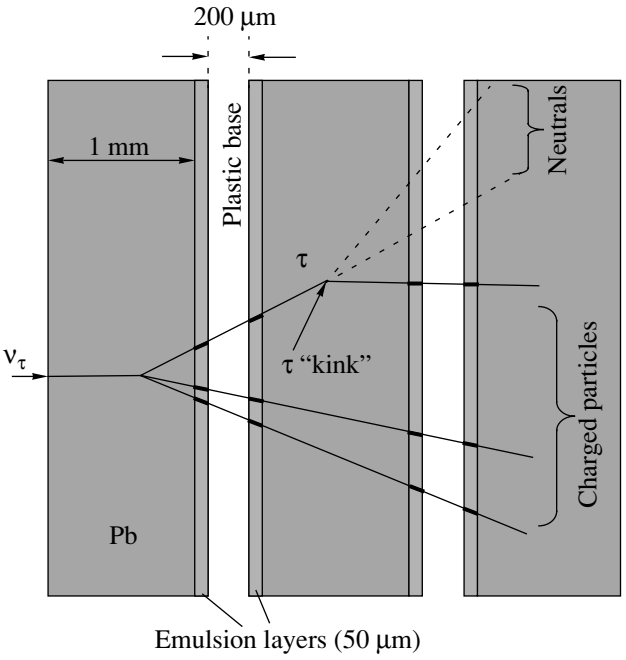

Fig. 1. Detection principle used by the OPERA detector for ν_τ and τ lepton detection.

*This article was submitted by the author in English.

**e-mail: marcos.dracos@ires.in2p3.fr

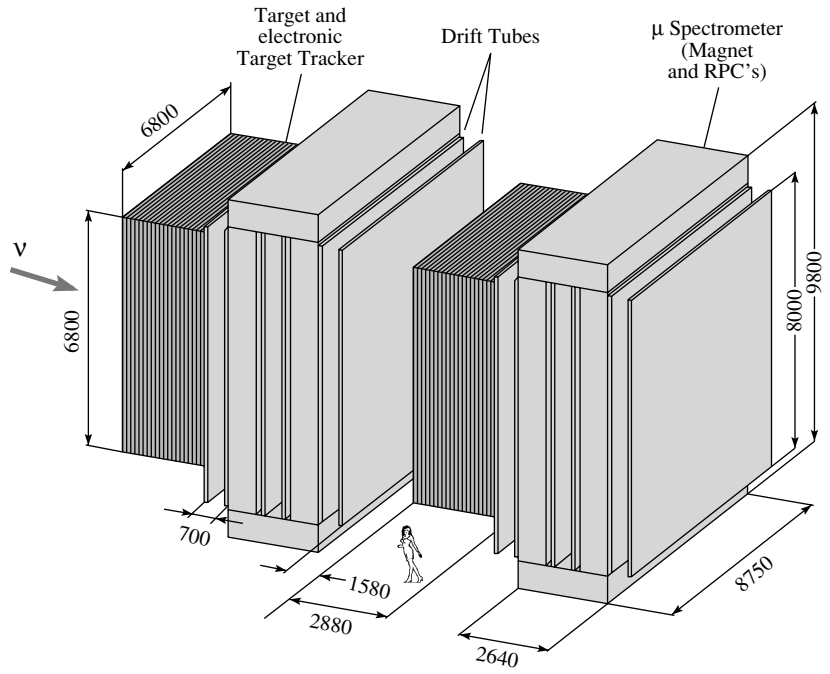

Fig. 2. Schematic view of the OPERA detector.

3. THE OPERA DETECTOR

The OPERA detector combines "passive" elements, as the emulsions, with electronic detectors ("hybrid" detector). The emulsions will be grouped in bricks, which will be extracted and analyzed each time an interesting event occurs. The main role of the electronic detectors will be to indicate which emulsion bricks to extract. These bricks will then be dismounted. Next, the emulsion films will be developed and sent to laboratories equipped with automatic scanning microscopes. Electronic detectors will also be used to reconstruct the event kinematics and reject various background sources like charm particle decays.

Figure 2 presents a schematic view of the OPERA detector where its main subdetectors can be seen. The detector consists of two identical parts called "Supermodules." Each Supermodule contains a target part and a muon spectrometer. The target part is composed of 31 walls (62 in total). Each wall contains a layer called the "brick wall" and just behind it a second layer called the "target tracker wall." The main part of the muon spectrometer is a dipolar magnet. Between the magnet iron slabs are inserted 22 layers of resistive plate chambers (RPC). In front, in the middle, and behind the magnet are placed three layers of Drift Tubes complemented by RPC's. The front part of the detector and the outer region of the spectrometer will also be equipped with RPC's to be used as veto to essentially reject "rock" muons (muons produced by neutrino interactions in the rock surrounding the LNGS experimental hall).

3.1. Target Bricks

The target bricks contain 56 lead/emulsion layers. Their dimensions are $12.7 \times 10.2 \times 7.54$ cm^3 and they weigh 8.6 kg. In each wall there are 64 rows of 52 bricks each. In total there will be 206 336 bricks leading to a target weight of the order of 1.8 kt. Each brick wall covers a surface of about 7×7 m^2.

In order to reduce the scanning load of the selected bricks, on the downstream face of each brick a changeable emulsion sheet will be placed, which will be scanned before opening the corresponding brick to be sure that the event is well located in this brick. If this is not the case, the brick is put back in its place. When an event is accepted by the experiment trigger system, the selected brick containing the neutrino interaction will be extracted by an automatic system. After the changeable sheet has been scanned and the presence of the interaction has been confirmed, the emulsion sheets of the brick will be developed and scanned. In the case where, after analysis of the changeable sheet, it appears that the extracted brick is not the good one, another brick can be extracted or the event is abandoned.

3.2. Target Tracker

For the location of the bricks containing the neutrino interaction point, plastic scintillator strips are

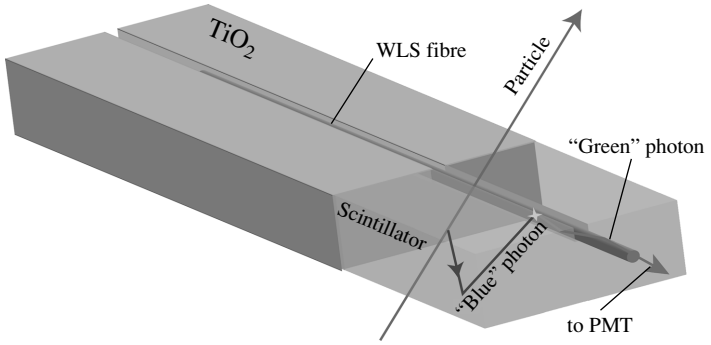

Fig. 3. Light detection technique used by the Target Tracker.

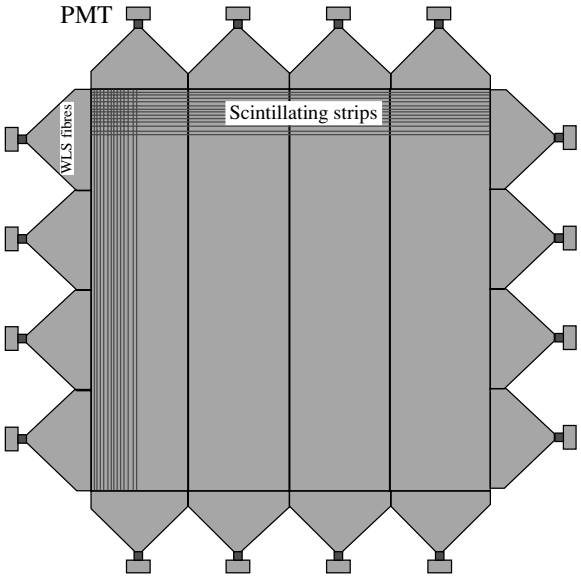

Fig. 4. Schematic view of a Target Tracker wall (7.6 × 7.6 m^2).

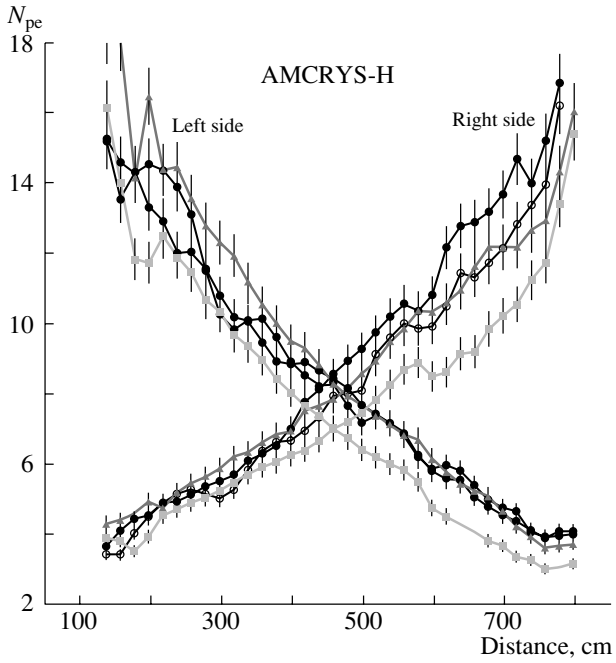

Fig. 5. Number of photoelectrons detected on each side of several AMCRYS-H plastic scintillator strips vs. the distance to the photomultipliers.

used. In order to cover the large brick wall surface, 7 m long strips are used. For the readout of the scintillation light generated in the strips, WLS (wave length shifting) fibres collect and propagate the light to their ends connected to two bialkali photomultipliers. Figure 3 illustrates this charged particle detection technique.

The target tracker walls inserted between the brick walls are composed of two planes with horizontal and vertical strips. Each plane is made of 4 modules of 64 strips each. Figure 4 shows a schematic view of a target tracker wall.

The plastic scintillator is made of polystyrene with 2% p-Terphenyl (primary fluor) and 0.02% POPOP (secondary fluor). The scintillating strips are produced by extrusion by AMCRYS-H,[1)] and they are coated by a thin diffusing white layer of TiO_2 coextruded at the same time as the strip production. On one side of the strips, a 2 mm deep groove is made during the extrusion to receive the 1 mm diameter WLS fibres. Figure 5 presents the number of photoelectrons observed on each side of several AMCRYS-H strips irradiated using 1.8 MeV electrons coming from a ^{90}Sr source. The WLS fibres were 1 mm Y-11(175)MJ fibres produced by Kuraray.[2)]

In order to detect the light coming from both sides of the 64 WLS fibres of each Target Tracker module, multianode Hamamatsu photomultipliers (PMT) are

[1)]AMCRYS-H, 60 Lenin avenue, Kharkov, 310001 Ukraine.

[2)]Kuraray Co., Methacrylic Resin Division, 8F Maruzen Building, 3-10, 2-Chrome, Hihon-bashi, Chuo-ku, Tokyo, 103-0027, Japan.

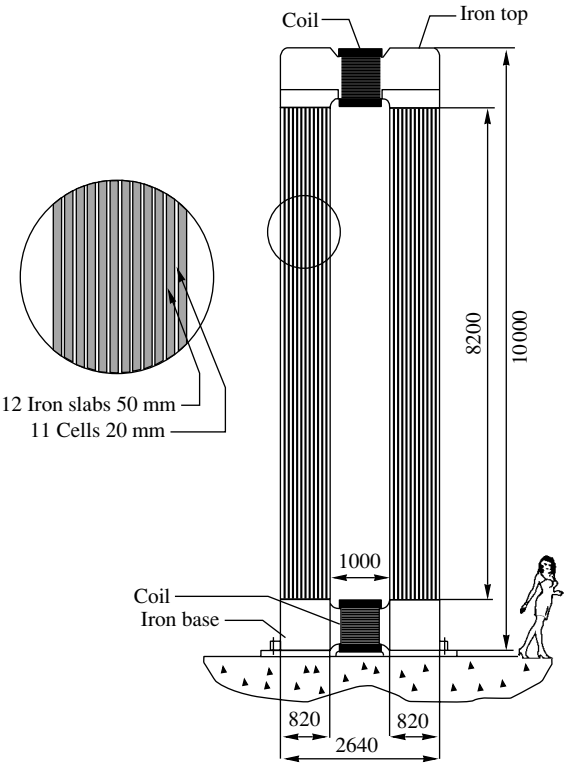

Fig. 6. Schematic view of the OPERA dipolar magnet.

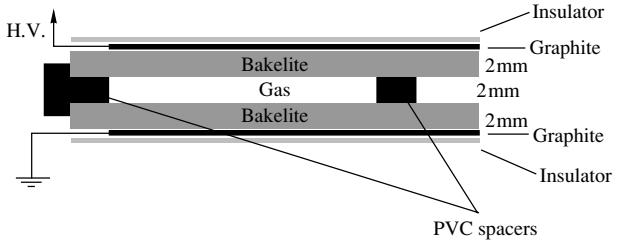

Fig. 7. Schematic view of the OPERA RPC's.

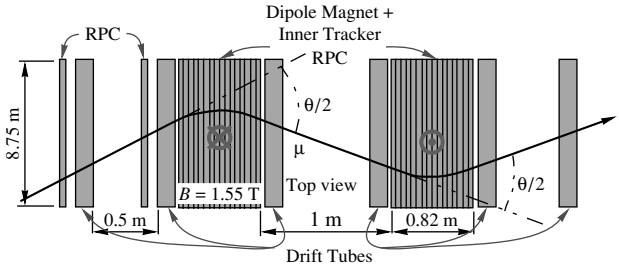

Fig. 8. Top view of one OPERA spectrometer.

used. These PMT's have a matrix of 8×8 channels with a very compact geometry ($3 \times 3 \times 7$ cm^3 including the resistor divider and connectors) allowing a target tracker wall thickness as small as 36 mm. The mean gain of these PMT's at the high voltage of 850 V is around 10^6, allowing efficient single photoelectron detection. The gain fluctuation between channels is compensated for by a dedicated readout chip developed for this application, which allows the electronic channel gain to be adjustable for each channel.

The main role of the target tracker is to identify, with high efficiency, the bricks containing the neutrino interaction. It can also help to reconstruct the event energy and measure the range of muons not reaching the spectrometers. The target tracker construction and installation will start by the end of 2003 and will last about two years.

3.3. Muon Spectrometer

The main part of the muon spectrometer is the dipolar magnet delivering a magnetic field of 1.55 T. Each magnet is composed of 5 cm thick 2×12 iron slabs. The 2 cm space between each slab is occupied by RPC layers. Figure 6 presents a lateral view of the OPERA magnet.

One RPC layer is made of 3×7 chambers (2.91×1.14 m^2 each). In total, 924 RPC bakelite chambers will equip the two OPERA spectrometers. Figure 7 shows a schematic view of the RPC's. The horizontal RPC strip pitch is 3.5 cm, while the vertical one is 2.6 cm. The RPC's signal will be used to determine the electric charge of the particles passing through and, especially, the muon charge in order to reduce the charm background producing wrong sign muons. The magnet and RPC installation at the LNGS underground laboratory (Hall C) has already started.

Precision trackers measuring the coordinates and the direction of muons escaping the target are placed in front, in the middle, and behind each dipole magnet. For this purpose, vertical drift tubes surrounded by two layers of high precision RPC's (with extracrossed strips) have been chosen. To cover well the whole surface of the target, the drift tubes have a length of 8 m. In order to reach the OPERA required momentum resolution ($\sim 25\%$ corresponding to a space resolution of 0.5 mm), a high detection efficiency, and multihit capability, the following parameters have been chosen: the tube diameter is 38 mm; the wire diameter is 50 μm; there are 4 staggered layers per plane, each with 168 tubes; there are 4032 channels per spectrometer. Figure 8 illustrates the spectrometer tracking strategy.

The installation of the spectrometers started in June 2003, and it will last up to July 2004 for the first one, while the second one will be finished in May 2005.

Expected number of signal and background events to be observed by the OPERA experiment for a 5 yr data taking period (CNGS beam intensity of 6.76×10^{19} p.o.t./yr and full mixing)

Δm^2, 10^{-3} eV^2	Number of events
Signal	
1.3	4.7
2.0	11.0
3.0	24.6
Background	
Δm^2 independent	1.06

4. OPERA PERFORMANCE

The CNGS construction is now well advanced, and it will start delivering the first beam mid-2006. The number of expected ν_τ events to be detected by the OPERA detector depends on the $\nu_\mu \leftrightarrow \nu_\tau$ oscillation parameters on one side and on the CNGS beam intensity on the other side. Considering the detector efficiency evaluated using a full detector simulation, a CNGS beam intensity of 6.76×10^{19} p.o.t./year and full mixing as suggested by Super-Kamiokande should result. The table gives the number of expected ν_τ events to be detected in a 5-yr period as a function of Δm^2. The latest results about Δm^2 give a value of 2.0×10^{-3} eV^2.

5. CONCLUSION

The OPERA experiment under installation in Gran Sasso underground laboratory is aiming to observe ν_τ appearance in a pure ν_μ CNGS beam. For this, OPERA uses a hybrid detector combing nuclear emulsion sheets and electronic detectors. The detector construction has already started, and it will be finished in the middle of 2006, when the CNGS beam will be ready.

REFERENCES

1. Y. Hayato, *Presentation at Aachen EPS 2003 Conference* (in press).
2. OPERA Collab., Experiment Proposal, CERN-SPSC-2000-028 and LNGS P25/2000 (2000).
3. G. Acquistapace *et al.*, CERN 98-02, INFN/AE-98/05.
4. K. Kodama *et al.*, Phys. Lett. B **504**, 218 (2001).

Physics of Atomic Nuclei, Vol. 67, No. 6, 2004, pp. 1097–1106. From Yadernaya Fizika, Vol. 67, No. 6, 2004, pp. 1125–1134.

NEUTRINO PHYSICS AND ASTROPHYSICS

Neutrinos in a Spherical Box*

Y. Giomataris[1)] and J. D. Vergados**

Theoretical Physics Division, University of Ioannina, Ioannina, Greece

Received November 19, 2003

Abstract—The purpose of the present paper is to study the neutrino properties as they may appear in the low-energy neutrinos emitted in the triton decay ${}^3_1\mathrm{H} \to {}^3_2\mathrm{He} + e^- + \bar{\nu}_e$ with maximum neutrino energy of 18.6 keV. The technical challenges to this end can be summarized as building a very large TPC capable of detecting low-energy recoils, down to a few 100 eV, within the required low-background constraints. More specifically, we propose the development of a spherical gaseous TPC of about 10 m in radius and a 200-MCi triton source in the center of curvature. One can list a number of exciting studies concerning fundamental physics issues that could be made using a large volume TPC and low-energy antineutrinos: (i) The oscillation length involving the small angle $\delta = \sin\theta_{13}$, directly measured in our ν_e disappearance experiment, is fully contained inside the detector. Measuring the counting rate of neutrino–electron elastic scattering as a function of the distance of the source will give a precise and unambiguous measurement of the oscillation parameters free of systematic errors. In fact, first estimates show that, even with a year's data taking, a sensitivity of a few percent for the measurement of the above angle will be achieved. (ii) The low-energy detection threshold offers a unique sensitivity for the neutrino magnetic moment which is about two orders of magnitude beyond the current experimental limit of $10^{-10}\mu_\mathrm{B}$. (iii) Scattering at such low neutrino energies has never been studied and any departure from the expected behavior may be an indication of new physics beyond the Standard Model. We present a summary of various theoretical studies and possible measurements, including a precise measurement of the Weinberg angle at very low momentum transfer.

1. INTRODUCTION

Neutrinos are the only particles in nature which are characterized by weak interactions only. They are thus expected to provide the laboratory for understanding the fundamental laws of nature. Furthermore, they are electrically neutral particles characterized by a very small mass. Thus, it is an open question whether they are truly neutral, in which case the particle coincides with its own antiparticle (i.e., they are Majorana particles), or they are characterized by some charge, in which case they are of the Dirac type (i.e., the particle is different from its antiparticle)[1]. It is also expected that the neutrinos produced in weak interactions are not eigenstates of the world Hamiltonian, and they are not stationary states, in which case one expects them to exhibit oscillations[1, 2]. As a matter of fact, such neutrino oscillations seem to have been observed in atmospheric neutrinos [3], interpreted as $\nu_\mu \to \nu_\tau$ oscillations, as well as ν_e disappearance in solar neutrinos [4]. These results have been recently confirmed by the KamLAND experiment [5], which exhibits evidence for reactor antineutrino disappearance. This has been followed by an avalanche of interesting analyses [6–10].

The purpose of the present paper is to discuss a new experiment to study the above neutrino properties as they may appear in the low-energy neutrinos emitted in the triton decay

$$ {}^3_1\mathrm{H} \to {}^3_2\mathrm{He} + e^- + \bar{\nu}_e $$

with maximum neutrino energy of 18.6 keV. This process has previously been suggested [11] as a means of studying heavy neutrinos like the now extinct 17-keV neutrino. The detection will be accomplished by employing gaseous Micromegas detectors, large TPC (time projection counters) detectors with good energy resolution and low background [12]. In addition, in this new experiment, we hope to observe or set much more stringent constraints on the neutrino magnetic moments. This very interesting question has been around for a number of years and it has been revived recently [13–16].

The existence of the neutrino magnetic moment can be demonstrated either in neutrino oscillations in the presence of strong magnetic fields or in electron-neutrino scattering. The latter is expected to dominate over the weak interaction in the triton experiment

*This article was submitted by the authors in English.

[1)]CEA, Saclay, DAPNIA, Gif-sur-Yvette, Cedex, France.

** e-mail: Vergados@cc.uoi.gr

since the energy of the outgoing electron is very small. Furthermore the possibility of directional experiments will provide additional interesting signatures. Even experiments involving polarized electron targets are beginning to be contemplated [17]. There are a number of exciting studies of fundamental physics issues that could be made using a large volume TPC and low-energy antineutrinos:

The oscillation length is comparable to the length of the detector. Measuring the counting rate of neutrino elastic scattering as a function of the distance of the source will give a precise and unambiguous measurement of the oscillation parameters free of systematic errors. First estimates show a sensitivity of a few percent for the measurement of $\sin^2\theta_{13}$.

The low-energy detection threshold offers a unique sensitivity for the neutrino magnetic moment, which is about two orders of magnitude beyond the current experimental limit of $10^{-10}\mu_B$. In our estimates below, we will use the optimistic value of $10^{-12}\mu_B$.

Scattering at such low neutrino energies has never been studied before. In addition, one may exploit the extra signature provided by the photon in radiative electron-neutrino scattering. As a result, any departure from the expected behavior may be an indication of physics beyond the Standard Model.

In the following, we will present a summary of various theoretical studies and possible novel measurements.

2. NEUTRINO MASSES AS EXTRACTED FROM VARIOUS EXPERIMENTS

At this point, it is instructive to elaborate a little bit on the neutrino mass combinations entering various experiments.

Cosmological constraints. We get [18, 19] $\Omega_\nu h^2 \leq 0.0076$ (95% C.L.), and for Majorana neutrinos, one has

$$\frac{\sum\limits_i m_i}{93.5\ \text{eV}} = \Omega_\nu h^2 \Rightarrow \sum_i m_i \leq 0.71\ \text{eV}/c^2 \quad (95\%\ \text{C.L.}).$$

The limit becomes 1.05 eV without the Ly-α forest data for Dirac neutrinos; the value of the upper limit is half of the above.

Neutrino oscillations. These, in principle, determine the mixing matrix and two independent mass-squared differences, e.g.,

$$\Delta m^2_{21} = m_2^2 - m_1^2, \quad \Delta m^2_{31} = m_3^2 - m_1^2.$$

They cannot determine the scale of the masses, e.g., the lowest eigenvalue m_1 and the two relative Majorana phases.

The end point triton decay. This can determine one of the masses, e.g., m_1 by measuring

$$(m_\nu)_{1\beta} \equiv m_\nu = \left| \sum_{j=1}^{3} U^*_{ej} U_{ej} m_j^2 \right|^{1/2}. \qquad (1)$$

Once m_1 is known, one can find $m_2 = [\Delta m^2_{21} + m_1^2]^{1/2}$ and $m_3 = [\Delta m^2_{31} + m_1^2]^{1/2}$ provided, of course, that the mixing matrix is known. Since the Majorana phases do not appear, this experiment cannot differentiate between Dirac and Majorana neutrinos. This can only be done via lepton-violating processes, like $0\nu\beta\beta$ decay and muon to positron conversion.

$0\nu\beta\beta$ decay. This provides an additional independent linear combination of the masses and the Majorana phases:

$$\langle m_\nu \rangle_{2\beta} \equiv \langle m_\nu \rangle = \left| \sum_{j=1}^{3} U_{ej} U_{ej} e^{i\lambda_j} m_j \right|. \qquad (2)$$

Muon to positron conversion. This also provides an additional relation

$$\langle m_\nu \rangle_{\mu e^+} = \left| \sum_{j=1}^{3} U^*_{\mu j} U^*_{ej} e^{-i\lambda_j} m_j \right|. \qquad (3)$$

Thus, the two independent relative CP phases can in principle be measurable. Therefore, these three types of experiments together can specify all parameters not settled by the neutrino oscillation experiments. Anyway, from the neutrino oscillation data alone, we cannot infer the mass scale. Thus the following scenarios emerge:

(i) The lightest neutrino is m_1 and its mass is very small. This is the normal hierarchy scenario. Then, $\Delta m^2_{21} = m_2^2$, $\Delta m^2_{31} = m_3^2$.

(ii) The inverted hierarchy scenario. In this case, the mass m_3 is very small. Then, $\Delta m^2_{21} = m_2^2 - m_1^2$, $\Delta m^2_{31} = m_1^2$.

(iii) The degenerate scenario. In such a situation, all masses are about equal and much larger than the differences appearing in neutrino oscillations. In this case, we can obtain limits on the mass scale as follows:

From triton decay. Then [20]

$$m_1 \approx (m_\nu)_{1\beta} \leq 2.2\ \text{eV}.$$

This limit is expected to improve substantially in the future [21].

From $0\nu\beta\beta$ decay. The analysis now depends on the mixing matrix and the CP phases of the Majorana neutrino eigenstates [1] (see discussion below). The best limit coming from $0\nu\beta\beta$ decay is

$$m_1 \approx \langle m_\nu \rangle_{2\beta} \leq 0.5\ \text{eV},$$

$$m_1 \approx \frac{\langle m_\nu \rangle_{2\beta}}{\cos 2\theta_{\rm solar}} \approx 2\langle m_\nu \rangle_{2\beta} \leq 1.0\ {\rm eV},$$

for the relative CP phase of the two strongly admixed states, 0 and π, respectively. These limits are going to greatly improve in the next generation of experiments (see, e.g., the review [1] and the experimental references therein).

3. ELASTIC ELECTRON–NEUTRINO SCATTERING

Elastic neutrino–electron scattering, which has played an important role in physics [22], is very crucial in our investigation, since it will be employed for the detection of neutrinos. So we will briefly discuss it before we embark on the discussion of the apparatus. Following the pioneering work of 't Hooft [23] as well as the subsequent work of Vogel and Engel [13], one can write the relevant differential cross section as follows:

$$\frac{d\sigma}{dT} = \left(\frac{d\sigma}{dT}\right)_{\rm weak} + \left(\frac{d\sigma}{dT}\right)_{\rm EM}. \quad (4)$$

We ignored the contribution due to the neutrino charged radius. We will not consider separately the scattering of electrons bound in the atoms, since such effects have recently been found to be small [24].

The cross section due to weak interaction alone takes the form [13]

$$\left(\frac{d\sigma}{dT}\right)_{\rm weak} = \frac{G_{\rm F}^2 m_e}{2\pi}\Bigg[(g_V + g_A)^2 \quad (5)$$
$$+ (g_V - g_A)^2\left(1 - \frac{T}{E_\nu}\right)^2 + (g_A^2 - g_V^2)\frac{m_e T}{E_\nu^2}\Bigg],$$

where $g_V = 2\sin^2\theta_{\rm W} + 1/2$ for ν_e, $g_V = 2\sin^2\theta_{\rm W} - 1/2$ for ν_μ and ν_τ, $g_A = 1/2$ for ν_e, and $g_A = -1/2$ for ν_μ and ν_τ. For antineutrinos, $g_A \to -g_A$. To set the scale, we see that

$$\frac{G_{\rm F}^2 m_e}{2\pi} = 0.445 \times 10^{-48}\frac{m^2}{\rm MeV}. \quad (6)$$

In the above expressions for ν_μ and ν_τ, only the neutral current has been included, while for ν_e both the neutral and the charge current contribute. The second piece of the cross section becomes

$$\left(\frac{d\sigma}{dT}\right)_{\rm EM} = \pi\left(\frac{\alpha}{m_e}\right)^2\left(\frac{\mu_l}{\mu_{\rm B}}\right)^2\frac{1}{T}\left(1 - \frac{T}{E_\nu}\right), \quad (7)$$

where in the mass basis μ_l^2 takes the form

$$\mu_l^2 = |c^2\mu_{11} + s^2\mu_{22}|^2,$$
$$\mu_l^2 = \mu_{21}^2 + |c\mu_{31} + s\exp(i\alpha_{CP})\mu_{32}|^2$$

for Dirac and Majorana neutrinos, respectively. For the definition of c and s, see Section 5 below. In the case of Dirac neutrinos, the off-diagonal elements of the magnetic moment were neglected. The angle α_{CP} is the relative CP phase of the dominant neutrino Majorana mass eigenstates present in the electron neutrino. The contribution of the magnetic moment can also be written as

$$\left(\frac{d\sigma}{dT}\right)_{\rm EM} = \sigma_0\left(\frac{\mu_l}{10^{-12}\mu_{\rm B}}\right)^2\frac{1}{T}\left(1 - \frac{T}{E_\nu}\right). \quad (8)$$

The quantity σ_0 sets the scale for the cross section and is quite small, $\sigma_0 = 2.5 \times 10^{-25}$ b.

The electron energy depends on the neutrino energy and the scattering angle and is given by

$$T \approx \frac{2(E_\nu\cos\theta)^2}{m_e}.$$

For $E_\nu = 18.6$ keV, one finds that the maximum electron kinetic energy is approximately $T_{\rm max} = 1.27$ keV [12]. Integrating the differential cross section between 0.1 and 1.27 keV, we find that the total cross section is

$$\sigma = 2.5\sigma_0.$$

It is tempting for comparison to express the above EM differential cross section in terms of the weak interaction, near the threshold of 0.1 keV, as follows:

$$\left(\frac{d\sigma}{dT}\right)_{\rm EM} = \xi_1^2\left(\frac{d\sigma}{dT}\right)_{\rm weak} \quad (9)$$
$$\times\left(\frac{\mu_l}{10^{-12}\mu_{\rm B}}\right)^2\frac{0.1\ {\rm keV}}{T}\left(1 - \frac{T}{E_\nu}\right).$$

The parameter ξ_1 essentially gives the ratio of the interaction due to the magnetic moment to that of the weak interaction. Evaluated at the energy of 0.1 keV, it becomes

$$\xi_1 \approx 0.50.$$

Its value, of course, will be larger if the magnetic moment is larger than $10^{-12}\mu_{\rm B}$. Anyway, the magnetic moment at these low energies can make a detectable contribution provided that it is not much smaller than $10^{-12}\mu_{\rm B}$.

In many cases, one would like to know the difference between the cross section of the electron neutrino and that of one of the other flavors, i.e.,

$$\chi(E_\nu, T) = \frac{d\sigma(\nu_e, e^-)/dT - d\sigma(\nu_\alpha, e^-)/dT}{d\sigma(\nu_e, e^-)/dT}, \quad (10)$$

where ν_α is either ν_μ or ν_τ. Then, from the above expression for the differential cross section, one finds

$$\chi = 2\frac{2-(m_eT/E_\nu^2)}{f_1(\theta_W)+2\sin^2\theta_W(1-T/E_\nu)^2-f_2(\theta_W)(m_eT/E_\nu^2)} \quad (11)$$

with

$$f_1(\theta_W)=(1+2\sin^2\theta_W)^2/(2\sin^2\theta_W), \quad f_2(\theta_W)=(1+2\sin^2\theta_W).$$

For antineutrinos, the above equation is slightly modified to yield

$$\chi = 2\frac{2-(m_eT/E_\nu^2)}{2\sin^2\theta_W+f_1(\theta_W)(1-T/E_\nu)^2-f_2(\theta_W)(m_eT/E_\nu^2)}. \quad (12)$$

Specializing (5), in the case of antineutrino–electron scattering, we get

$$\left(\frac{d\sigma}{dT}\right)_{\text{weak}} = \frac{G_F^2 m_e}{2\pi}[(2\sin^2\theta_W)^2 + (1+2\sin^2\theta_W)^2(1-T/E_\nu)^2 - 2\sin^2\theta_W(1+2\sin^2\theta_W)(m_eT/E_\nu^2)]. \quad (13)$$

This last equation can be used to measure $\sin^2\theta_W$ at very low momentum transfers, almost 30 years after the first historic measurement by Reiness, Gurr, and Sobel [22]. In the present experiment, we will measure the differential cross section as a function of T, which is essentially a straight line. With sufficient statistics, we expect to construct the straight line sufficiently accurately, so that we can extract $\sin^2\theta_W$ from both the slope and the intercept achieving high precision. We should mention that the present method does not suffer from the well-known suppression of the weak charge associated with other low-energy processes [25], including atomic physics experiments [26, 27]. This is due to the fact that the dependence on the Weinberg angle in these experiments comes from the neutral current vector coupling of the electron and/or the proton, involving the combination $1-4\sin^2\theta_W \approx 0.1$. Thus, in our approach, it may not be necessary to go through an elaborate scheme of radiative corrections (see the recent work by Erler *et al.* [28] and references therein).

4. EXPERIMENTAL CONSIDERATIONS

In this section, we will focus on the experimental considerations. One of the attractive features of the gaseous TPC is its ability to precisely reconstruct particle trajectories without precedent in the redundancy of experimental points, i.e., a bubble chamber quality with higher accuracy and real time recording of the events. Many proposals are actually under investigation to exploit the TPC's advantages for various astroparticle projects and especially solar or reactor neutrino detection and dark matter search [29–32]. A common goal is to fully reconstruct the direction of the recoil particle trajectory, which together with energy determination provides a valuable piece of information. The virtue of using the TPC concept in such investigations has now been widely recognized and a special international workshop has been recently organized in Paris [33]. The study of low-energy elastic neutrino–electron scattering using a strong tritium source was envisaged by Bouchez and Giomataris [34] by employing a large-volume gaseous cylindrical TPC. We will present here an alternate detector concept with different experimental strategy based on a spherical TPC design. A sketch of the principal features of the proposed TPC is shown in Fig. 1. For a more detailed description of the apparatus, including the neutrino source, the gas vessel, and detailed study of the detector [35–38] including a discussion of MICROMEGAS (MICROMEsh GAseous Structure) [39–41], the reader is referred to our previous work [42].

Our approach is radically different from all other neutrino oscillation experiments in that it measures the neutrino interactions, as a function of the distance source-interaction point, with an oscillation length that is fully contained in the detector; it is equivalent to many experiments made in the conventional way where the neutrino flux is measured at a single space point. Furthermore, since the oscillation length is comparable to the detector depth, we expect an exceptional signature: a counting rate oscillating from the triton source location to the depth of the gas volume, i.e., at first a decrease, then a minimum, and finally an increase. In other words, we will have a full observation of the oscillation process as has already been done in accelerator experiments with neutral strange particles (K^0). We summarize as follows:

The aim of the proposed detector will be the detection of very low energy neutrinos emitted by a strong tritium source through their elastic scattering on electrons of the target.

The (ν, e) elastic differential cross section is the sum of the charge and neutral current contributions

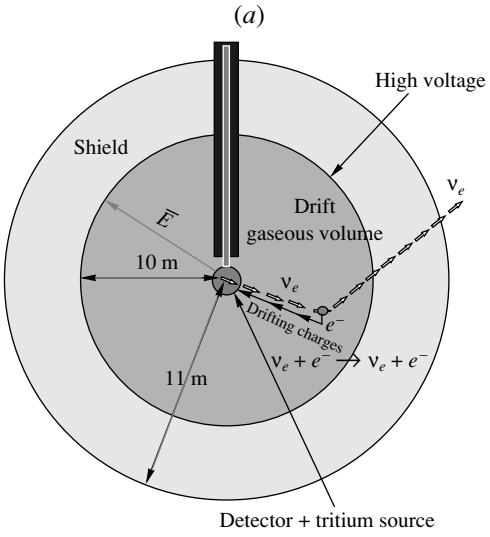

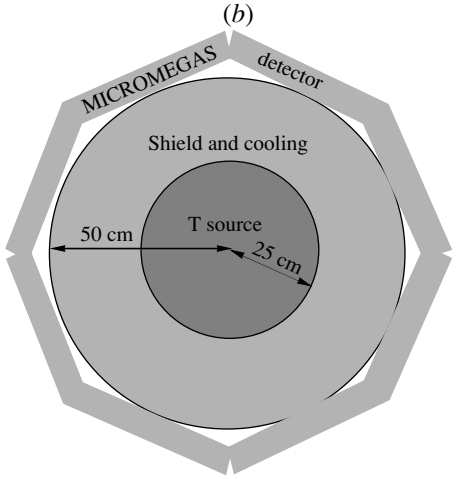

Fig. 1. The principal features of the proposed TPC (*a*) and a schematic view of the inner part of the vessel with the detector and the tritium source (*b*).

(see Section 3) and is a function of the energy. It is, however, quite small [see Eq. (6)].

Integrating this cross section up to energies of 15 keV, we get a very small value, $\sigma = 0.4 \times 10^{-47}$ cm^2. This means that, to get a significant signal in the detector, for a 200-MCi tritium source, we will need about 20 kt of gaseous material.

The elastic (ν, e) cross section, being dominated by the charge current, especially for low-energy electrons, will be different from that of the other flavors, which is due to the neutral current alone. This will allow us to observe neutrino oscillation enabling a modulation on the counting rate along the oscillation length. The effect depends on the electron energy T as is shown in Section 5.

We assume a spherical type detector, described in the previous section, filled with xenon gas at NTP and

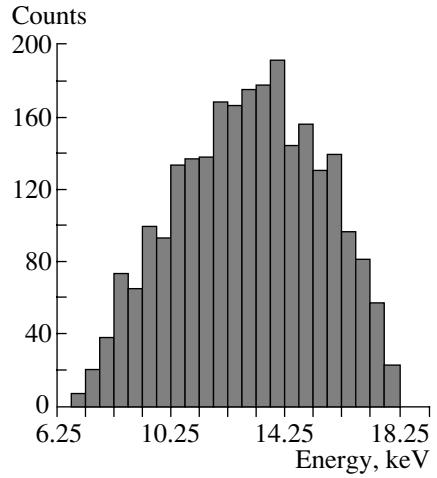

Fig. 2. Neutrino energy distribution with an imposed energy cutoff of 200 eV.

a tritium source of 20 kg, providing a very high intensity neutrino emission of 6×10^{18}/s. The Monte Carlo program is simulating all the relevant processes:

Beta decay and neutrino energy random generation.

Oscillation process of ν_e due to the small mixing angle θ_{13} [see Eq. (14) below].

Neutrino elastic scattering with electrons of the gas target.

Energy deposition, ionization processes, and transport of charges to the MICROMEGAS detector.

The first Monte Carlo simulations are giving a resolution of better than 10 cm, which is good enough for our needs. In Fig. 2, the energy distribution of the detected neutrinos, assuming an electron detection threshold of 200 eV, is exhibited. The energy is concentrated around 13 keV with a small tail to lower values.

In Figs. 3 and 4, we show the number of detected elastic events as a function of the distance L in bins of one meter for several hypotheses for the value of the mixing angle $\sin^2 2\theta_{13} = 0.170$, 0.085, and 0.045. We observe a decrease in the signal up to about 6.5 m and then a rise. Backgrounds are not yet included in this simulation, but the result looks quite promising; even in the case of the lowest mixing angle, the oscillation is seen, despite statistical fluctuations. We should point out that, in the context of this experiment, complete elimination of the backgrounds is not necessary. It is worth noting the following:

A source-off measurement at the beginning of the experiment will yield the background level to be subtracted from the signal.

Fitting the observed oscillation pattern will provide, for the first time, a stand-alone measurement of

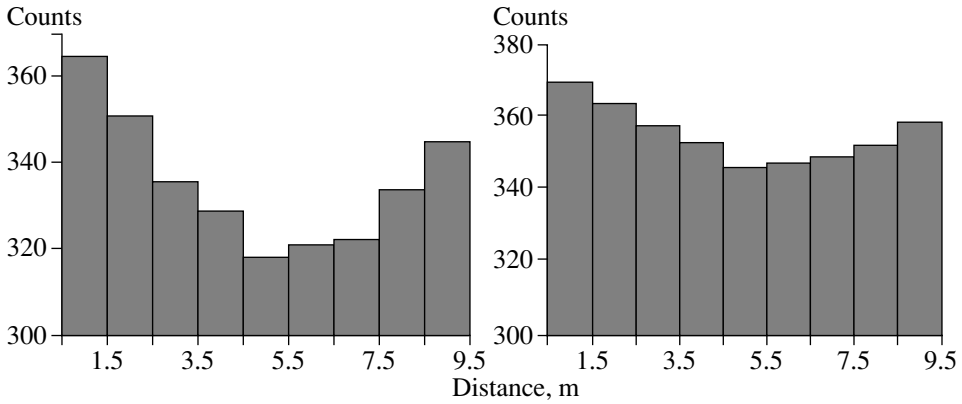

Fig. 3. Simulation of ν_e disappearance due to the large $\Delta m^2 = 2.5 \times 10^{-3}$ eV^2 involving the small mixing angle $\sin^2 2\theta_{13}$. The parameter $\chi(E_\nu, T)$ was not included in making the plots. On the left, we show results for $\sin^2 2\theta_{13} = 0.170$, while on the right we show results for $\sin^2 2\theta_{13} = 0.085$. One expects to unambiguously see the full oscillation inside the detector with the maximum disappearance occurring around 6.5 m.

the oscillation parameters, the mixing angle, and the mass square difference.

Systematic effects due to backgrounds or to bad estimates of the neutrino flux, which is the main worry in most of the neutrino experiments, are highly reduced in this experiment.

5. A SIMPLE PHENOMENOLOGICAL NEUTRINO MIXING MATRIX—SIMPLE EXPRESSIONS FOR NEUTRINO OSCILLATIONS

The available neutrino oscillation data (solar [4] and atmospheric [3]), as well as the KamLAND [5] results, can adequately be described by the following matrix:

$$\begin{pmatrix} \nu_e \\ \nu_\mu \\ \nu_\tau \end{pmatrix} = \begin{pmatrix} c & s & \delta \\ -\dfrac{s + c\delta}{\sqrt{2}} & \dfrac{c - s\delta}{\sqrt{2}} & \dfrac{1}{\sqrt{2}} \\ \dfrac{s - c\delta}{\sqrt{2}} & -\dfrac{c + s\delta}{\sqrt{2}} & \dfrac{1}{\sqrt{2}} \end{pmatrix} = \begin{pmatrix} \nu_1 \\ \nu_2 \\ \nu_3 \end{pmatrix},$$

up to order δ^2 ($\delta^2 < 4 \times 10^{-2}$). Sometimes, we will use θ_{13} instead of δ. Knowledge of this angle is very crucial for CP violation in the leptonic sector, since it may be complex even if the neutrinos are Dirac particles. In the above expressions, we have not absorbed the phases arising if the neutrinos happen to be Majorana particles, $\nu_k \xi_k = C\bar{\nu}_k^T$, where C denotes the charge conjugation, $\xi_k = e^{i\lambda_k}$, which guarantee that the eigenmasses are positive. The other entries are

$$c = \cos\theta_{\text{solar}}, \quad s = \sin\theta_{\text{solar}}$$

determined from the solar neutrino data [4, 6–10]

$$\tan^2\theta_{\text{solar}} \approx 0.35\text{–}0.42,$$
$$0.26 \leq \tan^2\theta_{\text{solar}} \leq 0.85 \quad (3\sigma),$$

while the analysis of KamLAND results [6–10] yields

$$\tan^2\theta_{\text{solar}} \approx 0.46\text{–}0.64,$$
$$0.29 \leq \tan^2\theta_{\text{solar}} \leq 0.86\ (3\sigma).$$

The solar neutrino oscillation (LMA solution) is given by

$$P(\nu_e \to \nu_e) \approx 1 - (\sin 2\theta_{\text{solar}})^2 \sin^2\left(\pi \frac{L}{L_{21}}\right),$$

$$L_{21} = \frac{4\pi E_\nu}{\Delta m_{21}^2}.$$

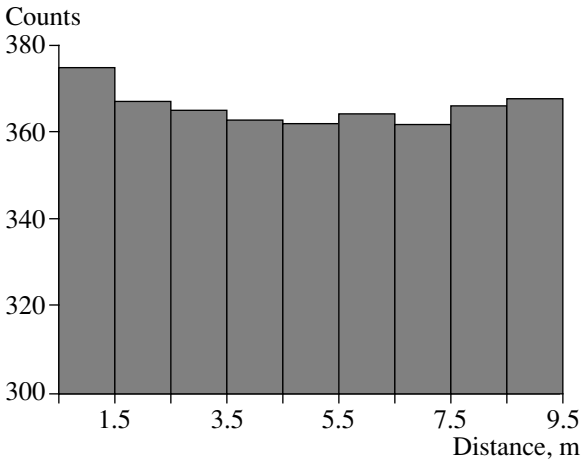

Fig. 4. The same as in Fig. 3 for $\sin^2 2\theta_{13} = 0.045$.

The analysis of both neutrino oscillation experiments and KamLAND [6–10] yields

$$\Delta m_{21}^2 = |m_2^2 - m_1^2| = (5.0\text{–}7.5) \times 10^{-5}\ \text{eV}^2.$$

The atmospheric neutrino oscillation takes the form

$$P(\nu_\mu \to \nu_\tau) = \sin^2\left(\pi \frac{L}{L_{32}}\right),$$

$$L_{32} = \frac{4\pi E_\nu}{\Delta m_{32}^2} \to \Delta m_{32}^2 = |m_3^2 - m_2^2| = 2.5 \times 10^{-3}\ \text{eV}^2.$$

We conventionally write

$$\Delta m_{32}^2 = \Delta m_{\text{atm}}^2, \quad \Delta m_{21}^2 = \Delta m_{\text{solar}}^2.$$

Corrections to disappearance experiments

$$P(\nu_e \to \nu_e) = 1 - \frac{(\sin 2\theta_{\text{solar}})^2 \sin^2\left(\pi \frac{L}{L_{21}}\right) + 4\delta^2 \sin^2\left(\pi \frac{L}{L_{32}}\right)}{(1+\delta^2)^2}. \tag{14}$$

The probability for $\nu_e \to \nu_\mu$ oscillation takes the form

$$P(\nu_e \to \nu_\mu) = \frac{\left[(\sin 2\theta_{\text{solar}})^2 + \delta \sin 4\theta_{\text{solar}}\right] \sin^2\left(\pi \frac{L}{L_{21}}\right)}{(1+\delta^2)^2} + \frac{4\delta^2 \sin^2\left(\pi \frac{L}{L_{32}}\right)}{(1+\delta^2)^2}, \tag{15}$$

while the oscillation probability $\nu_e \to \nu_\tau$ becomes

$$P(\nu_e \to \nu_\tau) = \frac{\left[(\sin 2\theta_{\text{solar}})^2 - \delta \sin 4\theta_{\text{solar}}\right] \sin^2\left(\pi \frac{L}{L_{21}}\right)}{(1+\delta^2)^2} + \frac{4\delta^2 \sin^2\left(\pi \frac{L}{L_{32}}\right)}{(1+\delta^2)^2}. \tag{16}$$

From the above expression, we see that the small amplitude δ term dominates in the case of triton neutrinos ($L \le L_{32}$, $L_{21} = 50 L_{32}$). In a different notation, $4\delta^2 \approx \sin^2 2\theta_{13}$.

In the proposed experiment, the neutrinos will be detected via the recoiling electrons. If the neutrino–electron cross section were the same for all neutrino species, one would not observe any oscillation at all. We know, however, that the electron neutrinos behave very differently due to the charge current contribution, which is not present in the other neutrino flavors. Thus, the number of observed electron events (ELEV) will vary as a function of L/E_ν as follows:

$$\text{ELEV} \propto \frac{d\sigma(\nu_e, e^-)}{dT}\left[1 - \chi(E_\nu, T) \times \frac{(\sin 2\theta_{\text{solar}})^2 \sin^2\left(\pi \frac{L}{L_{21}}\right) + 4\delta^2 \sin^2\left(\pi \frac{L}{L_{32}}\right)}{(1+\delta^2)^2}\right], \tag{17}$$

where

$$\chi(E_\nu, T) = \frac{d\sigma(\nu_e, e^-)/dT - d\sigma(\nu_\alpha, e^-)/dT}{d\sigma(\nu_e, e^-)/dT}$$

(ν_α is either ν_μ or ν_τ). In other words, χ represents the fraction of the ν_e–electron cross section, $\sigma(\nu_e, e^-)$, which is not due to the neutral current. Thus, the apparent disappearance oscillation probability will be quenched by this fraction. As have been seen (Section 3), the parameter χ, for $\sin^2\theta_{\text{W}} = 0.2319$, can be cast in the form

$$\chi(E_\nu, T) = \frac{2[2 - (m_e T/E_\nu^2)]}{4.6199 + 0.4638(1 - T/E_\nu)^2 - 1.4638(m_e T/E_\nu^2)}. \tag{18}$$

For antineutrinos, the previous expression becomes

$$\chi(E_\nu, T) = \frac{2[2 - (m_e T/E_\nu^2)]}{0.46384 + 4.6199(1 - T/E_\nu)^2 - 1.4638(m_e T/E_\nu^2)}. \tag{19}$$

We thus see that the parameter χ depends not only on the neutrino energy but also on the electron energy (see Figs. 5 and 6). Since in our experiment T is very low, there is no essential difference between the two expressions for χ.

It is interesting to see that, for a given neutrino energy, χ as a function of T is almost a straight line.

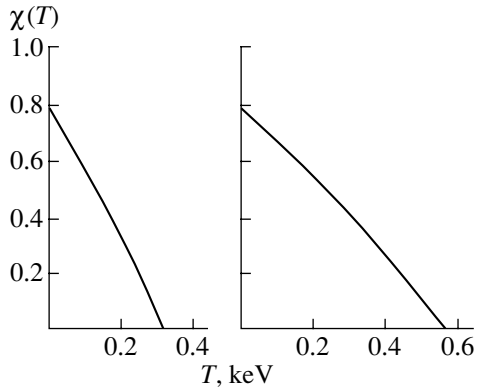

Fig. 5. The parameter χ as a function of the electron kinetic energy T for $E_\nu = 9$ keV on the left and 12 keV on the right.

We notice that, for large values of T, the factor χ is suppressed, which is another way of saying that, in this regime, in the case of the (ν_e, e^-) differential cross section, the charge current contribution is canceled by that of the neutral current.

In order to simplify the analysis, one may try to replace χ by an average value $\bar{\chi}(E_\nu)$, e.g., defined by

$$\bar{\chi}(E_\nu) = \frac{1}{T_{\max}(E_\nu)} \int_0^{T_{\max}(E_\nu)} \chi(E_\nu, T) dT. \qquad (20)$$

Then, surprisingly, one finds that $\bar{\chi}(E_\nu)$ is independent of E_ν with a constant value of 0.42. This is perhaps a rather high price one may have to pay for detecting the neutrino oscillations as proposed in this work. One may turn this into an advantage, however, since the disappearance dip in Eq. (17), in addition to its dependence on the familiar parameters, also depends on the electron energy.

Anyway, in the experiment involving a triton target, one will actually observe a sinusoidal oscillation as a function of the source–detector distance L with an amplitude which is proportional to the square of the small mixing angle δ. The relevant oscillation length is given by

$$L_{32} = 2.476m \frac{E_\nu(\text{MeV})}{\Delta m^2_{32}(\text{eV}^2)}.$$

In the present experiment for an average neutrino energy $E_\nu \approx 13$ keV and $\Delta m^2_{32} = 2.5 \times 10^{-3}$ eV^2, we find

$$L_{32} \approx 13.5 \text{ m}.$$

In other words, the maximum will occur close to the source at about $L = 7.5$ m. Simulations of the above neutrino oscillation involving ν_e disappearance due to the large $\Delta m^2 = 2.5 \times 10^{-3}$ eV^2, i.e., associated with the small mixing angle δ, are shown in Figs. 3 and 4. One clearly sees that the expected oscillation, present even for $(\sin 2\theta_{13})^2$ as low as 0.045, will occur well inside the detector.

Superimposed on this oscillation, one will see an effect due to the smaller mass difference, which will increase quadratically with the distance L.

The above simple neutrino oscillation formulas get modified: (i) in the presence of a magnetic field if the neutrino has a magnetic moment and/or (ii) if the heavier neutrinos have a finite lifetime.

6. RADIATIVE NEUTRINO–ELECTRON SCATTERING

The radiative neutrino decay for low-energy neutrinos is perhaps unobservable. Radiative neutrino decay in the presence of matter, in our case electrons, is, however, observable,

$$\nu_e(p_\nu) + e^- \longrightarrow \nu_e(p'_\nu) + e^-(p_e) + \gamma(k).$$

This occurs via the collaborative effect of electromagnetic and weak interactions, as is shown in Fig. 7. The evaluation of the cross section associated with these diagrams is rather complicated, but in the present case, the electrons are extremely nonrelativistic. Thus, in an intermediate electron propagator, we can retain the mass rather than the momenta by writing (Fig. 7) $(p_i - k)^\mu \gamma_\mu + m_e \approx 2m_e$, $(p_f + k)^\mu \gamma_\mu + m_e \approx 2m_e$ (exact results without this approximation will appear elsewhere). Then, after some tedious, but straightforward, trace calculations, one can perform the angular integrals over the three-body final states. Thus, to the leading order in the electron energy, one gets

$$k\frac{d\sigma(k, T_e)}{dT_e dk} = \sigma_\gamma \frac{m_e}{2\bar{E}^2_\nu}\left[\left(1 - \frac{k}{E_\nu}\right) g_V^2 \right. \qquad (21)$$
$$\left. + \left(\frac{E^2_\nu}{m^2_e}\left(1 - \frac{k}{E_\nu}\right) - \frac{1}{8}(4g_V^2 + g_V g_A)\right)\frac{T_e m_e}{E^2_\nu}\right],$$

where $\bar{E}_\nu = 13.0$ keV is the average neutrino energy and

$$\sigma_\gamma = 4\frac{8}{\pi^2}(G_\text{F}\bar{E}_\nu)^2\alpha \approx 2.0 \times 10^{-13} \text{ pb}$$

sets the scale for this process. The electron energy depends on the photon momentum k and the scattering angles. For a given k, there is the restriction

$$0 \le T_e \le \frac{2(E_\nu - k)^2}{m_e}.$$

From the above equations, we can immediately see that this process is roughly of order α down compared to the weak neutrino–electron scattering cross section. We also notice that the total cross section diverges logarithmically as the photon momentum

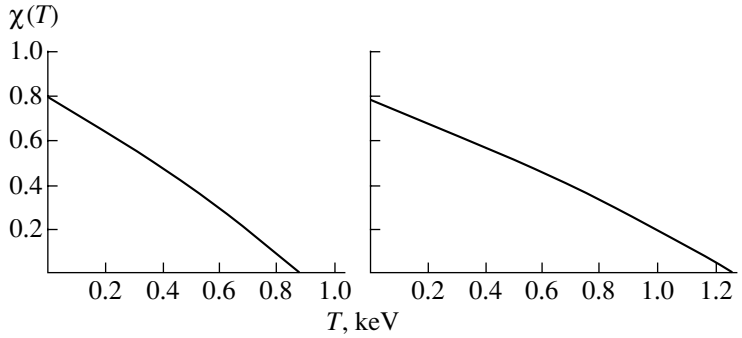

Fig. 6. The parameter χ as a function of the electron kinetic energy T for $E_\nu = 15$ keV on the left and 18 keV on the right.

goes to zero, reminiscent of the infrared divergence of bremsstrahlung radiation. In our case, we will adopt a lower photon momentum cutoff as imposed by our detector. We also notice that σ_γ characterizing this process is only a factor of three smaller than σ_0 characterizing the neutrino–electron scattering cross section due to the magnetic moment. We should bear in mind, however, the following:

(i) The magnetic moment is not known. σ_0 was obtained with the rather optimistic value $\mu_\nu = 10^{-12}\mu_\mathrm{B}$, which is two orders of magnitude smaller than the present experimental limit.

(ii) One now has the advantage of observing not only the electron but the photon as well.

Integrating over the electron energy, we get

$$k\frac{d\sigma(k)}{dk} = \sigma_\gamma \frac{E_\nu^2}{\bar{E}_\nu^2}\left(1-\frac{k}{E_\nu}\right)^3 \times \left[g_V^2 + \left(\frac{E_\nu^2}{m_e^2}\left(1-\frac{k}{E_\nu}\right) - \frac{1}{8}(4g_V^2 + g_V g_A)\right)\right. \times \left.\left(1-\frac{k}{E_\nu}\right)\right]. \quad (22)$$

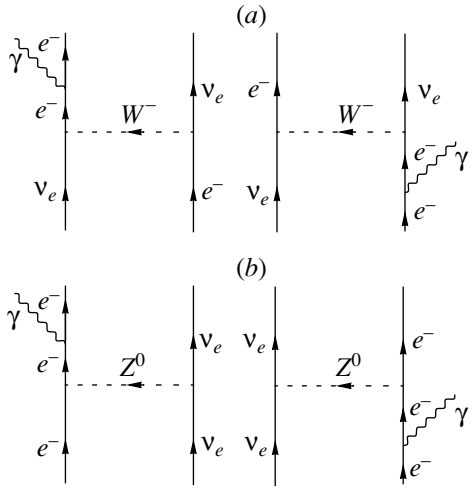

Fig. 7. The Feynman diagrams contributing to radiative neutrino–electron scattering via the charged current (a) and neutral current (b).

Integrating this cross section with respect to the photon momentum, we get

$$\sigma_\mathrm{tot} = \sigma_\gamma \frac{E_\nu^2}{\bar{E}_\nu^2}\left[\left(\frac{1}{2}g_V^2 - \frac{1}{4}g_A^2\right)\ln\frac{E_\nu}{E_\mathrm{cutoff}} + \frac{25}{24}g_V^2 - \frac{5}{48}g_A^2\right] \quad (23)$$

with the energy cutoff E_cutoff determined by the detector.

We have considered in our discussion only electron targets. For such low-energy antineutrinos, the charge current cannot operate on hadronic targets, since this process is not allowed as long as the target, being stable, is not capable of undergoing positron decay. The neutral current, however, can always make a contribution.

7. SUMMARY AND OUTLOOK

The outlook for the experiment is to provide high-statistics redundancy and high-precision measurement and minimize as much as possible the systematic uncertainties of experimental origin, which could be the main worry in the results of existing experiments. The physics goals of the new atmospheric neutrino measurement are summarized as follows:

(i) Establish the phenomenon of neutrino oscillations with a different experimental technique free of systematic biases. The oscillation length, associated with the small mixing angle $\sin\theta_{13}$ in the electronic neutrino, is fully contained in our detector. Thus, one hopes to measure all the oscillation parameters, including the small mixing angle, clarifying in this way the nature of the oscillation mechanism.

(ii) A high-sensitivity measurement of the neutrino magnetic moment, via neutrino–electron scattering. At the same time radiative neutrino–electron scattering will be investigated, exploiting the additional photon signature.

(iii) A precise measurement of $\sin^2\theta_W$ at very low momentum transfer, difficult to achieve in other experiments.

(iv) A new experimental investigation of neutrino decay.

(v) Other novel improvements of the experimental sensitivity are possible and must be investigated. The benefit of increasing the gas pressure of the detector, which leads to a proportional increase in the number of events, must be investigated.

(vi) The estimates presented above correspond to a year of data taking. In our experiment, however, in addition to increasing the pressure, there is no problem in increasing the data taking period up to 10 years or even longer, increasing our statistics accordingly. Thus, the prospect of reaching 100 000 detected events is quite realistic. This significant increase in the event rate is definitely going to be a great step forward towards improving the experimental accuracy and reducing the impact of background uncertainties.

REFERENCES

1. See, e.g., J. D. Vergados, Phys. Rep. **361**, 1 (2002); **133**, 1 (1986).
2. P. Vogel and J. F. Beacom, Phys. Rev. D **60**, 053003 (1999).
3. Y. Fukuda *et al.* (Super-Kamiokande Collab.), Phys. Rev. Lett. **86**, 5651 (2001); **85**, 3999 (2000); **81**, 1562 (1998).
4. Q. R. Ahmad *et al.* (SNO Collab.), Phys. Rev. Lett. **89**, 011301 (2002); **89**, 011302 (2002); **87**, 071301 (2001); K. Lande *et al.* (Homestake Collab.), Astrophys. J. **496**, 505 (1998); W. Hampel *et al.* (GALLEX Collab.), Phys. Lett. B **447**, 127 (1999); J. N. Abdurashitov *et al.* (SAGE Collab.), Phys. Rev. C **60**, 055801 (1999); G. L. Fogli *et al.*, Phys. Rev. D **66**, 053010 (2002).
5. K. Eguchi *et al.* (KamLAND Collab.), Phys. Rev. Lett. **90**, 021802 (2003); hep-ex/0212021.
6. J. N. Bahcall, M. C. Gonzalez-Garcia, and C. Peña-Garay, hep-ph/0212147.
7. H. Nunokawa *et al.*, hep-ph/0212202.
8. P. Aliani *et al.*, hep-ph/0212212.
9. M. Maltoni, T. Schwetz, and J. W. F. Valle, hep-ph/0212129; S. Pakvasa and J. W. F. Valle, hep-ph/0301061.
10. V. Barger and D. Marfatia, hep-ph/0212126.
11. G. Finocchiaro and R. E. Shrock, Phys. Rev. D **46**, 888 (1992); V. Barger and D. Marfatia, hep-ph/0212126.
12. Y. Giomataris, Ph. Rebourgeant, J. P. Robert, and C. Charpak, Nucl. Instrum. Methods Phys. Res. A **376**, 29 (1996); J. I. Collar and Y. Giomataris, Nucl. Instrum. Methods Phys. Res. A **471**, 254 (2001); J. Bouchez and Y. Giomataris, private communication.
13. P. Vogel and J. Engel, Phys. Rev. D **39**, 3378 (1989).
14. J. Schechter and J. W. F. Valle, Phys. Rev. D **24**, 1853 (1981); **25**, 283 (1982); S. Pakvasa and J. W. F. Valle, hep-ph/0301061.
15. A. V. Derbin, Yad. Fiz. **57**, 236 (1994) [Phys. At. Nucl. **57**, 222 (1994)].
16. V. N. Trofimov *et al.*, Yad. Fiz. **61**, 1373 (1998) [Phys. At. Nucl. **61**, 1271 (1998)].
17. T. L. Rashba, hep-ph/0104012.
18. D. N. Spergel *et al.* (WMAP Collab.), astro-ph/0302209.
19. O. Elgaroy *et al.*, Phys. Rev. Lett. **89**, 061301 (2002).
20. V. Lobashev *et al.*, Nucl. Phys. B (Proc. Suppl.) **91**, 523 (2001).
21. A. Osopwitz *et al.* (KATRIN Collab.), hep-ex/0109033.
22. F. Reines, H. S. Gurr, and H. W. Sobel, Phys. Rev. Lett. **37**, 315 (1976).
23. G. 't Hooft, Phys. Lett. B **37B**, 195 (1971).
24. G. J. Gounaris, E. A. Paschos, and P. I. Porfyriadis, Phys. Lett. B **525**, 63 (2002).
25. K. Hagiwawa *et al.* (Particle Data Group), Phys. Rev. D **66**, 010001 (2002).
26. S. C. Bennet and C. E. Wieman, Phys. Rev. Lett. **82**, 2484 (1999).
27. S. Sanguinetti *et al.*, physics/0303007.
28. J. Erler, A. Kurylov, and M. J. Ramsey-Musolf, hep-ph/0302149; P. Langkacker, *Precision Tests of the Standard Electroweak Model Advanced Series on Directions in High Energy Physics: 14* (World Sci., Singapore, 1995).
29. P. Gorodetzky *et al.*, Nucl. Instrum. Methods Phys. Res. A **433**, 554 (1999).
30. T. Ypsilantis, Europhys. News **27**, 97 (1996).
31. G. Bonvicini, D. Naples, and V. Paolone, Nucl. Instrum. Methods Phys. Res. A **491**, 402 (2002).
32. D. P. Snowden *et al.*, Phys. Rev. D **61**, 101301 (2000).
33. http://www.unine.ch/phys/tpc.html.
34. J. Bouchez and Y. Giomataris, DAPNIA-01-07 (Jun. 2001).
35. K. Zioutas *et al.*, Nucl. Instrum. Methods Phys. Res. A **425**, 480 (1999).
36. C. E. Aalseth *et al.*, Nucl. Phys. B (Proc. Suppl.) **110**, 85 (2002).
37. A. Magnon *et al.*, Nucl. Instrum. Methods Phys. Res. A **478**, 210 (2002).
38. S. Andriamonje *et al.*, DAPNIA-02-47, Nucl. Phys. B (in press).
39. Y. Giomataris, Nucl. Instrum. Methods Phys. Res. A **419**, 239 (1998).
40. J. Derre *et al.*, Nucl. Instrum. Methods Phys. Res. A **433**, 554 (1999).
41. J. Derre *et al.*, Nucl. Instrum. Methods Phys. Res. A **459**, 523 (2001).
42. Y. Giomataris and J. D. Vergados, hep-ex/0303045.

Physics of Atomic Nuclei, Vol. 67, No. 6, 2004, pp. 1107–1111. From Yadernaya Fizika, Vol. 67, No. 6, 2004, pp. 1135–1139.

NEUTRINO PHYSICS AND ASTROPHYSICS

ICARUS and Its Applications for Studies of Neutrino Interactions and Proton Decay*

J. Lagoda**
(for the ICARUS Collaboration[1])

University of Warsaw, Institute of Experimental Physics, Poland

Received November 17, 2003

Abstract—The main physics issues of the ICARUS experiment are observations of solar, atmospheric, beam, and supernova neutrinos and possibly of proton decay, with its unique experimental features, in which both high visual resolution and accurate calorimetry are combined. The ICARUS project represents a new generation of detectors, providing three-dimensional views of ionizing events and particle identification, working also as a good homogeneous calorimeter. A first module (T600) has been built and was successfully tested in an external site in Pavia (Italy) during summer 2001. Large samples of cosmic muon tracks and cosmic showers have been collected with a spectacular richness of details. On the basis of the experience acquired in the realization of the T600 module, four additional modules will be built to reach a total mass of 3000 t. The detector will be placed in the underground laboratory in Gran Sasso (LNGS).

1. INTRODUCTION

The ICARUS technology, first proposed by Rubbia [1] in 1977, combines the characteristics of a bubble chamber with the advantages of an electronic readout. The detector, which is essentially a large ionization chamber filled with ultrapure liquid argon (LAr), is an ideal device to study particle interactions: it is continuously sensitive, self-triggering, cost effective, simple to build in modular form, and sufficiently safe to be placed underground (no pressure, no flammable gas, etc.). This detector is also a superb calorimeter of very fine granularity and high accuracy.

A number of test detectors have been successfully operated over the years [2, 3]. The latest and largest one, the ICARUS T600 detector, was fully tested during summer 2001 in Pavia (Italy) on cosmic rays. All systems (cryogenics, LAr purification, readout chambers, photomultipliers, electronics, and DAQ) have been tested and performed as expected [4, 5]. A large number of cosmic ray events (long muon tracks, large muon bundles, electromagnetic and hadronic showers, low-energy events) have been recorded (Fig. 1).

2. THE ICARUS T600 DETECTOR

The ICARUS T600 is a large cryostat split into two identical, adjacent half-modules of internal dimensions $3.6 \times 3.9 \times 19.9$ m each. Each half-module contains an internal detector, composed of two time projection chambers (TPC), the field shaping system, monitors, probes, and photomultipliers. The TPC is formed by three parallel planes of wires, 3 mm apart, oriented at $0°, \pm 60°$ angles, with 3 mm of pitch between adjacent wires (see Figs. 2 and 3).

A uniform electric field, perpendicular to the wire planes, allows the drift of the ionization electrons towards the wire planes. The high-voltage system is composed of a cathode plane, parallel to the wire planes, and placed in the middle of each half-module. The field shaping electrodes ensure the uniformity of the field along the drift direction.

The detector is also equipped with a system of photomultipliers to detect scintillation light accompanying ionization events in LAr. This light is a monochromatic radiation with $\lambda = 128$ nm (VUV region). The photomultipliers, which have a diameter of 8 in., are placed behind the wire planes, and their glass windows are coated with a proper fluorescent wavelength shifter (TPB) (see Fig. 3). The "imaging" of ionizing events is possible thanks to the simultaneous use of the charge and the time of the signal. An external trigger or UV photons from scintillation provide a prompt signal, which allows measurement of the absolute drift time. Thus, each of the wires provides a two-dimensional projection

*This article was submitted by the author in English.

[1] L'Aquila, LNF, LNGS, Milan, Naples, Padova, Pavia, Pisa, Torino, ETH (Zürich), Beijing, Cracow, Katowice, Warsaw, Wroclaw, UCLA, Granada, INR (Moscow).

** e-mail: Justyna.Lagoda@fuw.edu.pl

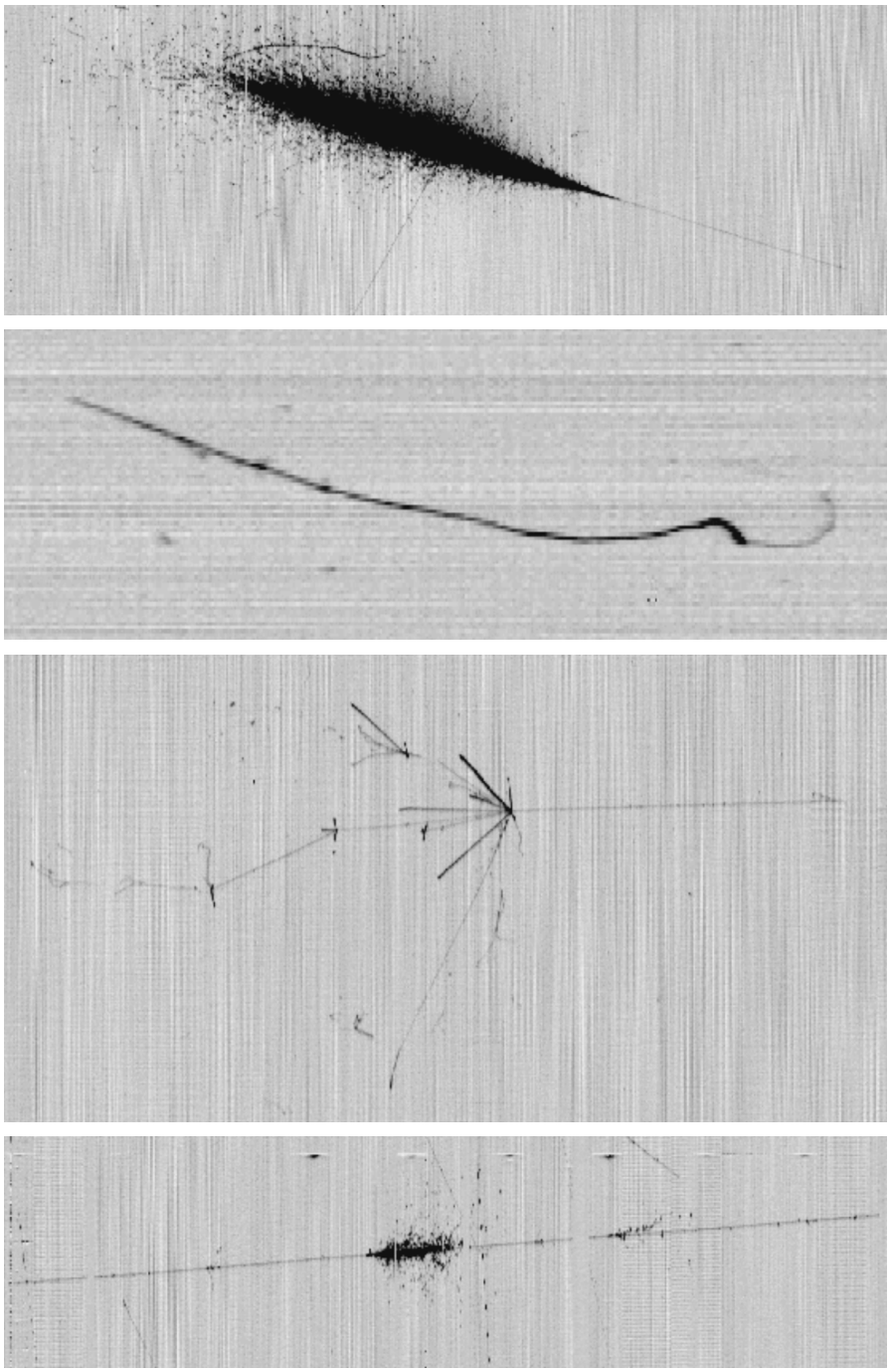

Fig. 1. Examples of cosmic-ray events recorded during the test period: an electromagnetic shower, a stopping and decaying muon, a hadronic interaction, and a long muon track with a cascade.

of the event, where one coordinate is given by the position of the wire and the other by the drift time (directly proportional, through the drift velocity, to the drift distance). The various projections have a common coordinate (the drift time), and a three-dimensional reconstruction is obtained by correlation of signals from two different planes and drift distance. An example of reconstruction of a long muon track is shown in Fig. 4 [4].

Particle momentum can be obtained from multiple scattering measurement or from range (for stopping particles). Measurement of momentum and the energy released by an ionizing particle per unit length provides a method for particle identification. As a baseline configuration, a detector consisting

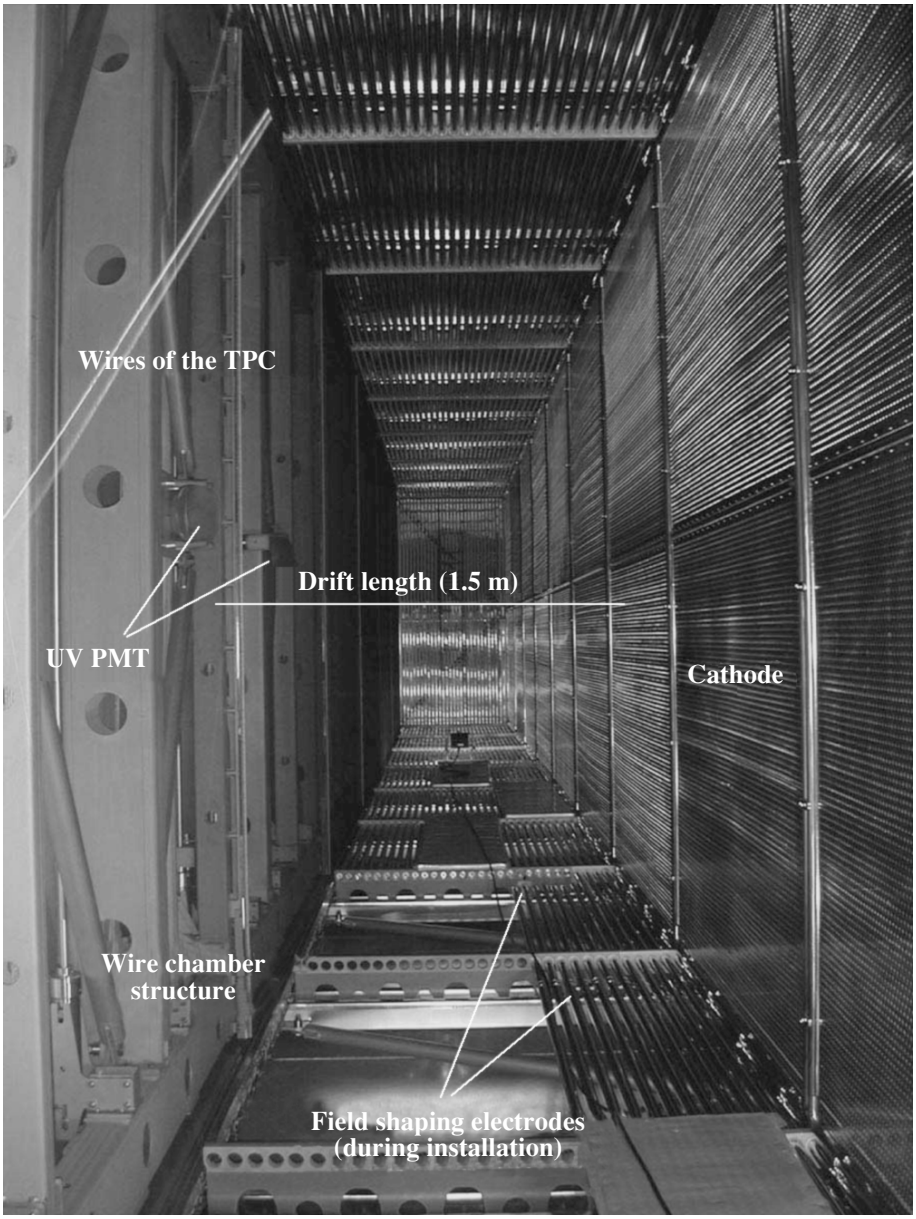

Fig. 2. Internal view of the T600 first half-module.

of T600 + 2 × T1200 modules complemented by a muon spectrometer is considered for the CNGS neutrino beam (Fig. 5).

3. PHYSICS PROGRAM

The main physics issues of the ICARUS experiment are the search for neutrino oscillation with the direct observation of atmospheric and beam neutrinos and the search for nucleon decay. In addition, ICARUS is also sensitive to solar and supernova neutrinos.

The goal of new atmospheric neutrino measurements is to firmly establish the evidence of neutrino oscillations with a different experimental technique. Atmospheric neutrinos have mean energy of the order of a few hundred MeV. Their interactions produce low-multiplicity events with a charged lepton accompanied by a nucleon and possibly one or two pions, but even complicated final states with multihadron products can be analyzed and reconstructed in ICARUS. Moreover, neutrino events can be analyzed down to production threshold, and hence ICARUS can really contribute to the understanding of the low-energy part of the atmospheric neutrino spectrum. The number of atmospheric neutrino CC events expected without oscillation in one year for a sensitive

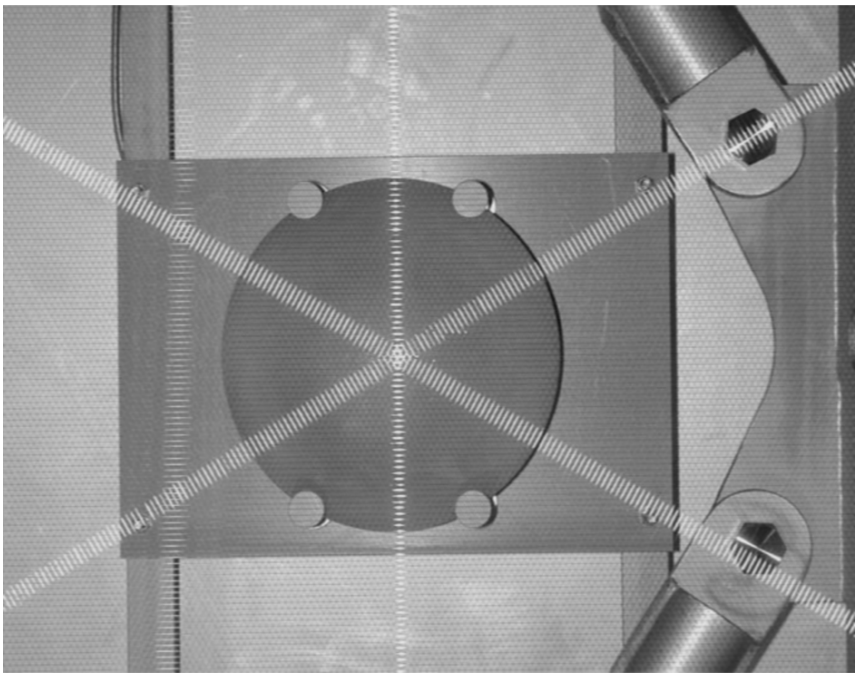

Fig. 3. Picture of a PMT behind the three wire planes.

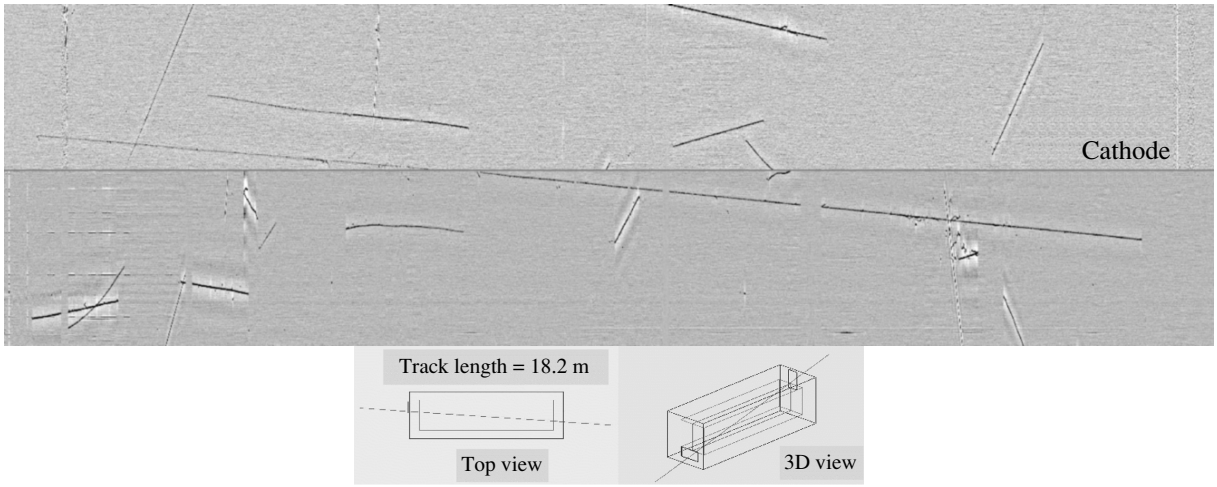

Fig. 4. Picture of a muon track crossing the cathode. The small picture below shows the three-dimensional reconstruction of the track.

mass of about 500 t is about 80 ν_μ and 60 ν_e interactions.

To better understand neutrino phenomenology, it is necessary to have compatible results from different kind of measurements. The properties of CNGS beam allow one to study oscillations by looking for the appearance of ν_τ CC events. ICARUS is able to perform a detailed reconstruction of these events, especially in the $\tau \to e\nu\nu$ decay mode. After cuts applied to reduce the ν_e background, the expected number of signal events in this channel is 11 (for $\Delta m^2 = 3 \times 10^{-3}$ eV^2 and 5-yr running of CNGS).

Thanks to its large sensitive mass and to its excellent tracking and particle identification capabilities, ICARUS is an ideal device for nucleon-decay detection. Using the dE/dx vs. range information, an excellent separation is obtained between kaons and pions. Thus, many exclusive channels can be sought simultaneously, for both proton and neutron decays. After 5-(kt yr) exposure, it is expected to reach the

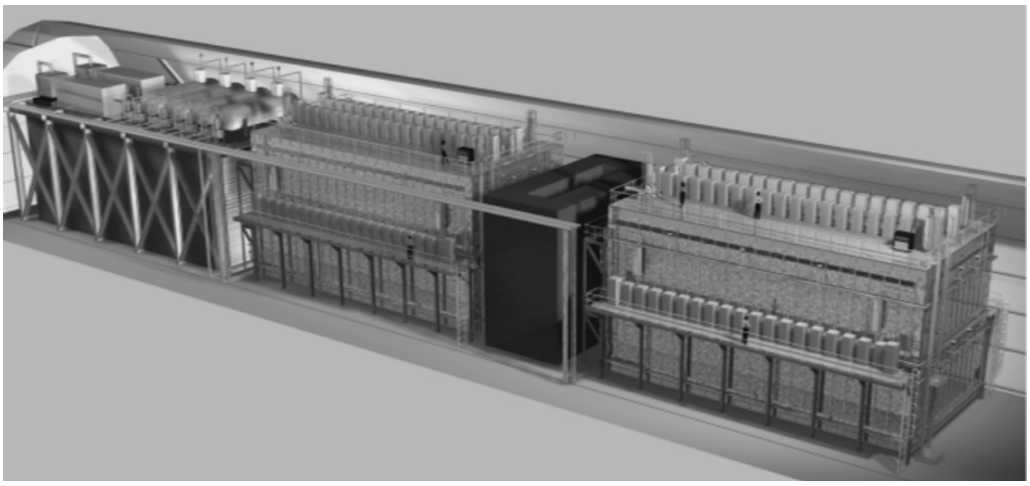

Fig. 5. The artistic view of the complete ICARUS detector in Hall B in LNGS. The T600 and two T1200 modules (each consisting of two T600 modules placed one on the top of the other) are shown, as well as the muon spectrometer.

limit of a few 10^{32} yr, and for a $p \to K^+\bar{\nu}$ decay mode, especially interesting for SUSY models, 5.7×10^{32} yr.

The ICARUS detector is sensitive to the ^{8}B part of solar neutrino spectrum and can detect the interactions by observing the electron produced in the following reactions: (1) elastic scattering (ES) on atomic electrons, which occurs with all flavors, and (2) absorption by an argon nucleus (inverse β decay) with Fermi transitions (F) to the 4.38-MeV isotopic analog state of ^{40}K and with Gamow–Teller (GT) transitions to several ^{40}K lower energy levels. Expected numbers of events in a T600 module per year are 38 for ES and 460 for F and GT, with a total visible energy larger than 8.8 MeV [6]. The detector is also capable of detecting supernova neutrinos via both channels mentioned above. Supposing a supernova explosion at a distance of 10 kpc, we expect about 250 events in the complete ICARUS detector (T3000). A detailed description of the ICARUS physics program can be found in [7, 8].

4. CONCLUSIONS

The test run of the ICARUS T600 module in Pavia was successful and showed that LAr TPC technology has achieved maturity. The recorded data is now being analyzed and used to refine the reconstruction tools. The module is ready to be installed in Hall B in LNGS in 2004 and the construction of additional modules is foreseen for the CNGS beam.

ACKNOWLEDGMENTS

J.L. was partially supported by KBN 5P03B09520 and KBN 621/E-78/SPB/ICARUS/P-03/DZ214/2003-05.

REFERENCES

1. C. Rubbia, CERN-EP/77-08 (1977).
2. P. Cennini *et al.* (ICARUS Collab.), Nucl. Instrum. Methods Phys. Res. A **345**, 230 (1994).
3. F. Arneodo *et al.* (ICARUS Collab.), Nucl. Instrum. Methods Phys. Res. A **498**, 292 (2002).
4. F. Arneodo *et al.*, Nucl. Instrum. Methods Phys. Res. A **508**, 287 (2003).
5. ICARUS Collab., *Analysis of the Liquid Argon Purity in the ICARUS T600 TPC* (in press).
6. I. Gil Botella and A. Rubbia, ICARUS-TM/02-13.
7. ICARUS Collab., ICARUS-TM/2001-03 LNGS P28/01 LNGS-EXP 13/89 add. 1/01.
8. ICARUS Collab., CERN/SPSC 2002-027 (SPSC-P-323).

Physics of Atomic Nuclei, Vol. 67, No. 6, 2004, pp. 1112–1118. From Yadernaya Fizika, Vol. 67, No. 6, 2004, pp. 1140–1145.

NEUTRINO PHYSICS AND ASTROPHYSICS

Physics and Present Status of the WITCH Experiment*

V. Yu. Kozlov, M. Beck, F. Ames[1)], D. Beck[2)], S. Coeck, P. Delahaye[1)], B. Delauré, V. V. Golovko, A. Lindroth, I. S. Kraev, T. Phalet, N. Severijns, and S. Versyck (and the ISOLDE and NIPNET Collaborations)**

IKS, K.U. Leuven, Leuven, Belgium

Received Novemver 4, 2003

Abstract—The WITCH experiment (Weak Interaction Trap for CHarged particles) is starting measurements at the ISOLDE facility at CERN at present. It has been set up to measure the energy spectrum of the recoiling daughter ions after nuclear beta decay for precision tests of the Standard Model of weak interactions. However, many other topics of interest are accessible. In this article, the possibilities of recoil spectroscopy with the WITCH experiment are discussed, as well as the principle of the setup and its present situation. © *2004 MAIK "Nauka/Interperiodica"*.

1. INTRODUCTION

The Standard Model (SM) of electroweak interactions is very successful in describing the interaction both qualitatively and quantitatively. Nevertheless, it contains many free parameters and ad hoc assumptions. One of these is that from the five possible types of weak interactions—vector (V), axial-vector (A), scalar (S), tensor (T), and pseudoscalar interaction (P)—just V and A interactions are present at a fundamental level. Together with maximal parity violation, this leads to the well-known $V-A$ structure of the weak interaction.

The effective Hamiltonian for β decay, including all possible interactions, is given by

$$\begin{aligned} H_\beta = \frac{G_\mathrm{F}}{\sqrt{2}} V_{ud} \Big[& (\bar{p}n)\left(\bar{e}\left(C_S + C_S'\gamma_5\right)\nu\right) \\ & + (\bar{p}\gamma_\mu n)\left(\bar{e}\gamma^\mu\left(C_V + C_V'\gamma_5\right)\nu\right) \\ & + \frac{1}{2}(\bar{p}\sigma_{\lambda\mu}n)\left(\bar{e}\sigma^{\lambda\mu}\left(C_T + C_T'\gamma_5\right)\nu\right) \\ & - (\bar{p}\gamma_\mu\gamma_5 n)\left(\bar{e}\gamma^\mu\gamma_5\left(C_A + C_A'\gamma_5\right)\nu\right) \\ & + (\bar{p}\gamma_5 n)\left(\bar{e}\gamma_5\left(C_P + C_P'\gamma_5\right)\nu\right)\Big] + \mathrm{h.c.} \end{aligned} \tag{1}$$

The coefficients C_i, C_i', $i \in \{S, V, T, A, P\}$, are the coupling constants for the S, V, T, A, and P interaction types. G_F is the Fermi coupling constant and V_{ud} is the ud-matrix element of the CKM matrix.

The presence of S- and T-type interactions is not yet experimentally ruled out with high precision. Most of the limits for the S and T coupling constants (C_S, C_S' and C_T, C_T') in the charged current sector are rather weak [1–6], i.e., of the order of 10% of the coupling constants of the V and A interactions (see table). This was deduced mostly from measurements of the β-neutrino angular correlation in nuclear β decay. For unpolarized nuclei, this correlation can be written as [7]

$$\omega(\theta_{\nu\beta}) = 1 + \frac{\dfrac{\mathbf{p}\cdot\mathbf{q}}{EE_\nu}a}{1 + \dfrac{\Gamma m}{E}b} \tag{2}$$

Experimental uncertainties of past determinations of the β–ν angular correlation coefficient a (The top part shows the measurements that determined that the weak interaction is of predominantly V and A type. The bottom part lists the best limits for S- and T-type interaction to date. They are at the level of 6% at best (68.3% C.L.). This corresponds to a mass of the exchange boson $m_\mathrm{boson} \approx$ 300 GeV when standard coupling is assumed.)

Nuclide	Δa	Ref.	Comment
^{6}He	0.05	[3]	$V-A$ structure
^{19}Ne	0.08	[3]	$V-A$ structure
^{23}Ne	0.04	[3]	$V-A$ structure
^{35}Ar	0.14	[3]	$V-A$ structure
^{6}He	0.003	[4]	$C_T/C_A < 6\%$ (C.L. = 68.3%)
^{32}Ar	0.0065	[5, 6]	$C_S/C_V < 8\%$ (C.L. = 68.3%)

*This article was submitted by the authors in English.

[1)]CERN, Geneva, Switzerland.
[2)]GSI-Darmstadt, Darmstadt, Germany.
** e-mail: Valentin.Kozlov@fys.kuleuven.ac.be, Marcus.Beck@fys.kuleuven.ac.be

$$\simeq 1 + a\frac{v}{c}\cos\theta\left[1 - \frac{\Gamma m}{E}b\right],$$

where E and E_ν are the total energy of the emitted β particle and the neutrino; $\theta_{\nu\beta}$ is the angle between the β particle and the neutrino; m is the rest mass of the electron, $\Gamma = \sqrt{1-(\alpha Z)^2}$, with α being the fine-structure constant and Z being the nuclear charge of the daughter nucleus; and v/c is the velocity of the β particle. The Fierz interference coefficient b has experimentally been shown to be small [8–10] and will be assumed to be zero.

The β–ν angular correlation coefficient a depends on the coefficients C_i, C_i'. For pure Fermi (F) and pure Gamow–Teller (GT) transitions, this dependence can be approximated as

$$a_{\mathrm{F}} \simeq 1 - \frac{|C_S|^2 + \left|C_S'\right|^2}{|C_V|^2}, \qquad (3)$$

$$a_{\mathrm{GT}} \simeq -\frac{1}{3}\left[1 - \frac{|C_T|^2 + \left|C_T'\right|^2}{|C_A|^2}\right].$$

In the SM, i.e., in the absence of S- and T-type interactions, $a_{\mathrm{F}} = 1$ and $a_{\mathrm{GT}} = -0.333$. Any admixture of S to V interaction in such a pure Fermi decay would result in $a < 1$. The measurement of a therefore yields information about the interactions involved. However, the neutrino cannot be detected directly in such an experiment, and the β–ν angular correlation has to be inferred from other observables. From properties of the general Hamiltonian of weak interaction [11] and of the Dirac γ matrices, it can be shown that V interaction takes place only between a particle and antiparticle with opposite helicities, while in the case of S interaction it takes place only between a particle and antiparticle with the same helicities. Therefore, in superallowed 0^+–0^+ Fermi decay, where β and neutrino spins have to be coupled to zero, a particle and antiparticle will be emitted preferably into the same directions for V interaction and into the opposite directions for S interaction. This will lead to a relatively large energy of the recoil ion for V interaction and a relatively small recoil energy for S interaction (Fig. 1).

The aim of the WITCH experiment is to improve the limits on S- and T-type interactions. For this the β–ν angular correlation will be determined with high precision by measuring the shape of the recoil energy spectrum. The table shows the uncertainties of a achieved in other experiments so far. Consequently, the WITCH experiment has to reach a precision of $\Delta a < 0.01$ to achieve its objective.

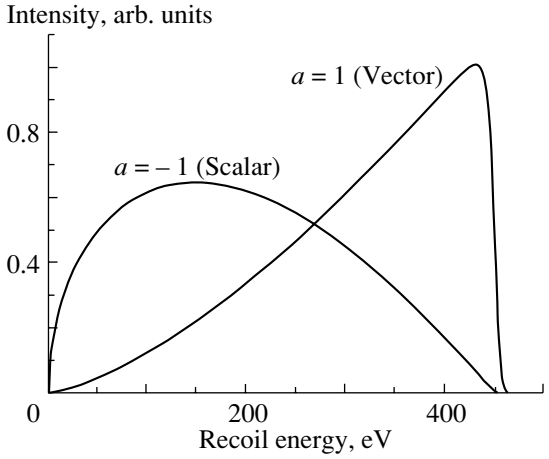

Fig. 1. Differential recoil energy spectrum for $a = 1$ and $a = -1$.

2. THE PRINCIPLE OF THE EXPERIMENT

An experiment to measure the shape of the recoil energy spectrum has two difficulties: (i) the β emitter is usually embedded in matter, which causes a distortion of the spectra due to the ion scattering in the source, leading to energy losses; (ii) the recoil ions have very low kinetic energy, making a precise energy measurement difficult. In order to avoid the first problem and to be as independent as possible from the properties of the isotopes to be used, the WITCH experiment will use a Penning trap to store radioactive ions. An ideal Penning trap can be defined as the superposition of a homogeneous magnetic field B and an electrostatic quadrupole field U, coaxial to the magnetic field. The combination of these particular fields allows a charged particle to be stored in a well-defined volume. Also, there is an exact solution of the particle's equations of motion [12].

The Penning trap has to capture, cool, center, and store the ions. To separate these functions in the WITCH setup, two Penning traps are used, a cooler trap and a decay trap (Fig. 2). First, the ions get trapped in the cooler trap, where they are cooled down to room temperature and centered. For this purpose, helium gas is injected into the trap as a buffer gas. Then the ions are ejected through a differential pumping barrier into the decay trap, where they are kept for a couple of half-lives, i.e., of the order of 1 to 10 s for the cases of interest. The ion cloud in the decay trap constitutes the source for the experiment [13].

To solve the second problem and measure the recoil energy spectrum, a retardation spectrometer will be used. The working principle of such a device is similar to the β spectrometers used for the determination of the neutrino rest mass in Mainz [14] and Troitsk [15]. The spectrometer consists of two

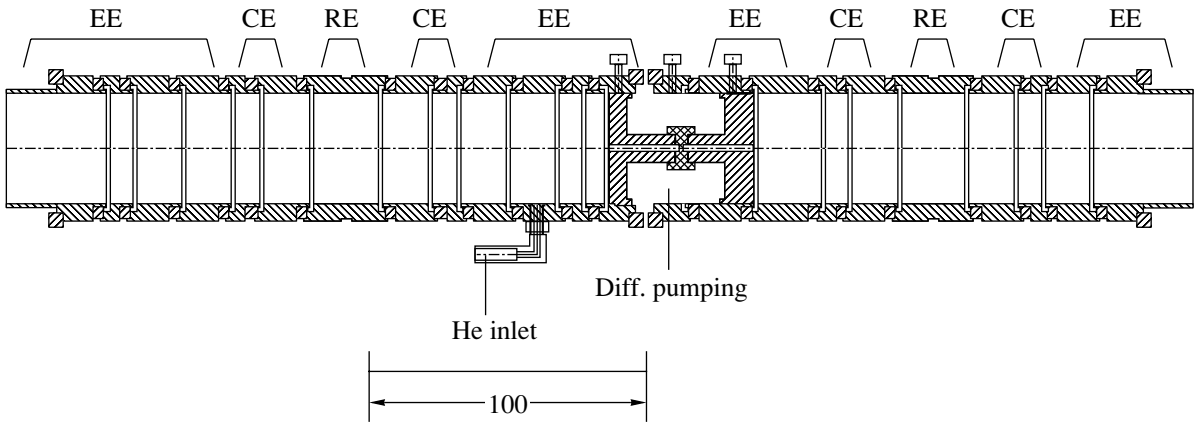

Fig. 2. Geometry of the Penning traps. The cooler trap (left) is separated from the decay trap (right) by a differential pumping barrier. The total length of the two traps is 42.8 cm. EE denotes the end-cap electrodes, CE the correction electrodes, and RE the central ring electrode of the traps. Also, the buffer gas inlet is shown.

magnets of $B_{\max} = 9$ T and $B_{\min} = 0.1$ T and an electrostatic retardation system. Recoil ions are created in the strong magnetic field region and pass on their way the region with a low magnetic field. Provided that the fields change sufficiently slowly along the path of the ions, their motion can be considered as adiabatic. According to the principle of adiabatic invariance of the magnetic flux, a fraction $1 - (B_{\min}/B_{\max}) \approx 98.9\%$ of the energy of the ion motion perpendicular to the magnetic field lines will be converted into energy of the ion motion along the magnetic field lines. Then, in the homogeneous region of low magnetic field $B_{\min}$, the total kinetic energy of the recoil ions can be probed by retarding them with a well-defined electrostatic potential. By counting how many ions pass the analysis plane for different retardation voltages, the cumulative recoil energy spectrum can be measured.

3. SETUP

An overview of the experimental setup is shown in Figs. 3 and 4. In a first step, the ions produced by the ISOLDE facility [16, 17] (CERN) get trapped by REXTRAP [18], a Penning trap which serves to bunch, cool, and purify the ion beams for the REX-ISOLDE project. Then they are transmitted through the horizontal beamline and a 90° bender with spherical electrodes into the vertical beamline of the WITCH setup. There the ions are electrostatically decelerated from 60 keV to 50 eV in several steps to enter the cooler trap. In the cooler trap, the ion cloud is prepared to be ejected through the differential pumping barrier into the second Penning trap, the decay trap. The latter is placed at the entrance of the retardation spectrometer. After β decay, the recoil ions emitted into the direction of the spectrometer spiral from the trap placed in the strong magnetic field into the weak field. In the homogeneous low-field region, the kinetic energy of the ions is probed by the retardation potential. The ions that pass this analysis region are reaccelerated to $\sim$10 keV to get off the magnetic field lines. The reacceleration also ensures constant detection efficiency for all recoil energies. Finally, the ions are focused with an einzellens onto a microchannel plate (MCP) detector. For normalization purposes, several β detectors are installed in the spectrometer section.

4. RECOIL SPECTRUM

The daughter ions from β decay can have different charge states $q = n \cdot e$ due to electron shake-off [19]. The recoil ions with energy E_{rec} and charge q will appear in the measured spectrum at a retardation voltage $U_{\text{ret}} = E_{\text{rec}}/q$ due to the retardation principle. The measured spectrum will thus be a superposition of the spectra of the various charge states, each with different endpoints $U_{0n} = E_0/(n \cdot e)$, $n \geq 1$, where E_0 is the endpoint energy of the recoil energy spectrum for $n = 1$ (Fig. 5). Consequently, when measuring the full recoil spectrum up to the endpoint energy E_0, the upper half of the spectrum will consist purely of events from charge state $n = 1$. Therefore this part of the spectrum will be used for analysis of the recoil spectrum shape.

Electron capture decay (EC) always accompanies β^+ decay and leads to a monoenergetic peak in the recoil energy spectrum at energy E_{EC}, above the endpoint energy E_0 of the continuous recoil spectrum from β^+ decay. By measuring these EC peaks for several suitable nuclides with different decay energies, an energy calibration can be done. Even more, EC peaks of different charge states n for the same nuclide will be reflected in the spectrum at different energies E_{EC}/n. The appearance of a peak also makes it possible to

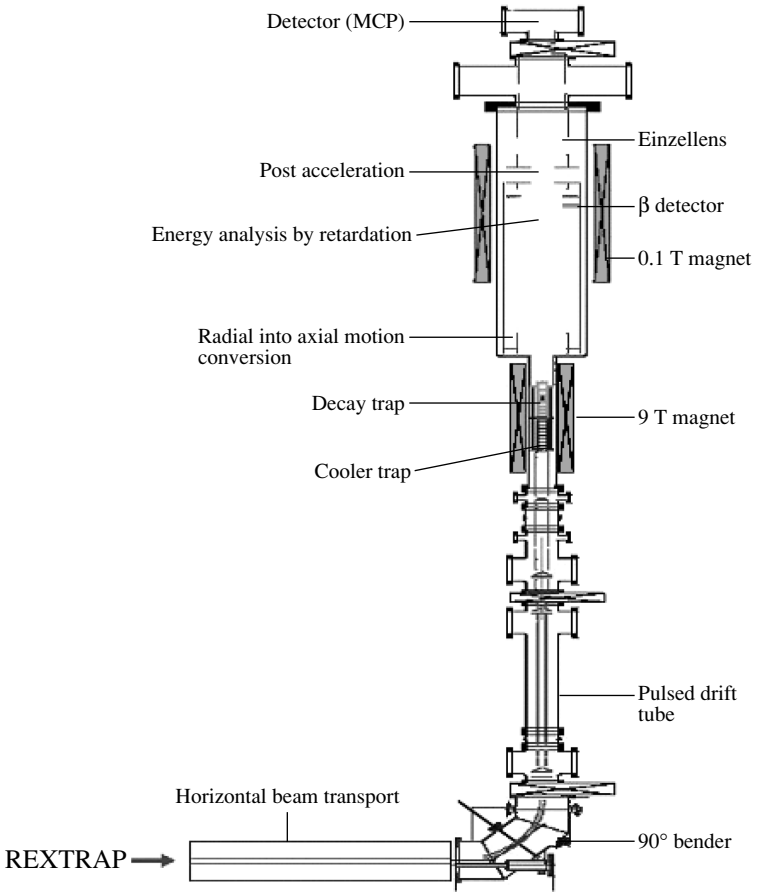

Fig. 3. Overview of the experimental setup.

detect EC decay even at very low EC/β^+-branching ratios.

Simulations show (Fig. 6) that, to reach a precision of $\Delta a = 0.005$ for a, the total number of events in the differential energy spectrum should be $N = 10^7$–10^8 and a minimum of $n_0 = 20$ channels in the upper half of the spectrum seems to be sufficient. The measurement time needed for that is $t \approx 3$ days for ^{35}Ar and $t \approx 10$ days for ^{26m}Al with a trap load of 10^6 ions. However, it can be pointed out that it should be feasible to increase the trap load by a factor of 10, which reduces the measurement time accordingly.

5. MORE PHYSICS WITH THE WITCH EXPERIMENT

The possibility of measuring the recoil energy spectrum with high precision for many different isotopes opens up a whole range of topics that can be investigated. Already the β–ν angular correlation contains information on many other phenomena beyond additional weak interaction types. For example, in mixed decays, it is dominated by the F/GT mixing ratio, while it is also influenced by induced weak currents [20–22]. Thus, with a measurement of a, the F/GT mixing ratio of a decay can be determined or the symmetries governing the induced currents can be tested (Subection 5.2). Other information that can be extracted from the recoil energy spectrum is the position of the EC peaks which yields the Q value of the decay with good precision (Subsection 5.1). Also the EC/β^+-branching ratio can be measured. A study of its Q-value dependence may yield new limits on the Fierz interference coefficient b [23] providing also limits on S or T interaction. Further, the charge state distribution after β decay can be determined for both β^+ and EC decay [24].

Finally, additional detectors can be added to the setup to perform in-trap spectroscopy. Adding more β detectors opens the possibility for β spectroscopy with a pure sample without any scattering of the β particles in the source. Adding γ detectors close to the trap may make also γ spectroscopy possible. Measuring both recoil ions and β particles or γ rays in coincidence will yield even more information. Two examples are presented in more detail in the following subsections.

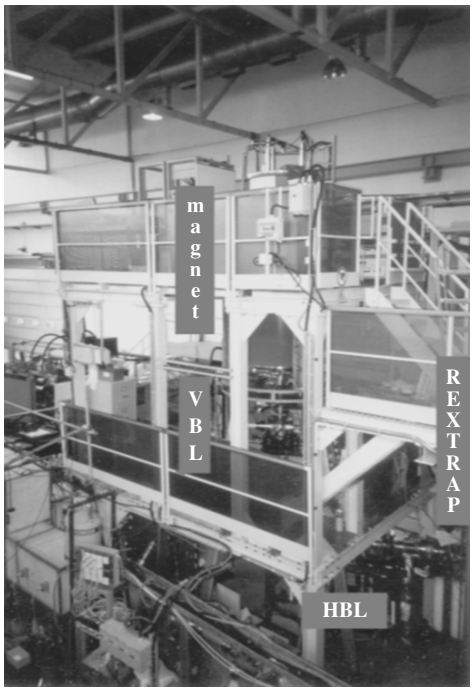

Fig. 4. ISOLDE hall. WITCH setup + platform (working area). Magnet system, as well as part of vertical beamline and horizontal beamline, is shown.

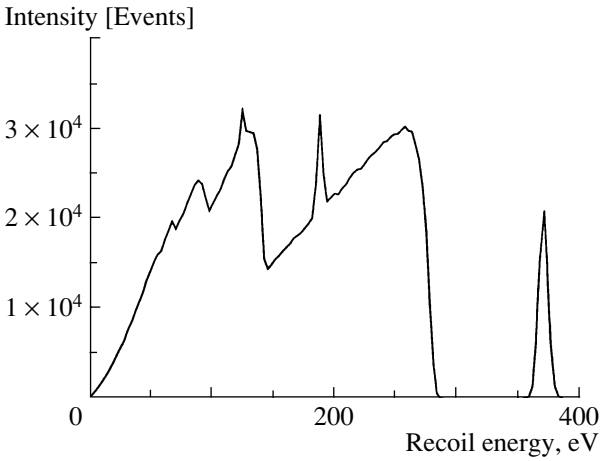

Fig. 5. Recoil energy spectrum calculated for ^{26m}Al.

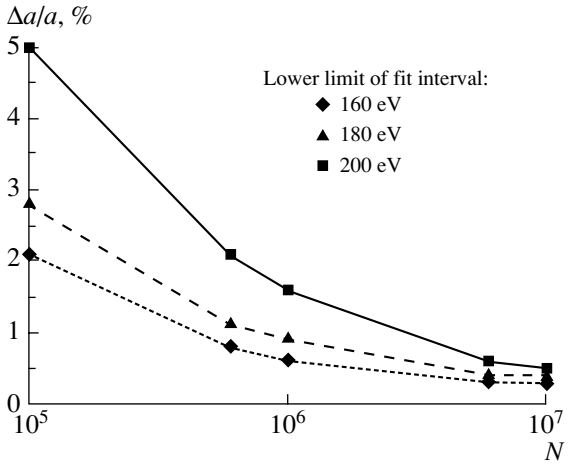

Fig. 6. Estimated precision on a (for ^{26}Al, C.L. = 68.3%) for different analysis intervals, depending on the total number of events N in the differential recoil spectrum.

5.1. Q Values

The EC peak position is $E_{\mathrm{EC}} = Q^2/2M$, where M is the rest energy of the recoil ion and Q is the Q value of the decay. This results in $\Delta Q/Q = 0.5\Delta E_{\mathrm{EC}}/E_{\mathrm{EC}}$ (Fig. 7). Here, ΔE_{EC} is the precision with which the position of the EC peak can be determined experimentally. The resolution of the WITCH experiment will be of order $\Delta E_{\mathrm{EC}}/E_{\mathrm{EC}} \approx 1\%$, yielding an uncertainty on Q of 0.5%. For $Q = 1$ MeV, this corresponds to $\Delta Q = 5$ keV. Since the peak position usually can be determined with higher precision than that given by the resolution, Q-value determinations with uncertainties of less than 1 keV may become possible with the WITCH experiment.

5.2. Induced Weak Currents

Induced weak currents can also modify the β–ν angular correlation [20–22]. In particular, weak magnetism will alter the β–ν angular correlation in GT decays and introduce a β-energy dependence. For a pure GT decay, this results in [20] $a \to a \cdot [1 - 8F_a(E - 0.5E_0) - 2F_bE_0]$, where F_a and F_b are two weak magnetism form factors, E is the β energy, and E_0 is the β endpoint. F_a can be extracted from a measurement of the β-energy dependence of a. Comparison with the weak magnetism form factor of an isobaric analog γ decay then constitutes a test of the conserved vector current hypothesis [20]. F_b can be used to search for second class currents [4, 22].

A coarse estimate of the influence of F_a on a can be extracted from the numbers given in [20]. In the $A = 12$ system, $F_a \sim 0.003/\mathrm{MeV}$ and $E_0 = O(10\ \mathrm{MeV})$. Therefore, a will deviate from its nominal value of $-1/3$ by more than 10% for the smallest and largest β energies. The WITCH experiment aims to achieve a precision of $\Delta a = 0.5\%$ or better. Therefore, it could be possible to determine the weak magnetism form factor with a precision of better than 5%.

6. STATUS

The horizontal beamline (Figs. 3 and 4) which connects the WITCH to the REXTRAP setup is fully operational and tested. Transfer tests showed ~100%

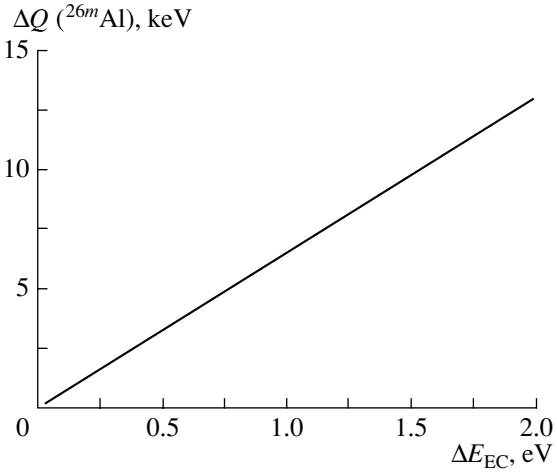

Fig. 7. Precision that can be achieved for the determination of the Q value from the EC-peak position (for ^{26m}Al). A precision of $\Delta Q = 1$ keV or better should be feasible.

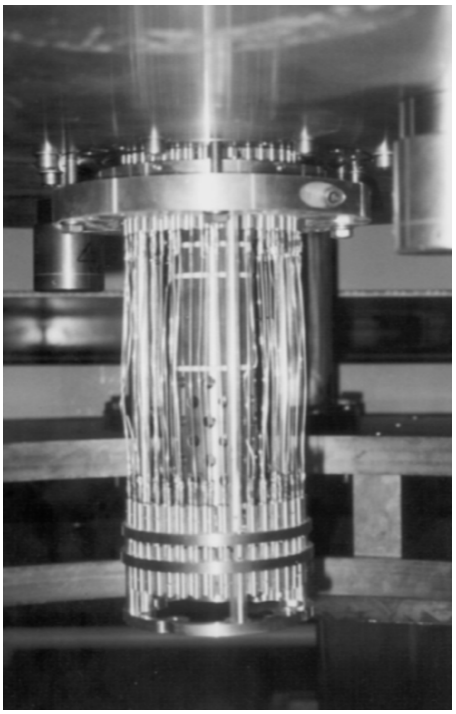

Fig. 8. WITCH trap structure inserted in the bore tube of 9-T magnet (drift electrodes and trap electrodes connection wires are visible).

efficiency of ion beam transport from REXTRAP to the first chamber of the vertical beamline, behind the 90° bender. The vertical beamline with the pulsed drift tube and deceleration electrodes has been installed and successfully tested for high-voltage reliability. Development of the high-voltage switching system is in progress. The cryostat with two superconducting magnets of 9 T and 0.2 T has been delivered, installed, and successfully tested by the company and by the WITCH group in situ. Both the cooler and the decay traps are fully assembled and the electrical connection of the trap electrodes is done (Fig. 8). The retardation electrodes for the spectrometer have been delivered to Leuven. The control system of WITCH is based on the LabVIEW[4)] programming environment and the core of the system should be finished before the end of 2003. During the shutdown period of the ISOLDE facility (until April 2004), several tests with a stable beam from REXTRAP will be done. The first measurement with a radioactive beam of ^{35}Ar is supposed to take place during 2004. This beamtime is intended to demonstrate the working principle of the WITCH setup.

WITCH has been approved as ISOLDE test experiment P111 by the ISC[5)] with a total of 18 shifts of the beam. Beyond this, more beamtime will be necessary to measure a recoil energy spectrum with high statistics and to investigate systematic effects.

ACKNOWLEDGMENTS

This work is supported by the European Union grants FMRX-CT97-0144 (the EUROTRAPS TMR network) and HPRI-CT-2001-50034 (the NIPNET RTD network), by the Flemish Fund for Scientific Research FWO, and by the project GOA 99-02 of the K.U. Leuven. It also was partly funded with a specialization fellowship of the Flemish Institute for the Stimulation of Scientific-Technological Research in Industry (IWT).

REFERENCES

1. P. Herczeg, Prog. Part. Nucl. Phys. **46**, 413 (2001).
2. N. Severijns *et al.*, Hyperfine Interact. **129**, 223 (2000).
3. J. S. Allen *et al.*, Phys. Rev. **116**, 134 (1959).
4. C. H. Johnson *et al.*, Phys. Rev. **132**, 1149 (1963).
5. E. G. Adelberger *et al.*, Phys. Rev. Lett. **83**, 1299 (1999).
6. A. Garcia *et al.*, Hyperfine Interact. **129**, 237 (2000).
7. J. D. Jackson, S. B. Treiman, and H. W. Wyld, Nucl. Phys. **4**, 206 (1957).
8. A. I. Boothroyd *et al.*, Phys. Rev. C **29**, 603 (1984).
9. J. S. Hardy *et al.*, Nucl. Phys. A **509**, 429 (1990).
10. A. S. Carnoy *et al.*, Nucl. Phys. A **568**, 265 (1994).
11. C. S. Wu and S. A. Moszkowski, *Beta Decay* (Wiley, New York, 1966).
12. G. Bollen *et al.*, Nucl. Instrum. Methods Phys. Res. A **368**, 675 (1996).

[4)] LabVIEW™ is a trademark of the National Instruments Corporation. http://www.ni.com.

[5)] ISOLDE Scientific Committee, now INTC: ISOLDE and Neutron Time-of-flight Committee.

13. M. Beck *et al.*, Nucl. Instrum. Methods Phys. Res. A **503**, 567 (2003).
14. E. Kugler *et al.*, Nucl. Instrum. Methods Phys. Res. B **70**, 41 (1992).
15. V. M. Lobashev and P. E. Spivak, Nucl. Instrum. Methods Phys. Res. A **240**, 305 (1985).
16. E. Kugler, Hyperfine Interact. **129**, 23 (2000).
17. http://isolde.web.cern.ch/ISOLDE/.
18. F. Ames *et al.*, in *Proceedings of the Conference on Exotic Nuclei and Atomic Masses, Bellaire, USA, 1998*; AIP Conf. Proc. **455**, 927 (1998).
19. A. H. Snell, *Alpha-, Beta-, and Gamma-Ray Spectroscopy* (North-Holland, Amsterdam, 1968), p. 1545.
20. M. Gell-Mann, Phys. Rev. **111**, 362 (1958).
21. B. R. Holstein, Rev. Mod. Phys. **46**, 789 (1974).
22. L. Grenacs, Ann. Rev. Nucl. Part. Sci. **35**, 455 (1985).
23. R. Sherr and R. H. Miller, Phys. Rev. **93**, 1076 (1954).
24. N. D. Scielzo *et al.*, Phys. Rev. A **68**, 022716 (2003).

Physics of Atomic Nuclei, Vol. 67, No. 6, 2004, pp. 1119–1123. From Yadernaya Fizika, Vol. 67, No. 6, 2004, pp. 1146–1150.

NEUTRINO PHYSICS AND ASTROPHYSICS

Results from the MUNU Experiment on Neutrino–Electron Scattering*

Z. Daraktchieva**
(for the MUNU Collaboration)

Institut de Physique, Neuchâtel, Switzerland

Received November 17, 2003

Abstract—The MUNU experiment studies electron antineutrino–electron elastic scattering. The detector is a time projection chamber surrounded by an anti-Compton detector. The distance between the reactor (serving as the neutrino source) and the detector is 18 m. Here, data are presented corresponding to 66.6-d live time reactor on and 16.7-d reactor off. The electron recoil spectrum obtained by using a visual scanning procedure is presented. The upper limit on the neutrino magnetic moment $\mu_\nu < 1.0 \times 10^{-10}\mu_B$ is derived.

1. THEORY OF THE EXPERIMENT

The MUNU experiment [1] studies $\bar{\nu}_e e$ elastic scattering and probes the possible existence of the magnetic moment of the electron antineutrino by comparing the measured cross section of the process with the one predicted from the weak interaction. The cross section is given by

$$\frac{d\sigma}{dT_e} = \frac{G_F^2 m_e}{2\pi}\left[(g_V + g_A)^2 + (g_V - g_A)^2 \times \left(1 - \frac{T_e}{E_\nu}\right)^2 + \left(g_A^2 - g_V^2\right)\frac{m_e T_e}{E_\nu^2}\right] + \frac{\pi\alpha^2\mu_\nu^2}{m_e^2}\frac{1 - T_e/E_\nu}{T_e},$$

$$g_V = 2\sin^2\theta_W + \frac{1}{2}, \quad g_A = -\frac{1}{2}.$$

In the above formula, the expression in brackets is the weak contribution to the cross section (from the Standard Model alone), while the last term is the contribution from the magnetic moment [2]. Here, E_ν is the neutrino energy, T_e is the electron recoil energy, μ_ν is the magnetic moment, and g_V and g_A are the coupling constants. The relative contribution of the magnetic moment term increases with a decrease of both the neutrino energy and the electron recoil energy.

2. MUNU EXPERIMENT

The electron antineutrino source of the MUNU experiment is a nuclear reactor of 2800 MW, which is situated in Bugey (France). The reactor emits neutrinos in the energy region 0–8 MeV. The neutrinos are mostly produced by the beta decay of the fission fragments of ^{235}U (54%), ^{239}Pu (33%), ^{241}Pu (6%), and ^{238}U (7%). The detector is situated 18 m from the reactor core and has an overburden corresponding to 20 m w.e. The neutrino flux in the lab is $10^{13}\nu\ \mathrm{cm}^{-2}\ \mathrm{s}^{-1}$.

The MUNU detector (Fig. 1), made from radiochemically pure materials, consists of three parts: a time projection chamber (TPC), an anti-Compton detector, and passive shielding. The main part of the detector is the TPC, filled with 11.4 kg of CF_4 gas at 3-bar pressure. The gas was selected because of its high density, good drifting properties, low Z (which reduces multiple scattering), and its absence of free protons. The gas is contained in a cylindrical transparent acrylic vessel with an active volume of 1 m^3, a length of 162 cm, and a diameter of 90 cm. The TPC orthogonal to the neutrino flux of the reactor is absolutely symmetric with respect to the reactor–detector axis. On one side of the TPC, a cathode is mounted and held at a negative voltage. On the other side of the TPC, an anode multiwire proportional plane is mounted, which consists of grid wires, anode wires, and an xy pickup plane (with perpendicular x and y stripes). The anode wires (20 μm each) are separated by potential wires (100 μm each).

The TPC acts as a target for the neutrinos and as a detector for the recoiling electrons at the same time. When a neutrino interacts with an electron from the gas, the electron starts to move and produces a track. The secondary ionization electrons from the track drift to the anode and are collected by the anode wires and multiplied. This gives an integrated anode signal, which corresponds to total deposited

*This article was submitted by the author in English.

** e-mail: Zornitza.Daraktchieva@unine.ch

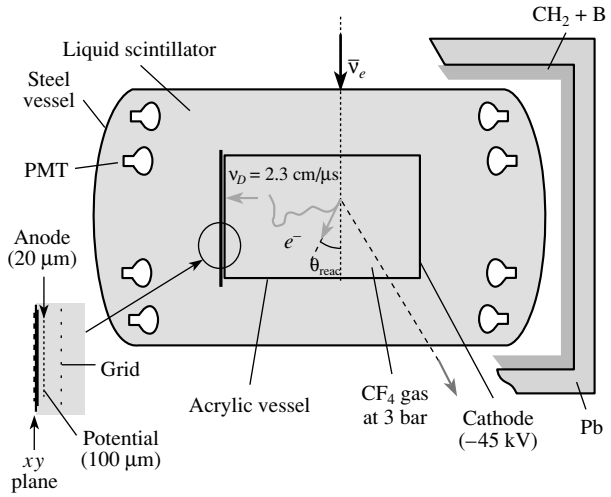

Fig. 1. The MUNU detector.

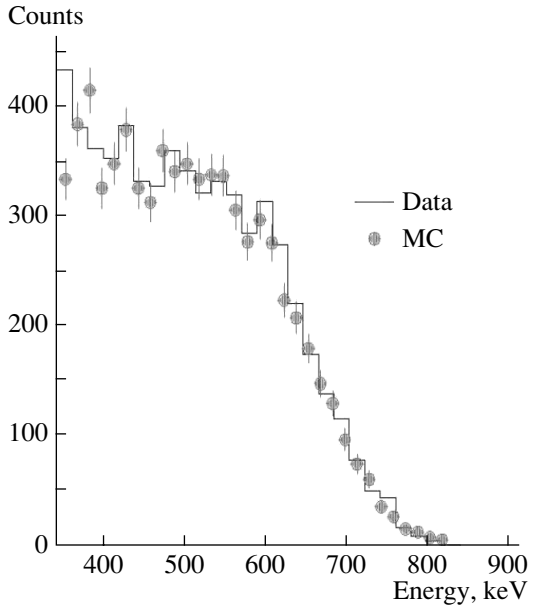

Fig. 2. A Compton spectrum of ^{54}Mn in the TPC compared with MC.

energy. The xy plane (pitch 3.5 mm) behind the anode provides spatial information on the tracks in the x and y directions. The third projection z is obtained from the time evolution of the signal. The second part of the detector is the anti-Compton detector, which surrounds the TPC and consists of 10 m^3 of liquid scintillator. The scintillator is contained in a steel vessel and viewed by 48 photomultipliers (24 on each side). It serves to veto muons and Compton electrons. The steel vessel has a 380-cm length and a 200-cm diameter. The efficiency of the anti-Compton for rejecting muons and gammas is 99.9% [3]. The third part of the detector is the passive shielding, which surrounds the anti-Compton. It consists of 15 cm of Pb and 8 cm of polyethylene boron and serves to absorb external gammas and neutrons.

The energy calibration of the TPC is done by using γ sources such as ^{137}Cs, ^{54}Mn, and ^{22}Na. The obtained Compton electron spectra are compared with MC simulations (GEANT3 code), where the effects of the resolution are also included. The obtained calibration plot with ^{54}Mn is shown in Fig. 2. The gain is monitored continuously throughout the data-taking period by also using cosmic muons [4].

The energy resolution of the detector is 8% (1σ) at 1 MeV, the angular resolution, as derived from the MC tracks scanned visually, is 10° (1σ) at 1 MeV, and the spatial resolution is 1.7 mm. The tracking capabilities of the MUNU detector are demonstrated in Fig. 3, which shows a fully contained single electron.

Concerning the background of the experiment, the presence of ^{222}Rn at the level of 0.7 mBq/m^3 was measured in the detector from ^{214}Bi–^{214}Po decays (from ^{222}Rn decay chain). In Fig. 4, one such coincidence is presented, the electron is from the β decay of ^{214}Bi, and α is from the α decay of ^{214}Po. Another possible source of background, namely, ^{85}Kr β decay, which is difficult to establish, was eliminated by setting the energy threshold at 700 keV above the endpoint.

An excess of events from the anode side were monitored during the experiment. This is possibly due to the greater complexity of the anode side: the grid, the potential wires, the anode wires, the xy readout plane. On the contrary, the cathode itself is very simple, made from a very pure copper foil. To eliminate the possible background from the anode side, only the electrons from the cathode side ($\theta_{\rm det} < 90°$) are accepted.

3. VISUAL SCANNING PROCEDURE

The selection of good events (fully contained single electrons) proceeds in two steps. The first step is an automatic data filtering, which eliminates the events identified as alpha, discharges, muons, Compton electrons, cosmic hits, or not fully contained electrons (radius >42 cm). The second step is a visual selection of the fully contained single electrons.

The fit of the first cm of the track of each single electron is done by eye [5]. From this fit one determines $\theta_{\rm reac}$ (the scattering angle with respect to the reactor axis) and $\theta_{\rm det}$ (the angle with respect to the detector axis). The electron recoil energy (T_e) is calculated from the integrated anode signal. The neutrino energy (E_ν) is reconstructed from the kinematics by using the scattering angle ($\theta_{\rm reac}$) and the electron recoil energy (T_e).

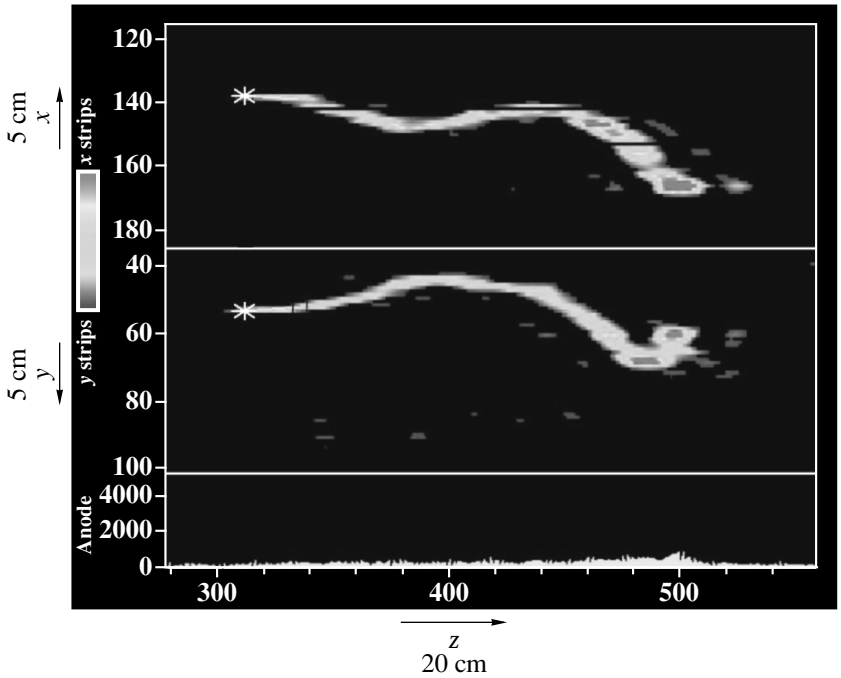

Fig. 3. A 1050-keV electron is shown. The integrated anode signal (at the bottom of the picture) and the fits of the first cm of the electron track on xz, yz projections are presented.

The following cuts are applied in the analyses: the energy cut ($T_e > 700$ keV), the angular cut ($\theta_{\rm det} < 90°$), and the kinematic cuts ($E_\nu > 0$, $\cos\theta_{\rm reac} > 0$ (forward electrons), $E_\nu > 0$, $\cos(\pi - \theta_{\rm reac}) < 0$ (backward electrons)). The live time was found to be around 60%. By using the visual scanning procedure, 66.6 d live time reactor on and 16.7-d live time reactor off are analyzed.

4. RESULTS FROM THE VISUAL SCANNING PROCEDURE

The angular distribution in $\cos\theta_{\rm reac}$ of the fully contained single electrons for the 66.6 d reactor-on is shown in Fig. 5. Here, in the histogram, the forward electrons and the backward electrons are marked by dark color. The slightly nonlinear angular response of the detector (estimated from MC) explains the accumulation of events around $\cos\theta_{\rm reac} = \pm 1$. Nevertheless, it is seen that there is a clear excess of events from the reactor direction in the reactor on data: forward (458) over backward (340) events.

The angular distribution of the fully contained single electrons for 16.7 d reactor-off is shown in Fig. 6. In contrast to the reactor on data, both the forward (130) and the backward (147) events are identical within the statistics. For energy higher than 700 keV, the integrated forward minus backward rate is -1.02 ± 1.00 counts per day (cpd), which is fully consistent with zero.

Both the forward and the backward energy distributions of the electrons for reactor on are shown in Fig. 7. Here, in the histogram, the forward electrons (signal plus background) are presented by a dotted line, while the backward electrons (background) are presented by a solid line. The total forward minus backward rate is 118 for 66.6 d, which gives 1.77 ± 0.42 cpd for energy higher than 700 keV. The forward minus backward energy distribution for reactor on is shown in Fig. 8.

Fig. 4. A beta–alpha coincidence. The electron is from the β decay of ^{214}Bi and the alpha is from the α decay of ^{214}Po.

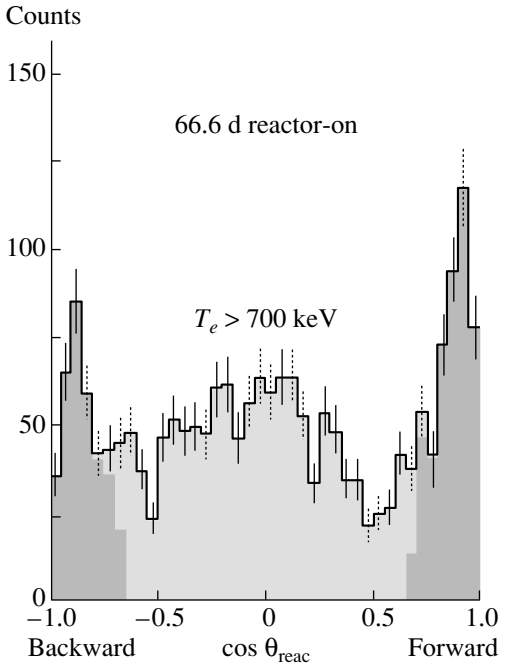

Fig. 5. Distribution of θ_{reac} for fully contained single electrons reactor on.

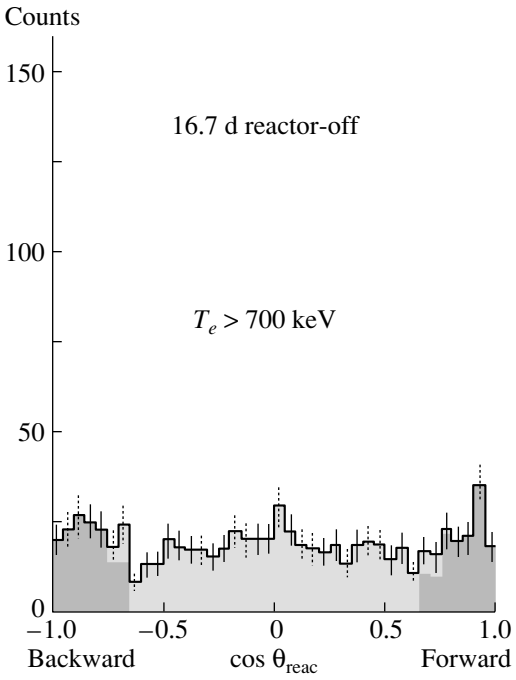

Fig. 6. Distribution of θ_{reac} for reactor off.

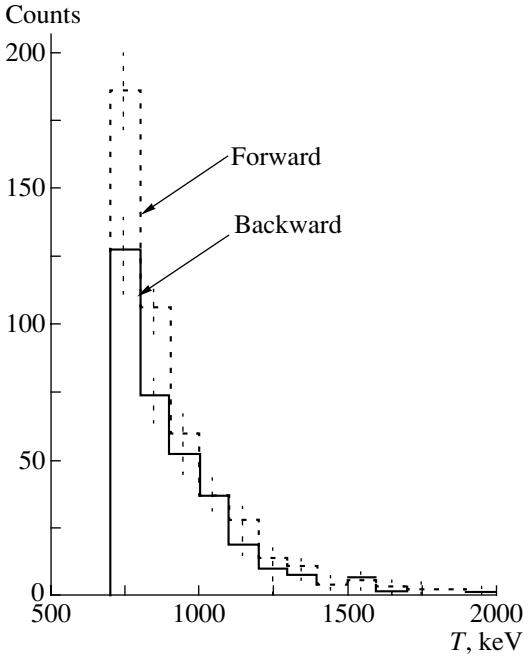

Fig. 7. Energy distribution of forward and backward electrons reactor on.

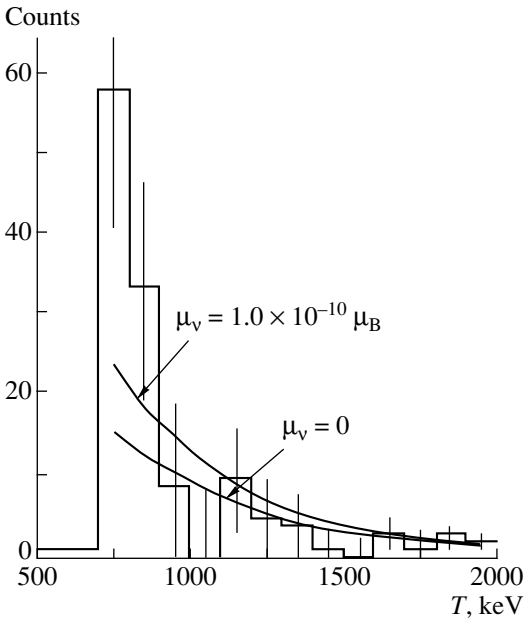

Fig. 8. Energy distribution of forward minus backward electrons reactor on.

The expected event rate for the zero magnetic moment was calculated by using our best knowledge of the reactor neutrino spectrum including the known activations of the fissile isotopes. The global acceptance is obtained from MC simulations of electron tracks in the detector and measurements with sources. The containment efficiency of the detector in the 42-cm fiducial radius, as well as the efficiency of the scanning, is also included in the calculations.

For $T_e \geq 700$ keV, a difference between the measured (1.77 ± 0.42 cpd) and expected (1.2 ± 0.1 cpd) rates is seen. This slight excess, however, is difficult to

explain with the neutrino magnetic moment, because the excess is only seen in the first two channels: 700 and 800 keV. It could result from some additional neutron activations beyond the ones taken into account. The low-energy part of the neutrino spectrum is not so well known; only calculations exist [2, 6]. This part of the neutrino spectrum corresponds to electron recoil energy below 900 keV.

To avoid the problems mentioned above, we restrict our analysis to the electron energies higher than 900 keV. The corresponding part of the neutrino spectrum is well known from direct measurements of the β spectrum of fission fragments [7] with a precision of order of 5%. At $T_e \geq 900$ keV, we have good agreement between the measured (0.41 ± 0.26 cpd) and expected (0.62 ± 0.05 cpd) rates.

The following limit of the electron antineutrino $\mu_\nu < 1.0 \times 10^{-10}\mu_B$ (90% C.L.) was derived from the energy distribution and the event rate by using the χ^2 method.

The expected spectrum for $\mu_\nu = 1.0 \times 10^{-10}\mu_B$ is presented in Fig. 8 as well as the calculated energy distribution for $\mu = 0$.

The result of the MUNU experiment improves the existing limits on the neutrino magnetic moments. Firstly, the recent limit from the direct measurement obtained by the TEXONO Collaboration [8] by using an ultra low background high purity germanium detector installed near the Kuo-Sheng reactor in Taiwan. The energy threshold is 12 keV. The reactor-on minus reactor-off was found to be identical, and from that the limit $\mu_\nu < 1.3 \times 10^{-10}\mu_B$ (90% C.L.) was reported. Secondly, the limit from the indirect measurement, from solar neutrinos, obtained from the Super-Kamiokande experiment. This experiment measured the electron recoil spectrum of solar ^{8}B neutrinos. From the spectrum shape, the limit $\mu_\nu^{sol} < 1.5 \times 10^{-10}\mu_B$ (90% C.L.) was derived [9].

5. CONCLUSION

The tracking capabilities of the MUNU detector allow us to measure both the scattering angle and the energy of the recoil electrons. The reactor signal is extracted by subtracting the background measured at the same time as the signal. Good agreement is observed for $T_e \geq 900$ keV between the measured and calculated spectra assuming $\mu_\nu = 0$. From these spectra, the upper limit of the magnetic moment of the electron antineutrino $\mu_\nu < 1.0 \times 10^{-10}\mu_B$ (90% C.L.) was derived.

REFERENCES

1. C. Amsler *et al.* (MUNU Collab.), Nucl. Instrum. Methods Phys. Res. A **396**, 115 (1997).
2. P. Vogel and J. Engel, Phys. Rev. D **39**, 3378 (1989).
3. C. Amsler *et al.* (MUNU Collab.), Phys. Lett. B **545**, 57 (2002).
4. M. Avenier *et al.* (MUNU Collab.), Nucl. Instrum. Methods Phys. Res. A **482**, 408 (2002).
5. Z. Daraktchieva *et al.* (MUNU Collab.), Phys. Lett. B **564**, 190 (2003).
6. V. I. Kopeikin *et al.*, Phys. At. Nucl. **60**, 172 (1997).
7. G. Zacek *et al.*, Phys. Rev. D **34**, 2621 (1986).
8. H. B. Li *et al.* (TEXONO Collab.), Phys. Rev. Lett. **90**, 131802 (2003).
9. J. Beacom and P. Vogel, Phys. Rev. Lett. **83**, 5222 (1999).

Physics of Atomic Nuclei, Vol. 67, No. 6, 2004, pp. 1124–1128. From Yadernaya Fizika, Vol. 67, No. 6, 2004, pp. 1151–1155.

NEUTRINO PHYSICS AND ASTROPHYSICS

Probing the Seesaw Mechanism with Neutrino Data and Leptogenesis*

M. Frigerio**

International School for Advanced Studies, Trieste, and INFN, Trieste Section, Trieste, Italy

Received November 4, 2003

Abstract—We use the current low-energy neutrino data to understand the structure of the neutrino mass matrix. Considering this information and assuming hierarchical neutrino Yukawa couplings, we use the seesaw formula to study the properties of the heavy right-handed neutrinos N_i. We find that successful baryogenesis via leptogenesis requires mass degeneracy and maximal mixing of N_1 and N_2.

1. SOME BASIC FEATURES OF THE NEUTRINO MASS MATRIX

In the flavor basis $(\nu_e, \nu_\mu, \nu_\tau)$, the Majorana mass matrix of light neutrinos, m, can be written in terms of the observables as

$$m = U^*_{\rm PMNS} m^{\rm diag} U^\dagger_{\rm PMNS}, \qquad (1)$$

where $m^{\rm diag} \equiv {\rm diag}(m_1, m_2, m_3)$ and

$$U_{\rm PMNS} = U(\theta_{12}, \theta_{23}, \theta_{13}, \delta) K_0,$$
$$K_0 = {\rm diag}(e^{i\rho}, 1, e^{i\sigma}).$$

Here, δ is the CP-violating Dirac phase, and ρ and σ are the two CP-violating Majorana phases. The matrix m should satisfy a number of experimental constraints. From solar, atmospheric, accelerator, and reactor neutrino experiments, we take the following input (at 90% C.L.) [1]:

$$\Delta m^2_{\rm sol} \equiv \Delta m^2_{12} = \left(7^{+10}_{-2}\right) \times 10^{-5}\ {\rm eV}^2, \qquad (2)$$
$$\tan^2\theta_{12} = 0.42^{+0.2}_{-0.1};$$
$$\Delta m^2_{\rm atm} \equiv \Delta m^2_{23} = \left(2.5^{+1.4}_{-0.9}\right) \times 10^{-3}\ {\rm eV}^2,$$
$$\tan\theta_{23} = 1^{+0.35}_{-0.25};$$
$$\sin\theta_{13} \lesssim 0.2.$$

A significant freedom in the structure of the mass matrix m still exists due to the unknown absolute mass scale m_1 and CP-violating phases ρ, σ [2]. In spite of this freedom, a generic feature of the matrix m emerges: all its elements are of the same order (within a factor of 10 or so of each other), except in some special cases. The reason for this is twofold:

(i) two large mixing angles θ_{12} and θ_{23};

(ii) a relatively weak hierarchy between the mass eigenvalues:

$$\frac{m_2}{m_3} \geq \sqrt{\frac{\Delta m^2_{\rm sol}}{\Delta m^2_{\rm atm}}} > 0.1\text{–}0.15. \qquad (3)$$

We will refer to the situation where all the matrix elements of m are of the same order and there are no special cancellations as the generic case. A strong hierarchy between certain elements of m can be realized only for specific values of the absolute mass scale and CP-violating phases.

We will be interested, in particular, in the vanishing of the ee entry of the mass matrix. Using Eq. (1) and the standard parametrization for the matrix U, one obtains

$$m_{ee} = \cos^2\theta_{13}(m_1 e^{-2i\rho}\cos^2\theta_{12} + m_2 \sin^2\theta_{12}) + \sin^2\theta_{13} e^{2i(\delta-\sigma)} m_3.$$

The condition $m_{ee} \to 0$ is satisfied for

$$\tan^2\theta_{13} \approx -\frac{m_1 e^{-2i\rho}\cos^2\theta_{12} + m_2 \sin^2\theta_{12}}{e^{2i(\delta-\sigma)} m_3}. \qquad (4)$$

In the limit $\sin\theta_{13} = 0$, Eq. (4) implies that $\rho \approx \pi/2$ and

$$m_1 \approx \frac{\tan^2\theta_{12}\sqrt{\Delta m^2_{\rm sol}}}{\sqrt{1-\tan^4\theta_{12}}} \approx (3\text{–}4) \times 10^{-3}\ {\rm eV}. \qquad (5)$$

This corresponds to the normal mass hierarchy ($m_1 \ll m_2 \ll m_3$). Nonzero $\sin\theta_{13}$ shifts the value of m_1 corresponding to $m_{ee} \to 0$. Taking into account the present upper bound on $\sin\theta_{13}$ [Eq. (2)], we find that relation (4) can be satisfied for $m_1 \lesssim 0.02$ eV. Notice that larger values of m_1 are forbidden because θ_{12} is far from the maximal value.

Let us call $\hat{m}$ the mass matrix in a basis rotated with respect to the flavor basis. While the neutrino

*This article was submitted by the author in English.

** e-mail: frigerio@he.sissa.it

masses m_i are of course basis-independent, the mixing angles and the phases take values $\hat{\theta}_{ij}$, $\hat{\delta}$, $\hat{\rho}$, $\hat{\sigma}$ different with respect to flavor basis. We will show that a very special structure of the right-handed (RH) neutrino sector is generated if the condition $\hat{m}_{ee} \to 0$ is realized in the basis where neutrino Yukawa couplings are diagonal. Notice that the condition $\hat{m}_{ee} \to 0$ is satisfied if the angles and the phases in the rotated basis fulfill Eq. (4). This is possible also for mass spectra different from the normal hierarchy. In this case, $m_2 \approx m_1 \gg \sqrt{\Delta m^2_{\rm sol}}$ and Eq. (4) can be satisfied, in particular, for $\hat{\theta}_{13} = 0$ and $\hat{\theta}_{12} = \pi/4$.

2. SEESAW AND THE MASSES OF RIGHT-HANDED NEUTRINOS

The seesaw mechanism of neutrino mass generation [3] provides a very simple and appealing explanation of the smallness of the neutrino mass. The low-energy neutrino mass matrix m is given in terms of the Majorana mass matrix of the RH neutrinos, M_R, and the Dirac mass matrix, $m_{\rm D}$, as

$$m = -m_{\rm D} M_R^{-1} m_{\rm D}^T. \tag{6}$$

While the elements of $m_{\rm D}$ are expected to be at or below the electroweak scale (≈ 100 GeV), the characteristic mass scale of RH neutrinos is naturally the GUT or parity-breaking scale. For example, in the case of one generation, to obtain $m \approx 0.1$ eV, one should take $M_R \approx 10^{14}$ GeV.

In the case of three generations, the situation is much more complicated: even if the 3×3 matrix m were completely known from experiments (see discussion in the previous section), one cannot infer the masses of RH neutrinos unless some assumption is made on the structure of $m_{\rm D}$. In the basis where the RH mixing is absorbed in M_R, the Dirac mass matrix can be written as

$$m_{\rm D} = U_L^\dagger m_{\rm D}^{\rm diag}, \tag{7}$$

where U_L is a unitary matrix and $m_{\rm D}^{\rm diag}$ is a real positive diagonal matrix. We will assume that $m_{\rm D}$ is an analog to the Dirac mass matrices of quarks, as is the case in many theories with quark–lepton symmetry (for example, in minimal $SO(10)$, one has $m_{\rm D} = m_U$ at the GUT scale). Therefore, we take $m_{\rm D}^{\rm diag} \equiv {\rm diag}(m_u, m_c, m_t)$ with

$$m_u \ll m_c \ll m_t,$$

even though we do not require the exact numerical coincidence of quark and neutrino Dirac masses. For numerical estimates, we will use the reference values

$$m_u = 1\ {\rm MeV}, \qquad m_c = 400\ {\rm MeV}, \qquad m_t = 100\ {\rm GeV}. \tag{8}$$

Inverting the seesaw formula (6), one obtains

$$M_R^{-1} = -m_{\rm D}^{-1} m (m_{\rm D}^{-1})^T \tag{9}$$
$$= -\begin{pmatrix} \dfrac{\hat{m}_{ee}}{m_u^2} & \dfrac{\hat{m}_{e\mu}}{m_u m_c} & \dfrac{\hat{m}_{e\tau}}{m_u m_t} \\ \cdots & \dfrac{\hat{m}_{\mu\mu}}{m_c^2} & \dfrac{\hat{m}_{\mu\tau}}{m_c m_t} \\ \cdots & \cdots & \dfrac{\hat{m}_{\tau\tau}}{m_t^2} \end{pmatrix},$$

where

$$\hat{m} \equiv U_L m U_L^T. \tag{10}$$

The matrix U_L defined in Eq. (7) describes the mismatch between the left-handed rotations diagonalizing the charged lepton and neutrino Dirac mass matrices and, therefore, it is the leptonic analog of the quark CKM mixing matrix. By analogy with the CKM matrix, where the mixing is small, one expects that the matrix U_L is close to the unit matrix. If $U_L = 1$, then $\hat{m} = m$, but, in general, $\hat{m}_{\alpha\beta}$ can be rotated with respect to the matrix elements in the flavor basis.

In the generic case, all $\hat{m}_{\alpha\beta}$ are of the same order and, since the denominators on the right-hand side of Eq. (9) are strongly hierarchical, the eigenvalues of M_R are hierarchical too: $M_1 \ll M_2 \ll M_3$. In particular, the largest eigenvalue of M_R^{-1} is given, to a very good approximation, by the dominant 11-element:

$$M_1 \approx \frac{1}{|(M_R^{-1})_{11}|} = \frac{m_u^2}{|\hat{m}_{ee}|}. \tag{11}$$

Moreover, all three RH mixing angles are tiny ($\lesssim m_u/m_c, m_c/m_t$).

In the special case $\hat{m}_{ee} \to 0$, or, more precisely, when

$$|\hat{m}_{ee}| \ll \frac{m_u}{m_c} |\hat{m}_{e\mu}|, \tag{12}$$

the 12-block of M_R^{-1} is dominated by the off-diagonal entries and, to a good approximation, the two lightest RH neutrinos have opposite CP parity and equal masses:

$$M_1 \approx M_2 \approx \frac{1}{|(M_R^{-1})_{12}|} \approx \frac{m_u m_c}{|\hat{m}_{e\mu}|}. \tag{13}$$

Notice that M_1 is increased by a factor $\sim m_c/m_u$ with respect to the generic case [Eq. (11)]. Moreover, the RH 1–2 mixing is nearly maximal, while the other mixing angles remain very small.

This behavior can be seen in the figure, where, assuming $\hat{m} = m$, we show the dependence of the RH neutrino masses on the lightest mass m_1 for different values of the Majorana phases of the light neutrinos

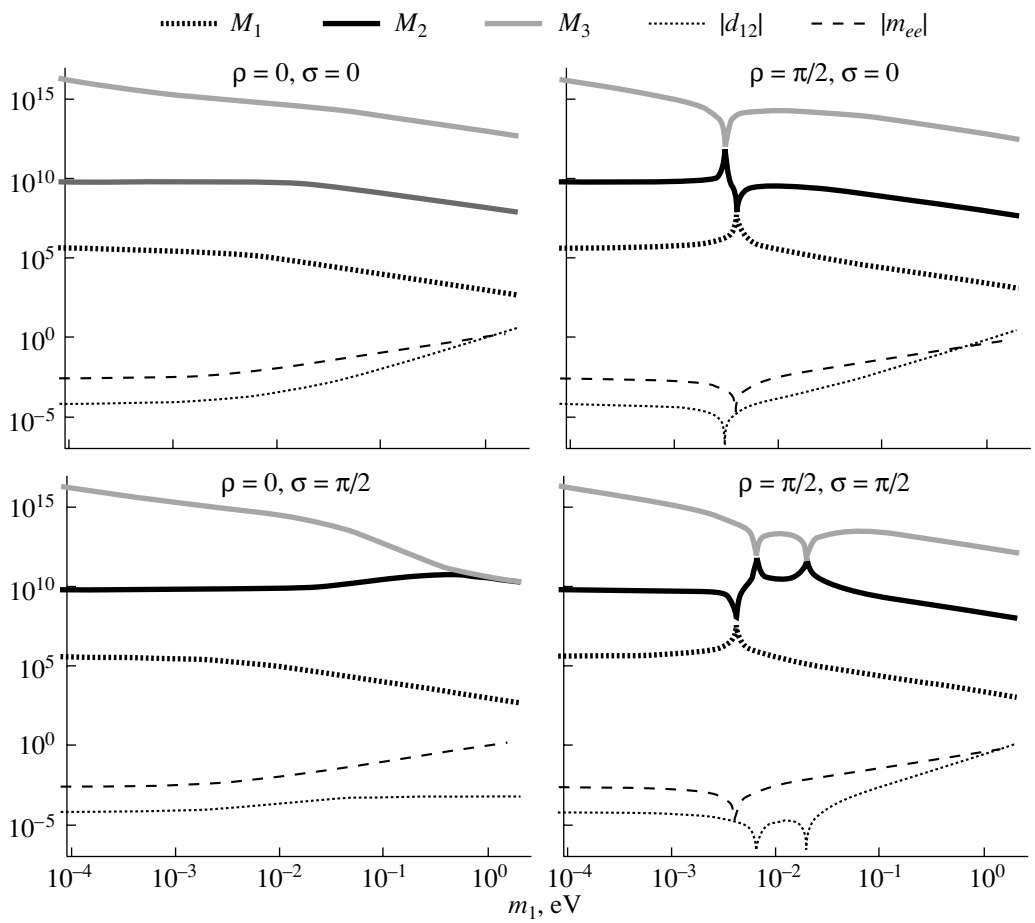

The masses of RH neutrinos M_i (in GeV) as functions of the light neutrino mass m_1 (thick curves) for different values of the Majorana phases of light neutrinos, ρ and σ. We assume normal mass ordering; $s_{13} = 0$; best fit values of solar and atmospheric mixing angles and mass squared differences [Eq. (2)]; values of Dirac-type neutrino masses $m_{u,c,t}$ given in Eq. (8). Also are shown $|d_{12}| \equiv |m_{ee}m_{\mu\mu} - m_{e\mu}^2|$ (in eV^2) (dotted curve) and $|m_{ee}|$ (in eV) (dashed curve) as functions of m_1.

ρ and σ. One sees immediately that the crossing points, where $M_1 \approx M_2$, correspond to $m_{ee} \to 0$. At the crossing points, the mixing between the levels becomes maximal.

The other possible level crossing ($M_2 \approx M_3$) is realized [4] when $d_{12} \to 0$, where $d_{12} \equiv (m_{ee}m_{\mu\mu} - m_{e\mu}^2)$. This can be checked in the figure.

3. BARYOGENESIS VIA LEPTOGENESIS?

Let us consider the constraints on the seesaw mass matrices coming from the requirement of successful baryogenesis via leptogenesis [5]. Successful means that one can reproduce the experimental value of the baryon-to-photon ratio [6],

$$\eta_B = (6.5^{+0.4}_{-0.3}) \times 10^{-10}. \qquad (14)$$

In the early Universe, at temperature $T \gtrsim M_i$, one can assume that RH neutrinos N_i are present in the thermal bath. If CP-violation occurs in the decays of N_i, a lepton asymmetry is produced:

$$\epsilon_i = \frac{\Gamma(N_i \to L\phi) - \Gamma(N_i \to \bar{L}\bar{\phi})}{\Gamma(N_i \to L\phi) + \Gamma(N_i \to \bar{L}\bar{\phi})},$$

where L and ϕ are the Standard Model lepton and Higgs doublets, respectively. The generated asymmetry can survive until today if decays take place out of equilibrium at $T \approx M_i$. Otherwise, inverse decay and scattering processes cancel the asymmetry (washout effects). In particular, when $M_1 \ll M_{2,3}$, only ϵ_1 can survive to the washout, since N_1 is still in thermal equilibrium at the time of $N_{2,3}$ decays and therefore $\epsilon_{2,3}$ are erased by reactions involving N_1. The leptonic asymmetry is converted into a baryonic one by electroweak $(B+L)$-violating processes (sphalerons [7]). One finds [8]

$$\eta_B \approx 0.01\epsilon_1\kappa_1,$$

where κ_1 is the suppression factor due to the washout effects.

In the generic case, it turns out [4] that washout effects lead to $\kappa_1 \lesssim 0.02$. The expression for the lepton asymmetry is [4]

$$\epsilon_1 \approx \frac{3}{16\pi}\frac{m_u^2}{v^2}.$$

Then the produced baryon-to-photon ratio is given, up to a factor of order one, by

$$\eta_B \approx 4\times 10^{-16}\left(\frac{m_u}{1\ \mathrm{MeV}}\right)^2\left(\frac{\kappa_1}{0.02}\right).$$

To reproduce the observed value of η_B, one would need $m_u \sim 1$ GeV. Thus, a successful leptogenesis requires $m_u \sim m_c$, which contradicts our assumption of a strong hierarchy between the eigenvalues of m_{D} and goes contrary to the simple GUT expectations. Therefore, the generic case does not lead to successful leptogenesis.

Let us now consider the predictions for leptogenesis in the special case $\hat{m}_{ee} \to 0$. Since N_1 and N_2 are quasi-degenerate and almost maximally mixed, ϵ_1 and ϵ_2 are almost equal. The dominant contribution to $\epsilon_{1,2}$ is given by [4]

$$\epsilon_1 \approx \epsilon_2 \approx \frac{1}{16\pi v^2}\frac{M_1}{M_1 - M_2} \times \frac{\mathrm{Im}[(m_{\mathrm{D}}^\dagger m_{\mathrm{D}})_{12}^2]}{(m_{\mathrm{D}}^\dagger m_{\mathrm{D}})_{11}} \approx \frac{1}{16\pi}\frac{m_c^2}{v^2}\xi, \quad (15)$$

where

$$\xi = \frac{M_1}{M_1 - M_2}\sin(\phi_1 - \phi_2) \quad (16)$$

and $(\phi_1 - \phi_2)$ is the relative Majorana phase between N_1 and N_2. The enhancement due to the quasi-degeneracy of N_1 and N_2 competes with the suppression due to their almost opposite CP parities: $(\phi_1 - \phi_2) \approx \pi$.

Starting from Eq. (9) and performing a detailed computation of the mass splitting and of the deviation of $\sin(\phi_1 - \phi_2)$ from zero, one finds

$$\xi \approx \frac{4k\tan\Delta}{(1+k)^2 + (1-k)^2\tan^2\Delta}, \quad (17)$$

where

$$k \equiv \frac{m_u^2|\hat{m}_{\mu\mu}|}{m_c^2|\hat{m}_{ee}|}, \quad \Delta \equiv \frac{1}{2}\arg\frac{\hat{m}_{e\mu}^2}{\hat{m}_{ee}\hat{m}_{\mu\mu}}. \quad (18)$$

For $|1-k| \ll 1/\tan\Delta$, Eq. (17) gives $\xi \approx \tan\Delta$, so that, for $\Delta \simeq \pi/2$, a significant enhancement of the asymmetries $\epsilon_{1,2}$ can be achieved.

The enhancement due to the degeneracy is restricted by the condition [9]

$$\frac{M_2 - M_1}{M_1} \gtrsim \frac{\Gamma_1}{M_1} = \frac{(m_{\mathrm{D}}^\dagger m_{\mathrm{D}})_{11}}{8\pi v^2}, \quad (19)$$

where Γ_1 is the N_1-decay width. Moreover, because of almost maximal 1–2 RH mixing, both N_1 and N_2 interact with the thermal bath mainly via the Yukawa coupling m_c/v. This implies that washout effects are much stronger than in the generic case. For example, using the values given in Eq. (8), we find $\kappa_1 \approx \kappa_2 \approx 6\times 10^{-5}$ [4].

Taking into account these constraints, one finally obtains [4]

$$\eta_B \approx 0.01\cdot 2\epsilon_1\kappa_1 \lesssim 1.9\times 10^{-8}\left(\frac{400m_u}{m_c}\right)^2 \times \left[1 + 0.14\log\left(\frac{m_c}{400m_u}\right)\right]^{-0.6}.$$

The value (14) of η_B can be reproduced for $m_u/m_c \gtrsim 2\times 10^{-3}$. This corresponds [4] to a relative splitting $(M_2 - M_1)/M_1 \lesssim 10^{-5}$.

Thus, in spite of strong washout effects, a sufficiently large baryon asymmetry can be generated in this special case, due to the enhancement related to the strong degeneracy of the RH neutrinos. For this to occur, not only the level crossing condition ($\hat{m}_{ee} \to 0$) has to be satisfied, but also the conditions $\Delta \approx \pi/2$ and $k \approx 1$ should be fulfilled, where Δ and k are defined in Eq. (18). All these requirements are consistent with the low-energy neutrino data. We have checked these analytic results by precise numerical calculations.

Other special cases corresponding to 2–3 level crossing or quasi-degeneracy of all three RH neutrinos do not lead to successful leptogenesis because of overly strong washout effects [4]. Therefore, the case $M_1 \approx M_2 \ll M_3$ with the features described above is singled out as the unique possibility of successful thermal leptogenesis.

If this case is not realized in nature, we can conclude that either m_{D} has a structure strongly different from other Dirac mass matrices or the seesaw is not the correct framework to explain both low-energy neutrino data and baryogenesis via leptogenesis.

ACKNOWLEDGMENTS

This paper is based on work done in collaboration with A.Y. Smirnov and E.K. Akhmedov. My participation in NANP'03 has been supported by the Italian MIUR under the program "Fenomenologia delle Interazioni Fondamentali." I would like to thank the conference organizers for the invitation and for the nice atmosphere created in Dubna. Thanks go to Y.A. Kamyshkov, S. Pakvasa, and J.D. Vergados for useful discussions.

REFERENCES

1. T. Nakaya (Super-Kamiokande Collab.), eConf C020620, SAAT01 (2002); hep-ex/0209036; S. Fukuda *et al.* (Super-Kamiokande Collab.), Phys. Lett. B **539**, 179 (2002); hep-ex/0205075; Q. R. Ahmad *et al.* (SNO Collab.), Phys. Rev. Lett. **89**, 011302 (2002); nucl-ex/0204009; K. Eguchi *et al.* (KamLAND Collab.), Phys. Rev. Lett. **90**, 021802 (2003); hep-ex/0212021; M. Apollonio *et al.* (CHOOZ Collab.), Phys. Lett. B **466**, 415 (1999); hep-ex/9907037.
2. M. Frigerio and A. Y. Smirnov, Nucl. Phys. B **640**, 233 (2002); hep-ph/0202247; Phys. Rev. D **67**, 013007 (2003); hep-ph/0207366.
3. T. Yanagida, in *Proceedings of the Workshop on the Unified Theory and Baryon Number in the Universe, Tsukuba, Japan, 1979*, Ed. by O. Sawada and A. Sugamoto, KEK Report 79-18 (1979), p. 95; S. L. Glashow, in *Proceedings of the Conference on Quarks and Leptons, Gargese, 1979*, p. 687; M. Gell-Mann, P. Ramond, and R. Slansky, in *Supergravity,* Ed. by P. van Nieuwenhuizen and D. Z. Freedman (North-Holland, Amsterdam, 1979), p. 315; R. N. Mohapatra and G. Senjanovic, Phys. Rev. Lett. **44**, 912 (1980).
4. M. Frigerio, E. K. Akhmedov, and A. Y. Smirnov, J. High Energy Phys. **09**, 021 (2003); hep-ph/0305322.
5. M. Fukugita and T. Yanagida, Phys. Lett. B **174**, 45 (1986).
6. D. N. Spergel *et al.*, Astrophys. J., Suppl. **148**, 175 (2003); astro-ph/0302209.
7. V. A. Kuzmin, V. A. Rubakov, and M. E. Shaposhnikov, Phys. Lett. B **155B**, 36 (1985).
8. W. Buchmuller, P. Di Bari, and M. Plumacher, Nucl. Phys. B **643**, 367 (2002); hep-ph/0205349.
9. A. Pilaftsis, Int. J. Mod. Phys. A **14**, 1811 (1999); hep-ph/9812256.

Physics of Atomic Nuclei, Vol. 67, No. 6, 2004, pp. 1129–1138. From Yadernaya Fizika, Vol. 67, No. 6, 2004, pp. 1156–1164.

NEUTRINO PHYSICS AND ASTROPHYSICS

θ_{13} Measurements at Accelerators*

A. Guglielmi**

Istituto Nazionale di Fisica Nucleare and Dipartamento di Fisica, Universitá di Padova G. Galilei, Italy

Received November 21, 2003

Abstract—The θ_{13} mixing angle measurements in the neutrino oscillation experiments at accelerators are presented with the perspectives for futures of neutrino beam facilities. Particular emphasis is devoted to near-term new neutrino beam options, such low energy beams and the off-axis technique. © *2004 MAIK "Nauka/Interperiodica".*

1. INTRODUCTION

The current long-baseline neutrino oscillation experiments are designed to unequivocally confirm the atmospheric neutrino anomaly and to establish the oscillation framework. In the standard scenario of three neutrino generations, the leptonic mixing matrix U, which translates between the mass eigenstates and the flavor eigenstates, can be parametrized in terms of six independent parameters to be experimentally measured: three mixing angles θ_{12}, θ_{13}, θ_{23}; two mass-squared differences Δm^2_{12}, Δm^2_{23}, where $\Delta m^2_{ij} = m^2_i - m^2_j$; and a CP violating phase δ. An interesting physical case is when only two of three neutrino flavors mix appreciably in the observed data. The solar neutrino measurements [1] and the KamLAND [2] long-baseline reactor experiment constrain the solar neutrino mixing angle and mass splitting to $0.32 < \tan^2\theta_{12} < 0.55$ and $6\times10^{-5} < |\Delta m^2_{12}| < 9\times10^{-5}$ eV^2 at 90% C.L. The atmospheric neutrino measurements [3] combined with the results of K2K [4] long-baseline and CHOOZ [5] reactor measurements constrain the atmospheric neutrino mixing angle and mass splitting to $0.9 < \sin^2\theta_{23} < 1$ and $|\Delta m^2_{23}| = 2.6 \pm 0.4$ eV^2 at 90% C.L. Both solar and atmospheric neutrino data are compatible with $\theta_{13} \simeq 0$ within the experimental sensitivity, favoring a near bimaximal mixing matrix with $|\Delta m^2_{23}| \simeq 30|\Delta m^2_{12}|$. As a consequence, the observed solar and atmospheric neutrino oscillation regimes are largely decoupled and they can be described by a two-neutrino formalism. The corresponding oscillation probability for a neutrino of energy E_ν propagating for a distance L in vacuum is

$$P(\nu_\alpha \to \nu_\beta) \sim \sin^2 2\theta \sin^2 \frac{1.27\Delta m^2(\mathrm{eV}^2)L(\mathrm{km})}{E_\nu(\mathrm{GeV})}. \quad (1)$$

In this framework, the CP-violating term, which is generated by the interference of the solar and atmospheric neutrino oscillation regimes, is absent. The resulting oscillation probabilities are described by only Δm^2_{23}, θ_{13}, and θ_{23}:

$$P(\nu_e \to \nu_\mu) = \sin^2\theta_{23}\sin^2 2\theta_{13}\sin^2\frac{\Delta m^2_{23}L}{4E_\nu}, \quad (2)$$

$$P(\nu_e \to \nu_\tau) = \cos^2\theta_{23}\sin^2 2\theta_{13}\sin^2\frac{\Delta m^2_{23}L}{4E_\nu}, \quad (3)$$

$$P(\nu_\mu \to \nu_\tau) = \cos^4\theta_{13}\sin^2 2\theta_{23}\sin^2\frac{\Delta m^2_{23}L}{4E_\nu}. \quad (4)$$

Over the next five years, the present generation of oscillation experiments at accelerators with long-baseline ν_μ beams (Table 1), K2K at KEK [4], MINOS at NuMI beam of FNAL [6], and ICARUS and OPERA [7] at the CNGS beam of CERN [8] are expected to confirm the $\nu_\mu \to \nu_\tau$ interpretation of the atmospheric ν deficit and measure $\sin^2 2\theta_{23}$ and $|\Delta m^2_{23}|$ within an accuracy of 10% if $|\Delta m^2_{23}| > 10^{-3}$ eV^2. K2K and MINOS are looking for neutrino disappearance by measuring the ν_μ survival probability as a function of neutrino energy, while ICARUS and OPERA will search for evidence of ν_τ interactions in conventional ν_μ beams. However, some open questions that could be addressed to accelerators will still remain:

(i) the angle θ_{13} that is the link between the solar and the atmospheric neutrinos;

(ii) the sign of Δm^2_{23} which determines the mass hierarchy of the three-family neutrinos;

(iii) the existence of a leptonic CP-violating phase $\delta \neq 0$.

*This article was submitted by the author in English.

**e-mail: alberto.guglielmi@pd.infn.it

Table 1. Main parameters for present and future long-baseline neutrino oscillation experiments at accelerators with conventional ν_μ beams

Neutrino facility	Proton energy, GeV	L, km	E_ν, GeV	p.o.t./yr ($\times 10^{19}$)
KEK PS	12	250	1.5	0.005
FNAL NuMI	120	735	3	36
CERN CNGS	400	732	17.4	4.5
CERN L.E. $\times 1.5$	400	732	1.8	6.7
CERN SPL	2.2	130	0.27	1000
JHF-OA PS	50	295	0.76	100

2. THE CAPITAL IMPORTANCE OF θ_{13}

Accounting for the contribution from Δm^2_{12} and not knowing a priori the size of θ_{13}, all six parameters of the mixing matrix are generally involved in the $P(\nu_\mu \to \nu_e)$ appearance probability for electron neutrinos in a muon neutrino beam:

$$
\begin{aligned}
P(\nu_e \to \nu_\mu) &= 4c^2_{13}s^2_{13}s_{23}\sin^2\frac{\Delta m^2_{13}L}{4E_\nu} \qquad (5)\\
&+ 8c^2_{13}s_{12}s_{13}s_{23}(c_{12}c_{23}\cos\delta - s_{12}s_{13}s_{23})\\
&\times \cos\frac{\Delta m^2_{23}L}{4E_\nu}\sin\frac{\Delta m^2_{13}L}{4E_\nu}\sin\frac{\Delta m^2_{12}L}{4E_\nu}\\
&- 8c_{13}c_{12}c_{23}s_{12}s_{13}s_{23}\\
&\times \sin\delta\sin\frac{\Delta m^2_{23}L}{4E_\nu}\sin\frac{\Delta m^2_{13}L}{4E_\nu}\sin\frac{\Delta m^2_{12}L}{4E_\nu}\\
&+ 4s_{12}c^2_{13}(c^2_{13}c^2_{23} + s^2_{12}s^2_{23}s^2_{13}\\
&- 2c_{12}c_{23}s_{12}s_{13}\cos\delta)\sin\frac{\Delta m^2_{12}L}{4E_\nu}\\
&- 8c_{12}s^2_{13}s^2_{23}\cos\frac{\Delta m^2_{23}L}{4E_\nu}\frac{aL}{4E_\nu}(1-2s^2_{13})\sin\frac{\Delta m^2_{13}L}{4E_\nu},
\end{aligned}
$$

where $s_{ij} = \sin\theta_{ij}$, $c_{ij} = \cos\theta_{ij}$, and $a \simeq 7.6 \times 10^{-5}\rho(\mathrm{g/cm^3})E_\nu(\mathrm{GeV})$ ($\mathrm{eV^2}$). In this formula [9], where only the first-order matter effects are accounted for, the first term is driven by θ_{13}, while the fourth is driven from the solar neutrino regime. The second term is CP-even and the third term, as well the last one, due to the matter effects for neutrino propagation, is CP-odd. It follows that the θ_{13} determination represents the necessary milestone for any subsequent search: mass hierarchy and CP leptonic violation searches.

The detection of the δ phase also represents a big step from the θ_{13} searches because of its intrinsic difficulties. In principle, this parameter can be extracted from the $\nu_e \to \nu_\mu$ oscillation probability

$$A_\delta = \frac{P(\nu_e \to \nu_\mu, \delta) - P(\nu_e \to \nu_\mu, \delta = 0)}{P(\nu_e \to \nu_\mu, \delta) + P(\nu_e \to \nu_\mu, \delta = 0)} \qquad (6)$$

by comparing the measured $P(\nu_e \to \nu_\mu)$ with the corresponding one from a Monte Carlo evaluation where $\delta = 0$ is imposed. Clearly, this measure will be very difficult because of the presence of different contributions to oscillation probability. The amplitude of the direct CP violation

$$
\begin{aligned}
A_{CP}(\delta) &= \frac{P(\nu_e \to \nu_\mu, \delta) - P(\bar\nu_e \to \bar\nu_\mu, \delta)}{P(\nu_e \to \nu_\mu, \delta) + P(\nu_e \to \nu_\mu, \delta)} \qquad (7)\\
&\simeq \frac{\sin 2\theta_{12}}{\sin\theta_{13}}\sin\delta\sin\frac{\Delta m^2_{12}L}{4E}
\end{aligned}
$$

can be measured by comparing the probabilities for ν_μ and $\bar\nu_\mu$ appearance in a ν_e and $\bar\nu_e$ neutrino beam, respectively. This term depends on the Solar neutrino parameters: A_{CP} will vanish if $\Delta m^2_{12} \to 0$ and $\sin 2\theta_{12} \to 0$. The phase δ can also be recognized by looking for the ν_μ and ν_e appearance in a ν_e and ν_μ neutrino beam, respectively (time-violation searches):

$$A_T(\delta) = \frac{P(\nu_e \to \nu_\mu, \delta) - P(\nu_\mu \to \nu_e, \delta)}{P(\nu_e \to \nu_\mu, \delta) + P(\nu_\mu \to \nu_e, \delta)}. \qquad (8)$$

Because the $\nu_\mu \to \nu_e$ leading oscillation probability is proportional to $\sin^2\theta_{13}$ and $A_\delta \sim 1/\sin\theta_{13}$, a strong interplay between δ and θ_{13} is envisaged. A small θ_{13} mixing will result in a large asymmetry term being observed in a poor oscillated event sample. Otherwise, a small asymmetry is expected to affect a copious oscillated event sample for a large θ_{13}. The two effects tend to balance, but the detector requirements for a such measurements are very different: high mass and reduced granularity/resolution in the first case against a small mass but a high resolution in the second.

However, measuring the oscillation probabilities themselves will be hard experimentally because the CHOOZ limit on the $\bar\nu_e$ disappearance, $\theta_{13} < 11^\circ$, translates to a $\nu_\mu \to \nu_e$ appearance probability limit of less than 10% at the appearance maximum in a high-energy muon-neutrino beam. In conventional ν_μ beams where neutrinos are produced by meson decay, the $\nu_\mu \to \nu_e$ experimental sensitivity will be limited by an unavoidable $\nu_e/\nu_\mu \sim 1\%$ contamination. This natural background will be increased by an expected significant number of ν_τ charge-current interactions from ν_μ to ν_τ oscillations, where τ decay into electrons a large fraction of the time. Furthermore, neutral pions in both neutral-current or charge-current interactions can fake an electron, providing also a possible background. Therefore, the measurement of

the θ_{13} mixing angle and investigation of leptonic CP violation will require

neutrino beams with high performances, intended as intensity purity and low associated systematics;

the use of detectors of unprecedent mass, granularity, and resolution;

dedicated experiments for neutrino cross section, hadron production, and particle identification measurements.

3. CONVENTIONAL HIGH-ENERGY NEUTRINO BEAMS

High-energy accelerators provide muon neutrino beams through the decay of π, K mesons produced by high-energy protons hitting needle-shaped light targets. In order to increase the angular acceptance of the beam line and, correspondingly, the neutrino flux, positive (negative) mesons are sign-selected and focused by large acceptance magnetic lenses into an approximately parallel beam in a long evacuated decay tunnel where ν_μ ($\bar{\nu}_\mu$) are generated. The residual hadrons and muons are stopped by a heavy absorber. In the case of positive charge selection, the ν_μ beam has typically a contamination of $\bar{\nu}_\mu$ at the few percent level (from the decay of the residual π^-, K^-) and around or less than 1% of ν_e and $\bar{\nu}_e$ coming from three-body $K^\pm$, K_0 decays and μ decay, which affect the experimental sensitivity in the oscillation searches. This conventional scheme, successfully applied in the past, is now used in the K2K and MiniBooNE experiments and in the NuMI and CNGS projects.

In order to predict energy spectra, intensity, and composition of these conventional neutrino beams, a sound knowledge of π and K production in the primary proton beam target is required. Indeed, the accurate description of the K^+ and K^0 fluxes relative to the π^+ flux is essential to calculate the ν_e initial content in the ν_μ beam. Direct measurements of π and K production in Be by 400-GeV/c protons were performed by the NA20 Collaboration [10] and by the SPY Collaboration [11] at 450 GeV/c. On the other hand, Monte Carlo generators of hadronic interactions have a poor accuracy for meson production, which limits the sensitivity to neutrino oscillation searches. The best agreement between predictions and data was found with the FLUKA standalone code [12], which reproduces the measured π and K yields at the level of ~ 20% in the momentum region 30–100 GeV/c, which is expected to contribute most to the ν flux [13]. Furthermore, an accurate description of the primary proton beam spot and focusing system as well as of the materials inserted in the beam line from the target to the dump (hadronic reinteraction processes) is also mandatory. Primary protons missing the target and tertiary particles produced in reinteractions in the materials along the beam line contribute to reduce the neutrino fluxes and increase the neutrino contamination from the defocused meson with wrong sign.

Table 2. The expected 90% C.L. sensitivity on θ_{13} measurements for $\delta = 0$ of long-baseline experiments for $\Delta m^2_{23} \sim 2.5 \times 10^{-3}$ eV^2 compared to the 90% C.L. CHOOZ limit $\sin^2 2\theta_{13} = 0.14$ ($\theta_{13} = 11^\circ$)

Experiment	Fiducial mass, kt	$\sin^2 2\theta_{13}$	θ_{13}, deg
MINOS	5.0	0.06	7.1
ICARUS + OPERA combined	2.4 + 1.8	0.03	5
ICARUS L.E. ×1.5	2.4	0.015	3.5
β Beam	440	0.0007	0.8
CERN SPL	440	0.003	1.3
JHF-OA SK	22.5	0.006	2.2
NuMI-OA	100	0.004	1.8
Neutrino factory	40	<0.00001	<0.1

These studies have been particularly relevant for the NOMAD experiment [14] searching for the $\nu_\mu \to \nu_\tau$ and $\nu_\mu \to \nu_e$ oscillations at CERN SPS, using the WANF [15] conventional ν_μ beam ($E_\nu \simeq 24$ GeV) produced by 450-GeV/c protons on a Be target. The presence of the $\nu_\mu \to \nu_e$ transitions was investigated looking for an excess of ν_e events with respect to the calculated natural contamination of the beam ($\nu_e/\nu_\mu \sim 1$%). The high resolution and granularity of the NOMAD detector allowed for a study of this conventional neutrino beam with unprecedented accuracy and statistics, resulting in a stringent benchmark for the neutrino beams for the K2K, NuMI, and CNGS projects. A complete analysis of this ν beam was performed by a beam line simulation from the Be target up to the NOMAD detector including the FLUKA generator with further corrections to the meson production based on the residual differences between the predicted and measured meson yield in Be. The agreement with the measured ν interactions in NOMAD was at the few percent level (Fig. 1) with a systematic error of ~ 8% on ν_μCC/p.o.t.; the energy-dependent uncertainty achieved on the ν_e/ν_μ ratio ranged from 4 to 7%, whereas its normalization uncertainty was 4.2%.

One noticeable characteristic of the current long-baseline experiments with conventional neutrino

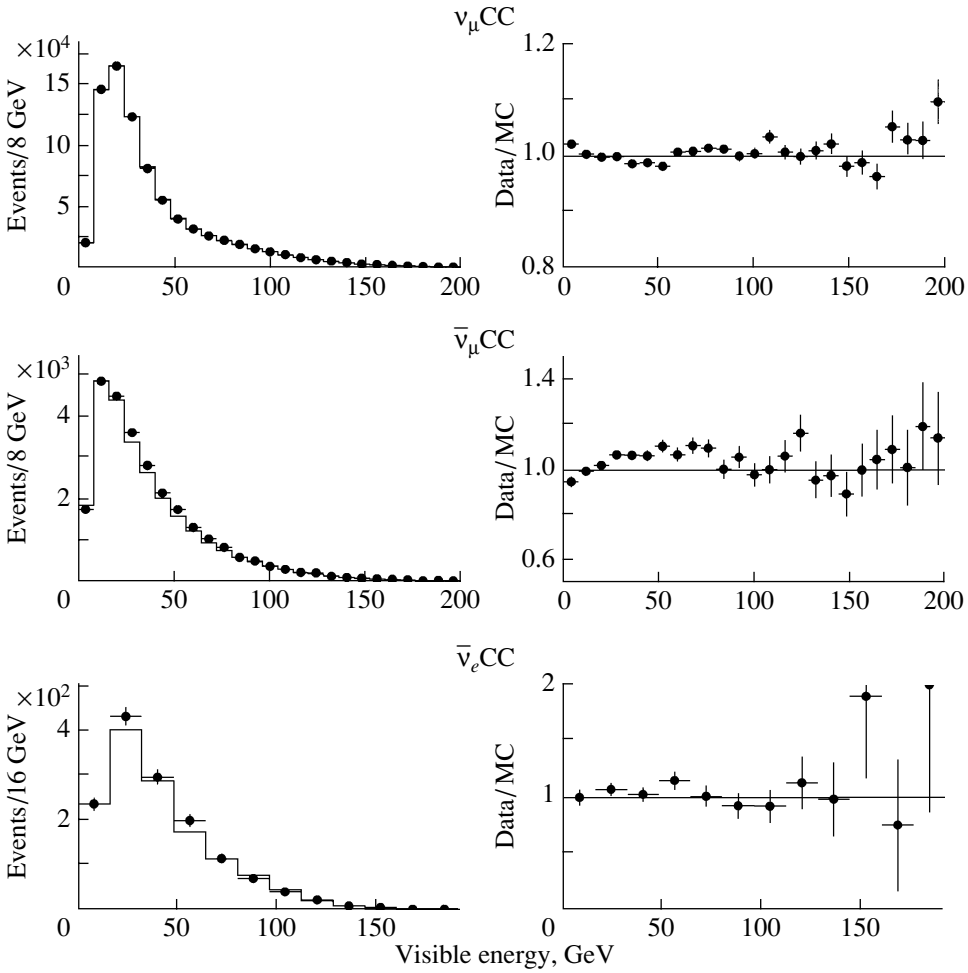

Fig. 1. Neutrino energy spectra (left) for the data (points with error bars) and the Monte Carlo (histogram) for ν_μCC, $\bar{\nu}_\mu$CC, and $\bar{\nu}_e$CC interactions in the neutrino mode and their corresponding ratios (right) in the NOMAD experiment [14]. Only the statistical errors are shown.

beams is that they can search for $\nu_\mu \to \nu_e$ beyond the CHOOZ limit even if they are not optimized for the θ_{13} studies (Table 2). In particular, the ICARUS and OPERA experiments [7] are expected to have a combined sensitivity on $\sin^2 2\theta_{13}$ (convoluted to δ and matter effects) a factor of 5 better than CHOOZ in the atmospheric parameter region for a five-year exposure to the CNGS beam at nominal intensity [16]. Depending on the δ phase and matter effects (sign of Δm_{23}), these sensitivities can be reduced by a factor of $\sim$1.5 [17].

The CNGS beam line design (Fig. 2) was accomplished on the basis of the previous WANF experience. The expected muon neutrino flux at the Gran Sasso site will be characterized by an average energy of 17.4 GeV and $\sim$0.8% ν_e to ν_μ contamination (Fig. 3). Due to the 732 km of baseline, the contribution to the neutrino beam from the K^0 and mesons produced in the reinteraction processes will be strongly reduced with respect to the WANF: the resulting systematics on the ν_e/ν_μ ratio is expected to be $\sim$3%.

4. BEYOND CONVENTIONS: NEUTRINO FACTORIES AND β BEAMS

As a completely alternative approach to conventional neutrino beams, whose knowledge suffers mainly from the uncertainties on the hadronic processes involved at the generation level and particle transport, the neutrino production by muon decay from a pure muon beam was considered. This is indeed a perfectly well known weak process and the μ beam can be well measured in momentum and intensity.

In the CERN proposed layout for a neutrino factory (νF) [18], a 4-MW proton beam is accelerated up to 2.2 GeV/c by a superconducting proton linac (SPL) to produce in a liquid mercury target low energy π which are collected by magnetic horns.

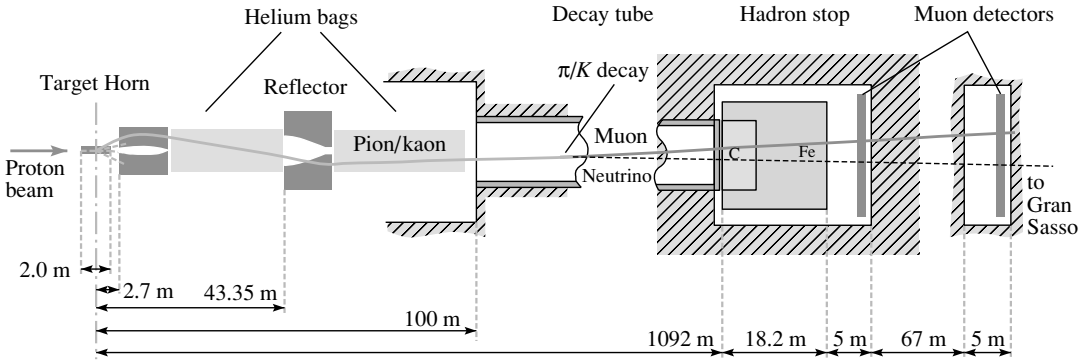

Fig. 2. Schematic layout of the future CNGS neutrino beam line.

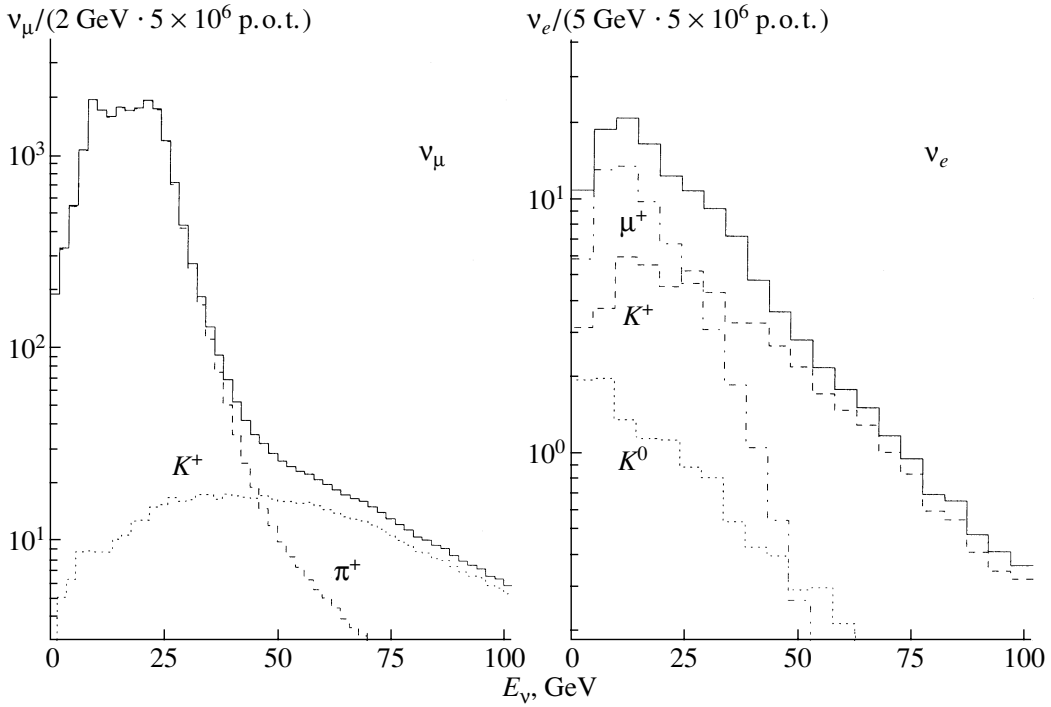

Fig. 3. Muon and electron neutrino flux spectra at the Gran Sasso Laboratories.

Muons produced from the π decay are then cooled and phase rotated before being accelerated through a recirculating linac system up to 50 GeV/c. These μ of well-defined charge and momentum are injected into the μ accumulator, where they will circulate until they decay, delivering along the two main straight sections two pure ν beams whose intensity is expected to be more than 100 times that in conventional beams. Both muon signs can be selected. The decay $\mu^+ \to e^+\nu_e\bar{\nu}_\mu$ ($\mu^- \to e^-\bar{\nu}_e\nu_\mu$) produces a pure well-collimated neutrino beam with equal numbers of $\bar{\nu}_\mu, \nu_e$ ($\nu_\mu, \bar{\nu}_e$), which allows the baseline to be extended to several thousand kilometers of distance. The optimal beam energy at the νF will be as large as possible: $E_\mu = 50$ GeV ($E_\nu \sim 34$ GeV). In fact, the neutrino flux ϕ_ν grows like E_ν^2 (in conventional neutrino beams, ϕ_ν is proportional to E_ν) and the number of charge current neutrino events from the oscillations $N_{\rm osc}$ measured by a detector at a distance L will be proportional to E_ν:

$$N_{\rm osc} \simeq \phi_\nu \sigma_\nu P_{\rm osc} \simeq \frac{E_\nu^3}{L^2} \sin^2 \frac{L}{E_\nu} \simeq E_\nu, \qquad (9)$$

where σ_ν is the corresponding neutrino interaction cross section and $P_{\rm osc}$ is the oscillation probability. Furthermore, the ν intensity can be precisely determined from the measurement of a monochromatic μ current circulating in the storage ring (absolute normalization at the 1% level). An accurate determi-

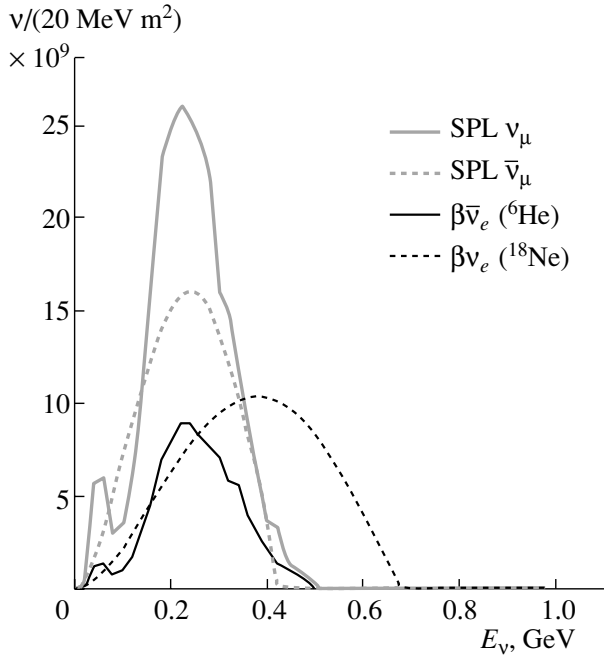

Fig. 4. Energy spectra of β beams and CERN SPL SuperBeams at 130 km of distance.

nation of μ momentum will allow for the measurement of the neutrino energy spectra at the detector site.

The νF lends itself naturally to the exploration of neutrino oscillations between ν flavors with high sensitivity to small mixing angles and small mass differences. The detector should be able to perform both appearance and disappearance experiments, providing final lepton identification and charge discrimination which is a tag of the initial flavor and of the oscillation. In particular, the search for $\nu_e \to \nu_\mu$ transitions appears to be very attractive at νF because this transition can be studied in the appearance mode looking for μ^- (appearance of wrong-sign μ) in neutrino beams where the neutrino type which is sought is totally absent (μ^+ beam in νF).

The intrinsic correlation between the θ_{13} angle and the δ phase in the $\nu_e \to \nu_\mu$ transition probability must be taken into account as well as the matter effects if neutrinos propagate for large distances through the Earth. The δ and θ_{13} parameters have to be measured simultaneously in both μ^+, μ^- beams exploiting the A_{CP} dependence from E_ν and L to disentangle them, requiring the use of a "near" ($L \sim 3000$ km) and a "far" ($L \sim 7000$ km) detector [19]. The uncertainties on atmospheric neutrino parameters can be ruled out by measuring at νF the $\bar{\nu}_\mu$ disappearance (precision on θ_{13} and Δm^2_{23} at the $\sim 1\%$ level). With a 40-kt magnetic detector (a la MINOS) exposed to both polarity beams, 10^{21} muon decays, it will be possible to explore the θ_{13} angle down to 1°, opening the possibility of measuring the δ phase if $|\Delta m^2_{12}| \geq 5 \times 10^{-5}$ eV^2. The case $\delta = 0$ (no CP violation) can be distinguished from $\delta = 90°$ (maximum CP violation) at 99% C.L. down to $\sin^2 2\theta_{13} \simeq 3 \times 10^{-4}$.

Another completely different strategy is to make a neutrino beam with decays of radiative isotopes after they are strongly accelerated: as for the neutrino factory, the neutrino spectrum of these β beams [20] is completely defined by the parent decay properties and by the Lorentz boost. In the CERN proposed scheme, ^{6}He and ^{18}Ne ions are produced by using $\sim$10% of protons from SPL and accelerated up to $\gamma(^6\mathrm{He}) = 60$ and $\gamma(^{18}\mathrm{Ne}) = 100$, respectively, by PS and SPS machines. These ions beams are then injected into a decay ring where two pure low energy $\bar{\nu}_e$ and ν_e beams per straight section can be produced. The flux intensities were estimated to be 2.9×10^{18} He decay/yr and 1.1×10^{18} Ne decay/yr. The physics reach of the β beams for 4400 kt yr exposure at 130 km of distance (Fig. 4) is comparable to the νF for $\sin^2 2\theta_{13} \simeq 1.2 \times 10^{-3}$.

5. NEAR TERM OPTIONS: LOW ENERGY BEAM, SUPERBEAMS, AND OFF-AXIS NEUTRINO BEAMS

The technical challenges associated with building either a β beam or a muon storage ring are much greater than those associated with a conventional beam, and therefore near-term neutrino beam solutions all will involve conventional beams which must be optimized for the $\nu_\mu \to \nu_e$ searches.

The possibility of improving the CERN to Gran Sasso neutrino beam performances for θ_{13} searches was investigated. The low-energy neutrino flux can be increased by a factor of 5 with respect to the current CNGS beam by an appropriate optimization of the target (a compact 1-m carbon rod) and of the focusing system [21]. In such a way, an intense low-energy neutrino flux, $E_{\nu_\mu} \simeq 1.8$ GeV with 0.9% of ν_e/ν_μCC event contamination and a $4.5\nu_\mu$CC $(10^{19}$ p.o.t. kt$)^{-1}$ event rate, can be obtained. With this low-energy CNGS L.E. neutrino beam (Fig. 5), the sensitivity to $\sin^2 2\theta_{13}$ can be increased by a factor of 7 greater than CHOOZ (matter effects and δ of CP not accounted for in the calculations). A further improvement can be obtained with the foreseen PS and SPS upgrade option, which will produce 50% more p.o.t./yr (Fig. 6: ICARUS–CNGS L.E. × 1.5, 7 yr of data taking).

A proton driver optimization to search for ν_μ–ν_e oscillations with a new generation of low-energy and high-intensity neutrino beams (SuperBeams) was also recently studied [22]. In terms of proton economy, the optimum beam energy was around 20 GeV,

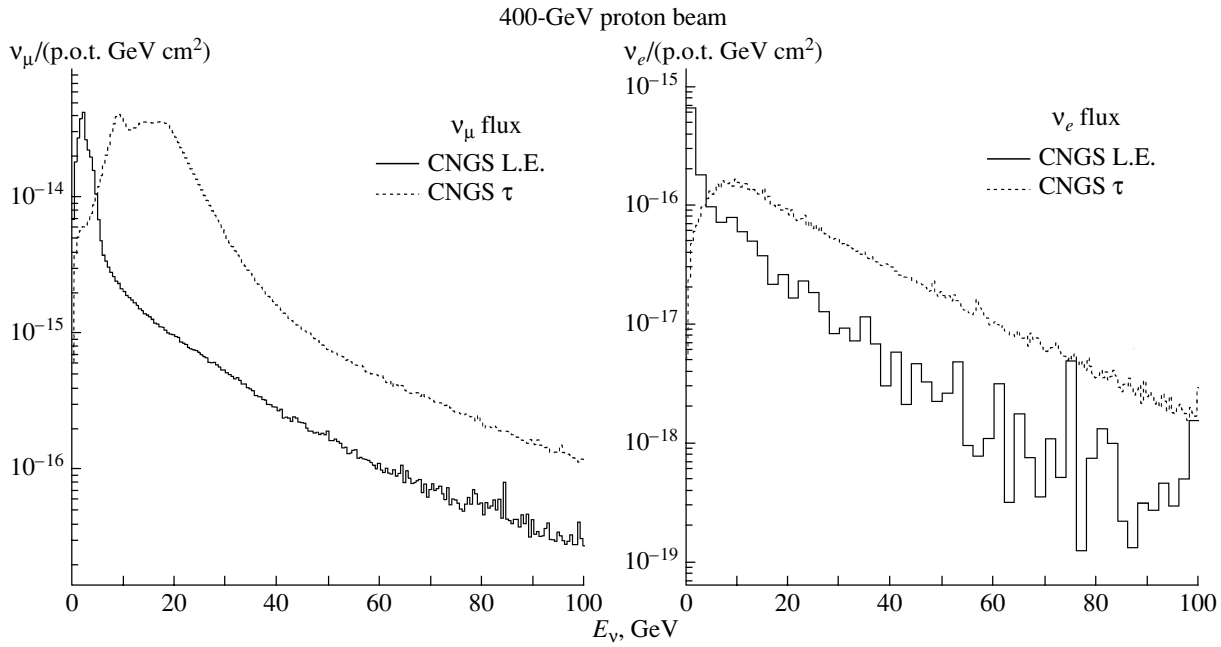

Fig. 5. The CERN low energy neutrino beams.

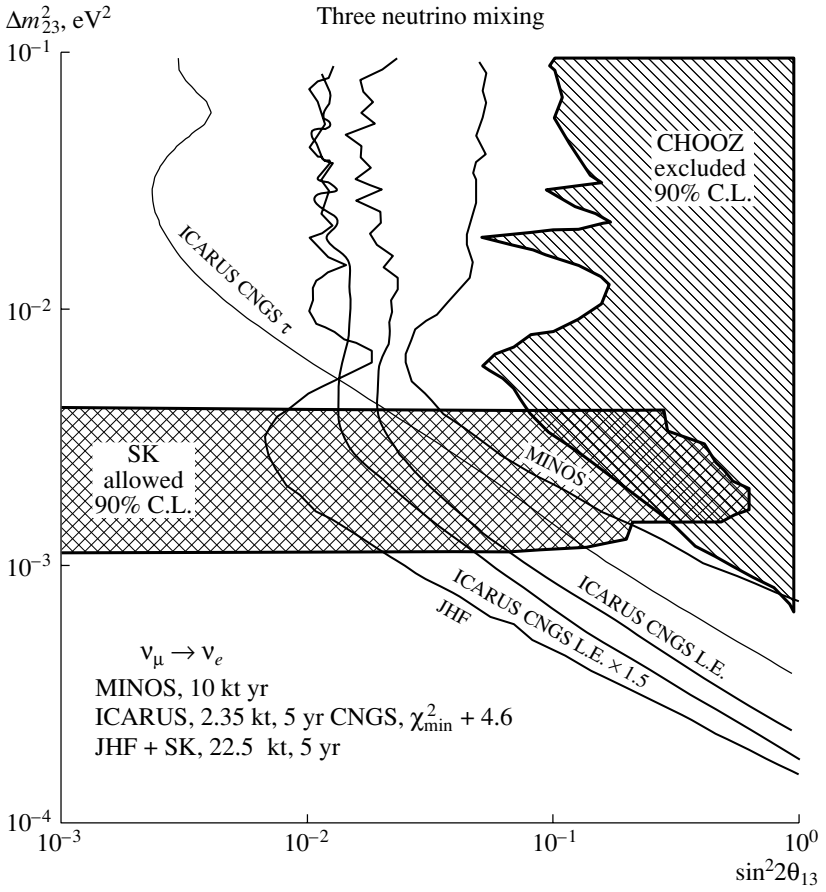

Fig. 6. Expected sensitivity on θ_{13} mixing angle (matter effects and CP-violation effects not included) for MINOS, ICARUS at nominal CNGS and at CNGS L.E. and CNGS L.E. × 1.5 beams, and JHF Off-Axis, compared to the CHOOZ exclusion plot.

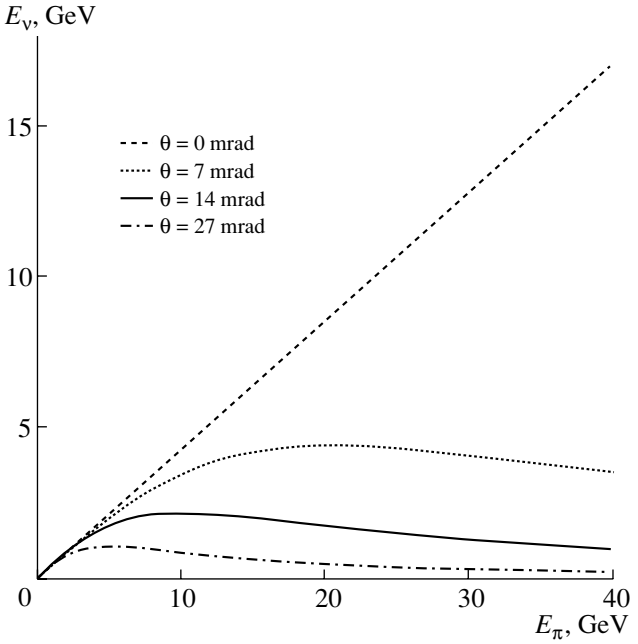

Fig. 7. Neutrino energy vs. the pion parent energy for different off-axis angle θ.

well matched to 732 km of baseline (i.e., CERN–Gran Sasso: average neutrino energy $E \sim 1.5$ GeV). A $\sin^2 2\theta_{13} \simeq 0.005$ sensitivity for $\Delta m^2_{23} \sim 2.5 \times 10^{-3}$ eV^2, matter effects and CP violation effect not accounted for, can be obtained for 2×10^{23} p.o.t./yr (about two orders of magnitude higher than the intensity deliverable by the current CERN PS) and a 5-yr exposure of the ICARUS 3-kt detector.

In the CERN SPL SuperBeam project [18, 23], the planned new SPL would deliver a 2.2-GeV proton beam with an intensity of 10^{23} p.o.t./yr on a Hg target to generate an intense π^+ (π^-) beam which will be focused by a suitable magnetic horn in a short decay tunnel. In such a way, an intense ν_μ ($\bar\nu_\mu$) beam, $\phi \sim 3.2 \times 10^{12} \nu_\mu$ (10^{23} p.o.t. m^2)$^{-1}$ at 50 km of distance, with an average energy of 0.27 GeV will be produced essentially via the π decay: $\pi^+ \to \nu_\mu \mu^+$, $\mu^+ \to \bar\nu_\mu \nu_e e^+$ (Fig. 4). The ν_e contamination from K will be suppressed by threshold effects and the resulting $\nu_e/\nu_\mu \sim 0.7\%$ ratio, essentially coming from the μ decay, will be known within a 2% error. The use of a near and far detector, the last at $L = 130$ km of distance in the Frejus tunnel, will allow for both ν_μ disappearance and $\nu_\nu \to \nu_e$ appearance experiments. With a far detector fiducial mass of 440 kt, 2 yr with ν_μ beam and 8 yr with the reversed-polarity $\bar\nu_\mu$ beam data taking, a good sensitivity in θ_{13} and δ of CP is expected, the case $\delta = 0$ distinguished at 99% C.L. by $\delta = 90^\circ$ above $\theta_{13} \sim 2^\circ$. Moreover, the combined use of both the SPL SuperBeam and the β beam will offer the possibility of investigating CP, T, and CPT violation at the same time with the same 130-km baseline.

An interesting option for the SuperBeams is the possibility of tilting the beam axis a few degrees with respect to the position of the far detector in order to obtain an almost monochromatic low-energy off-axis ν_μ beam with a smaller ν_e contamination than the direct beam. Accounting for the two-body π-decay kinematics, many different pion energies contribute to a selected energy of the neutrino produced at a given angle θ to the direction of the parent pion (Fig. 7):

$$E_\nu = \frac{m_\pi^2 - m_\mu^2}{2(E_\pi - p_\pi \cos\theta)}, \qquad (10)$$

where E_π, p_π, and m_π are the energy, the momentum, and the mass for the pion parent and m_μ is the muon mass. In fact, the ν_μ spectrum at a nonzero angle is peaked at a lower energy and is narrower than that at zero degrees due to the existence of a maximum possible energy in decays at a given angle θ to the direction of the parent pion:

$$E_{\nu,\max}(\theta) \simeq \frac{30\ \text{MeV}}{\theta}. \qquad (11)$$

This effect is more significant when $E_{\nu,\max}(\theta)$ is lower than the corresponding peak value of the neutrino spectrum on-axis because of a substantial rate of higher energy π, all of which decay into a narrower band of neutrino energies at this angle.

These neutrino beams have several advantages with respect to their corresponding on-axis. They are more intense, narrower, and lower energy beams without a large high-energy tail and they can allow a clean ν_e appearance experiment. To fully take advantage of such tools, both predominantly ν_μ and $\bar\nu_\mu$ are needed, the antineutrino beam run being 3 times more than the neutrino run due to the different ν_μ and $\bar\nu_\mu$ cross sections.

In the JHF project [24], a 50-GeV/c proton beam of 0.75 MW from a PS will produce a very intense π and K beam which axis will be tilted by 2° with respect to the position of the Super-Kamiokande detector at 295 km of distance. The resulting almost monochromatic $\sim$ 800-MeV ν_μ beam (Fig. 8) with 0.5% ν_e contamination will allow one to reach in five years a 90% C.L. sensitivity $\sin^2 2\theta_{13} \sim 0.006$ assuming $\delta = 0$, a factor of 20 more than the current limit set by CHOOZ. The foreseen machine upgrade to 4 MW in conjunction with a far detector having a fiducial volume of 0.54 Mt (Hyper-Kamiokande) will allow one to better investigate the CP violation phase. With 2 yr of ν_μ and 6 yr of $\bar\nu_\mu$ operations, a

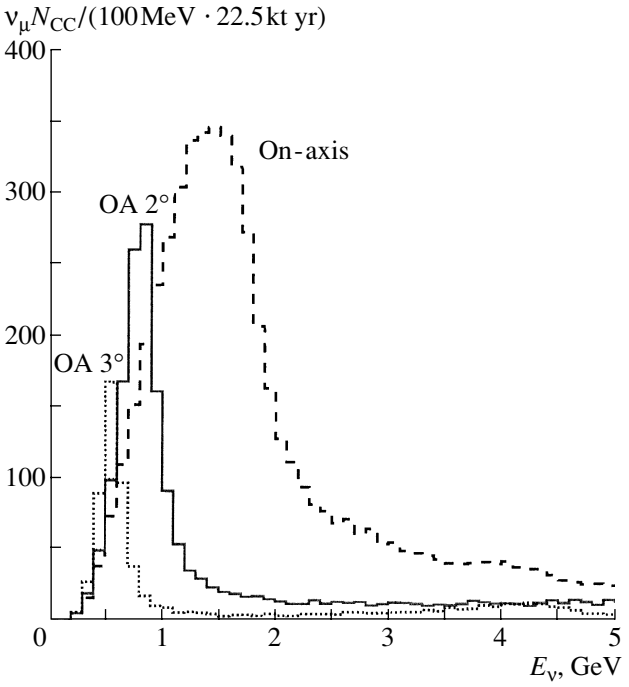

Fig. 8. J-park neutrino beam energy spectrum for different off-axis angle θ.

3σ sensitivity $\sin|\delta| > 20°$ for $\sin^2 2\theta_{13} \sim 0.01$ can be reached.

An upgraded NuMI Off-Axis neutrino beam [25], $E_\nu \sim 2$ GeV and a ν_e contamination less than 0.5%, with a 900-km long-baseline off-axis experiment, is under study at FNAL. In five years of data taking with a 20-kt detector, a factor of 10 better precision on $|\Delta m^2_{23}|$ and $\sin^2\theta_{23}$ than NuMI and CNGS can be achieved as well as a sensitivity $\sin^2 2\theta_{13} \sim 0.004$ at 90% C.L. A rather strong hint for CP violation, as $\sin^2 2\theta_{13} \geq 0.01$ and δ is close either $\pi/2$ or $3\pi/2$ can be obtained assuming that the neutrino mass hierarchy is already known. A 2-MW machine upgrade with a 100-kt fiducial mass (SNuMI-OA) and NuMI Off-Axis program was studied with the aim of reaching 10^{-3} sensitivity on $\sin^2 2\theta_{13}$ [25].

A project with the aim of measuring θ_{13} with a large water Čerenkov located in the Gulf of Taranto by comparing the ν_e component of the CNGS off-axis neutrino beam at different baselines is also under study [26].

REFERENCES

1. B. T. Cleveland *et al.* (Homestake Collab.), Astrophys. J. **496**, 505 (1998); J. N. Abdurashitov *et al.* (SAGE Collab.), JETP **95**, 181 (2002); W. Hampel *et al.* (GALLEX Collab.), Phys. Lett. B **447**, 127 (1999); M. Altmann *et al.* (GNO Collab.), Phys. Lett. B **490**, 16 (2000); Y. Fukuda *et al.* (Kamiokande Collab.), Phys. Rev. Lett. **77**, 1683 (1996); S. Fukuda *et al.* (Super-Kamiokande Collab.), Phys. Rev. Lett. **86**, 5651 (2001); R. Q. Ahmad *et al.* (SNO Collab.), Phys. Rev. Lett. **87**, 071301 (2001); **89**, 011301 (2002); **89**, 011302 (2002); nucl-ex/0309004 (2003).
2. K. Eguchi *et al.* (KamLAND Collab.), Phys. Rev. Lett. **90**, 021802 (2003).
3. K. S. Hirata *et al.* (Kamiokande Collab.), Phys. Lett. B **280**, 146 (1992); R. Becker-Szendy *et al.* (IMB Collab.), Phys. Rev. Lett. **69**, 1010 (1992); Nucl. Phys. B (Proc. Suppl.) **38**, 331 (1995); Y. Fukuda *et al.* (Super-Kamiokande Collab.), Phys. Rev. Lett. **81**, 1562 (1998); **85**, 3999 (2000); H. R. Gallagher *et al.* (Soudan 2 Collab.), Nucl. Phys. B (Proc. Suppl.) **66**, 290 (1998); M. Ambrosio *et al.* (MACRO Collab.), Phys. Lett. B **434**, 451 (1998).
4. K. Nishikawa *et al.* (K2K Collab.), E362KWK-PS Proposal (1995); M. H. Ahn *et al.* (K2K Collab.), Phys. Rev. Lett. **90**, 041801 (2003).
5. M. Apollonio *et al.* (CHOOZ Collab.), Phys. Lett. B **466**, 415 (1999).
6. The Fermilab NuMI Group, Fermilab Report NuMI-346 (1998); E. Ables *et al.* (MINOS Collab.), Fermilab Proposal P-875 (1995); E. Buckley-Geer *et al.* (MINOS Collab.), Nucl. Instrum. Methods Phys. Res. A **503**, 122 (2001).
7. F. Arneodo *et al.* (ICARUS Collab.), Nucl. Instrum. Methods Phys. Res. A **461**, 324 (2001); ICARUS Collab., CERN-SPSC/2002-27, SPSC-P-323 (Aug. 7, 2002); OPERA Collab., CERN-SPSC-P-318, LNGS-P25-00; M. Komatsu *et al.*, hep-ph/0210043.
8. G. Acquistapace *et al.*, CERN 98-02, INFN/AE-98/05 (1998); A. E. Ball *et al.*, SL-NOTE-2000-063 DI (CERN).
9. B. Richter, SLAC-PUB-8587, hep-ph/0008222 and references therein.
10. H. W. Atherton *et al.*, CERN Yellow Report 80-07 (1980).
11. G. Ambrosini *et al.* (NA56/SPY Collab.), Eur. Phys. J. C **10**, 605 (1999).
12. A. Fasso' *et al.*, in *Proceedings of the Monte Carlo 2000 Conference,* Ed. by A. Kling *et al.* (Springer-Verlag, Berlin, 2001), p. 955.
13. G. Collazuol *et al.*, Nucl. Instrum. Methods Phys. Res. A **449**, 609 (2000).
14. P. Astier *et al.* (NOMAD Collab.), Nucl. Phys. B **611**, 3 (2001); CERN-EP-2003-032, hep-ex/0306022; Nucl. Instrum. Methods Phys. Res. A **515**, 800 (2003); Phys. Lett. B **570**, 19 (2003).
15. L. Casagrande *et al.*, CERN Yellow Report 96-06 (1996).
16. M. Komatsu *et al.*, J. Phys. G **29**, 443 (2003).
17. P. Migliozzi and F. Terranova, Phys. Lett. B **563**, 73 (2003).
18. CERN Report 99-2, EFCA 99-197, Ed. by B. Autin, A. Blondel, and J. Ellis (1999); M. Apollonio *et al.*, CERN-TH-2002-208, hep-ph/0210192.

19. J. Burguet-Castell *et al.*, Nucl. Phys. B **608**, 301 (2001).
20. P. Zucchelli, Phys. Lett. B **532**, 166 (2002); B. Autin *et al.*, physics/0306106; S. Bouchez *et al.*, hep-ex/0310059.
21. A. Rubbia and P. Sala, J. High Energy Phys. **0209**, 004 (2002).
22. A. Ferrari *et al.*, hep-ph/0208047.
23. M. Mezzetto, J. Phys. G **29**, 1781 (2003) and references therein.
24. Y. Itow *et al.* (JHF Collab.), hep-ex/0106019.
25. D. A. Harris, in *Proceedings of the 10th International Workshop on Neutrino Telescopes, Venice, Italy, 2003*, Ed. by M. Baldo-Ceolin, Vol. 1, p. 203.
26. A. Grant, this conference.

Physics of Atomic Nuclei, Vol. 67, No. 6, 2004, pp. 1139–1146. From Yadernaya Fizika, Vol. 67, No. 6, 2004, pp. 1165–1171.

New MACRO Results on Atmospheric Neutrino Oscillations*

G. Giacomelli** and **A. Margiotta*****
(for the MACRO Collaboration)

Dipartimento di Fisica dell'Università di Bologna and INFN, Sezione di Bologna, Italy

Received November 17, 2003

Abstract—The final results of the MACRO experiment on atmospheric neutrino oscillations are presented and discussed. The data concern different event topologies with average neutrino energies of $\sim$3 and $\sim$50 GeV. Multiple Coulomb scattering of the high-energy muons in absorbers was used to estimate the neutrino energy of each event. The angular distributions, the L/E_ν distribution, the particle ratios, and the absolute fluxes all favor $\nu_\mu \to \nu_\tau$ oscillations with maximal mixing and $\Delta m^2 = 0.0023\ \mathrm{eV}^2$. A discussion is made on the Monte Carlos used for the atmospheric neutrino flux. Some results on neutrino astrophysics are also briefly discussed. © *2004 MAIK "Nauka/Interperiodica"*.

1. INTRODUCTION

MACRO was a large area multipurpose underground detector [1] designed to search for rare events and rare phenomena in the penetrating cosmic radiation. The experiment obtained important results on atmospheric ν_μ oscillations and performed ν_μ astronomy studies, indirect searches for weakly interacting massive particles (WIMPs), and searches for low-energy $\bar{\nu}_e$ from stellar gravitational collapses [2].

The detector was located in Hall B of the underground Gran Sasso Lab at an average rock overburden of 3700 m w.e.; it started data taking with part of the apparatus in 1989; it was completed in 1995 and was running in its final configuration until December 2000.

The detector had global dimensions of $76.6 \times 12 \times 9.3$ m and provided a total acceptance to an isotropic flux of particles of $\sim 10\,000$ m^2 sr. The detector (Fig. 1) was composed of three horizontal layers of liquid scintillation counters, 14 layers of limited streamer tubes, and one layer of nuclear track detectors. Vertically, it was divided into two parts: the lower part contained ten layers of streamer tubes, seven layers of rock absorbers, and two layers of liquid scintillators; the upper part was empty, contained the electronics, and was covered by one layer of scintillators and four layers of streamer tubes. The sides of the detector were covered with one layer of scintillators and six layers of limited streamer tubes, so as to obtain a closed box structure. Each of the subdetectors could be used in "stand-alone" and in "combined" mode.

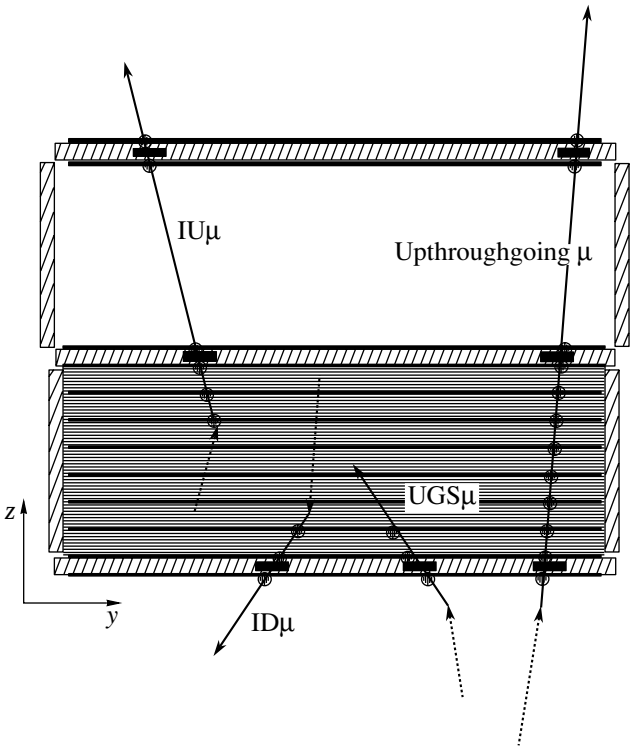

Fig. 1. Cross section of the detector, which also shows the various atmospheric neutrino topologies measured. The horizontal scintillators are indicated as dashed boxes, the streamer tubes as horizontal thick black lines, and the rock absorbers as boxes with horizontal thin lines. The sides of the detector were formed by one layer of scintillators and six layers of streamer tubes.

*This article was submitted by the authors in English.

**e-mail: giacomelli@bo.infn.it

***e-mail: margiotta@bo.infn.it

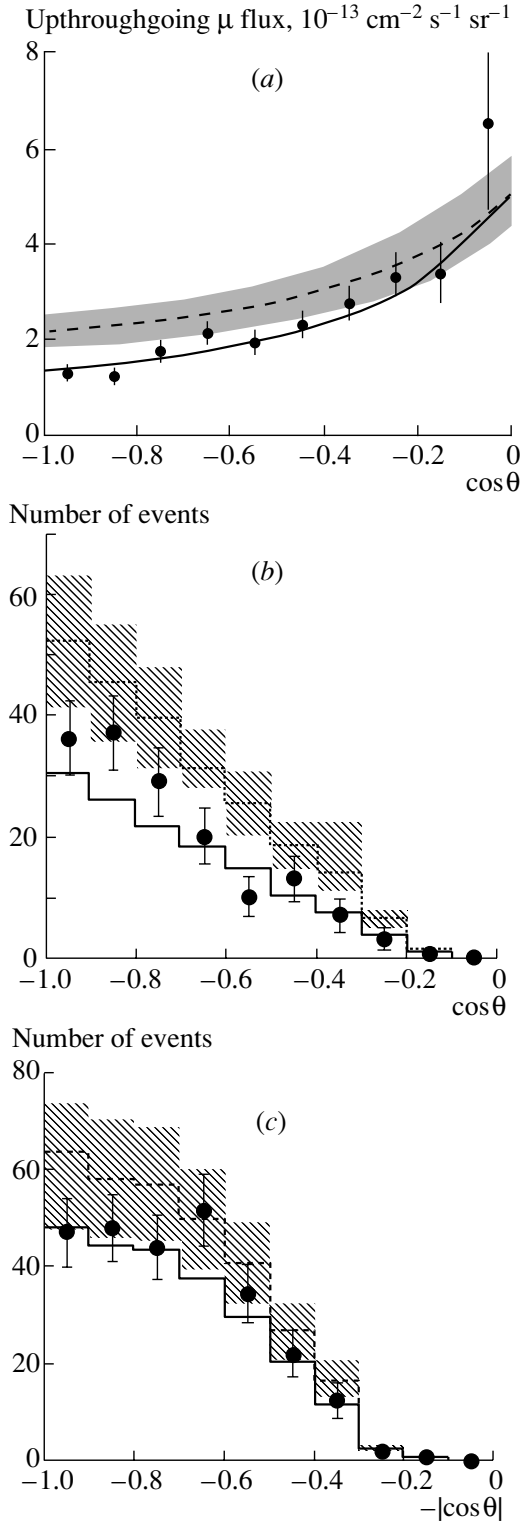

Fig. 2. Zenith distributions for the MACRO data (points) for (*a*) up through-going, (*b*) semicontained, and (*c*) up-stopping muons + down semicontained. The dashed lines are the no-oscillation MC predictions Bartol 96 (with scale error bands); the solid lines refer to $\nu_\mu \to \nu_\tau$ oscillations with maximal mixing and $\Delta m^2 = 2.3 \times 10^{-3}$ eV^2.

In the following, we shall briefly recall neutrino oscillation formulas and atmospheric neutrinos; then we shall discuss our main results including the ratio of vertical to horizontal muons and the study of the L/E_ν distribution. After a detailed analysis of the present situation of the different Monte Carlos (MCs), we summarize our atmospheric neutrino oscillation results and conclude with a short discussion of some neutrino astrophysics studies.

2. ATMOSPHERIC NEUTRINO OSCILLATIONS: MONTE CARLOS

Neutrino oscillations. If neutrinos have nonzero masses, one has to consider the three weak flavor eigenstates ν_e, ν_μ, ν_τ and the three mass eigenstates ν_1, ν_2, ν_3. The flavor eigenstates ν_l are linear combinations of the mass eigenstates ν_m. Neutrino oscillations depend on six independent parameters: two mass-squared differences Δm^2_{12} and Δm^2_{23}; three mixing angles θ_{12}, θ_{13}, θ_{23}; and the CP-violating phase δ. In the simple case of two flavor eigenstates (ν_μ, ν_τ), which oscillate with two mass eigenstates (ν_2, ν_3), and $\delta = 0$, one has

$$\nu_\mu = \nu_2 \cos\theta_{23} + \nu_3 \sin\theta_{23}, \quad (1)$$

$$\nu_\tau = -\nu_2 \sin\theta_{23} + \nu_3 \cos\theta_{23}. \quad (2)$$

The survival probability of a ν_μ beam is

$$P(\nu_\mu \to \nu_\mu) \simeq 1 - \sin^2 2\theta_{23} \sin^2\left(\frac{1.27\Delta m^2_{23} L}{E_\nu}\right), \quad (3)$$

where $\Delta m^2_{23} = m^2_3 - m^2_2$ and L is the distance traveled by the neutrino of energy E_ν from production to detection. The two-neutrino approximation is adequate for discussing our data.

Atmospheric neutrinos. High-energy (HE) primary cosmic rays (CRs), protons and nuclei, interact in the upper atmosphere producing a large number of pions and kaons, which decay yielding muons and muon neutrinos; then muons decay yielding ν_μ and ν_e. The ratios of their numbers are $N_{\nu_\mu}/N_{\nu_e} \simeq 2$ and $N_\nu/N_{\bar\nu} \simeq 1$. The atmospheric neutrinos are produced in a spherical shell at about 10–20 km above the ground and proceed towards the Earth. Atmospheric neutrinos have energies from a fraction of GeV up to more than 100 GeV and they travel distances L from a few tens of kilometers up to 13 000 km. An underground detector is "illuminated" by a flux of neutrinos from all directions and it can make oscillation studies for $1 < L/E_\nu < 10^4$ km/GeV.

MACRO detected up-going muon neutrinos via charged current interactions, $\nu_\mu \to \mu$; the up-going muons were identified with the streamer tube system

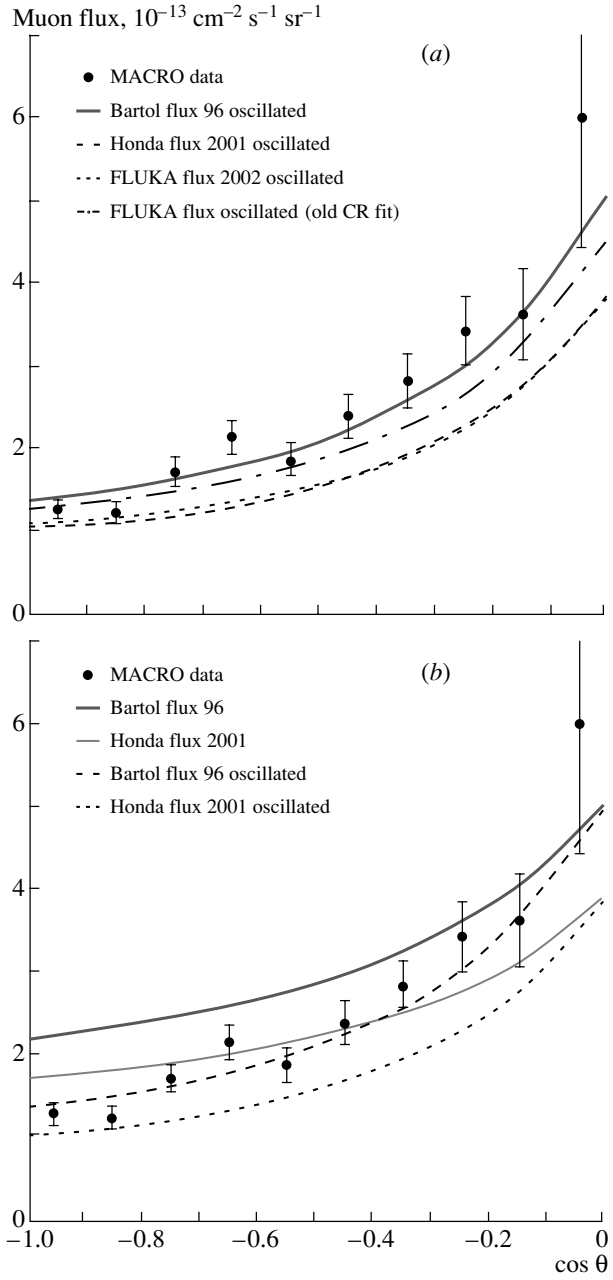

Fig. 3. (*a*) Comparison of the measured angular distribution for up through-going muons and the oscillated flux obtained from different MCs (for $\Delta m^2 = 2.3 \times 10^{-3}$ eV^2 and maximal mixing). The solid curve is the Bartol 96 flux; the dotted and the dashed curves at the bottom are the new Fluka and Honda fluxes; the dash-dotted line in the middle is the Fluka flux using a different (older) fit to the cosmic ray data. (*b*) Comparison of our measurements with the Bartol 96 and the new Honda 2001 oscillated and nonoscillated fluxes.

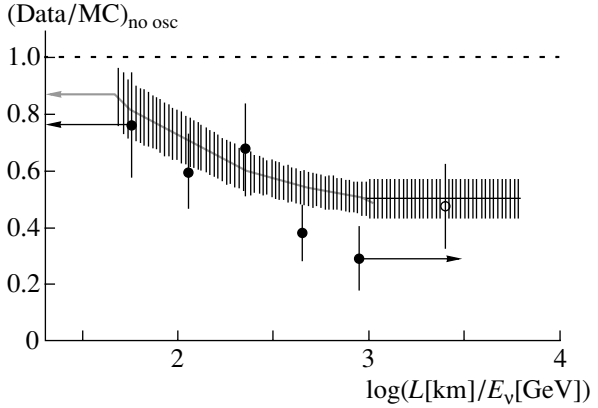

Fig. 4. Ratio (Data/MC)$_{\text{no osc}}$ as a function of estimated L/E_ν for the up through-going muon sample (closed circles) and the semicontained IUμ (open circle). For up through-going muons, the muon energy was estimated by MCS and E_ν by MC methods. The shaded regions represent the uncertainties in the MC predictions assuming $\sin^2 2\theta = 1$ and $\Delta m^2 = 0.0023$ eV^2. The horizontal dashed line at Data/MC = 1 is the expectation for no oscillations.

(for tracking) and the scintillator system (for time-of-flight measurement). The events measured and expected for the three measured topologies, indicated in Fig. 1, and the L/E_ν distribution deviate from Monte Carlo expectations without oscillations (Figs. 2–4 and Tables 1 and 2); the deviations point to the same $\nu_\mu \to \nu_\tau$ oscillation scenario [2–8].

Monte Carlos. The measured data of Fig. 2 were compared with different MC simulations. In the past, we used the neutrino flux computed by the Bartol 96 group [9] and the GRV94 [10] parton distribution. For the low-energy channels, the cross sections in [11] were used; the propagation of muons to the detector was done using the energy loss calculation by Lohmann *et al.* [12]. The total systematic uncertainty in the predicted flux of up through-going muons, adding in quadrature the errors, was estimated to be $\pm 17\%$; this is mainly a scale error that does not change the shape of the angular distribution. The error on the shape of the distribution is $\sim 6\%$. The detector was simulated using GEANT [13]. A similar MC (Honda 96) was used by the Super-Kamiokande Collaboration [14].

Recently, new improved MC predictions were made available by the Honda [14] and Fluka [15] groups. They include three-dimensional calculations of hadron production and decays and of neutrino interactions, an improved hadronic model, and new fits of the primary CR flux. The two MCs yield predictions for the nonoscillated and oscillated ν_μ fluxes in complete agreement with each other, equal to within a few percent (see Figs. 3*a*, 3*b*). The shapes of the angular distributions for oscillated and nonoscillated Bartol 96, new Fluka, and new Honda fluxes are the same to within a few percent (Figs. 3*a*, 3*b*). The absolute values of our up through-going muon data are about

Table 1. The number of events measured and the ratios $(\text{Data/MC})_{\text{no osc}}$ using the Bartol 96 MC for each topology

Topology	Measured events	$(\text{Data/MC})_{\text{no osc}}$
Up through-going	857	0.73
Semicontained (IU)	157	0.67
Up-stopping + down semicontained (UGS + ID)	262	0.83

20–30% above those predicted by the new Fluka and Honda MCs; this situation is also true for the new Super-Kamiokande data [16]; the measurements of the flux value at $\cos\theta = 0$ performed by various experiments do not seem to be conclusive [17]. Note that, in Fig. 3*a*, the new Fluka muon flux with an older CR fit is considerably above the new Fluka flux with the new CR fit. Our high-energy ν_μ data suggest that the new Honda and Fluka predictions should be raised by about 20–25%, probably because of the new CR fit used. The inclusion of the new ATTIC Collaboration measurements of primary CRs seems to lead to the old energy dependence of $E^{-2.71}$ [18]. Thus, the Bartol 96 MC may very probably still be used for the prediction of the absolute flux, besides predicting well the shape of the angular distribution. In the following, we shall use the predictions of this MC. It should be noted that the evidence for neutrino oscillations rests primarily with the shape of the angular distribution and this is the same in all MC calculations.

3. MACRO RESULTS ON ATMOSPHERIC NEUTRINOS

The up through-going muons come from ν_μ interactions in the rock below the detector; the ν_μ have a median energy $\bar{E}_\nu \sim 50$ GeV; muons with $E_\mu > 1$ GeV cross the whole detector. The data taking lifetime was slightly over 6 yr (full detector equivalent). The data, Table 1 and Fig. 2*a*, deviate in shape and in absolute value from the Bartol 96 MC predictions (see Section 2). This was first pointed out by MACRO in 1995 [4].

A large number of possible systematic effects and backgrounds that could affect the measurements were studied. One of the most significant checks was performed using only the scintillator system with two different and independent electronic systems [3, 8]. Two different final analyses of the up-through data have been performed: they agree to within 5%.

Assuming no oscillations, the number of expected up through-going muon events integrated over all zenith angles from Bartol 96 without oscillations is 1169; the measured number is 857 (Table 1). Thus, the ratio of the observed number of events to the Bartol 96 expectation is 0.73.

$\nu_\mu \to \nu_\tau$ versus $\nu_\mu \to \nu_s$. Matter effects due to the difference between the weak interaction effective potential for muon neutrinos with respect to sterile neutrinos (ν_s) would produce a different total number and a different zenith angle distribution of up through-going muons. The ratio $R_1 = N_{\text{vert}}/N_{\text{horiz}} = N(-1 < \cos\theta < -0.7)/N(-0.4 < \cos\theta < 0)$ was used to test the $\nu_\mu \to \nu_s$ oscillation hypothesis versus $\nu_\mu \to \nu_\tau$ [2, 6, 8]. The measured value is $R_{\text{meas}} = 1.38$; it should be compared to $R_\tau^{\min} = 1.61$ and $R_s^{\min} = 2.03$, which are the minimum values of the ratios for $\nu_\mu \to \nu_\tau$ and $\nu_\mu \to \nu_s$ oscillations for $\Delta m^2_{23} = 2.3 \times 10^{-3}$ eV^2 and maximal mixing.

For $\nu_\mu \to \nu_\tau$, the one-sided probability of measuring a value lower than R_{meas} is 7.2%. For $\nu_\mu \to \nu_s$ the probability is $P_s^{\text{best}} \simeq 1.5 \times 10^{-4}$; P_τ^{best} is about 480 times larger than P_s^{best}. Therefore, $\nu_\mu \to \nu_s$ oscillations (with any mixing) are excluded at about 99.8% C.L. with respect to $\nu_\mu \to \nu_\tau$ oscillations with maximal mixing [8].

Oscillation probability as a function of the ratio L/E_ν. E_ν was estimated by measuring the muon energy E_μ by means of the muon multiple Coulomb scattering (MCS) in the rock absorbers in the lower MACRO. The best method employed the streamer tubes in "drift mode," using the special electronics designed to search for magnetic monopoles [19]. The space resolution achieved was $\simeq 3$ mm. For each muon, seven variables were given in input to a neural network previously trained to estimate muon energies with MC events of known input energy crossing the detector at different zenith angles. The distribution of the ratio $R = (\text{Data/MC})_{\text{no osc}}$ obtained by this analysis is plotted in Fig. 4 as a function of L/E_ν [7]. Notice that the data extend from $L/E_\nu \sim$ 30 to 5000 km/GeV.

The internal up-going (IU) muons (~157 events, 285 expected, Table 1) come from ~4-GeV ν_μ interacting in the lower apparatus (Fig. 1). Compared to the no-oscillation prediction, there is a reduction of about a factor of two in the flux of these events, without any appreciable distortion in the shape of the zenith distribution (Fig. 2*b*) [5, 8]. The MC predictions for no oscillation in Figs. 2*b* and 2*c* are given by the dashed lines with a 21% systematic scale band. Notice that, at these energies, the Bartol 96, new Honda, and Fluka MCs agree well also in absolute values.

Table 2. Ratios between different event categories: $R_{\rm meas}$ is the measured value; R_0 is the expected value from the Bartol 96 MC without oscillations; the last column gives the one-sided probability compatible with a statistical fluctuation computed according to the a priori assumptions explained in the text

Ratio	$R_{\rm meas} \pm \sigma_{\rm stat}$	R_0	$R_0 \leq R_{\rm meas}$ probability
$N_{\rm vert}/N_{\rm horiz}$	1.38 ± 0.12	2.11	6.4×10^{-6}
$N_{\rm low}/N_{\rm high}$	0.85 ± 0.16	1.5	7.7×10^{-3}
$({\rm Data/MC})_{\rm IU}/({\rm Data/MC})_{\rm ID+UGS}$	0.60 ± 0.06	0.745	3.1×10^{-2}
Combination			3.4×10^{-7}

The up-stopping muons (UGS) are due to $\sim$3-GeV ν_μ interacting below the detector and yielding up-going muons stopping in the detector. The semicontained down-going muons (ID) are due to ν_μ-induced down-going muon tracks with a vertex in the lower MACRO. The two types of events (262 compared to 315 expected, Table 1) are identified by means of topological criteria; the lack of time information prevents one from distinguishing the two subsamples. The up-going ν_μ should all have oscillated completely, while the down-going ν_μ do not oscillate. The zenith distribution shows, as expected, a uniform deficit of about 25% of the measured number of events with respect to the no-oscillation prediction (Fig. 2*c*) [5, 8].

4. DETERMINATION OF THE OSCILLATION PARAMETERS

In the past, in order to determine the oscillation parameters, MACRO made fits to the shape of the up through-going muon distribution and to their absolute flux compared to the Bartol 96 MC prediction (with a 17% systematic scale uncertainty). The other data were only used to verify the consistency and make checks. The result was $\Delta m^2 = 0.0025$ eV^2 and maximal mixing.

Later, in [6, 7], the HE data for the zenith distribution, $R_1 = N_{\rm vert}/N_{\rm horiz}$, were combined with the HE neutrino energy measurement, $R_2 = N_{\rm low}/N_{\rm high}$. They are independent of the neutrino absolute flux; with these two pieces of information, the significance of observation of neutrino oscillations is about 4.7σ.

In order to reduce the effects of possible uncertainties in the MCs (to about 6%), we now use the following three independent ratios [8]:

(i) HE data: zenith distribution ratio $R_1 = N_{\rm vert}/N_{\rm horiz}$;

(ii) He data: neutrino energy measurement ratio $R_2 = N_{\rm low}/N_{\rm high}$;

(iii) low-energy data: ratio $R_3 = ({\rm Data/MC})_{\rm IU}/({\rm Data/MC})_{\rm ID+UGS} \simeq 0.78$.

Table 2 gives for each ratio the measured value $R_{\rm meas}$, the prediction R_0 for no oscillations using the Bartol 96 MC, and the probability value for no oscillations obtained allowing the predicted ratio to fluctuate around the mean value (considering the total number of events equal to the predicted value without oscillations). The no-oscillation hypothesis has a probability $P \sim 3.4 \times 10^{-7}$ (Table 2), ruling out the no-oscillation hypothesis by $\sim 5\sigma$. The formula used for combining independent probabilities is $P = P_1P_2P_3(1 - \ln P_1P_2P_3 + 1/2(\ln P_1P_2P_3)^2)$ [20].

By fitting the three ratios to the $\nu_\mu \to \nu_\tau$ oscillation formulas, we obtain $\sin^2 2\theta = 1$, $\Delta m^2 = 2.3 \times 10^{-3}$ eV^2 and the allowed region indicated in Fig. 5*a*.

We could also add the information on the absolute flux values of

(iv) HE data, assuming the validity of the Bartol 96 flux and a systematic scale error of 17%: $R_4 = N_{\rm meas}/N_{\rm Bartol-no\ osc} \simeq 0.73$, $P_4 \simeq 0.07$;

(v) low-energy semicontained muons, with a systematic scale error of 21%: $R_5 = N_{\rm meas}/N_{\rm Bartol-no\ osc} \simeq 0.67$, $P_5 \simeq 0.08$ (at these low energies the Bartol 96, Honda 2001, and Fluka 2002 MC neutrino fluxes are essentially equal).

Figure 5*a* shows the MACRO allowed regions for the $\nu_\mu \to \nu_\tau$ oscillation parameters in the $\Delta m^2 - \sin^2 2\theta$ plane using only the three ratios R_1, R_2, and R_3 (continuous line) and using also the two estimated absolute values, assuming the validity of the Bartol 96 fluxes (dashed line). In Fig. 5*b* are compared the MACRO, Super-Kamiokande (SK) [16], and Soudan 2 [21] allowed regions. All limiting lines are qualitative smoothed interpolations.

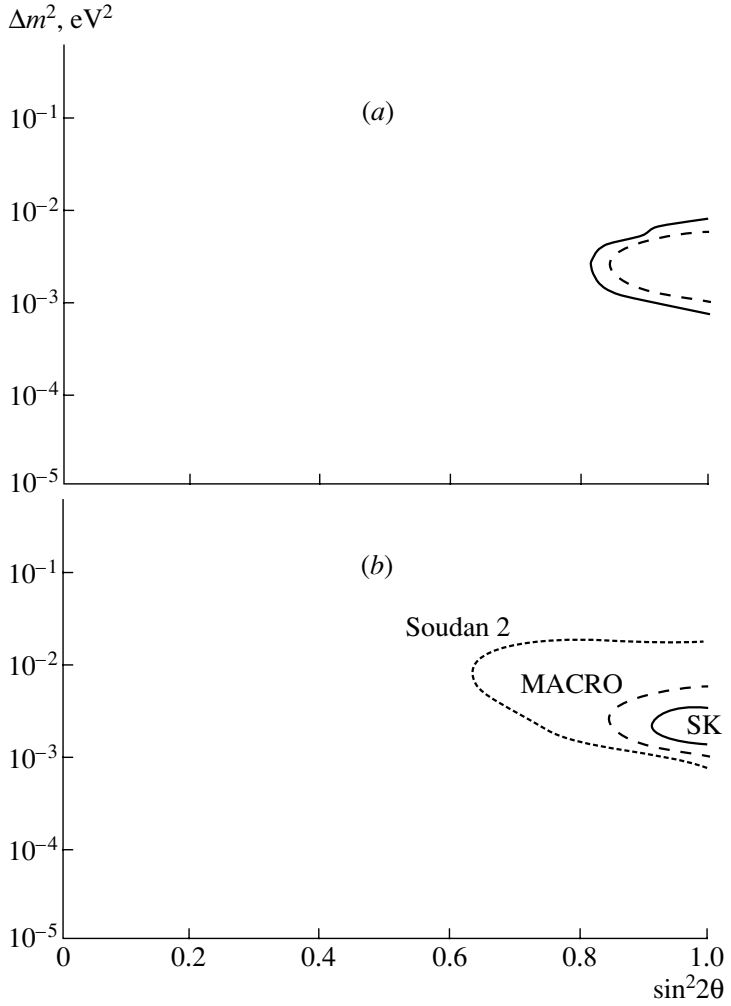

Fig. 5. Interpolated qualitative 90% C.L. contour plots of the allowed regions in the $\Delta m^2 - \sin^2 2\theta$ plane (a) for the MACRO data using only the ratios R_1, R_2, R_3 (outer continuous line) and using also the absolute values assuming the validity of the Bartol 96 fluxes (dashed line). (b) Comparison of the allowed regions for SK, MACRO, and Soudan 2 (all contours have been smoothed out and must be considered as qualitative).

5. NEUTRINO ASTROPHYSICS WITH MACRO

Search for astrophysical sources of high-energy muon neutrinos. HE ν_μ are expected to come from several galactic and extragalactic sources. Neutrino production requires astrophysical accelerators of protons and astrophysical "beam dumps." A sensitive search was made for up-going muons produced by neutrinos coming from celestial sources, interacting below the detector. Upper limits of 90% C.L. were established on the muon fluxes from specific celestial sources; the limits are in the range 10^{-15}–10^{-14} cm^{-2} s^{-1}. In the case of GX339-4 ($\alpha = 255.71°$, $\delta = -48.79°$) and Cir X-1 ($\alpha = 230.17°$, $\delta = -57.17°$), we have seven events: they have been considered as background; therefore, the upper flux limits are higher, but the events could also be an indication of signals [2, 3, 22]. The pointing capability of the detector was tested by determining the shadows of the Moon and the Sun on the primary CR flux [23].

A search for time coincidences of the up-going muons with γ-ray bursts was made. No statistically significant time correlation was found. A search was also made for a diffuse astrophysical neutrino flux for which an upper limit at the level of 1.5×10^{-14} cm^{-2} s^{-1} was established [24].

Indirect searches for WIMPs. WIMPs could be part of the galactic dark matter; they could be intercepted by celestial bodies, slowed down and trapped in their centers, where WIMPs and anti-WIMPs could annihilate and yield neutrinos of multi-GeV energy, in small angular windows from their centers. One of the best WIMP candidates could be the lowest mass neutralino.

A search was made for $\nu_\mu \to \mu$ coming from the center of the Earth using $10^\circ - 15^\circ$ cones around the vertical; we obtained muon flux limits of $\sim 10^{-14}$ cm^{-2} s^{-1}. The limits were compared with the predictions of a supersymmetric model by Bottino *et al.*; our data eliminate a sizable range of parameters used in the model [3, 25]. A similar procedure was used to search for muon neutrinos from the Sun: the upper limits are at the level of about 1.5×10^{-14} cm^{-2} s^{-1} [25].

Neutrinos from stellar gravitational collapses. A stellar gravitational collapse of the core of a massive star is expected to yield a burst of all types of neutrinos and antineutrinos with energies of 5–30 MeV in $\sim$10 s. The $\bar{\nu}_e$ can be detected via $\bar{\nu}_e + p \to n + e^+$ in the liquid scintillator. About 120 $\bar{\nu}_e$ events could have been detected in our 580-t liquid scintillator for a stellar collapse at the center of our Galaxy. Two separate electronic systems were used. Both had an energy threshold of $\sim$7 MeV and recorded pulse shape, charge, and timing information of the positron. Following a >7-MeV trigger, the first system PHRASE lowered its threshold to $\sim$1 MeV for 800 μs in order to detect (with a $\simeq$25% efficiency) the 2.2-MeV γ released in the capture reaction $n + p \to d + \gamma$ induced by the neutron produced in the primary process. A redundant supernova alarm system was in operation, alerting the physicists on shift; a procedure was defined to alert the various supernova observatories around the world [26]. MACRO was completed at the end of 1994; the first parts of the detector started operation in 1989. No stellar gravitational collapses in our Galaxy were observed from 1989 to 2000.

6. CONCLUSIONS

The MACRO detector took data from 1989 until the end of 2000. Important results were obtained in all the items listed in the proposal. In particular, for atmospheric neutrino oscillations, we analyzed different event topologies and different energies, exploited muon MCS in the detector to measure muon energies, and studied the effects of using different MCs. All data are in agreement with the hypothesis of $\nu_\mu \to \nu_\tau$ oscillations with maximal mixing and $\Delta m^2_{23} \simeq 2.3 \times 10^{-3}$ eV^2 and rule out the no-oscillation hypothesis by $\sim 5\sigma$.

In the search for GUT magnetic monopoles, MACRO obtained the best direct flux upper limit ($\Phi < 1.4 \times 10^{-16}$ cm^{-2} s^{-1} sr^{-1}) over the widest β range ($4 \times 10^{-5} < \beta < 1$) [19]. Studies were made on muon neutrino astronomy [22, 23], on seasonal solar and sidereal variations [2, 27], and on possible dark matter candidates: WIMPs, looking for muon neutrinos from the centers of the Earth and of the Sun, Nuclearites, and Q-balls [2, 28].

ACKNOWLEDGMENTS

We would like to acknowledge the cooperation of all the members of the MACRO Collaboration. MACRO was a collaboration of US and Italian institutions plus one Moroccan group; see [1] for the list of authors and institutions.

REFERENCES

1. S. Ahlen *et al.*, Nucl. Instrum. Methods Phys. Res. A **324**, 337 (1993); M. Ambrosio *et al.*, Nucl. Instrum. Methods Phys. Res. A **486**, 663 (2002).
2. G. Giacomelli *et al.*, *Lectures at the 6th Constantine Summer School, Algeria, 2002*; hep-ex/0211035.
3. M. Ambrosio *et al.*, Astropart. Phys. **9**, 105 (1998); hep-ex/0207043.
4. S. Ahlen *et al.*, Phys. Lett. B **357**, 481 (1995).
5. P. Bernardini, *Vulcano Workshop,* 1998; hep-ex/9809003; M. Ambrosio *et al.*, Phys. Lett. B **434**, 451 (1998); **478**, 5 (2000); G. Giacomelli *et al.*, hep-ph/9901355; hep-ex/0201032.
6. M. Ambrosio *et al.*, Phys. Lett. B **517**, 59 (2001); hep-ex/0106049.
7. M. Ambrosio *et al.*, Nucl. Instrum. Methods Phys. Res. A **492**, 376 (2002); Phys. Lett. B **566**, 35 (2003).
8. M. Ambrosio *et al.*, *Atmospheric Neutrino Oscillations with MACRO* (in preparation).
9. V. Agrawal *et al.*, Phys. Rev. D **53**, 1314 (1996).
10. M. Gluck *et al.*, Z. Phys. C **67**, 433 (1995).
11. P. Lipari *et al.*, Phys. Rev. Lett. **74**, 384 (1995).
12. W. Lohmann *et al.*, CERN 85-03.
13. http://wwwasd.web.cern.ch/wwwasd/geant/.
14. M. Honda *et al.*, Phys. Rev. D **64**, 053011 (2001); **52**, 4985 (1995).
15. G. Battistoni *et al.*, Astropart. Phys. **19**, 269 (2003); **19**, 291(E) (2003); in *Proceedings of the 28th ICRC, Tsukuba, Japan, 2003*.
16. Y. Hayato, in *Proceedings of the HEP EPS Conference, Aachen, 2003*; Y. Fukuda *et al.*, Phys. Rev. Lett. **81**, 1562 (1998); Phys. Lett. B **433**, 9 (1998).
17. M. F. Crouch, in *Proceedings of the 20th ICRC, Moscow, 1987*, Vol. 6, p. 165; M. Aglietta *et al.*, Astropart. Phys. **3**, 311 (1995); D. De Muth *et al.*, hep-ex/0304016.
18. R. Battiston, in *Proceedings of the 28th ICRC, Tsukuba, Japan, 2003*; T. Montaruli, in *Proceedings of the 28th ICRC, Tsukuba, Japan, 2003*.
19. M. Ambrosio *et al.*, Eur. Phys. J. C **25**, 511 (2002); G. Giacomelli and L. Patrizii, hep-ex/0302011.
20. B. Roe, *Probability and Statistics in Experimental Physics* (Springer, 1992), p. 128.
21. W. W. M. Allison *et al.*, Phys. Lett. B **449**, 137 (1999); T. Mann *et al.*, Nucl. Phys. B (Proc. Suppl.) **91**, 134 (2001); **110**, 349 (2002).

22. M. Ambrosio *et al.*, Astrophys. J. **546**, 1038 (2001); astro-ph/0002492.
23. M. Ambrosio *et al.*, Phys. Rev. D **59**, 012003 (1999); hep-ex/9807006; astro-ph/0302586.
24. M. Ambrosio *et al.*, Astropart. Phys. **19**, 1 (2003); S. Ahlen *et al.*, Astrophys. J. **412**, 301 (1993).
25. M. Ambrosio *et al.*, Phys. Rev. D **60**, 082002 (1999); hep-ex/9812020.
26. S. Ahlen *et al.*, Astropart. Phys. **1**, 11 (1992); M. Ambrosio *et al.*, Astropart. Phys. **8**, 123 (1998).
27. M. Ambrosio *et al.*, Phys. Rev. D **67**, 042002 (2003); astro-ph/0211119.
28. E. Witten, Phys. Rev. D **30**, 272 (1984); A. De Rujula and S. L. Glashow, Nature **312**, 734 (1984); D. Bakari *et al.*, hep-ex/0004019; M. Ambrosio *et al.*, Eur. Phys. J. C **13**, 453 (2000).

Physics of Atomic Nuclei, Vol. 67, No. 6, 2004, pp. 1147–1150. From Yadernaya Fizika, Vol. 67, No. 6, 2004, pp. 1172–1175.

NEUTRINO PHYSICS AND ASTROPHYSICS

MHD Origin of Density Fluctuations Deep within the Sun and Their Influence on Neutrino Oscillation Parameters in LMA MSW Scenario*

V. B. Semikoz**, **C. P. Burgess**[1)], **N. S. Dzhalilov**, **T. I. Rashba**[2)], **and J. W. F. Valle**[2)]

Institute of Terrestrial Magnetism, Ionosphere, and Radio Wave Propagation, Russian Academy of Sciences (IZMIRAN), Troitsk, Moscow oblast, 142092 Russia

Received November 17, 2003

Abstract—We analyze helioseismic waves near the solar equator in the presence of magnetic fields deep within the solar radiative zone. We find that reasonable magnetic fields can significantly alter the shapes of the wave profiles for helioseismic g modes. They can do so because the existence of density gradients allows g modes to resonantly excite Alfvén waves, causing mode energy to be funneled along magnetic field lines, away from the solar equatorial plane. The resulting waveforms show comparatively sharp spikes in the density profiles at radii where these resonances take place. Such matter density waves with known spatial structure are substituted as a matter density noise into the 2×2 Schrödinger equation for $\nu_{e,\mu}$ neutrinos oscillating within the Sun. Then we reexamine the sensitivity of solar neutrino oscillations to noise in the solar interior using the best current estimates of neutrino properties. Our results show that the measurement of neutrino properties at KamLAND provides new information about fluctuations in the solar environment on scales to which standard helioseismology constraints are largely insensitive. We also show how the determination of neutrino oscillation parameters from a combined fit of KamLAND and solar data depends strongly on the magnitude of solar density fluctuations. © *2004 MAIK "Nauka/Interperiodica".*

Our ansatz in the solution of the standard Schrödinger equation describing evolution of neutrinos in the Sun[3)] for the case $\rho' = 0$ is the numerical simulation of matter noise of an unknown amplitude (varied in linear magnetohydrodynamics (MHD) as $\rho'/\rho_0 =$ 2, 4, 8%) with a given correlation length $L_0 \sim l_{\rm osc}^{\rm LMA}$ that is strongly motivated through analytic solution of the full set of MHD equations [1, 2].

Note that, before, in all papers where similar problems concerning solar matter noise influence on MSW oscillations were considered [3–5], nobody found the correlation length of density perturbations self-consistently as was done first in [2].

In the one-dimensional linear model after transforming to Fourier space in the x and y directions, such as in $\mathbf{v} = \mathbf{v}(z)\exp(-i(\omega t - k_x x - k_y y))$, the full set of MHD equations for the eight perturbation functions, magnetic field $\mathbf{b} = \mathbf{B}'/B_0$, fluid velocity $\mathbf{v}$, pressure p', and density ρ', is replaced by one equation for the z component of the magnetic field, $b_z(z)$ [1]. Here, $\mathbf{B}_0 = (B_0, 0, 0)$ is a uniform background magnetic field assumed to be perpendicular to the equatorial plane ($x = y = 0$) in our one-dimensional model. We find b_z to be determined as the solution to the following second-order linear ordinary differential equation,

$$\left(1 - \frac{k_x^2 v_{\rm A}^2}{\omega^2}\right)\frac{d^2 b_z(z)}{dz^2} - \frac{N^2}{g}\frac{db_z(z)}{dz} + k_\perp^2\left(\frac{k_x^2 v_{\rm A}^2}{\omega^2} - 1 + \frac{N^2}{\omega^2}\right) b_z(z) = 0, \qquad (1)$$

where $k_\perp = \sqrt{k_x^2 + k_y^2}$; $N = \sqrt{g(\gamma - 1)/H\gamma}$ denotes the Brunt–Väisälä (buoyancy) frequency, which is almost constant within the radiative zone (RZ), $N \sim 10^{-3}$ s^{-1}, as well as the gravitational acceleration $g \sim 250$ m s^{-2}; $H = 0.1R_\odot$ is the height scale in the standard solar model (SSM); the Alfvén velocity $v_{\rm A} \equiv v_{\rm A}(z) = B_0/\sqrt{4\pi\rho_0(z)}$ given by the SSM density profile $\rho_0(z) = \rho_c \exp(-z/H)$ is the changing parameter ($v_{\rm A}(z) \sim \exp(z/2H)$); and $\gamma = c_p/c_V$ is the heat capacity ratio, e.g., in a hydrogen plasma $\gamma = 5/3$.

In the absence of the background magnetic field, $B_0 = v_{\rm A} = 0$, Eq. (1) describes g modes. In the

*This article was submitted by the authors in English.

[1)]Physics Department, McGill University, Montreal, Quebec, Canada.

[2)]AHEP Group, Instituto de Física Corpuscular, C.S.I.C., Universidad de Valencia, Edificio Institutos de Paterna, Valencia, Spain.

**e-mail: semikoz@izmiran.rssi.ru

[3)]See below Eq. (5).

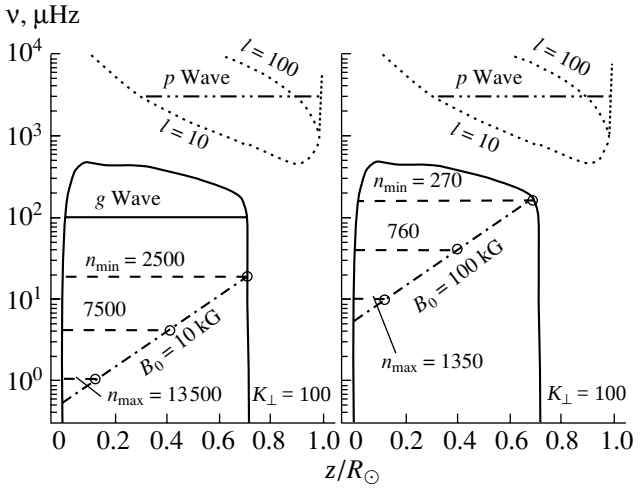

Fig. 1. Relevant frequencies plotted against radial position within the Sun. The solid curve gives the buoyancy frequency $N(z)$, while the dash-dotted lines are the Alfvén frequencies. Notice that $N(z)$ goes to zero at the solar center and at the top of RZ. The horizontal dashed lines represent the frequencies of magnetogravity waves computed from the exact MHD spectrum. These frequencies are plotted for the mode number, n, for fixed values $K_x = K_\perp = 100$. The two panels correspond to the two choices for the magnetic field: 10 (left) and 100 kG (right). Minimum and maximum mode numbers are indicated, with $n_{\min}$ defined by the condition that its resonance occurs at the top of RZ, $z_r(n_{\min}) = 0.7R_\odot$, and $n_{\max}$ having a resonance at $z_r(n_{\max}) = 0.12R_\odot$, where the matching of two spectrum branches happens (see in our works by Burgess *et al.* [1, 2]). The dotted curves denote acoustic (Lamb) frequencies for $l = 10$ and $l = 100$, while the double-dot-dashed horizontal line represents the trapping region for a p wave of frequency 3000 μHz and $l = 10$. The horizontal solid line represents the trapping region for a g wave of frequency 100 μHz. (From [2].)

presence of RZ magnetic fields, $B_0 \neq 0$, there appears a singularity at the Alfvén frequency, $\omega = k_x v_{\rm A}$, for which the coefficient in the first term vanishes. This automatically leads to singularities for each MHD functions containing derivatives of first order, db_z/dz, and, in particular, this leads to the spikes for the density perturbations to be substituted into the Schrödinger equation [see below Eq. (5)],

$$i\omega\frac{\rho'(z)}{\rho_0} = -\frac{\omega}{k_x H}\left(b_z - H\frac{db_z}{dz}\right) + ik_x v_x + ik_y v_y, \tag{2}$$

where transversal velocities $v_{x,y}$ also depend on db_z/dz. Such MHD perturbation functions diverge at the Alfvén resonant layer positions $z_r(n, B_0)$ unless the imaginary part of the eigenfrequency $\omega \equiv \omega(n, B_0, k_x, k_y) \equiv \omega_1(1 + id)$ is included.

The physical sense of the Alfvén resonance is seen in Fig. 1. The crosses of g modes with the Alfvén ones shown by circles for some fixed external parameters B_0, $k_{x,y}$ take place at discrete "points," $z_r(n)$, $n_{\min} < n < n_{\max}$, called resonant positions for an integer node number n. The Alfvén layer where efficient energy transfer from g modes to the Alfvén ones takes place due to the resonance $\omega_g = \omega_{\rm A}(n)$ has a finite width $\Delta z_r(n)$ given by the imaginary part of the eigenfrequency ω, $d \sim {\rm Im}\omega$ [2]. Such energy being funneled in the x direction along the background field $\mathbf{B}_0$ can lead to the heating of that layer and an enhancement of MHD perturbations.

The resonances $\omega_{\rm A}(n) = \omega_g(n)$ occur since $\omega_{\rm A} = k_x v_{\rm A}(z)$ grows with z up to the top of RZ for growing Alfvén velocity $v_{\rm A}(z) = B_0/\sqrt{4\pi\rho_0(z)}$.

Thus, our main task in the suggested model is the determination of the MHD spectrum given by the eigenvalue problem for the master Eq. (1). Using natural boundary conditions $v_z(0) = (\omega/k_x)b_z(0) = 0$ at the center of the Sun and the vanishing of the divergent solution $b_z(z) \sim e^{+k_\perp z}$ for $z_r < z < z_{\rm CZ}$, where $z_{\rm CZ}$ is the position of the bottom of the convective zone, one obtains the transcendental dispersion Eq. [2], from which one finds the approximate MHD spectrum for superlow frequencies, $\omega_1 \ll N$,

$$\frac{\omega_1}{N} = \frac{2K_\perp(z_r/2H + \ln 2)}{\pi n}, \tag{3}$$
$$d = \frac{\ln|\tan(\pi/\gamma)|}{2\pi n\,(1 - (z_r/2H + \ln 2)^{-1})}.$$

Obviously, eigenmodes $\omega_1(n)$ survive a long time, $|d(n)| \ll 1$, for large node numbers, $|n| \gg K_\perp \geq 1$, $K_\perp = k_\perp H$. The resonance layer position $z_r(n)$ is determined by the resonance condition $\omega_1(n) = k_x v_{{\rm A}c} e^{z_r(n)/2H}$, where $v_{{\rm A}c} = B_0/\sqrt{4\pi\rho_c} = B_0/43.4$ G [cm s^{-1}] and $\omega_1(n)$ is given by (3). Then the distance between the neighboring spikes $L_0(B_0) = z_r(n+1) - z_r(n)$ takes the asymptotic form

$$\lambda_z = L_0(B_0) = z_r(n+1, B_0) - z_r(n, B_0) \approx 2H/n, \tag{4}$$

which, e.g., for large node numbers $n \gtrsim 10^3$ allowed for magnetic fields $B_0 \sim$ kG in spectrum (3), equals $L_0 \sim 140$ km because $H \simeq 7 \times 10^4$ km.

This value is of the order of the LMA neutrino oscillation length, $L_0 \sim l_\nu^{\rm LMA}$, confirmed in the KamLAND experiment [6] that provides the parametric resonance for neutrino oscillations in RZ resulting for a moderate value of the density perturbation amplitudes, $\sqrt{\langle\xi^2\rangle} = \rho'/\rho_0 \sim$ a few percent, in a strong suppression of $\nu_e \to \nu_\mu$ conversions (survival probability P_{ee} increases).

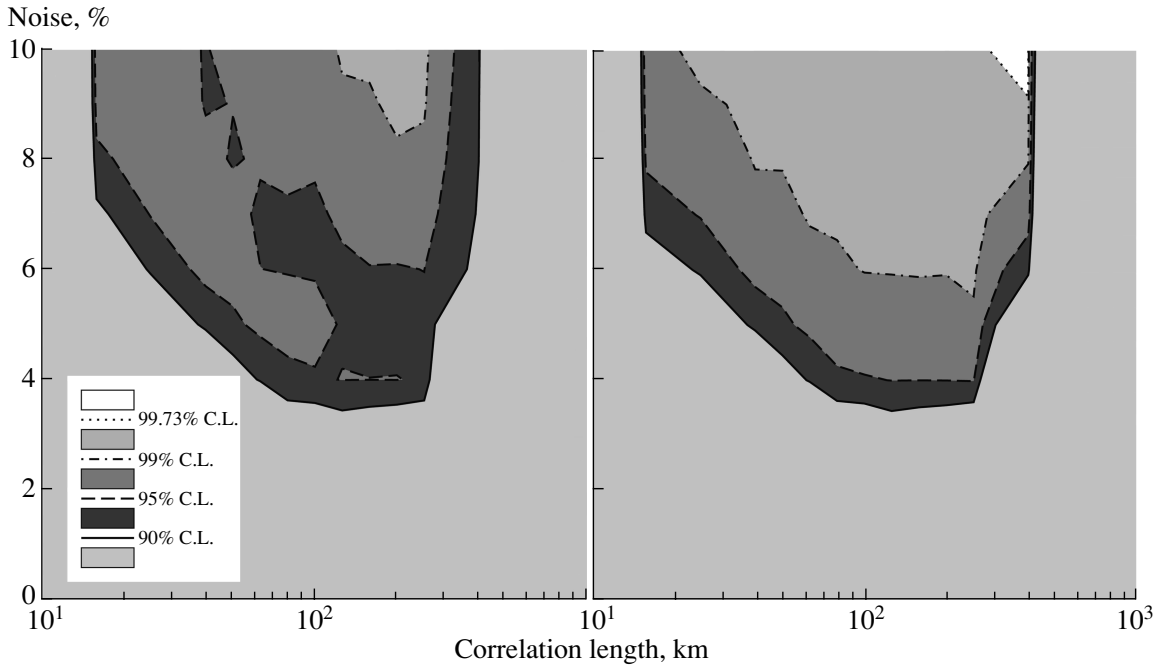

Fig. 2. Allowed regions for the solar noise parameters L_0 and ξ from the analysis of present solar neutrino + KamLAND data, when neutrino oscillation parameters are varied freely (left panel) or fixed at the present LMA best fit point (right panel). (From [1].)

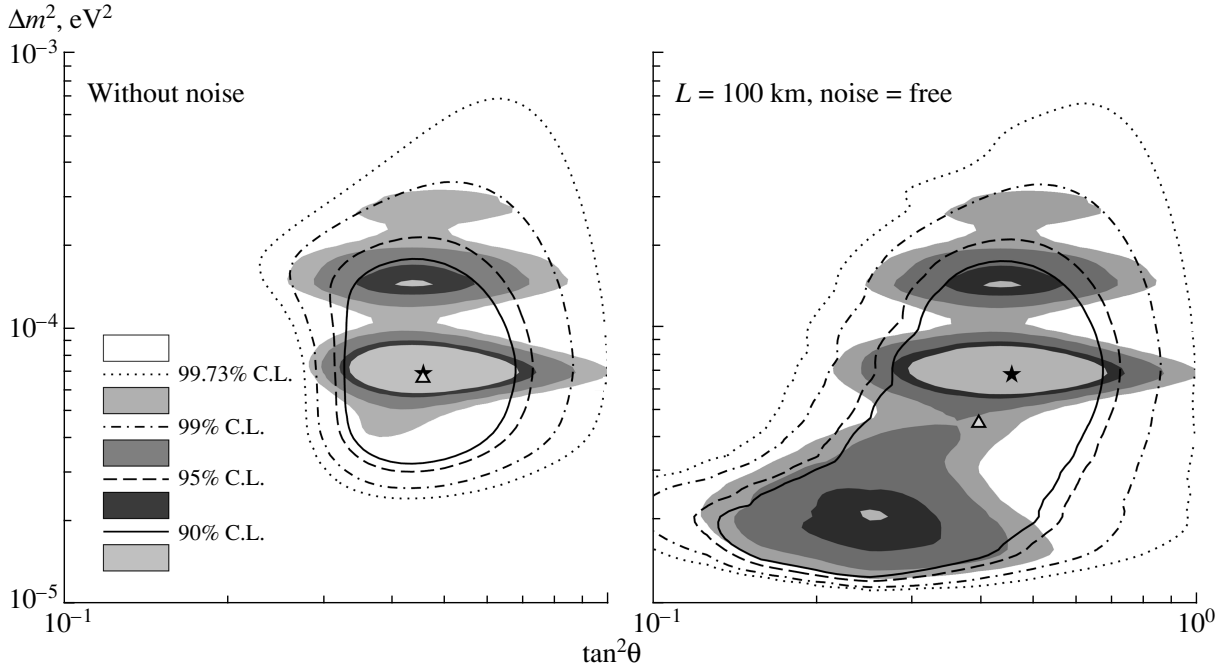

Fig. 3. Allowed regions for neutrino oscillation parameters Δm^2 and θ, for the "standard" noiseless Sun (left panel) and for a noisy Sun with arbitrary density noise magnitude ξ on a $L_0 = 100$ km spatial scale. The lines and shaded regions correspond to the analyses of solar and solar + KamLAND data, respectively. The best-fit point is indicated by a triangle (solar) or a star (solar + KamLAND). (From [1].)

The numerical code used in our work [1] provides the calculation of the neutrino survival probability at the detector accounting for neutrino propagation in the Sun, vacuum, and then through

the Earth. Solving the standard MSW problem [7] (notation is standard), we substituted into the Schrödinger equation describing neutrino evolution in the Sun,

$$i\frac{d}{dr}\begin{pmatrix}\nu_e\\ \nu_\mu\end{pmatrix}=\begin{pmatrix}G_{\rm F}\sqrt{2}Y_e\dfrac{\rho_0}{m_p}\left(1+\dfrac{\rho'}{\rho_0}\right)-\Delta m^2\dfrac{\cos 2\theta}{2E} & \Delta m^2\dfrac{\sin 2\theta}{2E}\\ \Delta m^2\sin 2\theta/2E & 0\end{pmatrix}\begin{pmatrix}\nu_e\\ \nu_\mu\end{pmatrix}, \quad (5)$$

a stationary profile of the matter density perturbations $\rho'(r)$ given in RZ by $\rho'(\mathbf{r},t)\to\rho'(z)\cos(\omega t-k_x x-k_y y)$ for which one can obtain analytically both the low-frequency spectrum, $\omega\ll N\sim 10^{-3}\,\mathrm{s}^{-1}$ (3), and the spatial structure given by the MHD perturbation wavelengths along the z axis, $\sim L_0$ (4). Thus, the parametric resonance provides a strong influence on the neutrino survival probability $P_{ee}(L_0,\xi,\delta,\theta)$ (about 50%) even for a small matter perturbation amplitude $\xi=\rho'/\rho_0$ ($\xi\sim 2\%$).

On the other hand, since complex amplitudes in linear MHD with an arbitrary phase for regular wave solutions are unknown, we simulated random density noise ($\langle\xi\rangle=0$) analogously to [3], while now we solved exact Eq. (5) finding complex wave functions $|\nu_a\rangle$ for many density perturbation realizations along each neutrino ray and only then averaging $P_{aa}=|\langle\nu_a\mid\nu_a\rangle|^2$ over these realizations and the SSM neutrino source distributions.

In this way, we considered two problems for the four varying parameters: L_0, $\xi\equiv\sqrt{\langle\xi^2\rangle}$, Δm^2, $\tan^2\theta$. First, running neutrino oscillation parameters (free parameters in the left panel in Fig. 2) or fixing them (the right panel in the same plot), we solved the inverse neutrino problem looking for bounds on noise parameters (L_0, ξ) in the deep solar interior or suggesting an MHD generalization of the inverse method in standard helioseismology (HSSM), $B_0=0$.

Second, vice versa, fixing $L_0=100$ km for some noise amplitudes, we explored noise influence on the LMA MSW solution to the solar neutrino problem (Fig. 3). In this case (direct problem), increasing ξ, one finds (for a high value $\xi=6\%$) that the best fit point in the global analysis of the solar and KamLAND data goes down to the lower strip disfavored by the present solar data analysis given for noiseless LMA MSW oscillations. It would be interesting to compare this prediction with future data, collecting more statistics in that experiment.

Finally, we should stress that the inverse method in HSSM based on long wavelengths of p, g modes (of the order $\gtrsim 10^3$–10^4 km) is not sensitive to small-scale density perturbations as given by the MHD model ($\sim$100 km) considered in [1, 2]. This means that the well-known HSSM bound $\xi<1\%$ [8] is not valid anywhere in the presence of RZ magnetic fields.

REFERENCES

1. C. P. Burgess *et al.*, Astrophys. J. **588**, L65 (2003).
2. C. P. Burgess *et al.*, Mon. Not. R. Astron. Soc. **348**, 609 (2004).
3. H. Nunokawa *et al.*, Nucl. Phys. B **472**, 495 (1996).
4. C. P. Burgess and D. Michaud, Ann. Phys. (N. Y.) **256**, 1 (1997); P. Bamert, C. P. Burgess, and D. Michaud, Nucl. Phys. B **513**, 319 (1998); hep-ph/9707542.
5. F. N. Loreti and A. B. Balantekin, Phys. Rev. D **50**, 4762 (1994).
6. K. Eguchi *et al.*, Phys. Rev. Lett. **90**, 021802 (2003).
7. S. P. Mikheev and A. Yu. Smirnov, Sov. J. Nucl. Phys. **42**, 913 (1985); Nuovo Cimento C **9**, 17 (1986); L. Wolfenstein, Phys. Rev. D **17**, 2369 (1978).
8. J. Christensen-Dalsgaard, *Lecture Notes*, p. 118; http://bigcat.obs.aau.dk/ jcd/oscilnotes/.

Physics of Atomic Nuclei, Vol. 67, No. 6, 2004, pp. 1151–1153. From Yadernaya Fizika, Vol. 67, No. 6, 2004, pp. 1176–1178.

NEUTRINO PHYSICS AND ASTROPHYSICS

KamLAND and Solar Antineutrino Spectrum*

B. C. Chauhan**, **J. Pulido, and E. Torrente-Lujan**[1)]

Centro de Física das Interacções Fundamentais (CFIF), Instituto Superior Técnico, Lisboa, Portugal

Received November 4, 2003

Abstract—We use the recent KamLAND observations to predict the solar antineutrino spectrum at some confidence limits. We find a scaling of the antineutrino probability with respect to the magnetic field profile—in the sense that the same probability function can be reproduced by any profile with a suitable peak field value—that can be utilized to obtain the general shape of the solar antineutrino spectrum. This scaling and the upper bound on the solar antineutrino event rate, which can be derived from the data, lead to: 1) an upper bound on the solar antineutrino flux and 2) the prediction of their energy spectrum. We get $\phi_{\bar{\nu}} < 3.8 \times 10^{-3}\phi(^8\mathrm{B})$ or $\phi_{\bar{\nu}} < 5.5 \times 10^{-3}\phi(^8\mathrm{B})$ at 95% C.L., assuming Gaussian or Poissonian statistics, respectively. For 90% C.L., these become $\phi_{\bar{\nu}} < 3.4 \times 10^{-3}\phi(^8\mathrm{B})$ and $\phi_{\bar{\nu}} < 4.9 \times 10^{-3}\phi(^8\mathrm{B})$. This provides an improvement by a factor of 3–5 with respect to the existing bounds. These limits are quite general and independent of the detailed structure of the magnetic field in the solar interior.

The recent KamLAND experiment [1] searching for antineutrinos of $E_{\bar{\nu}} > 1.8$ MeV via

$$\bar{\nu}_e + p \to n + e^+ \tag{1}$$

has provided evidence through the observation of reactor antineutrinos that the solution to the solar neutrino problem is dominated by matter oscillations with a large mixing angle (LMA). Spin flavor precession (SFP) [2–4], which provided very good fits to the data [5], must, if present, play a subdominant role. Such a possibility was recently investigated [6], its signature being the appearance of antineutrinos from the Sun [3, 7, 8]. The production of these antineutrinos must predominantly occur as a vacuum oscillation from the Sun to the Earth [6]

$$\nu_{e_L} \to \bar{\nu}_{\mu_R} \to \bar{\nu}_{e_R}, \tag{2}$$

with the first step in this sequence (SFP) occurring inside the Sun.

The amplitude for the $\nu_{e_L} \to \bar{\nu}_{\mu_R}$ transition was evaluated in perturbation theory for small μB, the product of the neutrino magnetic moment by the solar magnetic field, and found to be, assuming the LMA solution to be dominant [6],

$$A(\nu_{e_L} \to \bar{\nu}_{\mu_R}) = \frac{\mu B(r_i)\sin^2\theta(r_i)}{g_2'(r_i)}. \tag{3}$$

In this expression, r_i denotes the neutrino production point and g_2' is a function of the interaction potentials V_e, V_μ. Recently, we proposed a more realistic case [9] in which we convolute the neutrino production distribution spectrum with the solar magnetic field profile. In this way, the overall antineutrino production probability is obtained as

$$P(\nu_{e_L} \to \bar{\nu}_{e_R}) = \frac{1}{2}\int |A(\nu_{e_L} \to \bar{\nu}_{\mu_R})|^2 f_B(r_i)dr_i, \tag{4}$$

where the factor 1/2 comes from averaging over the vacuum oscillations [6], f_B represents the neutrino production distribution function for Boron neutrinos [10], and the integral extends over the whole production region.

Owing to this integration, the energy shape of probability (4) is largely insensitive to the magnetic field profile function. As a result, the infinite ambiguities about the shape of the solar field profile are circumvented. This fact can be illustrated by defining a scaling factor [9]

$$P_{\bar{\nu}}[B(r)] = kP^0_{\bar{\nu}}, \tag{5}$$

where $P^0_{\bar{\nu}}$ is the antineutrino production probability corresponding to the arbitrary reference field profile chosen. This scaling factor can be evaluated from (3) and (4).

As a consequence of the profile independence of the antineutrino probability shape, it is possible to extract a general solar antineutrino spectrum from the recent KamLAND observations. The normalization

*This article was submitted by the authors in English.

[1)]Departamento de Física, Universidad de Murcia, Spain; and CERN-TH, Geneve, Switzerland.

**e-mail: chauhan@gtae3.ist.utl.pt

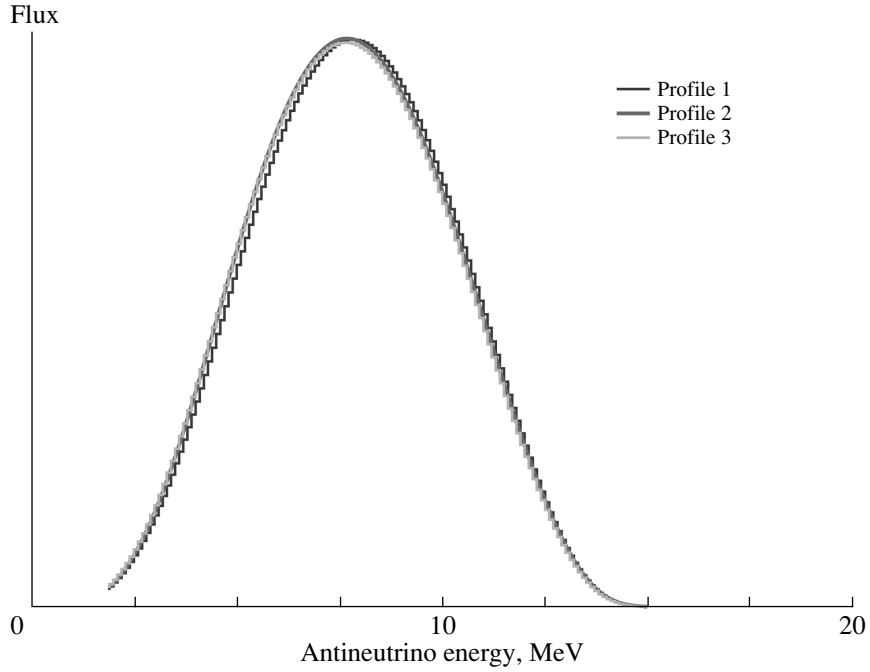

Fig. 1. Solar antineutrino spectra for three different solar field profiles.

of the spectrum can, of course, only be obtained in the future from a possible solar antineutrino event rate as seen by KamLAND.

The positron event rate in the KamLAND experiment originating from solar antineutrinos can be written as

$$S = Q_0 \int_{E_e^0}^{\infty} dE_e \int_{E_m}^{E_M} \epsilon(E_e^{'}) R(E_e, E_e^{'}) \phi_{\bar{\nu}}(E) \sigma(E) dE. \tag{6}$$

Here, Q_0 is a normalization factor, which takes into account the number of atoms of the detector and its live time exposure [1], and E is the antineutrino energy, related to the physical positron energy by $E_e^{'} = E - (m_N - m_P)$ to zero order in $1/M$, the nucleon mass. We thus have $E_m = 1.804$ MeV, while the KamLAND puts a lower energy cut at $E_e^0 = 2.6$ MeV in order to eliminate the background posed by the geo-neutrinos. The function ϵ ($\simeq 80\%$) and R denotes the detector efficiency, $R(E_e, E_e^{'})$ is the Gaussian energy resolution function of the detector, and the antineutrino cross section $\sigma(E)$ was taken from [11]. We considered energy bins of size $E_e = 0.425$ MeV in the KamLAND observation range 2.6–8.125 MeV [1].

The antineutrino event rate $S_{\bar{\nu}}[B(r)]$ follows the same scaling behavior as the probability (see Eq. (5)). We now make use of this behavior to obtain our upper limits on the total antineutrino flux and $\mu_\nu B_0$. We apply Gaussian probabilistic considerations to the global rate in the whole energy range, $E_e = 2.6$–8.125 MeV, and Poissonian considerations to the event content in the highest energy bins ($E_e > 6$ MeV) where KamLAND observes no signal. We take

$$S_{\bar{\nu}}^{\text{sun}} = S_{\text{obs}} - S_{\text{react}}(\text{LMA}), \tag{7}$$

where $S_{\text{obs}} = 54.3 \pm 7.5$ and $S_{\text{react}}(\text{LMA}) = 49 \pm 1.3$ is the signal expected for the best fit parameters of KamLAND ($\Delta m_{21}^2 = 6.9 \times 10^{-5}$ eV^2, $\sin^2 2\theta = 1$). At 90 (95)% C.L.,

$$S_{\text{obs}} - S_{\text{react}} = k S_{\bar{\nu}}^0 < 17.8 \quad (20.2) \tag{8}$$

leading to upper bounds on $\mu_\nu B_0$ and on the solar antineutrino flux at 90 and 95% C.L.:

$$\mu_\nu B_0 < 5.16 \times 10^{-19}\ \text{MeV}, \tag{9}$$
$$\phi_{\bar{\nu}} < 0.0034 \phi(^8\text{B})\ (90\%\ \text{C.L.});$$

$$\mu_\nu B_0 < 5.5 \times 10^{-19}\ \text{MeV}, \tag{10}$$
$$\phi_{\bar{\nu}} < 0.0038 \phi(^8\text{B})\ (95\%\ \text{C.L.}).$$

For Poisson statistics applied to the five highest energy bins ($E > 6$ MeV), the unified intervals [12] $[0, \epsilon_{\text{C.L.}}]$ are $[0, 2.44]$ at 90% C.L. and $[0, 3.09]$ at 95% C.L., leading to

$$\mu_\nu B_0 < 2.51 \times 10^{-19}\ \text{MeV}, \tag{11}$$
$$\phi_{\bar{\nu}} < 0.0049 \phi(^8\text{B})\ (90\%\ \text{C.L.});$$

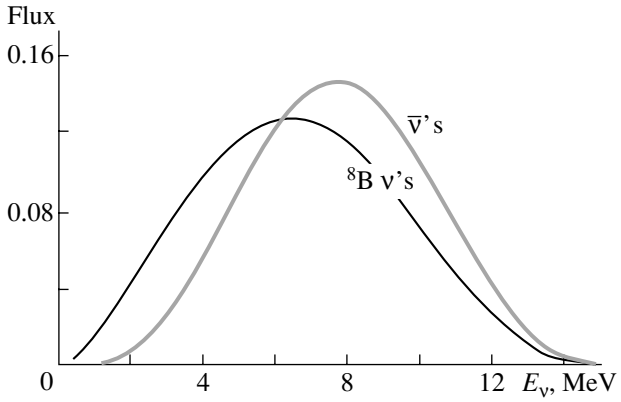

Fig. 2. The expected solar antineutrino spectrum and the ^{8}B neutrino one [10], both normalized to unity, showing the peak shift and the distortion introduced by the antineutrino probability.

$$\mu_\nu B_0 < 2.82 \times 10^{-19}\ \text{MeV}, \qquad (12)$$
$$\phi_{\bar{\nu}} < 0.0055\phi(^8\text{B})\ (95\%\ \text{C.L.});$$

which show an improvement by a factor of 3–5 with respect to the existing bounds on $\phi_{\bar{\nu}}$ from LSD [13].

The near independence of the antineutrino probability and event rate on the solar magnetic field profile is also necessarily reflected on the antineutrino spectral flux $\phi_{\bar{\nu}}(E)$ arriving at the Earth. In fact, one obviously has $\phi_{\bar{\nu}}(E) = \phi_{\text{B}}(E) \times P(E)$, where $\phi_{\text{B}}(E)$ is the Boron neutrino flux and $P(E)$ is the antineutrino appearance probability.

In Fig. 1, three curves of the solar antineutrino spectral flux corresponding to three very different profiles[2)] have been plotted for an arbitrary normalization of the flux. The generality and profile independence of the spectral flux is clearly seen in the figure, as they are all nearly coincident.

Finally, the near independence of the antineutrino probability leads to an antineutrino spectrum that is a modification of the parent ^{8}B one in a profile independent way. A comparison of the two spectra is displayed in Fig. 2, which clearly shows the peak shift and distortion introduced by the antineutrino probability.

To summarize, now that SFP is ruled out as a dominant effect for the solar neutrino deficit, it is important to investigate its still remaining possible signature in the solar neutrino signal, namely, an observable $\bar{\nu}_e$ flux. From the antineutrino production model expound here, an upper bound on the solar antineutrino flux can be derived, namely, $\phi_{\bar{\nu}} < 3.8 \times 10^{-3}\phi(^8\text{B})$ and $\phi_{\bar{\nu}} < 5.5 \times 10^{-3}\phi(^8\text{B})$ at 95% C.L., assuming, respectively, Gaussian or Poissonian statistics. For 90% C.L., we found $\phi_{\bar{\nu}} < 3.4 \times 10^{-3}\phi(^8\text{B})$ and $\phi_{\bar{\nu}} < 4.9 \times 10^{-3}\phi(^8\text{B})$, which shows an improvement relative to the previously existing bounds from LSD [13] by a factor of 3–5. These are practically independent of the detailed magnetic field profile in the core and radiative zone, and the energy spectrum of this flux is also found to be nearly profile independent. Furthermore, in view of the relation $\phi_{\bar{\nu}}(E) = \phi_{\text{B}}(E) \times P(E)$, the same effect also leads to a profile independent antineutrino spectrum.

ACKNOWLEDGMENTS

The work of the B.C.Ch. was supported by Fundação para a Ciência e a Tecnologia through the grant SFRH/BPD/5719/2001. E.T-L. acknowledges many useful conversations with P. Aliani, M. Picariello, and V. Antonelli; the hospitality of the CFIF (Lisboa); and the financial support of the Spanish CYCIT funding agency.

REFERENCES

1. K. Eguchi *et al.* (KamLAND Collab.), Phys. Rev. Lett. **90**, 021802 (2003).
2. J. Schechter and J. W. F. Valle, Phys. Rev. D **24**, 1883 (1981); **25**, 283(E) (1982).
3. C. S. Lim and W. J. Marciano, Phys. Rev. D **37**, 1368 (1988).
4. E. Kh. Akhmedov, Yad. Fiz. **48**, 599 (1988) [Sov. J. Nucl. Phys. **48**, 382 (1988)]; Phys. Lett. B **213**, 64 (1988).
5. B. C. Chauhan and J. Pulido, Phys. Rev. D **66**, 053006 (2002).
6. E. Kh. Akhmedov and J. Pulido, Phys. Lett. B **553**, 7 (2003).
7. E. Kh. Akhmedov, Zh. Éksp. Teor. Fiz. **95**, 1195 (1989) [Sov. Phys. JETP **68**, 690 (1989)]; R. S. Raghavan *et al.*, Phys. Rev. D **44**, 3786 (1991); C. S. Lim *et al.*, Phys. Lett. B **243**, 389 (1990); E. Kh. Akhmedov *et al.*, Phys. Rev. D **48**, 2167 (1993).
8. E. Torrente-Lujan, J. High Energy Phys. **04**, 054 (2003); Phys. Lett. B **441**, 305 (1998); **494**, 255 (2000); Nucl. Phys. B (Proc. Suppl.) **87**, 504 (2000); P. Aliani *et al.*, J. High Energy Phys. **02**, 025 (2003).
9. B. C. Chauhan *et al.*, Phys. Rev. D **68**, 033015 (2003).
10. J. N. Bahcall, http://www.sns.ias.edu/∼jnb/.
11. P. Vogel and J. F. Beacom, Phys. Rev. D **60**, 053003 (1999).
12. K. Hagiwara *et al.* (Particle Data Group), Phys. Rev. D **66**, 010001 (2002).
13. M. Aglietta *et al.*, Pis'ma Zh. Éksp. Teor. Fiz. **63**, 753 (1996) [JETP Lett. **63**, 791 (1996)].

[2)]For details see [9].

Physics of Atomic Nuclei, Vol. 67, No. 6, 2004, pp. 1154–1160. From Yadernaya Fizika, Vol. 67, No. 6, 2004, pp. 1179–1185.

NEUTRINO PHYSICS AND ASTROPHYSICS

Neutrino Properties from High-Energy Astrophysical Neutrinos*

S. Pakvasa**

Department of Physics and Astronomy, University of Hawaii, Honolulu, HI 96822, USA

Received November 17, 2003

Abstract—It is shown how high-energy neutrino beams from very distant sources can be utilized to learn about some properties of neutrinos such as lifetimes. Furthermore, even mixing elements such as U_{e3} and the CP-violating phase in the neutrino mixing matrix can be measured in principle. Pseudo-Dirac mass differences as small as 10^{-18} eV^2 can be probed as well. © *2004 MAIK "Nauka/Interperiodica".*

1. INTRODUCTION

We make two optimistic assumptions. The first one is that distant neutrino sources (e.g., AGNs and GRBs) exist and, furthermore, have detectable fluxes at high energies (up to and beyond PeV). The second one is that, in the not too far future, very large volume, well-instrumented detectors of sizes of order of 1 km^3 and beyond will exist and be operating, and furthermore will have (a) reasonably good energy resolution, (b) good angular resolution ($\sim 1^\circ$), and (c) low energy threshold (~ 100 GeV).

2. NEUTRINOS FROM ASTROPHYSICAL SOURCES

If these two assumptions are valid, then there are a number of uses these detectors can be put to [1]. In this talk, I want to focus on those that enable us to determine some properties of neutrinos, namely, probe neutrino lifetimes up to 10^4 s/eV (an improvement of 10^8 over current bounds) and pseudo-Dirac mass splittings to a level of 10^{-18} eV^2 (an improvement of a factor of 10^6 over current bounds) and potentially even measure quantities such as U_{e3} and the phase δ in the Maki–Nakagawa–Sakata–Pontecorvo (MNSP) matrix [2].

3. ASTROPHYSICAL NEUTRINO FLAVOR CONTENT

In the absence of neutrino oscillations, we expect almost no ν_τ content in astrophysical sources. From the most discussed and seemingly the most likely astrophysical high-energy neutrino sources [3], we expect nearly equal numbers of ν_μ and $\bar{\nu}_\mu$, half as many ν_e, and virtually no ν_τ. This comes about simply because the neutrinos are thought to originate in decays of pions (and kaons) and subsequent decays of muons. Most astrophysical targets are tenous even compared to the Earth's atmosphere and would allow for full muon decay in flight. There are some predictions for flavor-independent fluxes from cosmic defects and exotic objects such as evaporating black holes. Observation of tau neutrinos from these would have great importance. A conservative estimate shows that the prompt ν_τ flux is very small and the emitted flux is close to the ratio $1:2:0$. The flux ratio of $\nu_e:\nu_\mu:\nu_\tau = 1:2:0$ is certainly valid for those AGN models in which the neutrinos are produced in beam dumps of photons or protons on matter, in which mostly pion and kaon decay (followed by the decay of muons) supply the bulk of the neutrino flux.

Depending on the amount of prompt ν flux due to the production and decay of heavy flavors, there could be a small nonzero ν_τ component present. There are also possible scenarios in which the muons lose energy in matter or in strong magnetic fields [4], in which case the initial flux mixture becomes $\nu_e:\nu_\mu:\nu_\tau = 0:1:0$.

4. FLAVOR IDENTIFICATION

As we discuss below, flavor identification is crucial for the purpose at hand. Flavors are identified in a water Cherenkov detector as follows. ν_μ are identified by the μ produced by the charged current interactions and the resulting μ tracks in the detector, which are long at these energies. ν_e produce showers by both charged-current and neutral-current interactions. The total rate for showers includes those produced by neutral-current interactions of ν_μ and ν_τ as well, and those have to be (and can be) subtracted off to get the real flux of ν_e. Double-bang and

*This article was submitted by the author in English.

** e-mail: pakvasa@phys.hawaii.edu

lollipop events are signatures unique to tau neutrinos, made possible by the fact that tau leptons decay before they lose a significant faction of their energy. Double-bang events consist of a hadronic shower initiated by a charged-current interaction of the ν_τ followed by a second energetic shower (hadronic or electromagnetic) from the decay of the resulting tau lepton [5]. Lollipop events consist of the second of the double-bang showers along with the reconstructed tau-lepton track (the first bang may be detected or not). In principle, with a sufficient number of events, a fairly good estimate of the flavor ratio $\nu_e : \nu_\mu : \nu_\tau$ can be reconstructed, as has been discussed recently.

5. EFFECT OF OSCILLATIONS

The current knowledge of neutrino masses and mixings can be summarized as follows [6]. The mixing matrix is given to a good approximation by

$$U = \begin{pmatrix} c & -s & \epsilon \\ s/\sqrt{2} & c/\sqrt{2} & -1/\sqrt{2} \\ s/\sqrt{2} & c/\sqrt{2} & 1/\sqrt{2} \end{pmatrix}, \qquad (1)$$

where $c = \cos\theta$ and $s = \sin\theta$ with θ being the solar mixing angle given at about 30°, and $\epsilon = U_{e3} < 0.17$ limited by the CHOOZ bound. The mass spectrum has two possibilities, normal or inverted, with the mass differences given by $\delta m^2_{32} \sim \delta m^2_{\rm atm} \sim 3 \times 10^{-3}\ {\rm eV}^2$ and $\delta m^2_{21} \sim 7 \times 10^{-5}\ {\rm eV}^2$. Since $\delta m^2 L/4E$ for the distances to GRBs and AGNs (even for energies up to and beyond PeV) is very large ($>10^7$), the oscillations have always averaged out and the conversion and survival probabilities are given by

$$P_{\alpha\beta} = \sum_i |U_{\alpha i}|^2 |U_{\beta i}|^2, \qquad (2)$$

$$P_{\alpha\alpha} = \sum_i |U_{\alpha i}|^4. \qquad (3)$$

Assuming no significant matter effects en route, the mixing matrix in (1) leads to a propagation matrix P, given by

$$P = \begin{pmatrix} 1 - S/2 & S/4 & S/4 \\ S/4 & 1/2 - S/8 & 1/2 - S/8 \\ S/4 & 1/2 - S/8 & 1/2 - S/8 \end{pmatrix}, \qquad (4)$$

where S stands for $\sin^2(2\theta)$. As is obvious, for any value of the solar mixing angle, P converts a flux ratio of $\nu_e : \nu_\mu : \nu_\tau = 1 : 2 : 0$ into one of $1 : 1 : 1$. Hence, the flavor mix expected at arrival is simply an equal mixture of ν_e, ν_μ, and ν_τ, as was observed long ago [5, 7]. An initial flavor mix of $\nu_e : \nu_\mu : \nu_\tau = 0 : 1 : 0$ is converted by oscillations into one of $1/2 : 1 : 1$ for a solar angle corresponding to an S of 3/4. There are several other ways, arising from intrinsic properties of neutrinos, by which the flavor mix can change from the canonical $1 : 1 : 1$ figure. One, in particular, which gives rise to striking signatures, is the decay of neutrinos [8]. Before discussing these, let me motivate the possibility of neutrino decay.

6. NEUTRINO DECAY [9]

We now know that neutrinos have nonzero masses and nontrivial mixings. This is based primarily on the evidence for neutrino mixings and oscillations from the data on atmospheric neutrinos and on solar neutrinos. If this is true, then, in general, the heavier neutrinos are expected to decay into the lighter ones via flavor-changing processes. The only questions are (a) whether the lifetimes are short enough to be phenomenologically interesting (or are they too long?) and (b) what the dominant decay modes are.

Throughout the following discussion, to be specific, I will assume that the neutrino masses are at most of the order of a few eV. Since we are interested in decay modes that are likely to have rates (or lead to lifetimes) which are phenomenologically interesting, we can rule out several classes of decay nodes. First, consider radiative decays, such as $\nu_i \to \nu_j + \gamma$. Since the experimental bounds on μ_{ν_i}, the magnetic moments of neutrinos, come from reactions such as $\nu_e e \to e"\nu,"$ which are not sensitive to the final-state neutrinos, the bounds apply to both diagonal and transition magnetic moments and so can be used to limit the corresponding lifetimes. The bounds should really be on mass eigenstates [10], but since the mixing angles are large, it does not matter much. The current bounds are [11]

$$\begin{aligned} \tau_{\nu_e} &> 5 \times 10^{18}\ {\rm s}, \\ \tau_{\nu_\mu} &> 5 \times 10^{16}\ {\rm s}, \\ \tau_{\nu_\tau} &> 2 \times 10^{11}\ {\rm s}. \end{aligned} \qquad (5)$$

There is one caveat in deducing these bounds. Namely, the form factors are evaluated at $q^2 \sim O({\rm eV}^2)$ in the decay matrix elements, whereas, in the scattering from which the bounds are derived, they are evaluated at $q^2 \sim O({\rm MeV}^2)$. Thus, some extrapolation is necessary. It can be argued that, barring some bizarre behavior, this is justified [12].

An invisible decay mode with no new particles is the three-body decay $\nu_i \to \nu_j \nu_j \bar{\nu}_j$. Even at the full strength of Z coupling, this yields a lifetime of 2×10^{34} s, far too long to be of interest. There is an

indirect bound from Z decays which is weaker but still yields 2×10^{30} s [13].

Thus, the only decay modes which can have interestingly fast decays rates are two-body modes such as $\nu_i \to \nu_j + x$ and $\nu_i \to \bar{\nu}_j + x$, where x is a very light or massless particle, e.g., a Majoron.

The only possibility for fast invisible decays of neutrinos seems to lie with Majoron models [9]. There are two classes of models: the $I = 1$ Gelmini–Roncadelli [14] Majoron and the $I = 0$ Chikasige–Mohapatra–Peccei [15] Majoron. In general, one can choose the Majoron to be a mixture of the two; furthermore, the coupling can be to flavor as well as sterile neutrinos. The effective interaction is of the form

$$g_\alpha \bar{\nu}^c_\beta \nu_\alpha J, \tag{6}$$

giving rise to decay

$$\nu_\alpha \to \bar{\nu}_\beta (\text{or } \nu_\beta) + J, \tag{7}$$

where J is a massless $J = 0$, $L = 2$ particle, and ν_α and ν_β are mass eigenstates which may be mixtures of flavor and sterile neutrinos. Models of this kind which can give rise to fast neutrino decays and satisfy the bounds below have been discussed [16]. These models are unconstrained by μ and τ decays, which do not arise due to the $\Delta L = 2$ nature of the coupling. The $I = 1$ coupling is constrained by the bound on the invisible Z width; and requires that the Majoron be a mixture of $I = 1$ and $I = 0$ [17]. The couplings of ν_μ and ν_e (g_μ and g_e) are constrained by the limits on multibody π, K decays $\pi \to \mu\nu\nu\nu$ and $K \to \mu\nu\nu\nu$ and on μ–e university violation in π and K decays [18], but not sufficiently strongly to rule out fast decays. Direct limits on such decay modes are also very weak. The current strongest bound comes from solar neutrino results and are of order of $\tau/m \geq 10^{-4}$ s/eV [19]. This limit is based primarily on the nondistortion of the Super-Kamiokande spectrum [20] and takes into account the potentially competing distortion caused by oscillations (see also [21]) as well as the appearance of active daughter neutrinos. The SN 1987A data place no limit at all on these neutrino decay modes, since decay of the lightest mass eigenstate is kinematically forbidden, and with the inherent uncertainties in the neutrino fluxes, even a reasonable $\bar{\nu}_1$ flux alone can account for the data [22]. The strongest lifetime limit is thus too weak to eliminate the possibility of astrophysical neutrino decay by a factor about $10^7 \times (L/100 \text{ Mpc}) \times (10 \text{ TeV}/E)$. Some aspects of the decay of high-energy astrophysical neutrinos have been considered in the past. It has been noted that the disappearance of all states except ν_1 would prepare a beam that could in principle be used to measure elements of the neutrino mixing matrix, namely, the ratios $U^2_{e1} : U^2_{\mu 1} : U^2_{\tau 1}$ [23]. The possibility of measuring neutrino lifetimes over long baselines was mentioned in [24], and some predictions for decay in four-neutrino models were given in [25]. We have shown that the particular values and small uncertainties on the neutrino mixing parameters allow for the first time very distinctive signatures of the effects of neutrino decay on the detected flavor ratios. The expected increase in neutrino lifetime sensitivity (and corresponding anomalous neutrino couplings) by several orders of magnitude makes for a very interesting test of physics beyond the Standard Model; a discovery would mean physics much more exotic than neutrino mass and mixing alone. As shown below, neutrino decay because of its unique signature cannot be mimicked by either different neutrino flavor ratios at the source or other nonstandard neutrino interactions.

A characteristic feature of decay is its strong energy dependence: $\exp(-Lm/E\tau)$, where τ is the rest-frame lifetime. For simplicity, we will assume that decays are always complete, i.e., that these exponential factors vanish. The assumption of complete decay means that we do not have to consider the distance and intensity distributions of sources. We assume an isotropic diffuse flux of high-energy astrophysical neutrinos and can thus neglect the angular deflection of daughter neutrinos from the trajectories of their parents [26].

Disappearance only. Consider the case of no detectable decay products—that is, the neutrinos simply disappear. This limit is interesting for decay to "invisible" daughters, such as a sterile neutrino, and also for decay to active daughters if the source spectrum falls sufficiently steeply with energy. In the latter case, the flux of daughters of degraded energy will make a negligible contribution to the total flux at a given energy. Since coherence will be lost, we have

$$\phi_{\nu_\alpha} = \sum_{i\beta} \phi^{\text{source}}_{\nu_\beta}(E) |U_{\beta i}|^2 |U_{\alpha i}|^2 e^{-L/\tau_i(E)} \tag{8}$$
$$\overset{L \gg \tau_i}{\longrightarrow} \sum_{i(\text{stable}),\beta} \phi^{\text{source}}_{\nu_\beta}(E) |U_{\beta i}|^2 |U_{\alpha i}|^2,$$

where the ϕ_{ν_α} are the fluxes of ν_α, $U_{\alpha i}$ are elements of the neutrino mixing matrix, and τ are the neutrino lifetimes in the laboratory frame. Equations (5) correspond to the case where decay is complete by the time the neutrinos reach us, so only the stable states are included in the sum.

The simplest case (and the most generic expectation) is a normal hierarchy in which both ν_3 and ν_2 decay, leaving only the lightest stable eigenstate ν_1. In this case, the flavor ratio is $U^2_{e1} : U^2_{\mu 1} : U^2_{\tau 1}$ [23]. Thus, if $U_{e3} = 0$,

$$\phi_{\nu_e} : \phi_{\nu_\mu} : \phi_{\nu_\tau} \tag{9}$$

$$= \cos^2\theta_\odot : \frac{1}{2}\sin^2\theta_\odot : \frac{1}{2}\sin^2\theta_\odot \simeq 6:1:1,$$

where $\theta_\odot$ is the solar neutrino mixing angle, which we have set to 30° [6]. Note that this is an extreme deviation of the flavor ratio from that in the absence of decays. It is difficult to imagine other mechanisms that would lead to such a high ratio of ν_e to ν_μ. In the case of inverted hierarchy, ν_3 is the lightest and hence stable state, and so [6]

$$\phi_{\nu_e} : \phi_{\nu_\mu} : \phi_{\nu_\tau} = U_{e3}^2 : U_{\mu 3}^2 : U_{\tau 3}^2 = 0:1:1. \quad (10)$$

If $U_{e3} = 0$ and $\theta_{\rm atm} = 45°$, each mass eigenstate has equal ν_μ and ν_τ components. Therefore, decay cannot break the equality between the ϕ_{ν_μ} and ϕ_{ν_τ} fluxes, and thus the $\phi_{\nu_e} : \phi_{\nu_\mu}$ ratio contains all the useful information. The effect of a nonzero U_{e3} on the no-decay case of $1:1:1$ is negligible.

When U_{e3} is not zero and the hierarchy is normal, it is possible to obtain information on the values of U_{e3} as well as the CP-violating (CPV) phase δ [27]. The flavor ratio e/μ varies from 6 to 15 (as U_{e3} goes from 0 to 0.2) for $\cos\delta = +1$ but from 6 to 3 for $\cos\delta = -1$. The ratio τ/μ varies from 1 to 5 ($\cos\delta = +1$) or 1 to 0.2 ($\cos\delta = -1$) for the same range of U_{e3}. If the decays are not complete and if the daughter does not carry the full energy of the parent neutrino, the resulting flavor mix is somewhat different, but any case it is still quite distinct from the simple $1:1:1$ mix [6].

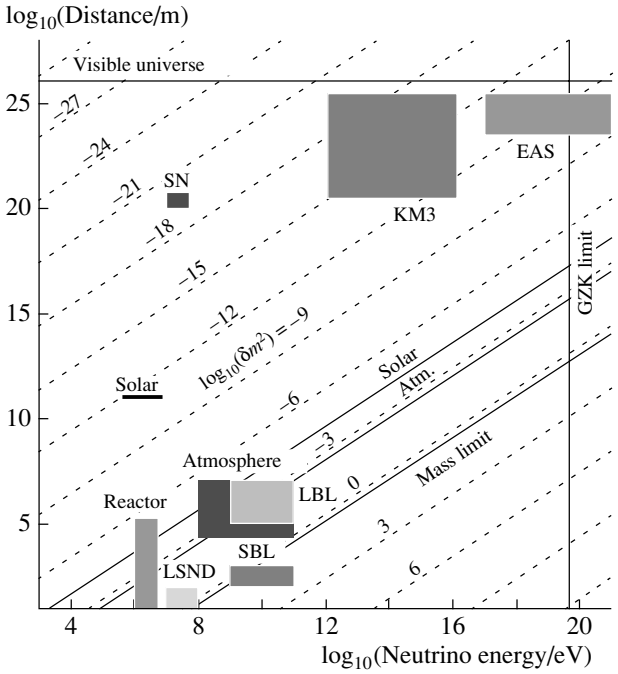

The ranges of distance and energy covered in various neutrino experiments. The diagonal lines indicate the mass-squared differences (in eV^2) that can be probed with vacuum oscillations; at a given L/E, larger δm^2 values can be probed by averaged-out oscillations. We focus on a neutrino telescope of 1-km scale (denoted "KM3"), or larger, if necessary. (From [28].)

7. PSEUDO-DIRAC NEUTRINOS WITH VERY SMALL MASS DIFFERENCES [28]

If each of the three neutrino mass eigenstates is actually a doublet with very small mass difference (smaller than 10^{-6} eV), then there are no current experiments that could have detected this. Such a possibility was raised here in Dubna by Bilenky and Pontecorvo in 1982 [29]. It turns out that the only way to detect such small mass differences ($10^{-12} > \delta m^2 > 10^{-18}$ eV^2) is by measuring flavor mixes of the high-energy neutrinos from cosmic sources (see figure).

Let $(\nu_1^+, \nu_2^+, \nu_3^+; \nu_1^-, \nu_2^-, \nu_3^-)$ denote the six mass eigenstates where ν^+ and ν^- are a nearly degenerate pair. A 6×6 mixing matrix rotates the mass basis into the flavor basis $(\nu_e, \nu_\mu, \nu_\tau; \nu'_e, \nu'_\mu, \nu'_\tau)$. In general, for six Majorana neutrinos, there would be 15 rotation angles and 15 phases. However, for pseudo-Dirac neutrinos, Kobayashi and Lim [30] have given an elegant proof that the 6×6 matrix $V_{\rm KL}$ takes the very simple form (to lowest order in $\delta m^2/m^2$)

$$V_{\rm KL} = \begin{pmatrix} U & 0 \\ 0 & U_R \end{pmatrix} \begin{pmatrix} V_1 & iV_1 \\ V_2 & -iV_2 \end{pmatrix}, \quad (11)$$

where the 3×3 matrix U is just the usual mixing matrix determined by the atmospheric and solar observations; the 3×3 matrix U_R is an unknown unitary matrix; and V_1 and V_2 are the diagonal matrices $V_1 = \mathrm{diag}(1,1,1)/\sqrt{2}$ and $V_2 = \mathrm{diag}(e^{-i\phi_1}, e^{-i\phi_2}, e^{-i\phi_3})/\sqrt{2}$, with the ϕ_i being arbitrary phases.

As a result, the three active neutrino states are described in terms of the six mass eigenstates as

$$\nu_{\alpha L} = U_{\alpha j}\frac{1}{\sqrt{2}}\left(\nu_j^+ + i\nu_j^-\right). \quad (12)$$

The nontrivial matrices U_R and V_2 are not accessible to active flavor measurements. The flavor conversion probability can thus be expressed as

$$P_{\alpha\beta} \quad (13)$$
$$= \frac{1}{4}\left|\sum_{j=1}^{3} U_{\alpha j}\left\{e^{i(m_j^+)^2 L/2E} + e^{i(m_j^-)^2 L/2E}\right\} U_{\beta j}^*\right|^2.$$

The flavor-conserving probability is also given by this formula, with $\beta = \alpha$. Hence, in the description of the three active neutrinos, the only new parameters are the three pseudo-Dirac mass differences, $\delta m_j^2 =$

Flavor ratios $\nu_e : \nu_\mu$ for various scenarios (The numbers j under the arrows denote the pseudo-Dirac splittings, δm_j^2, which become accessible as L/E increases. Oscillation averaging is assumed after each transition j. We have used $\theta_{\rm atm} = 45°$, $\theta_\odot = 30°$, and $U_{e3} = 0$.)

1 : 1	$\overrightarrow{3}$	4/3 : 1	$\overrightarrow{2,3}$	14/9 : 1	$\overrightarrow{1,2,3}$	1 : 1
1 : 1	$\overrightarrow{1}$	2/3 : 1	$\overrightarrow{1,2}$	2/3 : 1	$\overrightarrow{1,2,3}$	1 : 1
1 : 1	$\overrightarrow{2}$	14/13 : 1	$\overrightarrow{2,3}$	14/9 : 1	$\overrightarrow{1,2,3}$	1 : 1
1 : 1	$\overrightarrow{1}$	2/3 : 1	$\overrightarrow{1,3}$	10/11 : 1	$\overrightarrow{1,2,3}$	1 : 1
1 : 1	$\overrightarrow{3}$	4/3 : 1	$\overrightarrow{1,3}$	10/11 : 1	$\overrightarrow{1,2,3}$	1 : 1
1 : 1	$\overrightarrow{2}$	14/13 : 1	$\overrightarrow{1,2}$	2/3 : 1	$\overrightarrow{1,2,3}$	1 : 1

$(m_j^+)^2 - (m_j^-)^2$. In the limit that they are negligible, the oscillation formulas reduce to the standard ones and there is no way to discern the pseudo-Dirac nature of the neutrinos.

***L/E*-dependent flavor ratios.** Given the enormous path length between astrophysical neutrino sources and the Earth, the phases due to the relatively large solar and atmospheric mass-squared differences will average out (or equivalently, decohere). The probability for a neutrino telescope to measure the flavor ν_β is then

$$P_\beta = \sum_\alpha w_\alpha \sum_{j=1}^{3} |U_{\alpha j}|^2 |U_{\beta j}|^2 \left[1 - \sin^2\left(\frac{\delta m_j^2 L}{4E}\right)\right], \tag{14}$$

where w_α represents the fraction of the flavor α present initially. In the limit that $\delta m_j^2 \to 0$, Eq. (14) reproduces the standard expressions. The new oscillation terms are negligible until E/L becomes as small as the tiny pseudo-Dirac mass-squared splittings δm_j^2.

The flavors deviate from the democratic 1/3 value by

$$\delta P_e = -\frac{1}{3}\left[\frac{3}{4}\chi_1 + \frac{1}{4}\chi_2\right], \tag{15}$$

$$\delta P_\mu = \delta P_\tau = -\frac{1}{3}\left[\frac{1}{8}\chi_1 + \frac{3}{8}\chi_2 + \frac{1}{2}\chi_3\right],$$

where $\chi_i = \sin^2(\delta m_i^2 L/4E)$.

The table shows how the $\nu_e : \nu_\mu$ ratio is altered if we cross the threshold for one, two, or all three of the pseudo-Dirac oscillations. The flavor ratios deviate from 1 : 1 when one or two of the pseudo-Dirac oscillation modes is accessible. In the ultimate limit where L/E is so large that all three oscillating factors have averaged to 1/2, the flavor ratios return to 1 : 1, with only a net suppression of the measurable flux, by a factor of 1/2.

8. COSMOLOGY WITH NEUTRINOS

We know from supernova studies that there are several effects of neutrino masses and mixings on the observation of neutrino bursts. A pulse spreads in time due to dispersion of velocities (from nonzero mass); a pulse separates into several pulses due to a neutrino of a given flavor being a mixture of different mass eigenstates and the original flavor composition can change due to mixing and oscillations. One can apply these considerations to neutrino pulses from sources which are at cosmological distances. Then the effects come to depend on cosmological parameters.

For example, the time difference [31] between two mass eigenstates which left at the same time is given by

$$\Delta t \approx z/H \left[1 - \frac{(3+q_0)}{2} z \ldots\right] \frac{1}{2}\left[\frac{m_1^2}{E_1^2} - \frac{m_2^2}{E_2^2}\right], \tag{16}$$

where E_i are the energies observed at Earth and z, H, and q have the usual meanings. The spreading of a pulse of a given mass neutrino is given by

$$\Delta t \approx z/H \left[1 - \frac{(3+q_0)}{2} z \ldots\right] \frac{1}{2} m^2 \left\{\frac{1}{E_1^2} - \frac{1}{E_2^2}\right\}. \tag{17}$$

Finally, the conversion probability for an emitted flavor α to become β at detection is given by

$$P_{\alpha\beta} = \sin^2(2\theta)\sin^2(\phi/2), \tag{18}$$

where the phase ϕ is [24]

$$\phi \cong z/H \left[1 - \frac{(3+q_0)}{2} z \ldots\right] \frac{\delta m^2}{2E}. \tag{19}$$

The basic flight time factors are rather small; for eV neutrino masses and GeV energies, $\Delta t \sim 50$ ms at 1000 MPc. These time spreads and separation may be shorter than the times involved in the production process, thus making them difficult to observe. With the flavor mix of the incoming beam determined as discussed above, $P_{\alpha\beta}$ and hence the phase ϕ can be deduced by comparison with expected initial relative fluxes. Provided the phase $\phi/2$ is not too large (and $\sin^2(\phi/2)$ does not average to 1/2), one has sensitivity to the parameters z, q_0, and H.

With such measurements of Δt and ϕ, one can potentially measure these cosmological parameters. This would be the first time that the redshift or other cosmological parameters are measured for anything

other than light. There is another advantage of using neutrinos. This is the fact that the initial flavor mixing only depends on microphysics and so the comparison is free from problems such as evolution or worries about standard candles, etc.

9. EXPERIMENTAL DETECTABILITY

Deviations of the flavor ratios from $1:1:1$ due to possible decays are so extreme that they should be readily identifiable [32]. Upcoming high-energy neutrino telescopes, such as IceCube [33], will not have perfect ability to measure the neutrino flux in each flavor separately. However, the quantities we need are closely related to observables, in particular, in the limit of ν_μ–ν_τ symmetry ($\theta_{\rm atm} = 45^\circ$ and $U_{e3} = 0$), in which all mass eigenstates contain equal fractions of ν_μ and ν_τ. In that limit, the fluxes for ν_μ and ν_τ are always in the ratio $1:1$, with or without decay. This is useful since the ν_τ flux is the hardest to measure.

Detectors such as IceCube will be able to directly measure the ν_μ flux by long-ranging muons which leave tracks through the detector. The charged-current interactions of ν_e produce electromagnetic showers. However, these are hard to distinguish from hadronic showers caused by all flavors through their neutral-current interactions or from the charged-current interactions of ν_τ (an initial hadronic shower followed by either an electromagnetic or a hadronic shower from the tau-lepton decay). We thus consider our only experimental information to be the number of muon tracks and the number of showers.

The relative number of shower events to track events can be related to the most interesting quantity for testing decay scenarios, i.e., the ν_e to ν_μ ratio. The precision of the upcoming experiments should be good enough to test the extreme flavor ratios produced by decays. If electromagnetic and hadronic showers can be separated, then the precision will be even better.

In comparing, for example, the standard flavor ratios of $1:1:1$ to the possible $6:1:1$ generated by decay, the larger electron neutrino flux will result in a substantial increase in the relative number of shower events. The details of this observation depend on the range of muons generated in or around the detector and the ratio of charged to neutral current cross sections. The measurement will be limited by the energy resolution of the detector and the ability to reduce the atmospheric neutrino background. The atmospheric background drops rapidly with energy and should be negligibly small at and above the PeV scale.

10. DISCUSSION AND CONCLUSIONS

The flux ratios we discuss are energy-independent because we have assumed that the ratios at production are energy-independent, that all oscillations are averaged out, and that all possible decays are complete. In the standard scenario with only oscillations, the final flux ratios are $\phi_{\nu_e} : \phi_{\nu_\mu} : \phi_{\nu_\tau} = 1:1:1$. In the cases with decay, we have found rather different possible flux ratios, for example, $6:1:1$ in the normal hierarchy and $0:1:1$ in the inverted hierarchy. These deviations from $1:1:1$ are so extreme that they should be readily measurable.

If we are very fortunate [34], we may be able to observe a reasonable number of events from several sources (of known distance) and/or over a sufficient range in energy. Then the resulting dependence of the flux ratio $\nu_e : \nu_\mu$ on L/E as it evolves from, say, 6 (or 0) to 1 can be clear evidence of decay and further can pin down the actual lifetime instead of just placing a bound.

To summarize, we suggest that, if future measurements of the flavor mix at the Earth of high energy astrophysical neutrinos find it to be

$$\phi_{\nu_e} : \phi_{\nu_\mu} : \phi_{\nu_\tau} = \alpha : 1 : 1, \qquad (20)$$

then

(i) $\alpha = 1$ (the most boring case) confirms our knowledge of the MNSP [2] matrix and our prejudice about production mechanism;

(ii) $\alpha \approx 1/2$ indicates that the source emits pure ν_μ and the mixing is conventional;

(iii) $\alpha > 1$ indicates that neutrinos decay with normal hierarchy;

(iv) $\alpha \ll 1$ would mean that neutrino decays occur with inverted hierarchy;

(v) values of α which cover a broader range (3 to 15) and deviation of the μ/τ ratio from 1 (between 0.2 to 5) can yield valuable information about U_{e3} and $\cos\delta$. Deviations of α which are less extreme (between 0.7 and 1.5) can also probe very small pseudo-Dirac δm^2 (smaller than 10^{-12} eV^2).

Incidentally, in the last three cases, the results have absolutely no dependence on the initial flavor mix and so are completely free of any dependence on the production model. Thus, either one learns about the production mechanism and the initial flavor mix, as in the first two cases, or one learns only about the neutrino properties, as in the last three cases. In any case, it should be evident that the construction of very large neutrino detectors is a "no-lose" proposition.

ACKNOWLEDGMENTS

This talk is based on published and ongoing work in collaboration with John Beacom, Nicole Bell, Dan Hooper, John Learned, and Tom Weiler. I thank them for a most enjoyable collaboration. I also thank Vera Kovalenko, Vadim Bednyakov, and their colleagues for outstanding hospitality in Dubna.

This work was supported in part by the USDOE under grant no. DE-FG03-94ER40833.

REFERENCES

1. S. Pakvasa, in *Proceedings of the 9th International Symposium on Neutrino Telescopes, Venice, Italy, 2001*, Ed. by M. Baldo-Ceolin, Vol. 2, p. 603; hep-ph/0105127.
2. Z. Maki, M. Nakagawa, and S. Sakata, Prog. Theor. Phys. **28**, 870 (1962); V. Gribov and B. Pontecorvo, Phys. Lett. B **28B**, 493 (1969); the generalization to three flavors first appeared in B. W. Lee, S. Pakvasa, R. E. Shrock, and H. Sugawara, Phys. Rev. Lett. **38**, 937 (1977).
3. J. G. Learned and K. Mannheim, Annu. Rev. Nucl. Part. Sci. **50**, 603 (2000) and references therein.
4. J. P. Rachen and P. Mészáros, Phys. Rev. D **58**, 123005 (1998); astro-ph/9802280.
5. J. G. Learned and S. Pakvasa, Astropart. Phys. **3**, 267 (1995).
6. S. Pakvasa and J. W. F. Valle, hep-ph/0301061.
7. H. Athar, M. Jezabek, and O. Yasuda, Phys. Rev. D **62**, 103007 (2000); hep-ph/0005104; L. Bento, P. Keränen, and J. Maalampi, Phys. Lett. B **476**, 205 (2000); hep-ph/9912240.
8. J. F. Beacom, N. Bell, D. Hooper, *et al.*, Phys. Rev. Lett. **90**, 181301 (2003); hep-ph/0211305.
9. S. Pakvasa, AIP Conf. Proc. **542**, 99 (2000); hep-ph/0004077.
10. J. F. Beacom and P. Vogel, Phys. Rev. Lett. **83**, 5222 (1999); hep-ph/9907383.
11. These are deduced in [9] from the current bounds on the magnetic moments: Review of Particle Properties, Particle Data Group (C. Caso *et al.*), Eur. Phys. J. C **3**, 1 (1998).
12. J-M. Frère, R. B. Nevzorov, and M. I. Vysotsky, Phys. Lett. B **394**, 127 (1997); hep-ph/9608266.
13. M. Bilenky, S. M. Bilenky, and A. Santamaria, Phys. Lett. B **301**, 287 (1993).
14. G. B. Gelmini and M. Roncadelli, Phys. Lett. B **99B**, 411 (1981).
15. Y. Chikasige, R. Mohapatra, and R. Peccei, Phys. Rev. Lett. **45**, 1926 (1980).
16. J. W. F. Valle, Phys. Lett. B **131B**, 87 (1983); G. B. Gelmini and J. W. F. Valle, Phys. Lett. B **142B**, 181 (1984); A. S. Joshipura and S. D. Rindani, Phys. Rev. D **46**, 3008 (1992); A. Acker, A. Joshipura, and S. Pakvasa, Phys. Lett. B **285**, 371 (1992); A. Acker, S. Pakvasa, and J. Pantaleone, Phys. Rev. D **45**, R1 (1992).
17. K. Choi and A. Santamaria, Phys. Lett. B **267**, 504 (1991).
18. V. Barger, W. Y. Keung, and S. Pakvasa, Phys. Rev. D **25**, 907 (1982).
19. J. F. Beacom and N. F. Bell, Phys. Rev. D **65**, 113009 (2002); hep-ph/0204111.
20. S. Fukuda *et al.*, Phys. Rev. Lett. **86**, 5656 (2001); hep-ex/0103033.
21. A. Bandyopadhyay, S. Choubey, and S. Goswami, Phys. Lett. B **555**, 33 (2003); hep-ph/0204173; A. S. Joshipura, E. Massó, and S. Mohanty, Phys. Rev. D **66**, 113008 (2002); hep-ph/0203181.
22. J. A. Frieman, H. E. Haber, and K. Freese, Phys. Lett. B **200**, 115 (1988).
23. S. Pakvasa, Lett. Nuovo Cimento **31**, 497 (1981); Y. Farzan and A. Yu. Smirnov, Phys. Rev. D **65**, 113001 (2002); hep-ph/0201105.
24. T. J. Weiler, W. A. Simmons, S. Pakvasa, and J. G. Learned, hep-ph/9411432.
25. P. Keränen, J. Maalampi, and J. T. Peltoniemi, Phys. Lett. B **461**, 230 (1999); hep-ph/9901403.
26. M. Lindner, T. Ohlsson, and W. Winter, Nucl. Phys. B **607**, 326 (2001); **622**, 429 (2002); astro-ph/0105309.
27. J. F. Beacom, N. Bell, D. Hooper, *et al.*, hep-ph/0309267.
28. J. F. Beacom, N. Bell, D. Hooper, *et al.*, hep-ph/0307151.
29. S. M. Bilen'kii and B. B. Pontecorvo, Sov. J. Nucl. Phys. **38**, 248 (1983); L. Wolfenstein, Nucl. Phys. B **186**, 147 (1981); S. T. Petcov, Phys. Lett. B **110B**, 245 (1982).
30. M. Kobayashi and C. S. Lim, Phys. Rev. D **64**, 013003 (2001); hep-ph/0012266.
31. L. Stodolsky, Phys. Lett. B **473**, 61 (2000); astro-ph/9911167.
32. J. F. Beacom, N. Bell, D. Hooper, *et al.*, hep-ph/0307025; F. Halzen and D. Hooper, Rep. Prog. Phys. **65**, 1025 (2002); astro-ph/0204527.
33. A. Karle, astro-ph/0209556; A. Goldschmidt, Nucl. Phys. B (Proc. Suppl.) **110**, 516 (2002).
34. G. Barenboim and C. Quigg, Phys. Rev. D **67**, 073024 (2003); hep-ph/0301220.

Physics of Atomic Nuclei, Vol. 67, No. 6, 2004, pp. 1161–1171. From Yadernaya Fizika, Vol. 67, No. 6, 2004, pp. 1186–1194.

NEUTRINO PHYSICS AND ASTROPHYSICS

The Baikal Neutrino Experiment: Status and Beyond*

V. M. Aynutdinov, V. A. Balkanov, I. A. Belolaptikov[1)], L. B. Bezrukov, N. M. Budnev[2)], A. G. Chensky[2)], D. V. Chernov[3)], I. A. Danilchenko, Zh.-A. M. Dzhilkibaev, G. V. Domogatsky, A. N. Dyachok[2)], O. N. Gaponenko, O. A. Gress[2)], T. I. Gress[2)], A. M. Klabukov, A. I. Klimov[4)], S. I. Klimushin, K. V. Konischev[1)], A. P. Koshechkin, V. F. Kulepov[5)], L. A. Kuzmichev[3)], Vy. E. Kuznetzov, B. K. Lubsandorzhiev, S. P. Mikheyev, M. B. Milenin[5)], R. R. Mirgazov[2)], N. I. Moiseiko[3)], E. A. Osipova[3)], A. I. Panfilov, G. L. Pan'kov[2)], L. V. Pan'kov[2)], Yu. V. Parfenov[2)], A. A. Pavlov[2)], E. N. Pliskovsky[1)], P. G. Pokhil, V. A. Polecshuk, E. G. Popova[3)], V. V. Prosin[3)], M. I. Rosanov[6)], V. Yu. Rubtzov[2)], Yu. A. Semeney[2)], B. A. Shaibonov, Ch. Spiering[7)], O. Streicher[7)], B. A. Tarashansky[2)], R. V. Vasiliev[1)], E. A. Vyatchin, R. Wischnewski[7)], I. V. Yashin[3)], and V. A. Zhukov**

Institute for Nuclear Research, Russian Academy of Sciences, Moscow, Russia

Received December 2, 2003

Abstract—The present status of the Baikal Neutrino Experiment and the present results of a search for upward going atmospheric neutrinos, WIMPs, and magnetic monopoles obtained with the NT-200 detector are reviewed. The results of a search for very high-energy neutrinos are presented as well. An upper limit on the $\nu_e + \nu_\mu + \nu_\tau$ neutrino diffuse flux of $E^2\Phi(E) < 1.3 \times 10^{-6}$ cm^{-2} s^{-1} sr^{-1} GeV within a neutrino energy range of 10^4–10^7 GeV is obtained, assuming an E^{-2} behavior of the neutrino spectrum and a flavor ratio $\nu_e : \nu_\mu : \nu_\tau = 1 : 1 : 1$. We also describe the moderate upgrade of the NT-200 planned for the next few years and present a possible detector on the Gigaton scale. © *2004 MAIK "Nauka/Interperiodica".*

1. INTRODUCTION

The Baikal Neutrino Telescope is operated in Lake Baikal, Siberia at a depth of 1.1 km. The present stage of the telescope NT-200 [1] was put into operation on April 6th, 1998, and consists of 192 optical modules (OMs). An umbrella-like frame carries 8 strings, each with 24 pairwise arranged OMs. Three underwater electrical cables and one optical cable connect the detector with the shore station.

The OMs are grouped in pairs along the strings. They contain 37-cm diameter QUASAR photomultipliers (PMs), which were developed specially for this project [2]. The two PMs of a pair are switched in coincidence in order to suppress the background from bioluminescence and PM noise. The pair defines a channel.

A trigger is formed by the requirement of $\geq N$ hits (with hit referring to a channel) within 500 ns; here, N is typically set to a value of three or four. For such events, the amplitude and the time of all the hit channels are digitized and sent to shore.

Lake Baikal's deep water is characterized by an absorption length of $L_{\rm abs}(480\ {\rm nm}) = 20$–$24$ m, a scattering length of $L_s = 30$–70 m, and a strongly anisotropic scattering function $f(\theta)$ with a mean cosine of the scattering angle $\overline{\cos}(\theta) = 0.85$–$0.9$.

We are presenting new results including data taken in 1999 (268 live days). The data taken in 2000 are presently being analyzed. We also describe an upgrade of the NT-200 by three sparsely instrumented distant outer strings, which increase the fiducial volume for high-energy cascades to an order of 10 Mt ("NT-200+" telescope). A prototype string of 140-m length with 12 optical modules was deployed

*This article was submitted by the authors in English.

[1)]Joint Institute for Nuclear Research, Dubna, Russia.
[2)]Irkutsk State University, Irkutsk, Russia.
[3)]Skobeltsyn Institute of Nuclear Physics MSU, Moscow, Russia.
[4)]Kurchatov Institute, Moscow, Russia.
[5)]Nizhni Novgorod State Technical University, Nizhni Novgorod, Russia.
[6)]St. Petersburg State Marine University, St. Petersburg, Russia.
[7)]DESY–Zeuthen, Germany.
**e-mail: belolap@nusun.jinr.ru

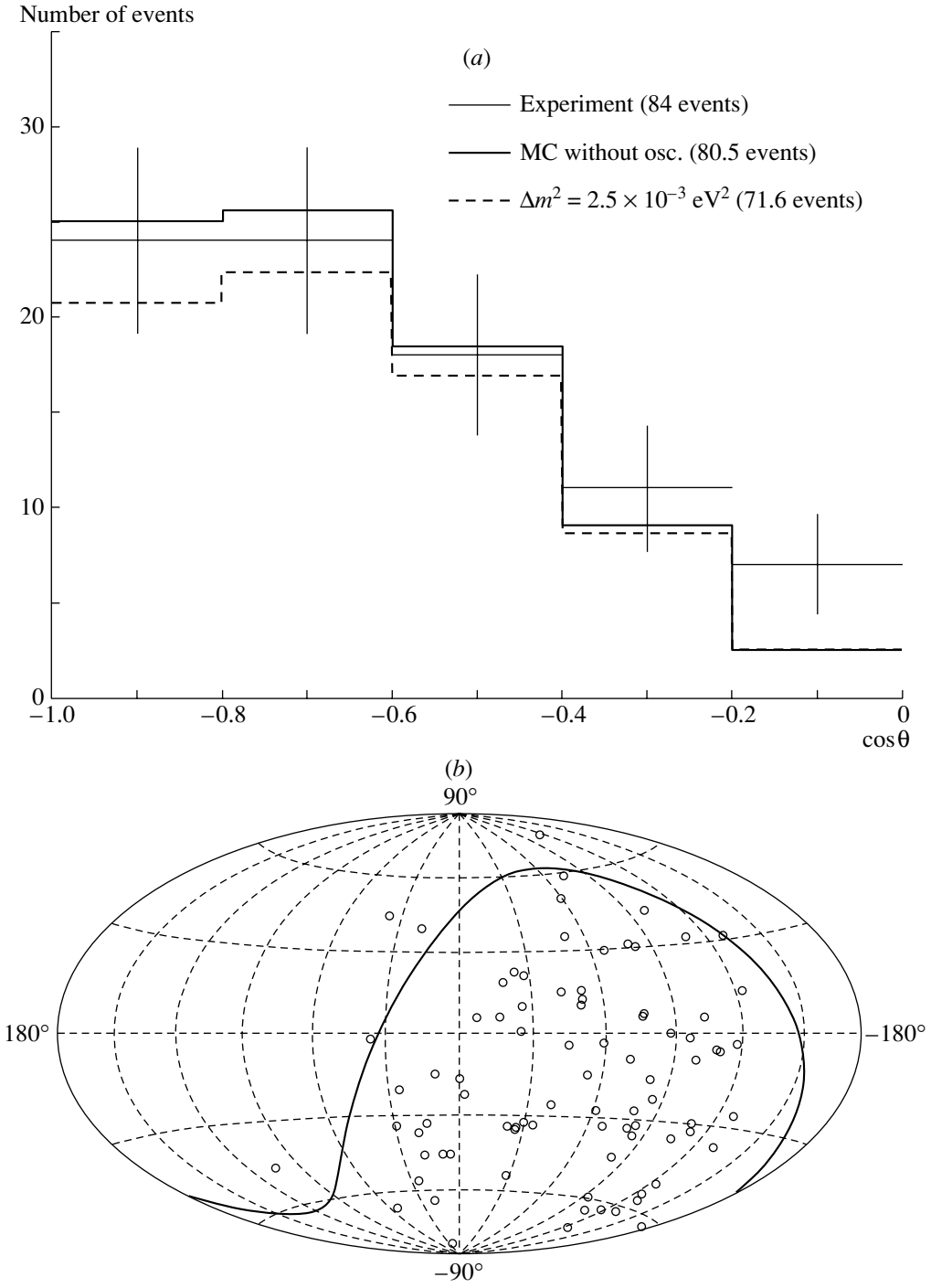

Fig. 1. (*a*) Angular distribution of 1998/1999 experimental events and MC data. (*b*) Skyplot (galactic coordinates) of neutrino events. The solid curve shows the Earth's equator.

in March 2003, and the electronics, data acquisition, and calibration systems for the NT-200+ have been tested.

2. ATMOSPHERIC MUON NEUTRINOS

The clearest signature of neutrino induced events is a muon crossing the detector from below. The track reconstruction algorithms, as well as the background rejection, have been described in [3]. The energy threshold of NT-200 for this particular analysis (15–20 GeV) is much smaller than of AMANDA (∼50 GeV) and makes the detector sensitive to the distortion of the atmospheric neutrino angular spectrum caused by neutrino oscillations. Atmospheric

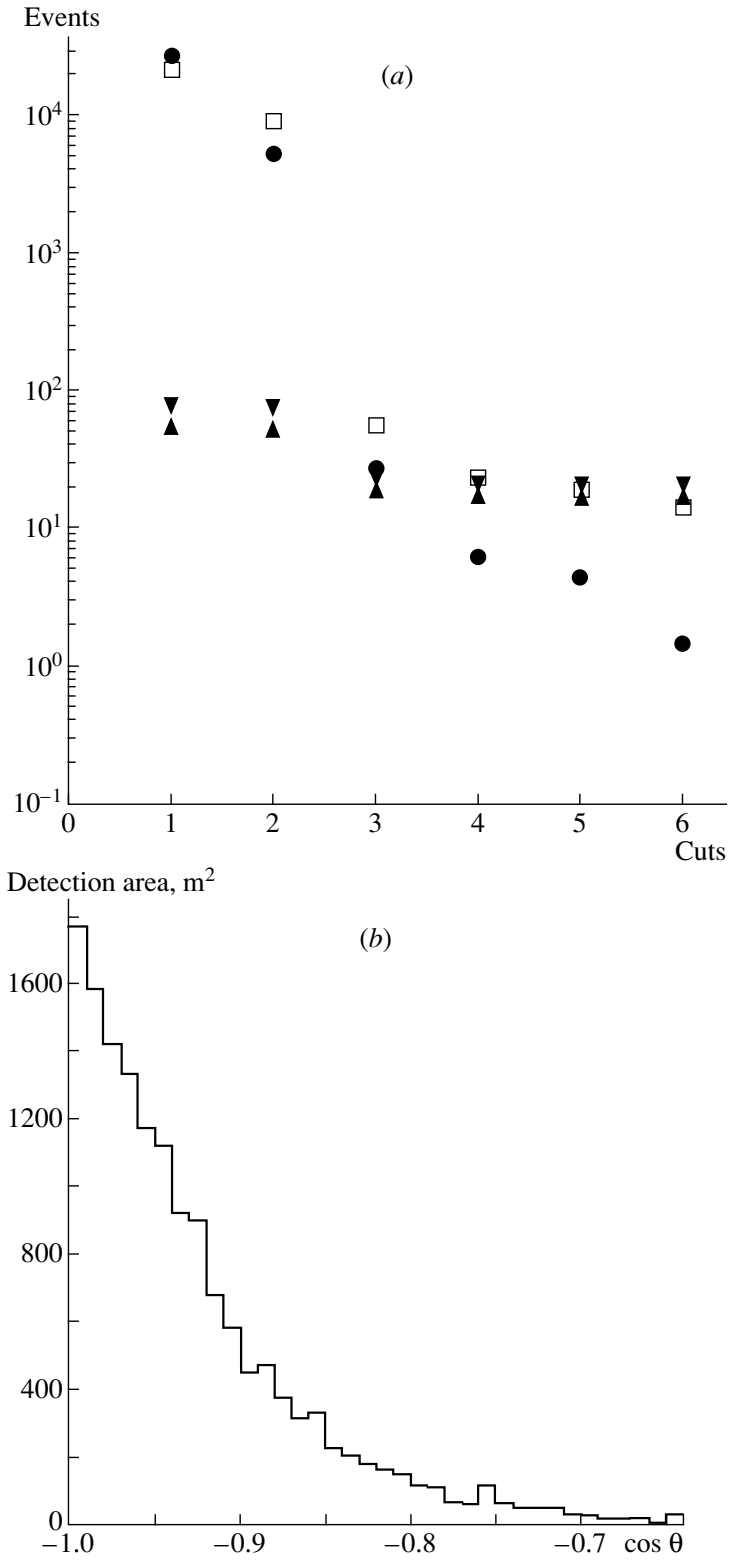

Fig. 2. (*a*) Number of selected events vs. a cut level (squares—experiment, circles—MC background expectation, triangles—MC expected signal due to atmospheric neutrinos: upward triangles—with oscillations, downward triangles—without oscillations). (*b*) Detection area after WIMP cuts as a function of the zenith angle.

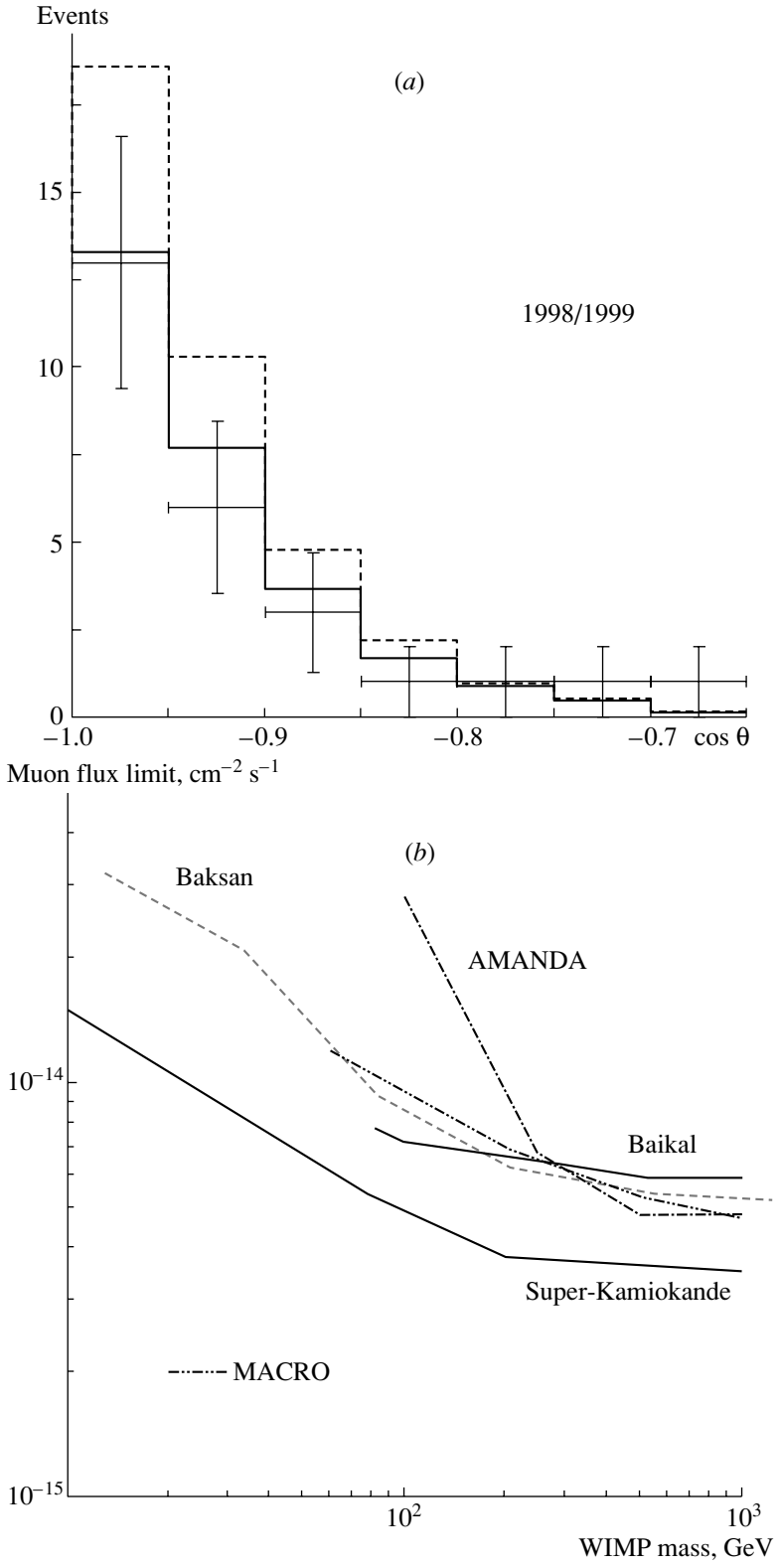

Fig. 3. (*a*) Angular distributions of selected neutrino candidates, as well as expected distributions, in a case with and without oscillations (solid and dashed histograms, respectively). (*b*) Muon flux limits as a function of WIMP mass.

neutrinos serve as an important calibration tool and demonstrate the understanding of the detector performance. The data set of the years 1998 and 1999 yields 84 upward going muons. The MC simulation of upward muon tracks due to atmospheric neutrinos gives 80.5 events. The angular distribution for both the experiment and the simulation, as well as for the skyplot of upward muons, are shown in Fig. 1.

3. SEARCH FOR NEUTRINOS FROM WIMP ANNIHILATION

The search for WIMPs with the Baikal neutrino telescope is based on a possible signal of nearly vertically upward going muons exceeding the flux of atmospheric neutrinos. The method of event selection relies on the application of a series of cuts, which are tailored to the response of the telescope to nearly vertically upward moving muons [3]. The number of the selected events for the 1999 data for the downward going muon background and for the atmospheric neutrino as function of the stepwise tightened cut level is shown in Fig. 2*a*. Figure 2*b* shows the dependence of the detection area on the cosine of the zenith angle θ. The applied cuts select muons with $-1 < \cos\theta < -0.65$ and result in a detection area of about 1800 m^2 for vertically upward going muons.

The energy threshold of muons for this analysis is $E_{\rm thr} \sim 10$ GeV, i.e., significantly lower than for the analysis described in Section 2 ($E_{\rm thr} \sim 15$ GeV). Therefore, the effect of the oscillations has to be strongly visible. We expect a muon event suppression of 25–30% due to neutrino oscillations.

From 502 d of effective data taking between April 1998 and February 2000, 26 events in the specified angular region have been selected as neutrino candidates. The angular distribution of these events is presented in Fig. 3*a*. In the same picture, the expected angular distributions for atmospheric neutrinos (Bartol flux [4]) with oscillations (using Super-Kamiokande parameter set $\Delta m^2 = 2.5 \times 10^{-3}$ eV^2 with full mixing, $\theta_m \approx \pi/4$, [5]) and without oscillations are shown. Within 1σ statistical uncertainties, the experimental angular distribution is consistent with the prediction including neutrino oscillations.

There are two main uncertainties in the counting rate calculations of events due to atmospheric neutrinos: the systematic uncertainties of the atmospheric neutrino flux and uncertainties of calculations of the effective area for upward going events. In the first case this value is about 20% [6]. The good coincidence of the selected event number vs. cut tightness (Fig. 2) for the data and expected rates supports our estimate of an uncertainty of $\leq$10% for the effective area for upward muon tracks.

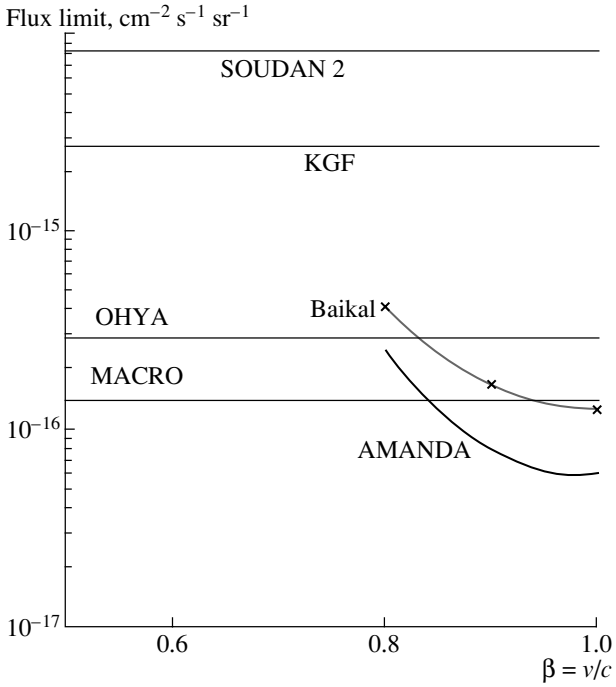

Fig. 4. Upper limits on the flux of fast monopoles obtained in different experiments.

Regarding the 26 detected events as being induced by atmospheric neutrinos and no events by WIMPs, one can derive an upper limit on the flux of muons from the center of the Earth due to annihilation of neutralinos—the favored candidate for cold dark matter.

The 90% C.L. muon flux limits for different neutralino masses obtained with NT-200 ($E_{\rm thr} >$ 10 GeV) in 1998 and 1999 are shown in Fig. 3*b* and compared to limits obtained by Baksan [7], MACRO [8], Super-Kamiokande [9], and AMANDA [10].

4. SEARCH FOR RELATIVISTIC MAGNETIC MONOPOLES

Events due to relativistic monopoles ($\beta > 0.75$) are distinguished by their high light output, allowing identification of events beyond the geometrical boundaries of the detector. The search strategy has been described in [11]. An improved analysis including data from 1996 to 1999 yields a limit about a factor of two below the limit published earlier. This limit is compared to those from other experiments [12–16] in Fig. 4.

5. SEARCH FOR EXTRATERRESTRIAL HIGH-ENERGY NEUTRINOS

The BAIKAL survey for high-energy neutrinos searches for bright cascades produced at the neutrino interaction vertex in a large volume around the

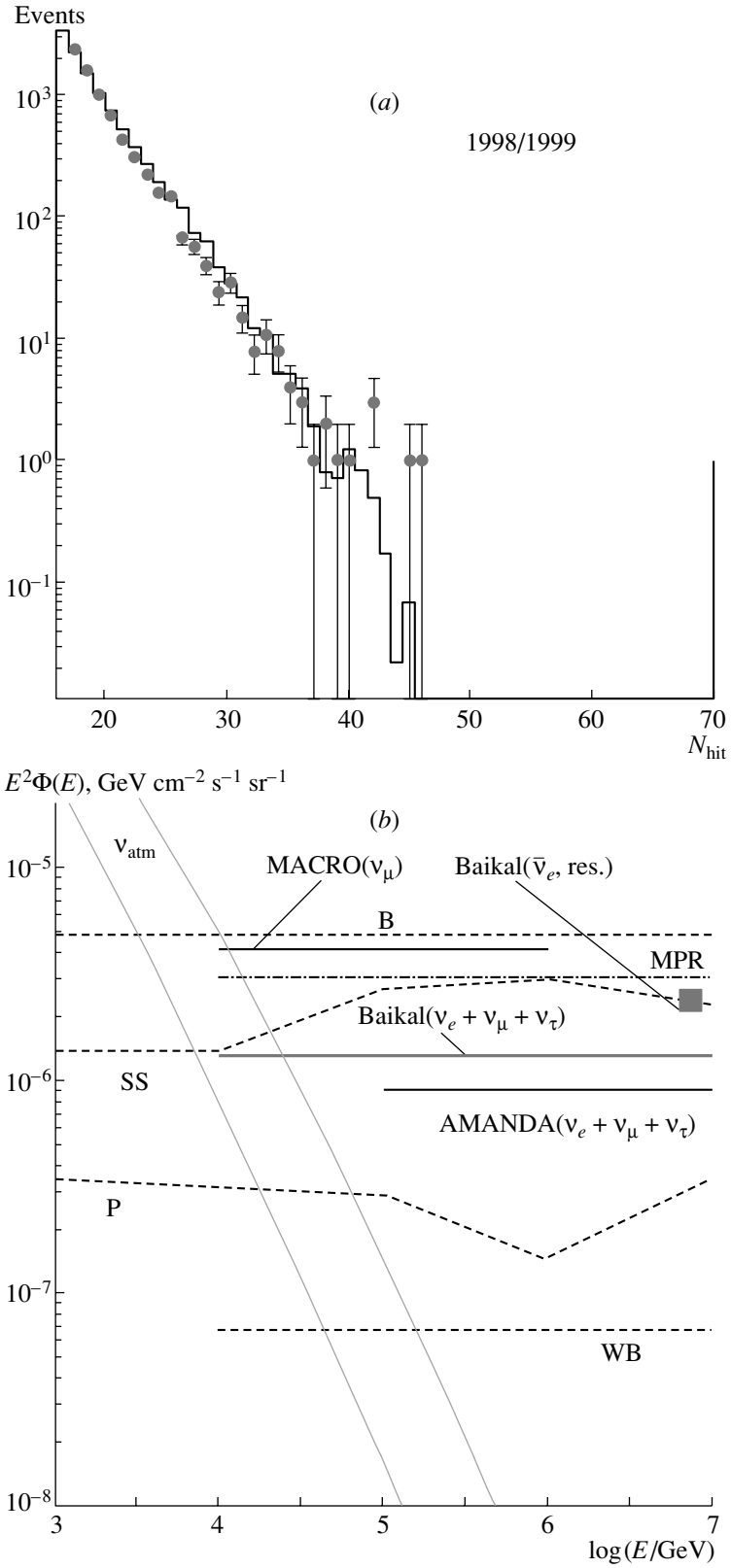

Fig. 5. (*a*) Distribution of hit channel multiplicity; dots are experiment, histogram is an expectation from atmospheric muons. (*b*) Experimental upper limits on the neutrino fluxes as well as flux predictions in different models of neutrino sources (see text).

neutrino telescope. Lack of significant light scattering allows us to monitor a volume exceeding the geometrical volume by an order of magnitude. This results in sensitivities of the NT-200 comparable to those of the much larger AMANDA detector. The background to this search are bright bremsstrahlung flashes along downward muons passing far outside the array. The method has been described in [17, 18]. Results from the data recorded in 1998 (234 live days) have been presented elsewhere [18, 19]. For the analysis of the data recorded in 1999 (268 live days) we used 1.78×10^5 events with hit channel multiplicity $N_{\rm hit} > 10$.

Figure 5*a* shows the $N_{\rm hit}$ distribution for the experiment (dots) as well as the one expected for the background from atmospheric muons (histogram). The experimental distribution is consistent with the background expectation. No statistically significant excess over the background expectation from atmospheric muons has been observed. Since no events with $N_{\rm hit} > 46$ are found in our data, we can derive upper limits on the flux of high energy neutrinos that would produce events with $N_{\rm hit} > 50$.

The detection volume $V_{\rm eff}$ for neutrino produced events with $N_{\rm hit} > 50$ that fulfill all trigger conditions was calculated as a function of neutrino energy and zenith angle θ. $V_{\rm eff}$ rises from $2{\times}10^5$ m^3 for 10 TeV up to 6×10^6 m^3 for 10^4 TeV and significantly exceeds the geometrical volume $V_g \approx 10^5$ m^3 of NT-200. Given an E^{-2} behavior of the neutrino spectrum and a flavor ratio $\nu_e : \nu_\mu : \nu_\tau = 1 : 1 : 1$, the combined 90% C.L. upper limit obtained with the Baikal neutrino telescope NT-200 (502 d) is about twice below previous results [19]:

$$E^2\Phi_{\nu_e+\nu_\mu+\nu_\tau} < 1.3 \times 10^{-6}\ \text{cm}^{-2}\ \text{s}^{-1}\ \text{sr}^{-1}\ \text{GeV}. \quad (1)$$

The model independent limit on $\bar{\nu}_e$ at W-resonance energy is

$$\Phi_{\bar{\nu}_e} \leq 5.4 \times 10^{-20}\ \text{cm}^{-2}\ \text{s}^{-1}\ \text{sr}^{-1}\ \text{GeV}^{-1}. \quad (2)$$

Figure 5*b* shows our upper limits and the limits obtained by other experiments [20, 21] as well as theoretical limits obtained by Berezinsky (B) [22], by Waxman and Bahcall (WB) [23], by Mannheim *et al.* (MPR) [24], and predictions for neutrino fluxes from Stecker and Salamon (SS) [25] and Protheroe (P) [26].

6. NT-200+ AND BEYOND

The recently derived upper limits on ν_e fluxes by BAIKAL and AMANDA are about $E^2\Phi_\nu \approx (3{-}5) \times 10^{-7}$ cm^{-2} s^{-1} sr^{-1} GeV and cover the region of optimistic theoretical predictions. However, a flux sensitivity at the level of $E^2\Phi_\nu < 10^{-7}$ cm^{-2} s^{-1} sr^{-1} GeV,

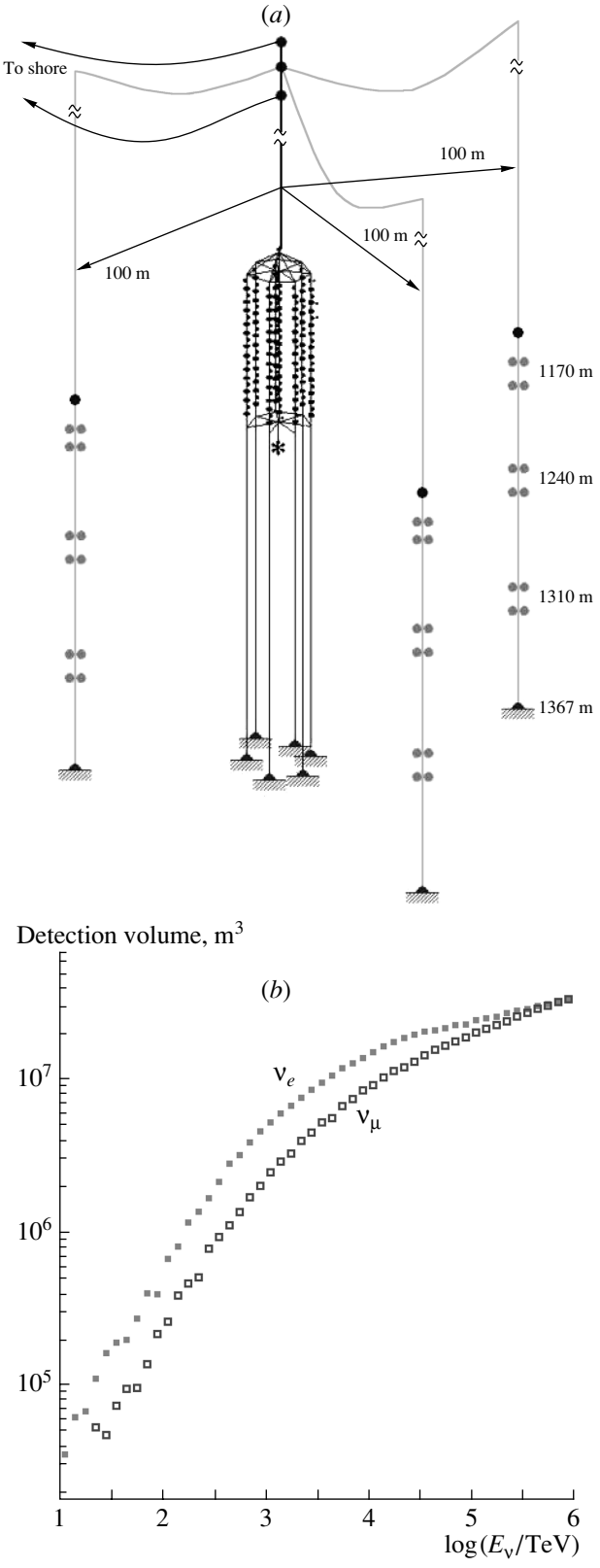

Fig. 6. (*a*) Sketch of NT-200+. (*b*) Detection volume of NT-200+ for ν_e and ν_μ.

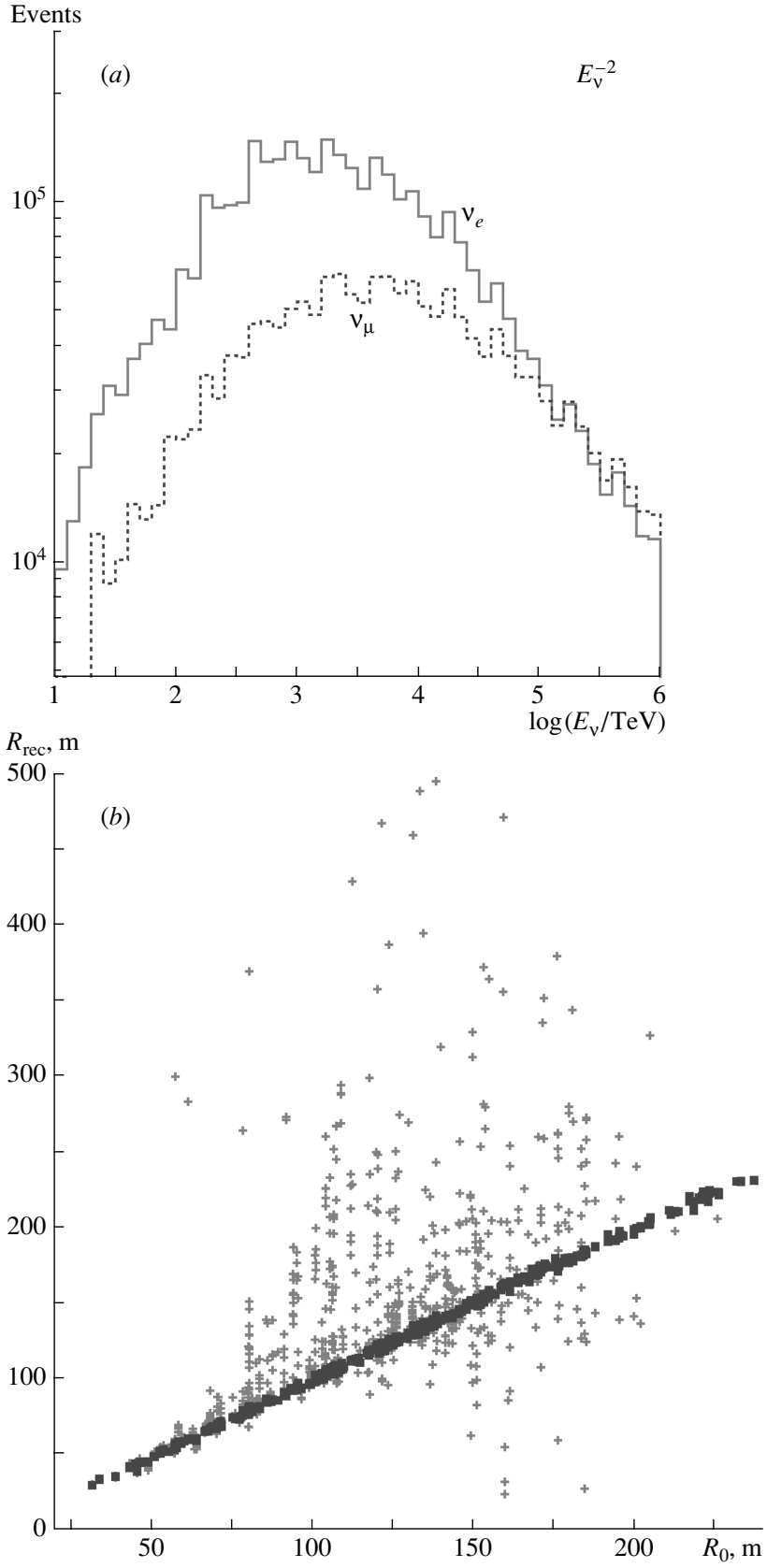

Fig. 7. (*a*) Energy distribution of expected events induced by diffuse ν_e and ν_μ fluxes. (*b*) Reconstructed vs. simulated coordinates of cascades in NT-200+ (rectangles) and NT-200 (crosses).

which would test a variety of other models, requires detection volumes on the order of 10 Mt.

We envisage an upgrade of NT-200 to this scale by three sparsely instrumented distant outer strings. The basic principle will be the search for cascades produced in the large volume below NT-200. This configuration, christened NT-200+, will not only result in an increased detection volume for cascades, but also allow for a precise reconstruction of the cascade vertex and energy within the volume spanned by the outer strings.

A schematic view of NT-200+ is shown in Fig. 6*a*. It will comprise the neutrino telescope NT-200 itself as well as three 140 m long outer strings with three double pairs of OMs spaced vertically by 70 m. The outer strings are arranged at a distance of 100 m around NT-200 at the edges of an equilateral triangle. Their top OMs are located at the level of the bottom OMs of NT-200. A water volume of 4.4×10^6 m^3 is surrounded by the outer strings and NT-200.

Moderate event selection requirements will allow us to achieve a large detection volume for neutrino events and to suppress the background effectively. The detection volumes for isotropic ν_e and ν_μ fluxes are shown in Fig. 6*b*. The value of V_{eff} for ν_e induced events rises from 7×10^5 m^3 for 100 TeV up to 4×10^7 m^3 for 10^6 TeV. Normalized energy distributions of expected event rates from ν_e and ν_μ fluxes following an inverse power law with the spectral index $\gamma = 2$ are presented in Fig. 7*a*. Most of the expected events will be produced by neutrinos from the energy range 10^2–10^5 TeV, with a mean energy around 1 PeV. In Fig. 7*b*, reconstructed vs. simulated coordinates of cascades in NT-200+ (rectangles) and NT-200 (crosses) are shown. The reconstruction accuracy significantly improves in the case of NT-200+.

Assuming $\gamma = 2$ and a flavor ratio $\nu_e : \nu_\mu : \nu_\tau = 1 : 1 : 1$, a 90% C.L. limit on the ν_e flux of

$$E^2 \Phi_{\nu_e + \bar{\nu}_e} = 9 \times 10^{-8} \text{ cm}^{-2} \text{ s}^{-1} \text{ sr}^{-1} \text{ GeV} \qquad (3)$$

could be established from 3-yr recorded data.

MC simulations have shown that the detection volume of NT-200+ for PeV cascades would vary only moderately if NT-200 as the central part of NT-200+ is replaced by a single string of OMs. Figure 8 gives the detection volume for different configurations as a function of cascade energy. The standard configuration of NT-200+ is marked by open rectangles. The other configurations comprise a single string instead of NT-200: a standard string of 70-m length and 24 OMs (closed rectangles), a half-string with 12 OMs covering 35 m (circles), and a 70 m long string sparsely equipped with 12 OMs (triangles). The configuration with the long 12-OM string shows an energy behavior very close to the one of NT-200+.

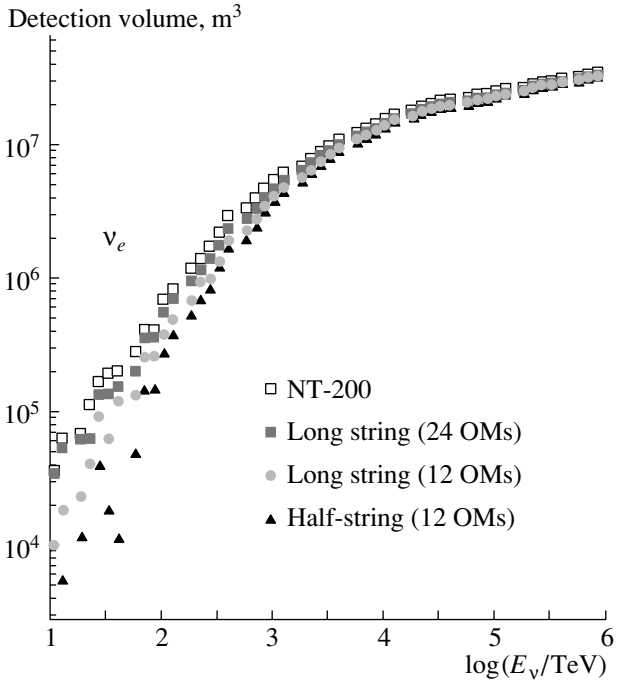

Fig. 8. Detection volumes of different configurations.

For neutrino energies higher than 100 TeV, such a configuration could be used as the basic subarray of a Gigaton Volume Detector (GVD). Rough estimations show that a (0.7–0.9)-Gt detection volume for neutrino induced high-energy cascades may be achieved with about 1300 OMs arranged on 91 strings. A top view of the GVD, as well as sketch of one basic subarray, is shown in Fig. 9. The physical capabilities of GVD at very high energies cover the typical spectrum of cubic kilometer arrays. We are presently working on simulations to optimize the response for TeV muons, maintaining at the same time the cubic kilometer scale for cascades with energies above 100 TeV.

7. CONCLUSIONS AND OUTLOOK

The deep underwater neutrino telescope NT-200 in Lake Baikal has been taking data since April 1998. Using the first 502 live days, 84 neutrino induced upward going muons have been selected. Limits on the diffuse high-energy $\nu_e + \bar{\nu}_e$ flux, as well as on the $\bar{\nu}_e$ flux at the W-resonance energy, have been derived. Also, limits on the excess of the muon flux due to WIMP annihilation in the center of the Earth and on the flux of fast magnetic monopoles have been obtained. The additional analysis of the experimental data accumulated during 2000–2002 will allow us to decrease these limits by a factor of 2–3.

Within the next few years, we plan to upgrade the Baikal neutrino telescope to the 10-Mt detector NT-200+ with a sensitivity of approximately

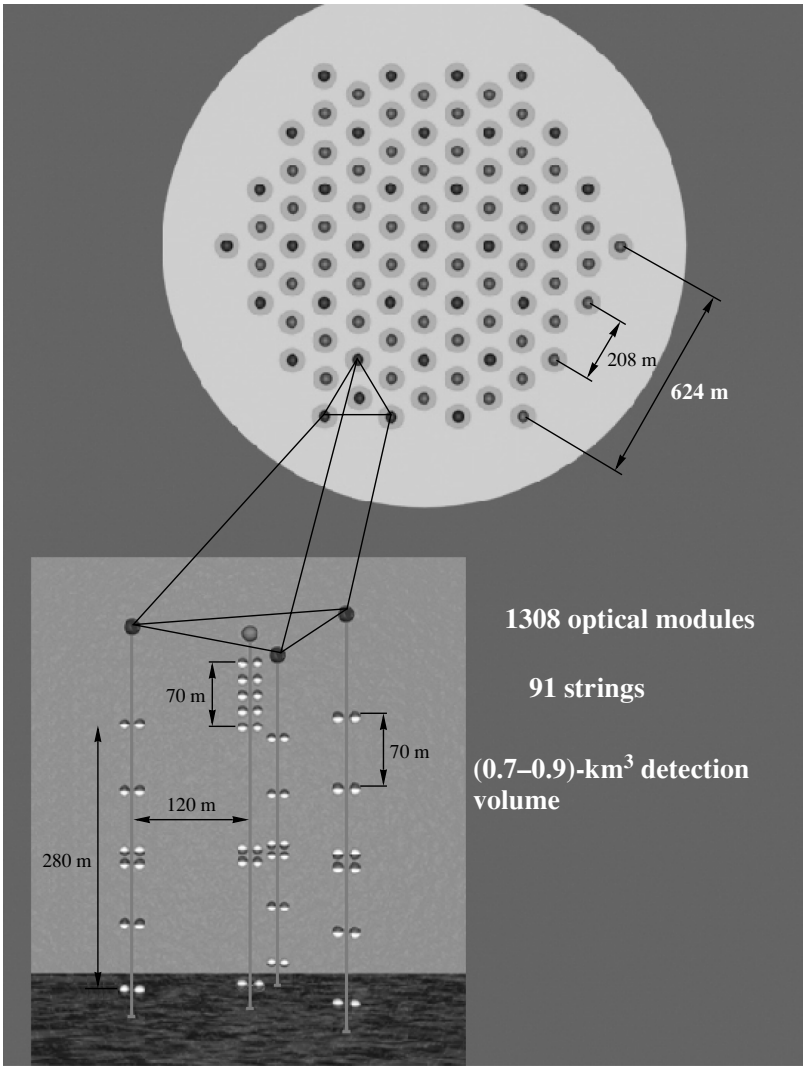

Fig. 9. Top view of GVD as well as a sketch of one of its subarrays.

10^{-7} cm^{-2} s^{-1} sr^{-1} GeV for a diffuse neutrino flux within the energy range 10^2–10^5 TeV. NT-200+ will search for neutrinos from AGNs, GRBs, and other extraterrestrial sources, neutrinos from cosmic ray interactions in the Galaxy, as well as high-energy atmospheric muons with $E_\mu > 10$ TeV. In parallel to this short term goal, we started research and development activities towards a GVD in Lake Baikal.

ACKNOWLEDGMENTS

This work was supported by the Russian Ministry of Research, the German Ministry of Education and Research, and the Russian Foundation for Basic Research (project nos. 03-02-31004, 02-02-17031, 02-07-90293, and 01-02-17227), grant NSh-1828.2003.2, and by the Russian Federal Program "Integration" project no. E0248.

REFERENCES

1. I. Belolaptikov *et al.*, Astropart. Phys. **7**, 263 (1997).
2. R. I. Bagduev *et al.*, Nucl. Instrum. Methods Phys. Res. A **420**, 138 (1999).
3. I. Belolaptikov *et al.*, Astropart. Phys. **12**, 75 (1999).
4. V. Agrawal, T. Gaisser, P. Lipari, and T. Stanev, Phys. Rev. D **53**, 1314 (1996).
5. A. Habig *et al.*, in *Proceedings of the 28th ICRC, Tsukuba, Japan, 2003*, p. 1255.
6. T. Gaisser and M. Honda, Ann. Rev. Nucl. Part. Sci. D **52**, 153 (2002).
7. M. M. Boliev *et al.*, Nucl. Phys. B (Proc. Suppl.) **48**, 83 (1996); O. Suvorova, hep-ph/9911415.
8. M. Ambrosio *et al.*, Phys. Rev. D **60**, 082002 (1999).
9. A. Habig *et al.*, in *Proceedings of the 27th ICRC, Hamburg, 2001*, p. 1558.
10. J. Ahrens *et al.*, Phys. Rev. D **66**, 032006 (2002).
11. V. Balkanov *et al.*, Nucl. Phys. B (Proc. Suppl.) **91**, 438 (2001).
12. M. Ambrosio *et al.*, Eur. Phys. J. C **25**, 511 (2002).

13. J. Thorn *et al.*, Phys. Rev. D **46**, 4846 (1992).
14. H. Adarkar *et al.*, in *Proceedings of the 21st ICRC, Adelaide, 1990*, Vol. 10, p. 95.
15. S. Orito *et al.*, Phys. Rev. Lett. **66**, 1951 (1992).
16. E. Andres *et al.*, in *Proceedings of the 8th International Workshop on Neutrino Telescopes, Venice, 1999*, Vol. 2, p. 63; astro-ph/9906203.
17. V. A. Balkanov *et al.*, Astropart. Phys. **14**, 61 (2000).
18. V. A. Balkanov *et al.*, in *Proceedings of the 9th International Workshop on Neutrino Telescopes, Venice, 2001*, Ed. by Milla Baldo Ceoline, p. 591; astro-ph/0105269.
19. V. A. Balkanov *et al.*, Nucl. Phys. B (Proc. Suppl.) **118**, 363 (2003).
20. M. Ambrosio *et al.*, Nucl. Phys. B (Proc. Suppl.) **110**, 519 (2002).
21. M. Kowalski *et al.*, in *Proceedings of the 28th ICRC, Tsukuba, Japan, 2003*, p. 1301.
22. V. Berezinsky *et al.*, *Astrophysics of Cosmic Rays* (North-Holland, Amsterdam, 1990).
23. E. Waxman and J. Bahcall, Phys. Rev. D **59**, 023002 (1999).
24. K. Mannheim *et al.*, astro-ph/9812398.
25. F. Stecker and M. Salamon, astro-ph/9501064.
26. R. Protheroe, Astron. Soc. Pac. **163**, 585 (1997); astro-ph/9809144.

Physics of Atomic Nuclei, Vol. 67, No. 6, 2004, pp. 1172–1176. From Yadernaya Fizika, Vol. 67, No. 6, 2004, pp. 1195–1199.

NEUTRINO PHYSICS AND ASTROPHYSICS

The ANTARES Neutrino Project*

I. A. Sokalski**
(on behalf of the ANTARES Collaboration)

INFN, Sezione di Bari, Italy

Received November 17, 2003

Abstract—The ANTARES project aims to build a deep underwater Cherenkov neutrino telescope in the Mediterranean Sea. Currently the experiment is in the construction phase and has recently achieved two important milestones. The electro-optical cable to shore and the junction box that will distribute power to detector strings and allow data transmission have been deployed on the seafloor. A prototype string and a string for environmental parameter measurement have been deployed, connected to the cable using a manned submarine. Data have been sent to shore. The final ANTARES detector, consisting of 12 strings each equipped with 75 photomultiplier tubes, is planned to be fully deployed and taking data by the end of 2006. © *2004 MAIK "Nauka/Interperiodica"*.

1. INTRODUCTION

The neutrino is an attractive tool for astrophysical investigations since interacting weakly they can escape from the source and travel large distances to the Earth without interaction and without deflection by magnetic fields. Nevertheless, due to the same property, large-volume neutrino detectors are needed. ANTARES is one of the several ongoing projects [1–6] on underwater/ice neutrino telescopes. Given the presence of AMANDA at the South Pole, a detector in the Mediterranean will allow coverage of the whole sky. The ANTARES Collaboration (Astronomy with a Neutrino Telescope and Abyss environmental RESearch) was formed in 1996 and currently joins about 200 scientists and engineers from France, Germany, Italy, Russia, Spain, the Netherlands, and the United Kingdom. The project aims to detect atmospheric and extraterrestrial neutrinos with energies above $E_\nu \sim 10$ GeV by means of the detection of the Cherenkov light that is generated in water by charged particles which are produced in νN interactions. After an extensive R&D program, the collaboration moved into construction of a detector in the Mediterranean Sea at a depth of 2400 m, 50 km offshore from La Seyne sur Mer, near Toulon (42°50′ N, 6°10′ E).

2. R&D STAGE

In 1996–1999, an intense R&D program was performed. The deployment and recovery technologies, electronics, and mechanical structures were developed and tested with more than 30 deployments of autonomous strings. The environmental properties at the detector site were investigated [7, 8].

Concerning the optical backgrounds, it was found that a baseline 1-p.e. counting rate of ~ 60 kHz is measured by a 10-in. PMT. The counting rate increases during short bursts up to several megahertz due to bioluminescence. These bursts lead to a dead time of less than 5% per each PMT. However, the long-term measurements that were performed with the so-called prototype string in 2003 (see below) showed that these rates and the burst fraction are sometimes substantially higher (Fig. 1). The experimental work to understand the differences between previous results with autonomous mooring lines and the prototype string is in progress. Perhaps, to suppress the high background, harder cuts will have to be applied, which will slightly increase the energy threshold without altering the detection efficiency of >100-GeV neutrino events. Light transmission loss for glass containers that house PMTs was found to be strong in long-term tests for up-looking surfaces. It led to the decision to turn all PMTs downward. Signal loss due to biofouling and sedimentation was measured to be 1.6% after eight months at the equator of glass sphere saturating with time. The optical properties of water at the site of the experiment were measured over several years. The effective attenuation length varies in a range $48 < L_{\rm att} < 61$ m, while the scattering length is $L_{\rm scatt} > 200$ m for blue light ($\lambda = 466$ nm). Only 5% of the photons emitted by an isotropic source located 24 m from the PMT are collected out of a 10-ns time window, being delayed

*This article was submitted by the author in English.

**e-mail: Igor.Sokalski@ba.infn.it

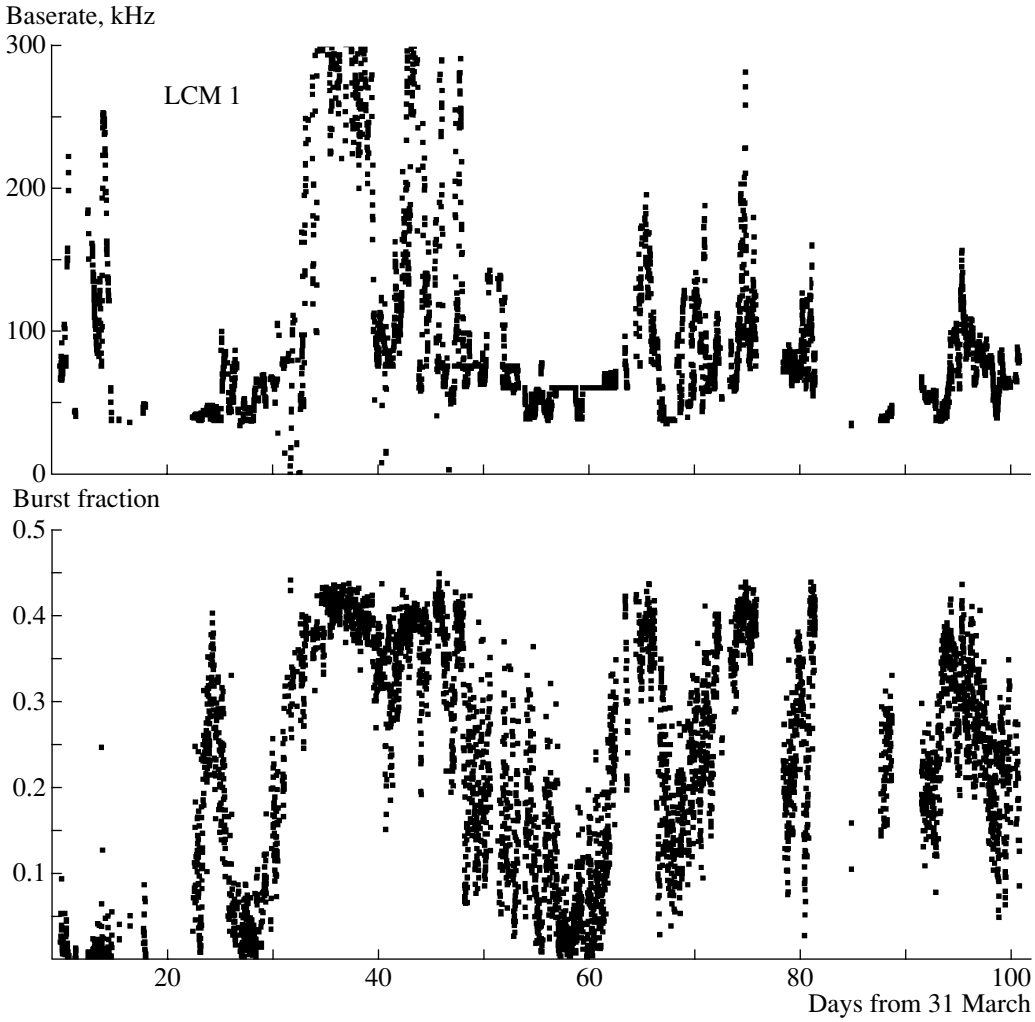

Fig. 1. Summary of counting rate in three PMTs during 65 d of "prototype string" operation in April–May 2003. (Top) The average baseline rate. (Bottom) The fraction of time that the rate is significantly higher than this average baseline rate (burst fraction).

due to scattering. This allows a good time resolution needed for event reconstruction.

The ANTARES R&D program culminated with the deployment and eight-month operation of a 350-m-long "demonstrator string" (November 1999–July 2000) instrumented with seven PMTs at a depth of 1100 m, 40 km off the coast of Marseille. The string was controlled and read out via a 37-km-long electro-optical cable connected to the shore station. It allowed testing of the deployment procedure with a full-scale string and positioning system and collection of $\sim 5 \times 10^4$ sevenfold coincidences from atmospheric muons. Relative distances were measured with an accuracy of $\sim$5 cm, and accuracy of absolute positioning was $\sim$1 m. The angular distribution of atmospheric muons was reproduced and the fraction of multimuon events was found to be $\sim$50% which is in agreement with expectation for such a shallow depth as 1100 m.

3. ANTARES DETECTOR

After this R&D experience, the Collaboration moved to the next stage: construction of a 12-string detector [2] which can be considered as a step toward a 1-km^3 detector (Fig. 2). Strings are anchored on the seafloor and held taut by buoys. Each string is instrumented with 75 optical modules (OMs) [9] containing 10-in. Hamamatsu R7081-20 PMTs housed in glass spheres. OMs are grouped in triplets at 25 levels separated by 14.5 m. Three PMTs in each triplet are oriented at 45° to the nadir. Strings are separated from each other by $\sim$70 m. All the strings are connected to a junction box (JB) by means of electro-optical link cables. The JB is connected to

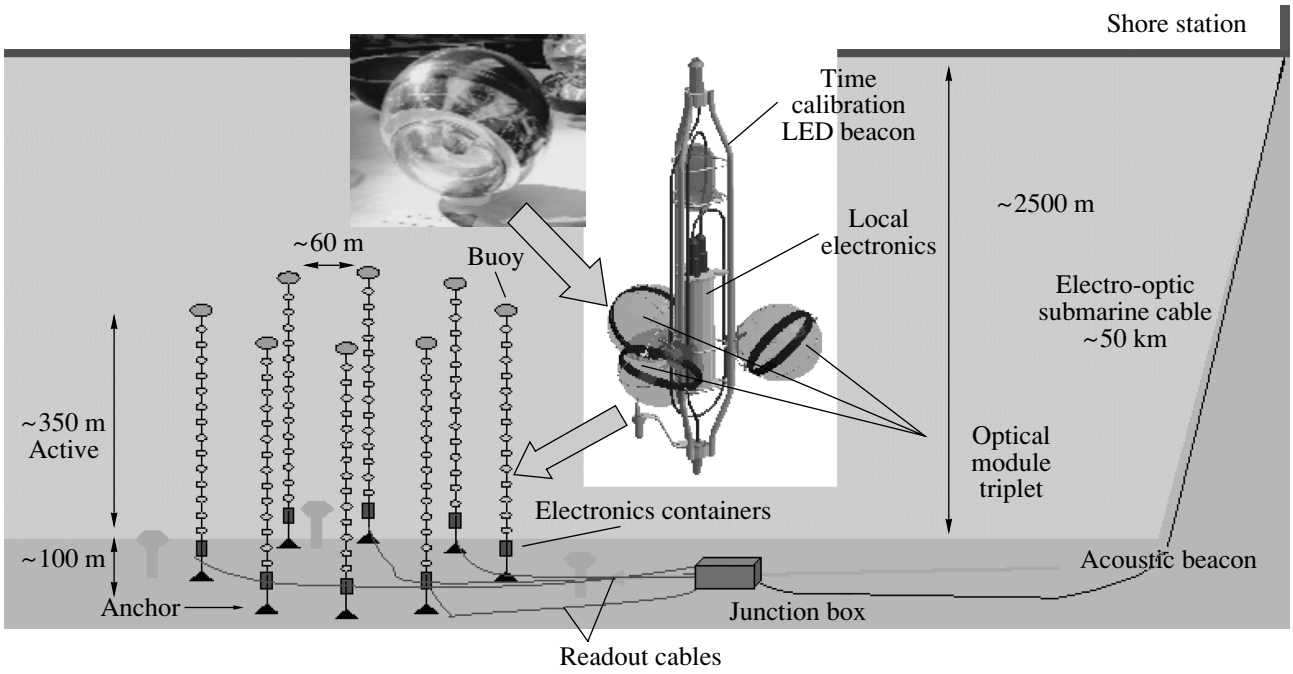

Fig. 2. Schematic view of the ANTARES 12-string detector.

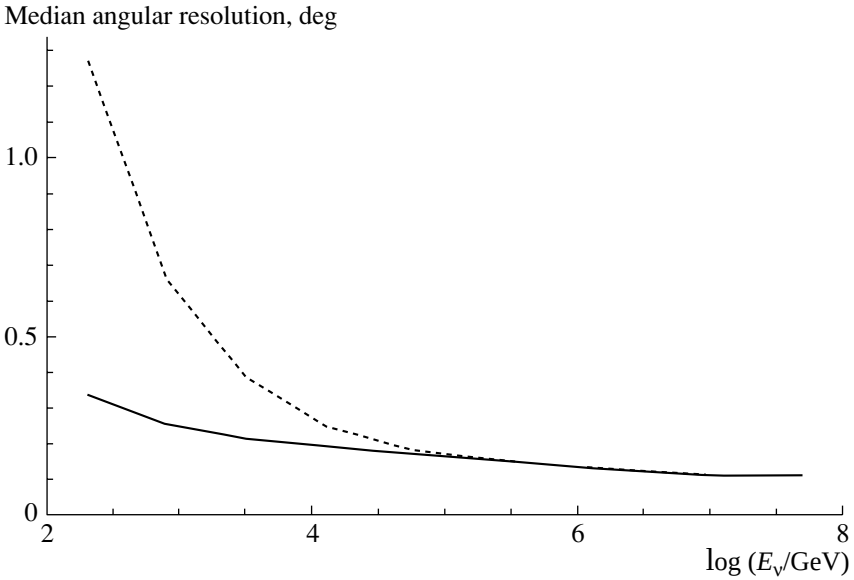

Fig. 3. Angular resolution of the ANTARES detector vs. E_ν: median of the distribution of the angle in the space between the reconstructed muon track and true muon track (solid curve) or the parent neutrino track (dashed curve).

the shore station by a 50-km-long 48-fiber electro-optical cable. Undersea connections are performed with a manned submarine. PMT signals are processed by analog ring samplers ASIC, which measure the arrival time and charge for 1-p.e. pulses (99% of the pulses) and perform waveform digitization for larger amplitudes. Digitized data from each OM are sent to shore (~1 GB/s/detector). The data flow is reduced down to ~1 MB/s by means of an on-shore data filter [10]. A 100 PC farm is foreseen on shore to process and collect the data. The telescope will be complemented with an instrumentation string for hydrological parameter measurements and for calibration purposes. The deployment of the detector is planned for 2004–2006. The important milestones

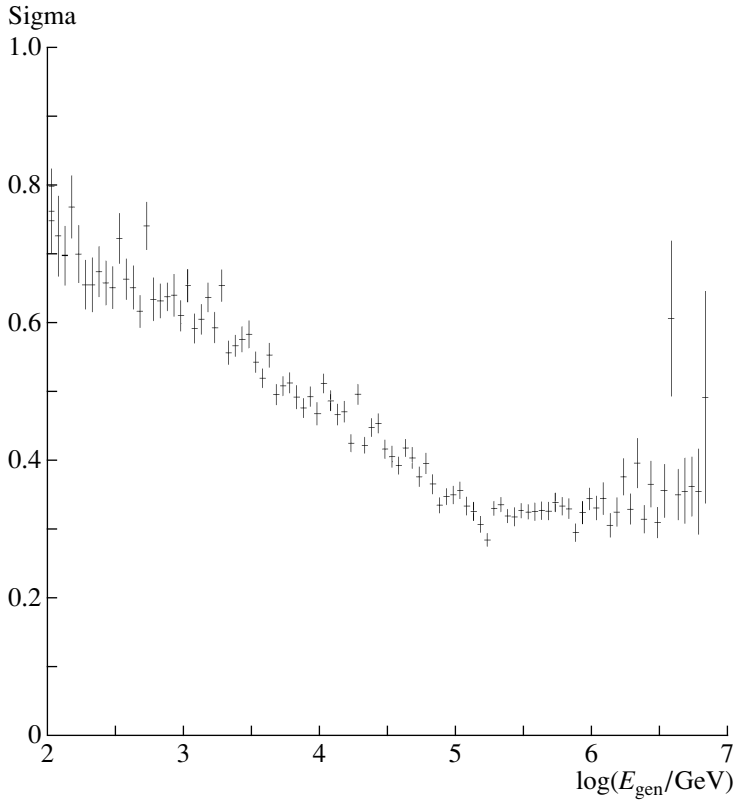

Fig. 4. Energy resolution of the ANTARES detector: sigma of the distributions of $\log(E_{rec}/E_t)$ (where E_{rec} is reconstructed muon energy and E_t is true energy) vs. muon generated energy E_{gen}.

that have been achieved by the Collaboration are as follows:

The electro-optical cable connecting the detector and shore station was deployed in October 2001.

The industrial production of 900 OMs started in April 2002.

Since December 2002, the JB has been in communication with the shore station.

In December 2002 and February 2003, the "prototype instrumentation string" and the "prototype detection string" (equipped with 15 OMs) were successfully deployed [11] (recovered in May and July 2003, respectively).

In March 2003, both strings were connected to the JB with the Nautile manned submarine and data taking started.

The aim of the deployment and operation of two prototype strings was to test all the components of the future detectors in their final design. Mechanical problems occurred: one fiber for clock signal transmission was found to be broken and one connector leaked. After recovery of the strings, it was found that these problems occurred due to manufacturers who changed the design without notification. Solutions have been found for the final detector design and strict quality control will be applied.

A detailed description of the ANTARES physics performance can be found in [12]. The angular resolution of the 12-string detector (Fig. 3) is about 0.2° for $E_\nu \geq 100$ TeV, where it is limited only by the PMT TTS and light scattering, and $\sim 0.5^\circ - 1^\circ$ at $E_\nu \sim 0.1-10$ TeV, where accuracy is dominated by $\nu-\mu$ kinematics. Energy resolution (Fig. 4) improves at high energies: dispersion of the $\log(E_{rec}/E_t)$ distribution (where E_t is the true energy and E_{rec} is the reconstructed energy, respectively) is around $\sigma \approx 0.5$ at $E_\nu \sim 5$ TeV and $\sigma \approx 0.3$ for $E_\nu \geq 100$ TeV. The effective area for muons grows from $A_{eff} = 0.01$ km^2 at $E_\nu = 1$ TeV to $A_{eff} = 0.06$ km^2 at $E_\nu = 10$ PeV. The sensitivity of the detector to diffuse neutrino fluxes achieved by rejecting the background with an energy cut of $E_{cut} = 50$ GeV allows one to reach the Waxmann and Bahcall limit [13] in three years. The ANTARES sensitivity for pointlike source searches (90% C.L.) assuming E^{-2} differential ν flux is in the range $(4-50) \times 10^{-16}$ cm^{-2} s^{-1} after one year, which gives a real hope to detect a signal from the most promising sources (e.g., galactic microquasars [14]). The ANTARES potential for WIMP searches is high enough to improve existing experimental upper limits on ν-induced muon fluxes from neutralino annihilation in the Sun and on relativistic magnetic monopole

flux obtained by other detectors by an order of magnitude.

4. CONCLUSIONS

The construction of the ANTARES detector is under way. It is planned to be fully deployed and to start taking data by the end of 2006. Calculations based on the data on environmental conditions at the site of the experiment and on studied properties of electronic components show that predicted sensitivity of the detector to diffuse neutrino fluxes, pointlike neutrino searches, and WIMP searches is better by several orders of magnitude compared to data published by other experimental groups. The deployment of the ANTARES neutrino telescope can be considered as a step toward the deployment of a 1-km^3 detector in the Mediterranean Sea.

REFERENCES

1. P. Desiati *et al.* (AMANDA Collab.), astro-ph/0306536; http://amanda.uci.edu/.
2. E. Aslanides *et al.* (ANTARES Collab.), astro-ph/9907432; http://antares.in2p3.fr/.
3. R. Wischnewski *et al.* (Baikal Collab.), astro-ph/0305302; http://nt200.da.ru/.
4. A. Goldschmidt *et al.* (IceCube Collab.), Nucl. Phys. B (Proc. Suppl.) **110**, 516 (2002); http://icecube.wisc.edu/.
5. G. Riccobene *et al.* (NEMO Collab.), in *Proceedings of the 2nd Workshop on Methodical Aspects of Underwater/Ice Neutrino Telescopes, Hamburg, 2001*, p. 61; http://nemoweb.lns.infn.it/.
6. S. E. Tzamarias *et al.* (NESTOR Collab.), Nucl. Instrum. Methods Phys. Res. A **502**, 150 (2003); http://www.nestor.org.gr/.
7. P. Amram *et al.*, Astropart. Phys. **13**, 127 (2000).
8. P. Amram *et al.*, Astropart. Phys. **19**, 253 (2003).
9. P. Amram *et al.*, Nucl. Instrum. Methods Phys. Res. A **484**, 369 (2002).
10. M. C. Bouwhuis (for the ANTARES Collab.), in *Proceedings of the 28th ICRC, Tsukuba, Japan, 2003*, p. 1541.
11. M. Circella (for the ANTARES Collab.), in *Proceedings of the 28th ICRC, Tsukuba, Japan, 2003*, p. 1529.
12. T. Montaruli *et al.* (ANTARES Collab.), astro-ph/0207531; physics/0306057; J. J. Hernández-Rey *et al.* (ANTARES Collab.), Nucl. Phys. B (Proc. Suppl.) **114**, 211 (2003).
13. E. Waxmann and J. N. Bahcall, Phys. Rev. D **59**, 023002 (1999).
14. C. Distefano *et al.*, Astrophys. J. **575**, 378 (2002).

Physics of Atomic Nuclei, Vol. 67, No. 6, 2004, pp. 1177–1181. From Yadernaya Fizika, Vol. 67, No. 6, 2004, pp. 1200–1203.

NEUTRINO PHYSICS AND ASTROPHYSICS

Astrophysical Tau Neutrinos and Their Detection by Large Neutrino Telescopes*

E. V. Bugaev[**], **T. Montaruli**[1),2)], **and I. A. Sokalski**[2)]

Institute for Nuclear Research, Russian Academy of Sciences, Moscow, Russia

Received November 11, 2003

Abstract—We present results of the detailed Monte Carlo calculation of the rates of double-bang events in a 1-km^3 underwater neutrino telescope taking into account the effects of τ-neutrino propagation through the Earth. As an input, the moderately optimistic theoretical predictions for diffuse neutrino spectra of AGN jets are used. © *2004 MAIK "Nauka/Interperiodica".*

1. INTRODUCTION

During recent years there have been many discussions [1, 2] on the possibilities of very high-energy τ-neutrino detection by large neutrino telescopes, which would prove oscillations of muon neutrinos of astrophysical origin ("astrophysical long baseline experiment" [3]). It is known now that neutrino oscillations definitely exist. Nevertheless, the detection of astrophysical τ neutrinos is still very interesting and useful, e.g., for a better understanding of neutrino properties as well as properties of astrophysical sources [4].

Intrinsic flux of τ neutrinos from a typical source in which there is acceleration of protons and production of neutrinos through pp and $p\gamma$ reactions is very small. The dominant channel of τ-neutrino birth is through the inclusive production of charmed mesons [5],

$$pp, p\gamma \longrightarrow D_S^+ + X, \quad D_S^+ \longrightarrow \tau\nu_\tau, \qquad (1)$$

and the smallness of ν_τ flux follows from the relations

$$\frac{\sigma_{\gamma p\to DX}}{\sigma_{\gamma p\to \pi X}} \lesssim 10^{-3}, \quad \frac{\mathrm{Br}(D_S^+ \to \nu_\tau)}{\mathrm{Br}(\pi \to \nu_\mu)} \sim 7\times 10^{-2}. \qquad (2)$$

Therefore, the production of ν_τ at source is negligible, and if all muons can decay, the following proportion can be expected for the three flavors:

$$\Phi^0_{\mathrm{std}} = \{\phi^0_e, \phi^0_\mu, \phi^0_\tau\} = \left\{\frac{1}{3}, \frac{2}{3}, 0\right\}. \qquad (3)$$

Assuming maximal atmospheric mixing and $U_{e3} = 0$, that is,

$$\sin\theta_{13} = 0, \quad \sin 2\theta_{23} = 1, \qquad (4)$$

one obtains, after averaging over many oscillations, the ideal equipartition between neutrino flavors in the astrophysical neutrino flux at the Earth,

$$\Phi_{\mathrm{std}} = \left\{\frac{1}{3}, \frac{1}{3}, \frac{1}{3}\right\}, \qquad (5)$$

independently on the value of the solar mixing angle θ_{12}. Moreover, in the case when there is maximal atmospheric mixing and $U_{e3} = 0$, for any proportions between flavors at the source one has, after propagation, the equality $\phi_\mu = \phi_\tau$ [4].

The experimental verification of the relation $\phi_\mu = \phi_\tau$ by detection of astrophysical diffuse fluxes of ν_τ and ν_μ with flavor identification capabilities is very important, because the inequality $\phi_\mu \neq \phi_\tau$ is predicted in some exotic scenarios, e.g., [4], (i) if CPT invariance is violated in the neutrino sector and the neutrino and antineutrino mixing matrices do not coincide, ϕ_μ, in general, is not equal to ϕ_τ, (ii) if neutrinos can decay [6] *en route* from the sources to the Earth, the neutrino fluxes and flavor ratios are very sensitive to uncertainties in the neutrino mixing matrix and strongly depend on the hierarchy of neutrino masses. So, the inequality $\phi_\mu \neq \phi_\tau$ would reveal unconventional neutrino physics.

Inside of some astrophysical and cosmological objects there are processes in which very energetic quarks and gluons fragmenting into jets of hadrons are expected to be produced. Even the usual inclusive spectrum of high-energy pp or $p\gamma$ collisions always contains the jet component (described well by perturbative QCD). Jets can appear in decays of (hypothetical) supermassive particles which, in turn,

*This article was submitted by the authors in English.

1)Physics Department, Bari University, Italy.
2)INFN/Bari, Italy.
** e-mail: bugaev@pcbai10.inr.ruhep.ru

are produced in decays of topological defects [7], in processes of superheavy dark matter annihilation inside of stars [8], and in the process of Hawking evaporation of primordial black holes [9]. It was shown in [10] that decays of top quarks contained in the jets lead to production of ν_τ flux from the jets, which is of the same order as ν_μ and ν_e fluxes (at large neutrino energies, close to the value of the jet mass). This means that the intrinsic ν_τ flux from the sources in which the jet phenomena are essential is, in general, not suppressed (in comparison with intrinsic ν_μ and ν_e fluxes).

In this paper, we studied the possibility of detection of extragalactic diffuse ν_τ fluxes by large ($\sim$1 km^3) underwater neutrino telescopes. In Section 2, we discuss the general problems connected with the detection of very high-energy ν_τ ($E_\nu \gtrsim 10^6$ GeV). In Section 3, we present the diffuse neutrino spectra for the AGN jets chosen for the numerical calculations. Details of the calculations, results, and conclusions are given in Section 4.

2. DETECTION OF τ NEUTRINOS

The main feature of charge current interactions of τ neutrinos is the fact that τ leptons decay long before they lose a large fraction of their energy. This leads to the absence of absorption of τ neutrinos during their propagation through the Earth and, as a consequence, to the characteristic modification of the neutrino spectrum after crossing the Earth (there is a pileup of events with energies around $\sim$ 100 TeV if the incident neutrino spectrum is not too steep). At neutrino energies of $\sim 10^6$–10^7 GeV, the τ-lepton track length becomes larger than $\sim$ 100 m (in water) and it becomes possible to identify τ-neutrino interactions in large neutrino telescopes by selection of "double-bang" or "lollipop" events [1]. A double-bang event consists of two showers and a τ-lepton track connecting them. The first (hadronic) shower is initiated by the charge current interaction of τ neutrino, and the second one (hadronic or electromagnetic) is produced by the τ-lepton decay. In lollipop events, one of these showers is not detected (e.g., if the τ-neutrino interaction takes place outside of the detector).

The detection of events with double-bang structure would reliably indicate the appearance of τ neutrinos in the detector, because this signature is unique. However, the probability of observing a double-bang event P_{DB} decreases with neutrino energy for $E_\nu > 10^8$ GeV (due to τ-lepton range increase). The lollipop structure is not so spectacular, although the observation probability P_L of lollipop events at $E_\nu \sim 10^8$ GeV is considerably (by a factor of 10 [11]) larger than P_{DB}.

Diffuse astrophysical and cosmological neutrino fluxes in the ultrahigh-energy region $E_\nu > 10^9$ GeV (GZK neutrinos (see, e.g., [12]), hypothetical neutrino fluxes from topological defects [13], from Z-bursts [14], etc.) are too small and inaccessible for a study by underwater neutrino telescopes. Registration of τ neutrinos of such energies can be accomplished by detecting the air showers caused by τ leptons produced by neutrino–nucleon interactions far away from the detector ("Earth-skimming idea" [15]). The huge modern air shower detectors (e.g., the HiRes [16] or the Pierre Auger detector [17]) could be suitable for such experiments, but expected event rates are low.

3. DIFFUSE NEUTRINO SPECTRA FROM AGN JETS

The concrete calculations were carried out with two theoretical diffuse neutrino spectra from AGNs.

1. The curve denoted by "MPR (limit)" in the figure is the generic upper bound on the diffuse neutrino spectrum from AGN jets obtained by Mannheim, Protheroe, and Rachen [18]. This limit was found using the assumption that the AGN source is not completely optically thin for a cosmic ray flux: due to opacity effects, there is a spectral break between 10^7 and 10^{11} GeV in the escaping cosmic ray spectrum (the resulting cosmic ray spectrum is a combination of several model spectra with different values of the spectral break and with the fixed $E_{\max}$ ($E_{\max} = 10^{11}$ GeV), and the normalization of the resulting spectrum is such that the cosmic ray intensity does not exceed the proton spectrum estimated from observations). Neutrinos are mostly produced in decays of mesons from accelerated proton interactions with synchrotron photons emitted by high-energy electrons in the jets. It is noted in [18] that various models of AGN jets (see, e.g., [19–21]) predict diffuse neutrino spectra that are compatible with the MPR limit (at the important neutrino energy range below $\sim 10^7$ GeV).

2. The model by Protheroe [21] (the curve denoted by "P" in the figure) is the optically thick proton blazar model, in which it is assumed that the target for the pion production is provided by the thermal UV photons emitted from the accretion disc rather than by the synchrotron photons produced in the jets. The diffuse neutrino spectrum is normalized to the experimental data on the γ-ray background. It is seen from the figure that the prediction of this model is, indeed, not in the contradiction with the MPR bound if $E_\nu \leq 10^7$ GeV. The proton blazar model, developed by

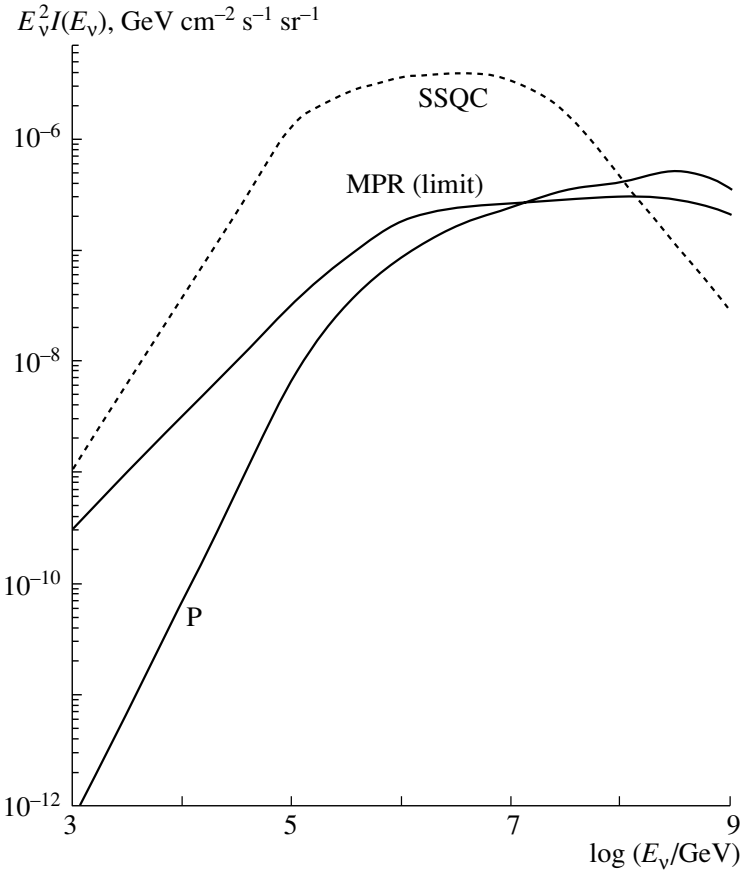

Different theoretical predictions for diffuse neutrino ($\nu_\mu + \overline{\nu}_\mu$) spectra from AGNs: MPR (limit)—upper bound for ν_μ flux from AGN jets [18], P—ν_μ flux for proton blazar model of [21], SSQC—prediction of ν_μ flux from radio-quiet AGNs [22].

Mannheim [19] (in which accelerated protons interact with the synchrotron radiation of jet electrons) predicts a very similar diffuse neutrino spectrum.

One should note that the prediction given by Stecker and Salamon [22] for diffuse neutrino spectrum from radio-quiet AGNs is much more optimistic (SSQC curve in the figure) at neutrino energies of $E_\nu \sim 10^6$–10^7 GeV. Their model, however, predicts a nonthermal spectrum of x rays at energies below $\sim$500 keV (these x rays result from reprocessing of γ rays from pion decays by electromagnetic cascades due to the high photon density near the black hole) while the observed x-ray spectra of radio-quiet AGNs (as well as the spectrum of the diffuse x-ray background) turn over steeply below $\sim$ 100 keV with no sign for a nonthermal component [23]. Therefore, the existing x-ray data cannot be used for a normalization of the radio-quiet AGN neutrino spectrum (the authors of [22] normalized their spectrum, rather arbitrarily, on 30% of the diffuse x-ray background). This is the reason why we did not use SSQC flux in our calculations. Besides, SSQC neutrino flux is now almost excluded from measurements on the AMANDA [24] and Baikal [25] neutrino telescopes.

4. RESULTS AND DISCUSSIONS

First estimates of double-bang event rates using a 1-km^3 neutrino telescope were done in [26] for down-going τ neutrinos only. Detailed calculations of τ-neutrino propagation through the Earth carried out by Dutta *et al.* [27] (using power law incident neutrino spectra) showed that, in spite of the absence of neutrino absorption, the contribution of lower-hemisphere events to the total event rate in a telescope cannot be too large. This is due to a strong decrease of neutrino energies during propagation. It was concluded in [27] that the most promising way to detect τ-neutrino astrophysical fluxes is an analysis of shower events in the telescope.

In this article we present results on Monte Carlo calculations of rates of double-bang events in a 1-km^3 telescope for both hemispheres using the diffuse

Number of totally contained double-bang events in the 1-km^3 detector per year

Spectrum	Rate ($N_{-2\pi}/N_{2\pi}/N_{4\pi}$)		
	NEMO-like		
[21]	1.0	2.1	3.1
[18]	1.4	3.1	4.5
	IceCube-like		
[21]	0.7	1.6	2.3
[18]	1.0	2.3	3.3

neutrino spectra shown in the figure. We simulate both DIS charge current and neutral current neutrino interactions for all flavors in the energy range 10^3 GeV $< E_\nu < 10^9$ GeV using the CTEQ3_DIS structure functions. For τ-lepton propagation, we used the MUM code [28] that was updated taking into account the corrections for photonuclear interactions of τ leptons [29]. Some details of the calculations and the resulting neutrino fluxes of all flavors after propagation through the Earth were presented in our previous work [30].

The rate of totally contained double-bang events is given by the formula

$$N = 2\pi\rho N_{\rm A}\int\limits_{-1}^{1}\int\limits_{E_{\rm min}}^{\infty} V_{\rm eff}(E_{\nu_\tau},\theta) \times I(E_{\nu_\tau},\theta)\sigma^{\rm CC}(E_{\nu_\tau})dE_{\nu_\tau}d\cos\theta.$$

Here, $N_{\rm A}$ is the Avogadro number, ρ is the density of the medium (we use $\rho = 1$ g cm^{-3}, which is close to sea water/ice density), $I(E_{\nu_\tau},\theta)$ is the differential ν_τ flux entering the detector at the zenith angle θ, and $\sigma^{\rm CC}$ is the total deep inelastic neutrino cross section (charge current part). $V_{\rm eff}$ is the effective volume given by the relation

$$V_{\rm eff}(E_{\nu_\tau},\theta) = S_p(\theta)(L - R_\tau(E_{\nu_\tau})),$$

where S_p is the projected area for the tracks generated isotropically in azimuth at the fixed θ directions on a detector of parallelepiped form, L is the geometrical distance between the entry and exit point, and R_τ is the τ-lepton range. The minimum value of the neutrino energy $E_{\rm min} = 2\times10^6$ GeV corresponds to a τ-lepton range of $R_\tau^{\rm min} = 70$ m.

The double-bang topology can be considered as a background free signature of τ-neutrino appearance [1], since there should be no atmospheric muons that could produce in the detector two showers with comparable amounts of photons. Nevertheless, this reasonable assumption needs to be verified through a full simulation.

Concrete calculations were done for two geometries of the neutrino detector:

$$1\times1\times1\ {\rm km}\quad ({\rm IceCube\text{-}like}\,[31]),$$
$$1.4\times1.4\times0.6\ {\rm km}\quad ({\rm NEMO\text{-}like}\,[32]).$$

In the table, the corresponding double-bang rates for the lower, upper, and both hemispheres are shown. The calculated values for the upper hemisphere are 3–6 times lower compared to [26], since more optimistic predictions for diffuse neutrino fluxes were used there.

Finally, we found, using the theoretical predictions in [18, 21] for AGN diffuse neutrino fluxes, that in a 1-km^3 neutrino telescope one can expect a marginally observable rate of double-bang events from τ neutrinos.

REFERENCES

1. J. G. Learned and S. Pakvasa, Astropart. Phys. **3**, 267 (1995).
2. F. Halzen and D. Saltzberg, hep-ph/9804354.
3. J. G. Learned and K. Mannheim, Ann. Rev. Nucl. Part. Sci. **50**, 679 (2000).
4. G. Barenboin and C. Quigg, Phys. Rev. D **67**, 073024 (2003).
5. H. Athar *et al.*, hep-ph/0112222.
6. J. F. Beacom *et al.*, Phys. Rev. Lett. **90**, 181301 (2003).
7. P. Bhattacharjee and G. Sigl, Phys. Rep. **327**, 109 (2000).
8. I. M. Albuquerque, L. Hiu, and E. W. Kolb, Phys. Rev. D **64**, 083504 (2001).
9. J. H. MacGibbon and B. J. Carr, Astrophys. J. **371**, 447 (1991); E. V. Bugaev and K. V. Konishchev, Phys. Rev. D **65**, 123005 (2002).
10. J. H. MacGibbon and U. F. Wichoski, hep-ph/0111436.
11. J. F. Beacom *et al.*, hep-ph/0307025.
12. R. Engel, D. Seckel, and T. Stanev, Phys. Rev. D **64**, 093010 (2001); O. E. Kalashev *et al.*, Phys. Rev. D **65**, 103003 (2002).
13. G. Sigl *et al.*, Phys. Rev. D **59**, 043504 (1999).
14. S. Yoshida, G. Sigl, and S. Lee, Phys. Rev. Lett. **81**, 5505 (1998); T. J. Weiler, Astropart. Phys. **11**, 303 (1999).
15. J. L. Feng *et al.*, Phys. Rev. Lett. **88**, 161102 (2002).
16. T. Abu-Zayyad *et al.*, Astrophys. J. **557**, 686 (2001).
17. Pierre Auger Observatory, http://www.auger.org.
18. K. Mannheim, R. J. Protheroe, and J. P. Rachen, Phys. Rev. D **63**, 023003 (2001).
19. K. Mannheim, Astropart. Phys. **3**, 295 (1995).
20. F. Halzen and E. Zas, Astrophys. J. **488**, 669 (1997).
21. R. J. Protheroe, Astron. Soc. Pac. **163**, 585 (1997).

22. F. W. Stecker and M. H. Salamon, Space Sci. Rev. **75**, 341 (1996).
23. A. A. Zdziarski, Mon. Not. R. Astron. Soc. **281**, L9 (1996).
24. J. Ahrenc *et al.*, astro-ph/0303218.
25. V. Aynutdinov *et al.*, astro-ph/0305302.
26. H. Athar *et al.*, Phys. Rev. D **62**, 093010 (2000).
27. S. I. Dutta *et al.*, Phys. Rev. D **62**, 123001 (2000); **66**, 077302 (2002).
28. I. A. Sokalski, E. V. Bugaev, and S. I. Klimushin, Phys. Rev. D **64**, 074015 (2001).
29. E. V. Bugaev and Yu. Shlepin, Phys. Rev. D **67**, 034027 (2003).
30. E. V. Bugaev, T. Montaruli, and I. A. Sokalski, astro-ph/0305284.
31. IceCube Project, http://icecube.wisc.edu.
32. NEMO Project, http://nemoweb.lns.infn.it.

Physics of Atomic Nuclei, Vol. 67, No. 6, 2004, pp. 1182–1187. From Yadernaya Fizika, Vol. 67, No. 6, 2004, pp. 1204–1209.

NEUTRINO PHYSICS AND ASTROPHYSICS

Lithium Experiment on Solar Neutrinos to Weight the CNO Cycle*

A. V. Kopylov, I. V. Orekhov, V. V. Petukhov, A. E. Solomatin, and M. N. Arnoldov[1)]**

Institute for Nuclear Research, Russian Academy of Sciences,
pr. Shestidesyatiletiya Oktyabrya 7a, Moscow, 117312 Russia

Received December 1, 2003

Abstract—The measurement of the flux of beryllium neutrinos with an accuracy of about 10% and CNO neutrinos with an accuracy of 20–30% will enable one to find the flux of *pp* neutrinos in the source with an accuracy better than 1% using the luminosity constraint. The future experiments on νe^- scattering will enable one to measure with very good accuracy the flux of beryllium and *pp* neutrinos on the Earth. The ratio of the flux of *pp* neutrinos on the Earth and in the source will enable one to find with very good accuracy a mixing angle $\theta_\odot$. A lithium detector has high sensitivity to CNO neutrinos and can find the contribution of the CNO cycle to the energy generated in the Sun. This will be a stringent test of the theory of stellar evolution and combined with other experiments will provide a precise determination of the flux of *pp* neutrinos in the source and a mixing angle $\theta_\odot$. The work on the development of the technology of a lithium experiment is now in progress. © *2004 MAIK "Nauka/Interperiodica".*

The remarkable progress achieved in a number of experiments with solar neutrinos [1] with a culmination of KamLAND [2] has shown unambiguously that solar neutrinos do oscillate and the parameters of neutrino oscillations belong to the MSW LMA region [3], which is now split into two subregions, so that at 3σ we have[2)]

$$5.1 \times 10^{-5} < \Delta m^2 < 9.7 \times 10^{-5}\ \text{eV}^2,$$

$$1.2 \times 10^{-4} < \Delta m^2 < 1.9 \times 10^{-4}\ \text{eV}^2,$$

for a mixing angle $\theta_\odot$

$$0.29 < \tan^2\theta_\odot < 0.86.$$

The peculiar thing is that probably the most decisive result about oscillation of solar neutrinos was obtained in an experiment (KamLAND) detecting not solar neutrinos but antineutrinos from reactors.

Further progress can be achieved by increasing the accuracy of measurements of neutrino fluxes. Here, some new aspect has arisen, which is connected with the possibility of drastically increasing the accuracy in the evaluation of the contribution of the *pp* chain to the total luminosity of the Sun. The luminosity constrained was first suggested on a quantitative basis by Spiro and Vignaud [4]. The point is that, as is known, there are basically two sources of solar energy: the *pp* chain of reactions and CNO cycle; the latter is presented in Fig. 1. Each neutrino source contributes a definite value to the solar luminosity, so that the energy balance can be written

$$0.913 f_{pp} + 0.002 f_{pep} + 0.07 f_{\text{Be}} + 0.0071 f_{\text{N}} + 0.0079 f_{\text{O}} = 1 \quad (1)$$

for all neutrino sources with the coefficient by the reduced neutrino flux >0.0001. Here, the neutrino fluxes f_x are given in a reduced (relative to the predicted ones by the standard solar model (SSM) BP2000 [5]) and the solar luminosity is normalized to 1. The coefficients at f_{pp}, f_{pep}, and f_{Be} were obtained from values of Table 1 [6]. The coefficients at f_{N} and f_{O} were calculated by taking into account the energy produced for each ^{13}N neutrino in a first half-cycle CNO,

$$\alpha(^{13}\text{N}) = M(^{12}\text{C}) + 2M(^1\text{H}) - M(^{14}\text{N}) - \langle E_\nu\rangle(^{13}\text{N}) = 11.00\ \text{MeV}, \quad (2)$$

and for each ^{15}O neutrino for the second half-cycle CNO,

$$\alpha(^{15}\text{O}) = M(^{14}\text{N}) + 2M(^1\text{H}) - M(^4\text{He}) - M(^{12}\text{C}) - \langle E_\nu\rangle(^{15}\text{O}) = 14.01\ \text{MeV}. \quad (3)$$

At the present epoch of the evolution of the Sun, the CNO cycle is closed; i.e., the concentration of ^{14}N

*This article was submitted by the authors in English.

1)Institute of Physics and Power Engineering, Obninsk, Russia.

**e-mail: kopylov@al20.inr.troitsk.ru

2)The new results in SNO experiment (nucl-ex/0309004) have shown (at 1σ) that $\Delta m^2 = 7.1^{+1.2}_{-0.6}$ eV^2 and $\theta = 32.5^{+2.1}_{-2.3}$ deg.

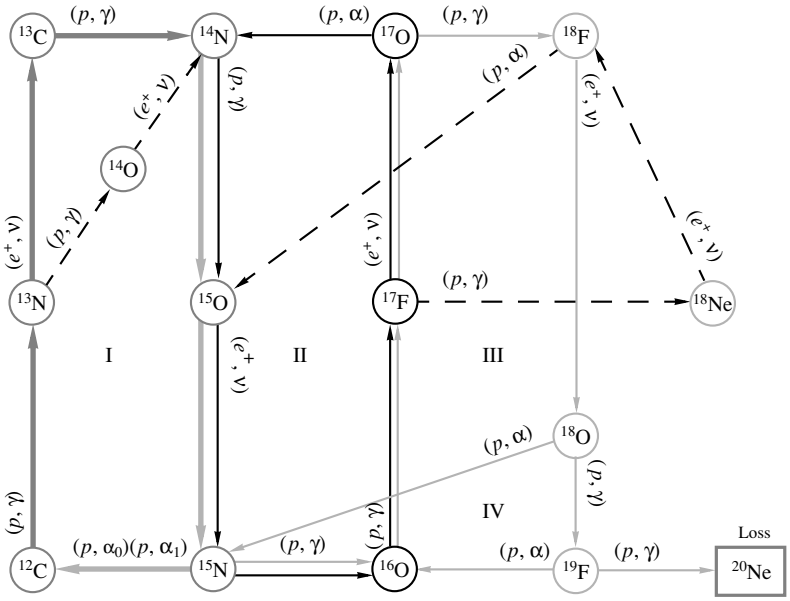

Fig. 1. The CNO cycle of thermonuclear reactions.

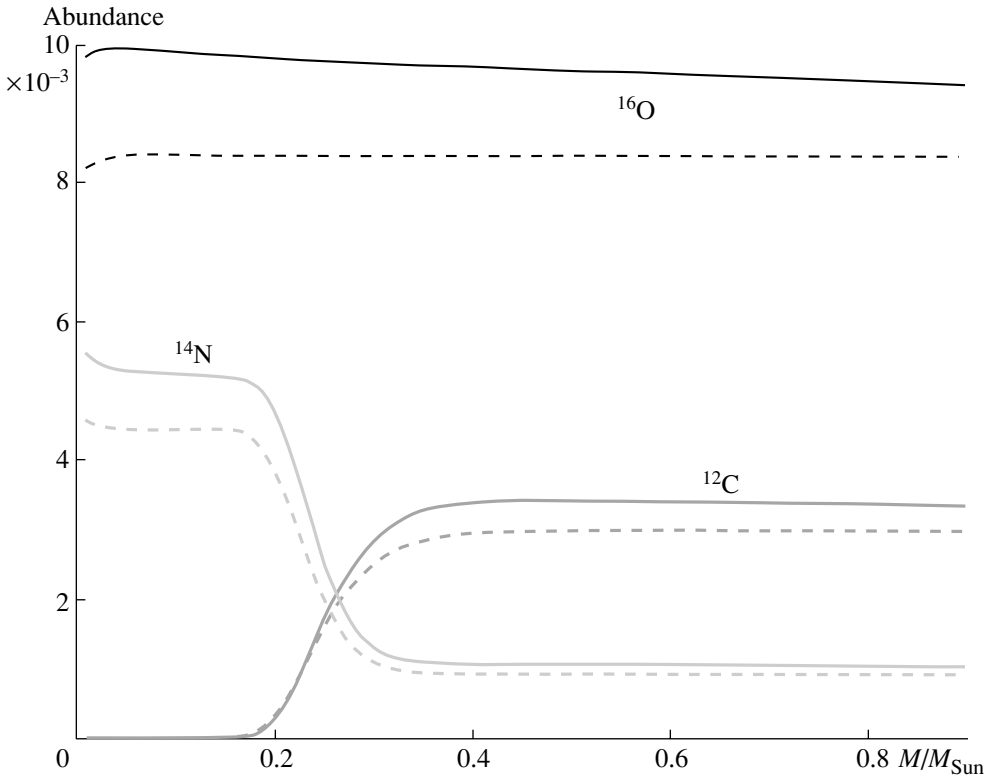

Fig. 2. The abundances of ^{12}C and ^{14}N in the interior of the Sun with diffusion in the matter of the Sun (solid curves) and without diffusion (dashed curves).

is close to the equilibrium one, as one can see from Fig. 2, drawn according to the numbers presented in Table 4.4 from [7]. At the early stage of solar evolution, the abundance of ^{14}N in the interior of the Sun is still low; consequently, the CNO cycle is not yet closed. From expression (1), it follows that beryllium neutrinos contribute 7% to the solar luminosity, while the CNO cycle (neutrinos from ^{13}N and ^{15}O) contributes

Standard Model predictions (BP2000): solar neutrino fluxes and neutrino capture rates, with 1σ uncertainties from all sources (combined quadratically)

Source	Flux, 10^{10} cm^{-2} s^{-1}	Cl, SNU	Ga, SNU	Li, SNU
pp	$5.95(1.00^{+0.01}_{-0.01})$	0.0	69.7	0.0
pep	$1.40 \times 10^{-2}(1.00^{+0.015}_{-0.015})$	0.22	2.8	9.2
hep	9.3×10^{-7}	0.04	0.1	0.1
^{7}Be	$4.77 \times 10^{-1}(1.00^{+0.10}_{-0.10})$	1.15	34.2	9.1
^{8}B	$5.05 \times 10^{-4}(1.00^{+0.20}_{-0.16})$	5.76	12.1	19.7
^{13}N	$5.48 \times 10^{-2}(1.00^{+0.21}_{-0.17})$	0.09	3.4	2.3
^{15}O	$4.80 \times 10^{-2}(1.00^{+0.25}_{-0.19})$	0.33	5.5	11.8
^{17}F	$5.63 \times 10^{-4}(1.00^{+0.25}_{-0.25})$	0.0	0.1	0.1
Total		$7.6^{+1.3}_{-1.1}$	128^{+9}_{-7}	$52.3^{+6.5}_{-6.0}$

only 1.5%. Thus, according to SSM, the contribution of the CNO cycle to the total energy generated in the Sun is small, but, nevertheless, at a certain phase of the experiment this will be the principal limitation in evaluating the physical quantities. For example, if the flux of beryllium neutrinos is evaluated with an accuracy better than 10%, the beryllium uncertainty will be less than 1% [8], so that the major uncertainty to the luminosity in this case will come from the CNO cycle. Then the measurement of the flux of neutrinos from the CNO cycle with an accuracy of about 20–30% will enable one to find the flux of *pp* neutrinos in the source with an accuracy better than 1%. At the present time, a new generation of solar neutrinos is under development. Some of these detectors are oriented to measure precisely the flux of *pp* neutrinos on the Earth by means of νe^- scattering [9]. The cross section of this reaction is calculated with high accuracy, so principally they can do the high-precision measurements. The effect in the νe^- scattering experiment is determined mainly by electron neutrinos; the contribution of neutrinos of other flavors is small and easily calculable. The ratio of these two values, the flux of electron *pp* neutrinos on the Earth and the flux of *pp* neutrinos in the source, i.e., in the Sun, will give the survival probability and, consequently, a mixing angle. This is a very good approach. In some way, it is similar to the "charge current–neutral current" strategy in the SNO experiment. But here one value, the flux of *pp* neutrinos in the source, is found by measuring the flux of beryllium and CNO neutrinos, while the other value, the flux of electron *pp* neutrinos on the Earth, is found by measuring the effect in a νe^--scattering detector. This strategy becomes possible only because the contribution to the solar luminosity of beryllium and CNO neutrino-generated reactions is relatively small, so that modest accuracy in the evaluation of the flux of these neutrinos produces with high accuracy the flux of *pp* neutrinos in the source.

The present limit for the contribution of the CNO cycle is 7.3% [10]. In the next few years, even in an optimistic scenario of progress with the solar neutrino experiments, it will hardly be possible to decrease this limit below 5%. Therefore, future experiments will not be able to exclude the weight of the CNO cycle in the solar energy as much as 4.5%. But in this case, the weight of a *pp* chain will be not 98.5%, as is estimated now, but only 95.5%. The difference is 3% and this is a fundamental limitation. The accuracy in the evaluation of the flux of *pp* neutrinos generated in the Sun will be limited by this uncertainty. Thus, to go further, one needs to know the real weight of the CNO cycle. This can be done by a lithium detector because it has high sensitivity to neutrinos generated in the CNO cycle, which contribute 30% to the expected rate. If the accuracy in a lithium experiment is on the level of 10%, then the weight of CNO neutrinos will be determined with an uncertainty of about 0.5% in the absolute value of the contribution to the solar luminosity. This result will be important for two reasons. First, it will provide direct proof of the theory of stellar evolution. So far, we have no experimental evidence that the CNO cycle does exist. These data will show how correct is our understanding of the evolution of the stars. For main sequence stars with higher temperature than the Sun, the CNO cycle is a major source of energy. In fact, the fate of the Sun is also a CNO cycle star. Figure 2 shows the expected concentrations of ^{12}C and ^{14}N in the interior of the Sun. One can see a peculiar distribution of these isotopes across the radius of the Sun. Carbon is

burned in nuclear reactions, while nitrogen is accumulated until the equilibrium concentration. To test experimentally whether the real picture corresponds to our understanding is very important.

The second reason is that these data combined with the results of other experiments will enable one to find with unprecedented accuracy the flux of *pp* neutrinos in the source and the mixing angle $\theta_\odot$ from the ratio of the flux of electron neutrinos on Earth to the one in the source.

The rates in a lithium detector from different neutrino sources are presented in Table 1 [10]. If one takes the mixing angle $\tan^2\theta = 0.41$, the total rate will be 21 SNU, and the contribution of the CNO cycle is 30%. To find the flux of CNO neutrinos, one should subtract the rates from *pep*, ^{7}Be, and ^{8}B neutrinos. Even the current accuracies in the evaluation of these fluxes and of mixing angle theta solar enable one to do it taking into consideration that an accuracy of 20–30% in the evaluation of the fluxes from the CNO cycle is adequate for the task, as was explained earlier. The flux of *pep* neutrinos is found from the flux of *pp* neutrinos because the ratio of these fluxes is well known. More accurate measurement of the flux of beryllium neutrinos will help in a further correction of data. This will be done in the Borexino and KamLAND experiments. Thus, for further progress in the study of solar neutrinos, it is vital to measure the capture rate by a lithium target. There is some ambiguity due to an unknown factor: What is the contribution of ^{13}N and ^{15}O neutrinos? In fact, the situation in this aspect is quite good for a lithium target because due to a relatively high threshold of this detector the rate from ^{13}N neutrinos is much less than the one from ^{15}O neutrinos: the ratio is approximately 1/5 (see Table 1 in [6]). This helps in the interpretation of the data because the uncertainty of the rate from CNO neutrinos depends mainly upon the uncertainty of the ^{15}O neutrino flux.

To find the contribution of beryllium neutrinos, one should know not only the flux of beryllium neutrinos but also the shape of the energy spectrum of these neutrinos due to thermal broadening. The details of this were discussed in [11]. The point is that, in laboratory conditions, the ^{7}Be line will not produce ^{7}Be on lithium since the reaction of ^{7}Be production is reverse to electron capture by ^{7}Be. If one considers electron screening in terrestrial atoms, the energy of the beryllium line is even lower than the threshold for ^{7}Be production. But in the Sun, high temperature produces thermal broadening of the ^{7}Be line, as was discussed in [12] and later was computed with high accuracy by Bahcall [13]. Because of this, some fraction of the line with energy higher than the threshold will produce ^{7}Be. The effect is model dependent. The fact that the measured flux of boron neutrinos is in good agreement with the one predicted by BP2000 shows that the model gives the correct temperature map of the interior of the Sun; hence, there is good reasoning to believe that the thermal broadening of the beryllium line is described by the model correctly.

The substantial issue is that, while the contribution of the CNO cycle to the solar energy is only 1.5%, the weight of neutrinos from the CNO cycle in the production rate of ^{7}Be on ^{7}Li is about 30%, so that, for the total capture rate expected for a lithium target of 21 SNU, neutrinos from the CNO cycle contribute 7 SNU. If we take the parameters of neutrino oscillations from the allowed region, make the estimates for a detector with 10 t of lithium, and take pure statistical uncertainties, then the capture rate on a lithium target can be measured with an accuracy of approximately 1 SNU for 16 runs total performed during four years of measurements. Here, the efficiency of counting of ^{7}Be was taken to be about 90%, which is, in principle, possible to do by means of cryogenic detectors [14]. After subtracting the rate from these three sources of a *pp* chain, one gets the rate from neutrinos of the CNO cycle. Now we have two possibilities: first, we can take the ratio of ^{13}N to ^{15}O neutrinos as a given by a SSM, or we can find separately the contribution of these two neutrino sources to the total capture rate solving the system of two equations

$$\begin{cases} L_{\rm H} + L_{\rm CN} + L_{\rm NO} = L_\odot, \\ R_{\rm H} + R_{\rm CN} + R_{\rm NO} = R_{\rm Li}. \end{cases} \quad (4)$$

Here, $L_{\rm H}$, $L_{\rm CN}$, and $L_{\rm NO}$ are the contributions to the solar luminosity of the *pp* chain and two half-cycles of the CNO cycle; $R_{\rm Li}$ and $R_{\rm H}$ are the measured and estimated rates for the hydrogen sequence in a lithium detector; $R_{\rm CN}$ and $R_{\rm NO}$ mean the rates from neutrinos born in ^{13}N and ^{15}O decays; $R = yL/4\pi r_{\rm Sun}^2\varepsilon$, where $r_{\rm Sun}$ is the distance from the Sun to the Earth, ε is the energy contributed to the Sun per one neutrino emitted in each half-cycle of the CNO cycle, and y is the capture rate per one neutrino of ^{13}N or ^{15}O spectra. One can see from these equations that, in principle, it is possible to find separately the fluxes of ^{13}N and ^{15}O neutrinos. The contributions of the energies associated with ^{13}N and ^{15}O neutrinos are close, as one can see from expressions (2) and (3). As concerns the rate of a lithium detector, the situation here is very different. The contribution of ^{15}O neutrinos is 5 times bigger than the one of ^{13}N neutrinos. In other words, the straight lines corresponding to equations of the system (4) are not parallel and the system of equations has a solution.

The idea to use a lithium target for the detection of solar neutrinos was expressed on the eve of solar neutrino research [15], and this subject was investigated in a number of papers [14, 16]. A lithium experiment is a radiochemical experiment, and as a target, metallic lithium is planned to be used. The solar neutrinos are captured by ^{7}Li (the abundance is 92%) and ^{7}Be is produced in the reaction

$$^7\mathrm{Li} + \nu \rightarrow {}^7\mathrm{Be} + e^-.$$

The isotope ^{7}Be has a half-life of 53 d and decays to ^{7}Li by means of electron capture. The aim is to extract ^{7}Be from lithium and to count the number of extracted atoms. The measured capture rate is converted into a neutrino flux. The main advantage of a lithium detector is that the transition ^{7}Be–^{7}Li is superallowed; hence, the cross section can be calculated with very good accuracy, as was done in [13]. How does one extract beryllium from metallic lithium? The basic principle is the following. The chemical compounds of beryllium with nitrogen (Be_3N_2) and oxygen (BeO) have extremely low solubility in lithium, on the level of 10^{-13} mole percent. At the beginning of the exposure, some of the beryllium sample (about 10 mg) is introduced into the target (10 t of lithium). This concentration of beryllium by far exceeds the equilibrium quantity. Beryllium captures nitrogen or oxygen atoms which are always present in lithium as impurities and is converted into a beryllium nitride or beryllium oxide. The same happens with the beryllium atom produced by solar neutrinos. These compounds of beryllium are ready to precipitate on any surface provided that they make contact with it. This condition is rarely realized in a bulk quantity of lithium because the ratio of the surface to the volume is negligible. But if a stream of lithium is passed through a fine-mesh filter with a very large surface, this contact is guaranteed. Thus, the extraction procedure consists in pumping lithium through a filter and then collecting the beryllium atoms by means of extraction from an aqueous phase, where all beryllium present on a lithium film from the filter is dissolved. The optimization of the technology consists in finding the conditions under which the extraction process is efficient. Initially, the work was done with samples of ^{7}Be produced in lithium by protons with an energy of about 10–100 MeV. This is not very good technology because ^{7}Be is produced mainly on the surface of the sample, not inside of the lithium sample, and the extraction of ^{7}Be produced by this method was far from the real experimental conditions. Now we use 14-MeV neutrons of a D–T neutron source as a ^{7}Be generator. Using this method, one can guarantee that ^{7}Be is really produced inside of a lithium sample. Another problem is how to count the extracted atoms of ^{7}Be. Through the decay of ^{7}Be, an Auger electron is released with an energy of 55 eV. This energy is too small for counting by the traditional counting technique. In principle, it is possible to use a cryogenic detector, as was demonstrated in [14]. This method is the only possible way to get high-precision measurements. But as was shown earlier, it is not absolutely necessary to have accuracy of measurements on the level of 1 SNU. A good physical result will be obtained even with the modest accuracy of about 5 SNU (25%). In this case, one can use an efficiency of counting of about 8%. ^{7}Be decays 10% of the time to the excited level of ^{7}Li, which emits a gamma with an energy of 478 keV. This energy is very convenient for counting. In the background spectrum, there is a very populated line at 511 keV, so to discriminate the background from this line one should use a gamma spectrometer with a very good energy resolution. This can be realized by means of a low-background gamma spectrometer using high-purity germanium detectors. The assembly of the detectors which can be used in this case is similar to one module planned to be used in a Majorana project [17]. The work on the development of the technique of a lithium detector is now in progress at the Institute for Nuclear Research, Russian Academy of Sciences, in Moscow and at the Institute of Physics and Power Engineering in Obninsk.

To summarize, we should note that a lithium experiment is the only way to find with unprecedented accuracy the energy produced by a *pp* chain of reactions in the interior of the Sun by means of measuring the fluxes of neutrinos generated in the CNO cycle. This information is vital for further study of the thermonuclear processes in the interior of the Sun and can be effectively used for precise measurement of the mixing angle $\theta_\odot$. The study of CNO is very important also as a precise test of the theory of stellar evolution.

ACKNOWLEDGMENTS

This work was supported in part by the Russian Foundation for Basic Research (project no. 01-02-16167-A) and by the grant of Russia Leading Scientific Schools LSS-1782.2003.2.

We deeply appreciate the very stimulating discussions with G. Zatsepin, L. Bezrukov, V. Kuzmin, and V. Rubakov.

REFERENCES

1. B. T. Cleveland *et al.*, Astrophys. J. **496**, 505 (1998); J. N. Abdurashitov *et al.*, JETP **95**, 181 (2002); W. Hampel *et al.* (GALLEX Collab.), Phys. Lett. B **447**, 127 (1999); T. Kirsten, *Talk Given at the XX International Conference on Neutrino Physics and*

Astrophysics (NU2002), Munich, Germany, 2002; M. Altmann *et al.*, Phys. Lett. B **490**, 16 (2000); E. Bellotti *et al.* (GNO Collab.), Nucl. Phys. B (Proc. Suppl.) **91**, 44 (2001); Y. Fukuda *et al.*, Phys. Rev. Lett. **77**, 1683 (1996); S. Fukuda *et al.*, Phys. Rev. Lett. **86**, 5651 (2001); Q. R. Ahmad *et al.* (SNO Collab.), Phys. Rev. Lett. **87**, 071301 (2001); **89**, 11301 (2002).

2. K. Eguchi *et al.* (KamLAND Collab.), hep-ex/0212021.
3. V. Barger and D. Marfatia, hep-ph/0212126; G. L. Fogli, E. Lisi, A. Marrone, and D. Montanino, hep-ph/0212127; M. Maltoni, T. Schwetz, and J. W. F. Valle, hep-ph/0212129; A. Bandyopadhyay, S. Choubey, R. Gandi, and S. Goswami, hep-ph/0212146; J. N. Bahcall, M. C. Gonzalez-Garcia, and C. Peña-Garay, hep-ph/0212147; P. C. de Hollanda and A. Yu. Smirnov, hep-ph/0212270.
4. M. Spiro and D. Vignaud, Phys. Lett. B **242**, 279 (1990).
5. J. N. Bahcall, M. N. Pinsonneault, and S. Basu, astro-ph/0010346.
6. J. N. Bahcall, hep-ph/0108148.
7. J. N. Bahcall, *Neutrino Astrophysics* (Cambridge Univ. Press, Cambridge, 1998).
8. A. Kopylov, *Lithium Project*, in *LowNU2003 Conference, Paris, France, 2003*; A. Kopylov and V. Petukhov, hep-ph/0301016; hep-ph/0306148.
9. M. Nakahata, *XMASS Project*, in *LowNU2003 Conference, Paris, France, 2003*.
10. J. N. Bahcall, M. C. Gonzalez-Garcia, and C. Peña-Garay, astro-ph/0212331.
11. J. N. Bahcall, Preprint IASSNS-AST 93/40 (1994).
12. G. V. Domogatsky, Preprint No. 153, FIAN (Moscow, 1969).
13. J. N. Bahcall, Rev. Mod. Phys. **50**, 881 (1978).
14. M. Galeazzi, G. Gallinaro, F. Gatti, *et al.*, Phys. Lett. B **398**, 187 (1997).
15. J. N. Bahcall, Phys. Lett. **3**, 332 (1964); G. T. Zatsepin and V. A. Kuzmin, in *Proceedings of the 9th ICRC, London, 1965*, p. 1024.
16. J. K. Rowly, in *Proceedings of the Conference on Status and Future of Solar Neutrino Research, BNL, 1978*, p. 265; E. P. Veretenkin, V. N. Gavrin, and E. A. Yanovich, At. Energy **58**, 65 (1985); A. V. Kopylov, A. N. Likhovid, E. A. Yanovich, and G. T. Zatsepin, in *Proceedings of the International School on Particles and Cosmology, Baksan Valley, Russia, 1993*, Ed. by E. N. Alekseev, V. A. Matveev, Kh. S. Nirov, and V. A. Rubakov (World Sci., Singapore, 1993), p. 63; S. N. Danshin, G. T. Zatsepin, A. V. Kopylov, *et al.*, Fiz. Élem. Chastits At. Yadra **28**, 3 (1997) [Phys. Part. Nucl. **28**, 1 (1997)]; A. V. Kopylov, Phys. At. Nucl. **63**, 1272 (2000).
17. F. Avignone, this Conference.

Physics of Atomic Nuclei, Vol. 67, No. 6, 2004, pp. 1188–1194. From Yadernaya Fizika, Vol. 67, No. 6, 2004, pp. 1210–1216.

DARK MATTER

WMAP Data and Recent Developments in Supersymmetric Dark Matter*

U. Chattopadhyay[1)], A. Corsetti, and P. Nath**

Department of Physics, Northeastern University, Boston, USA

Received November 4, 2003

Abstract—A brief review is given of the recent developments in the analyses of supersymmetric dark matter. Chief among these is the very accurate determination of the amount of cold dark matter in the universe from analyses using WMAP data. The implications of this data for the mSUGRA parameter space are analyzed. It is shown that the data admits solutions on the hyperbolic branch of the radiative breaking of the electroweak symmetry. A part of the hyperbolic branch lies in the so-called inversion region, where the LSP neutralino χ_1^0 becomes essentially a pure Higgsino and degenerates with the next-to-the-lightest neutralino χ_2^0 and the light chargino $\chi_1^\pm$. Thus, some of the conventional signals for the observation of supersymmetry in colliders (e.g., the missing energy signals) do not operate in this region. On the other hand, the inversion region contains a high degree of degeneracy of $\chi_1^0, \chi_2^0, \chi_1^\pm$ leading to coannihilations, which allow for the satisfaction of the WMAP relic density constraints deep on the hyperbolic branch. Further, an analysis of the neutralino–proton cross sections in this region reveals that this region can still be accessible to dark matter experiments in the future. Constraints from $g_\mu - 2$ and from $B_s^0 \to \mu^+\mu^-$ are discussed. Future prospects are also discussed. © *2004 MAIK "Nauka/Interperiodica".*

1. INTRODUCTION

Very recently, the data from the Wilkinson Microwave Anisotropy Probe (WMAP) has allowed analyses of the cosmological parameters to a high degree of accuracy [1, 2]. These analyses also indicate unambiguously the existence of cold dark matter (CDM) and put sharp limits on it. At the same time, over the past decade experiments for the direct detection of dark matter have made enormous progress [3–6], with reliable limits emerging on the CDM component in direct laboratory experiments. Further, experiments are planned which in the future will be able to improve the sensitivities by several orders of magnitude [7–9]. In this paper we will give a brief review of the recent developments in supersymmetric dark matter. (For a sample of other recent reviews see [10].) We will review the constraints on the analyses of dark matter from $g_\mu - 2$ and from $B_{s,d}^0 \to \mu^+\mu^-$. We will also discuss the effects of nonuniversalities and the effects of the constraints of Yukawa coupling unification. One of the main focuses of our analysis will be the study of dark matter on the hyperbolic branch [11] (and focus point region [12], which is a subpiece of the hyperbolic branch) and its implications for the discovery of supersymmetry [13]. As is well known, SUGRA models with R parity provide a candidate for supersymmetric dark matter. This is so because in SUGRA unified models [14, 15] one finds that over a large part of the parameter space the lightest supersymmetric particle (LSP) is the lightest neutralino, which with R parity conservation becomes a candidate for cold dark matter. (An interesting alternate possibility discussed recently is that of axionic dark matter [16].) In the simplest version of SUGRA models [14, 15], mSUGRA, which is based on a flat Kähler potential, the soft sector of the theory is parametrized by $m_0, m_{1/2}, A_0, \tan\beta$, where m_0 is the universal scalar mass, $m_{1/2}$ is the universal gaugino mass, A_0 is universal trilinear coupling, and $\tan\beta = \langle H_2\rangle/\langle H_1\rangle$, where H_2 gives mass to the up quark and H_1 gives mass to the down quark and the lepton. The minimal model can be extended by considering a curved Kähler manifold and also a curved gauge kinetic energy function. Specifically, these allow one to include nonuniversalities in the Higgs sector, in the third generation sector, and in the gaugino sector consistent with flavor changing neutral currents [17–21].

2. CONSTRAINTS ON DARK MATTER ANALYSES

There are a number of constraints that must be imposed in the theoretical analyses of supersymmetric dark matter. These include the constraints from

*This article was submitted by the authors in English.

[1)]Department of Theoretical Physics, Indian Association for the Cultivation of Science, Jadavpur, Kolkata, India; e-mail: tpuc@iacs.res.in

** e-mail: nath@neu.edu

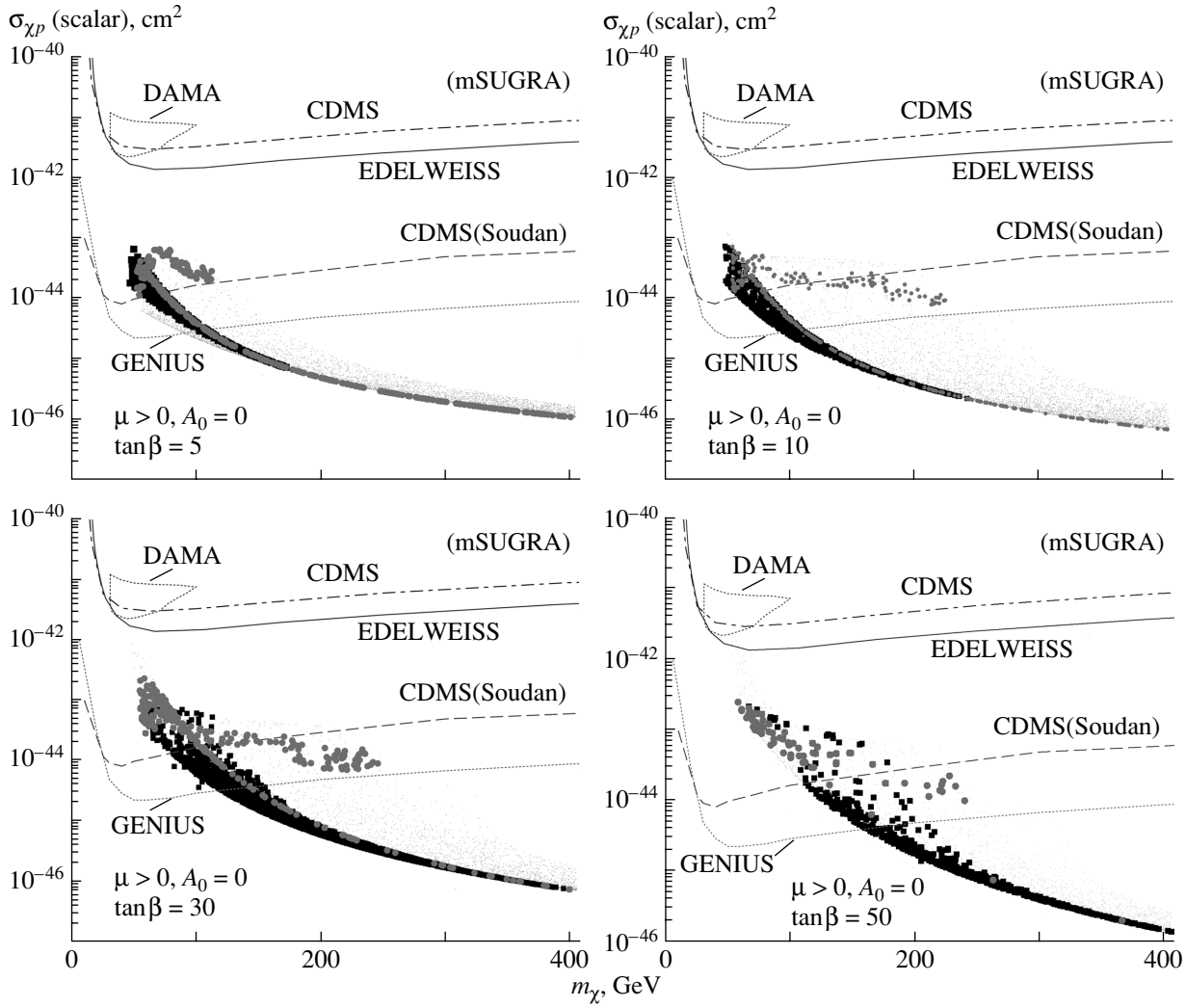

Fig. 1. Exhibition of the neutralino–proton scalar cross section for values of $\tan\beta$ of 5, 10, 30, 50 and $A_0 = 0$, and $\mu > 0$. The dots are the points satisfying mSUGRA constraints and the grey circles additionally satisfy the relic density constraint of $0.1 < \Omega h^2 < 0.3$. The black squares satisfy the 2σ constraint on $b \to s + \gamma$ and $g_\mu - 2$. The limits of various current and future experiments are also indicated. (Taken from [27].)

$g_\mu - 2$, the flavor changing neutral current (FCNC) constraints, constraints from $B_s^0 \to \mu^+\mu^-$ limits, and constraints from the currents limits on the relic density for cold dark matter. Here we discuss some of these. We begin with a discussion of the $g_\mu - 2$ constraint. The analysis of $g_\mu - 2$ has been under scrutiny for a considerable period of time. In supersymmetry, it is predicted that the effects of supersymmetric electroweak corrections to $g_\mu - 2$ can be of the same size as the standard model electroweak [22]. Furthermore, the sign of the supersymmetric electroweak correction is correlated with the sign of the Higgs mixing parameter μ [23, 24]. It is also known that the effects of extra dimensions on $g_\mu - 2$ are substantially smaller than the effects from supersymmetric loop corrections [25]. Experimentally, the situation is still somewhat unsettled due to the ambiguity in the errors of the hadronic corrections. A recent estimate of the difference between experiment and the standard model gives [26] a $\sim 3\sigma$ effect. Further, the sign of the difference in these analyses is positive indicating a positive μ. In Fig. 1 we give a numerical analysis of the neutralino–proton cross section $\sigma_{\chi p}$, which enters in the direct detection of dark matter. The results are taken from the analysis of [27]. The analysis shows that the $g_\mu - 2$ constraint is very strong and eliminates a large part of the parameters space consistent with the relic density constraints. The analysis also shows that a very substantial part of the parameter space consistent with $g_\mu - 2$ and relic density constraints will be accessible to future dark matter detectors.

We turn now to the implications of a positive μ for

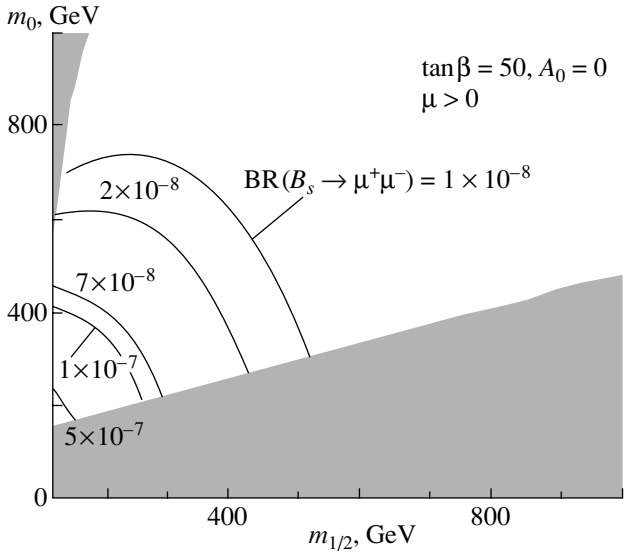

Fig. 2. An exhibition of the allowed parameter space in m_0–$m_{1/2}$ from the limits on the $B_s^0 \to \mu^+\mu^-$ branching ratio. (Taken from [13].)

Yukawa coupling unification and the implications of the Yukawa unification constraint on supersymmetric dark matter analyses. It is known that b–τ unification prefers $\mu < 0$ [28]. The above arises from the fact that a negative correction to the b-quark mass is desired for b–τ unification and a negative correction is most readily manufactured if μ is negative. However, closer scrutiny shows that the sign of the loop correction to the b-quark mass is not rigidly tied to the sign of μ. Thus the dominant correction to the b-quark mass arises from the gluino exchange diagram and the sign of this correction is determined by the sign of $\mu M_{\tilde{g}}$ (see [29] and the references quoted therein). At same time, the supersymmetric correction to $g_\mu - 2$ is governed mainly by the chargino exchange and the sign of that contribution is determined by the term $\mu\tilde{m}_2$ [30]. Thus it is possible to relax the rigid relationship between the μ sign and the sign of the loop correction to the b-quark mass while maintaining the usual connection between the sign of μ and the sign of the supersymmetric loop correction to $g_\mu - 2$. The solution to this relaxation is provided by nonuniversalities that allow one to switch the sign of $M_{\tilde{g}}$ relative to the sign of $\tilde{m}_2$. This switch in sign can be seen to arise group theoretically when the gaugino mass terms have nontrivial group transformations. Thus, for example, in $SU(5)$ the gaugino masses in general transform like the $(24 \times 24)_s$ representation of $SU(5)$. Now $(24 \times 24)_s = 1 + 24 + 75 + 200$, and for the 24 plet on the right hand side the $SU(3) \times SU(2) \times U(1)$ gaugino masses are in the ratio $M_3 : M_2 : M_1 = 2 : -3 : -1$, and there is a relative sign between the M_3 and the M_2. Similarly for $SO(10)$, the gaugino masses transform like the $(45 \times 45)_{\rm sym}$ representations of $SO(10)$, where $(45 \times 45)_{\rm sym} = 1 + 54 + 210 + 770$. Here, the 54 plet representation on the right hand side gives [31] $M_3 : M_2 : M_1 = 1 : -3/2 : -1$ and one finds once again that M_3 and M_2 have opposite signs. The above possibilities allow for [32, 33] (see also [34]) $\mu > 0$, $\Delta a_\mu > 0$, $\Delta_b^{\tilde{g}} < 0$ allowing for b–τ unification for a positive μ. Detailed analyses of these can be found in [32, 33], where the implications of Yukawa unification on supersymmetric dark matter are also discussed.

Next we discuss the implications of the $B_{s,d}^0 \to l^+l^-$ constraint. In the Standard Model (SM) $\mathrm{BR}(\bar{B}_s^0 \to \mu^+\mu^-) = (3.1 \pm 1.4) \times 10^{-9}$. However, this branching ratio may lie beyond the reach of RUNII, which may reach a sensitivity of $10^{-(7-8)}$. It turns out that in SUSY/SUGRA models the $\mathrm{BR}(\bar{B}_s^0 \to \mu^+\mu^-) \sim \tan^6\beta$ for large $\tan\beta$ [35]. This arises from the so-called counterterm diagram. Because of the large $\tan\beta$ factor, the branching ratio in SUSY models can get much larger than in the SM. Specifically, in mSUGRA the branching ratio can be as large as $O(10^{-6})$ and within reach of RUNII [36]. Further, it was found that CP phases can provide an extra enhancement of $\sim 10^2$ in some cases (see Ibrahim and Nath in [36]). Thus SUSY enhancement brightens the prospect for the observation of this decay at Fermilab. Further, the observation of $B_{s,d}^0 \to l^+l^-$ will be evidence for SUSY even before the sparticles are seen directly in colliders. In Fig. 2, the implications of the constraints of various limits on the $B_{s,d}^0 \to l^+l^-$ branching ratio are given. Thus, for example, a branching ratio $\mathrm{BR}(B_{s,d}^0 \to l^+l^-) = 10^{-8}$ can probe the parameter space in $m_{1/2} - m_0$ in the range up to 600–700 GeV for $\tan\beta = 50$, $A_0 = 0$, and $\mu > 0$.

3. THE HYPERBOLIC BRANCH, SUPERSYMMETRY, AND DARK MATTER

It was shown quite sometime ago that the radiative breaking of supersymmetry has two branches: an ellipsoidal branch (EB) and a hyperbolic branch (HB). This can be exhibited easily by examining the relation for radiative breaking that determines μ [11], i.e.,

$$C_1 m_0^2 + C_3 m_{1/2}'^2 + C_2' A_0^2 + \Delta\mu_{\rm loop}^2 = \mu^2 + \frac{1}{2}M_Z^2, \quad (1)$$

where $\Delta\mu_{\rm loop}^2$ arise from loop corrections to the effective potential [37]. When $\tan\beta$ is small, the loop corrections are typically small, and, furthermore,

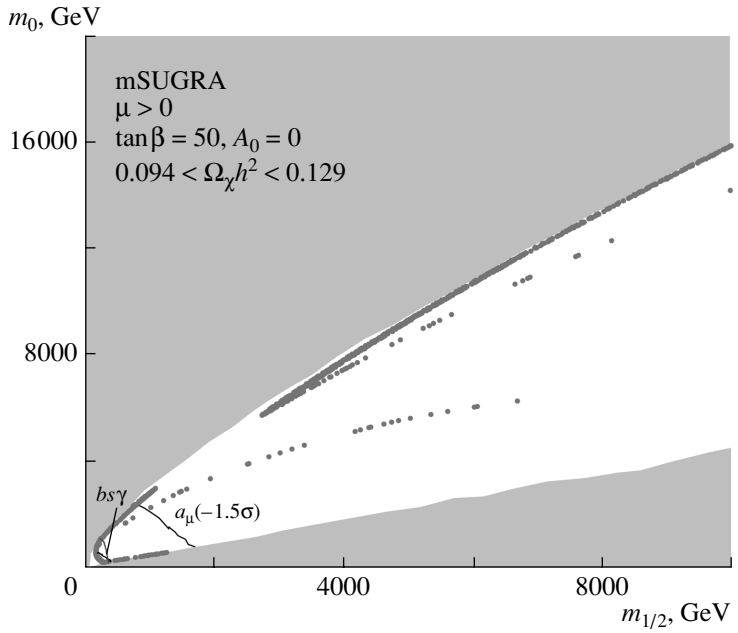

Fig. 3. Regions allowed by the WMAP relic density constraints in the m_0–$m_{1/2}$ plane for $\tan\beta = 50$ with a 2σ error corridor around the WMAP constraint. (Taken from [13].)

$C_1, C_2', C_3 > 0$ and the variation of these parameters with the renormalization group scale are also small. In this case, the radiative breaking of the electroweak symmetry is realized on the ellipsoidal branch and there is an upper limit to the soft parameters for a fixed value of μ. However, for other regions of the parameter space, specifically when $\tan\beta$ is large, one finds that $\Delta\mu^2_{\rm loop}$ is large and, furthermore, the scale dependence of some of the coefficients C_i is rather large. Specifically, in this case, if one chooses a scale Q_0, where the loop correction $\Delta\mu^2_{\rm loop}$ is minimized, one finds that the coefficient C_1 at Q_0 turns negative and the hyperbolic branch is realized. Thus, on the hyperbolic branch, m_0, $m_{1/2}$ can get very large for fixed μ. A very interesting phenomenon of inversion occurs when $M_i \gg |\mu|$. In this case, an examination of the neutralino mass matrix and of the chargino mass matrix shows that $\chi^0_1, \chi^0_2, \chi^\pm_1$ are essentially degenerate with mass μ. More specifically, one finds that [13] (for other analyses that explore the implications of WMAP data see [38, 39])

$$M_{\chi^0_1} = \mu - \frac{M_Z^2}{2}(1 - \sin 2\beta)\left[\frac{\sin^2\theta_{\rm W}}{M_1 - \mu} + \frac{\cos^2\theta_{\rm W}}{M_2 - \mu}\right]; \quad (2)$$

$$M_{\chi^0_2} = \mu + \frac{M_Z^2}{2}(1 + \sin 2\beta)\left[\frac{\sin^2\theta_W}{M_1 + \mu} + \frac{\cos^2\theta_{\rm W}}{M_2 + \mu}\right];$$

$$M_{\chi^\pm_1} = \mu + \frac{M_W^2\cos^2\beta}{\mu} - \frac{M_W^2}{\mu}\frac{(M_2\cos\beta + \mu\sin\beta)^2}{M_2^2 - \mu^2}.$$

In the inversion region, the squarks and sleptons and the gluino may lie in the several TeV region and, thus, may not be easily observable in accelerators. Here, the lightest particles are $h^0, \chi^0_1, \chi^0_2, \chi^\pm_1$, where $m_{\chi^0_1} \simeq m_{\chi^\pm_1} \simeq m_{\chi^0_2} \simeq \mu$. We note that the mass relations here are in gross violation of the scaling laws [40]. Further, the quantities relevant for the observation of the lightest supersymmetric particles, in this case, are the mass differences $\Delta M^\pm = m_{\chi^\pm_1} - m_{\chi^0_1}$ and $\Delta M^0 = m_{\chi^0_2} - m_{\chi^0_1}$. While $m_{\chi^0_1}, m_{\chi^\pm_1}, m_{\chi^0_2}$ may lie in the several hundred GeV region, $\Delta M^\pm$ and ΔM^0 lie in the 1–10 GeV region. The smallness of the mass differences makes the observation of these particles rather difficult, since the decay of the NLSP, and also of the light chargino, will result in rather soft particles, which may not be observable at the LHC. Situations of this type have been discussed in other contexts in the literature [41, 42]. However, quite surprisingly the satisfaction of the relic density constraints can occur easily in the inversion region. This is so because, as pointed out already, in the inversion region there is a near degeneracy of $m_{\chi^0_1}$, $m_{\chi^\pm_1}$, $m_{\chi^0_2}$, which implies a lot of coannihilation. Specifically, one has coannihila-

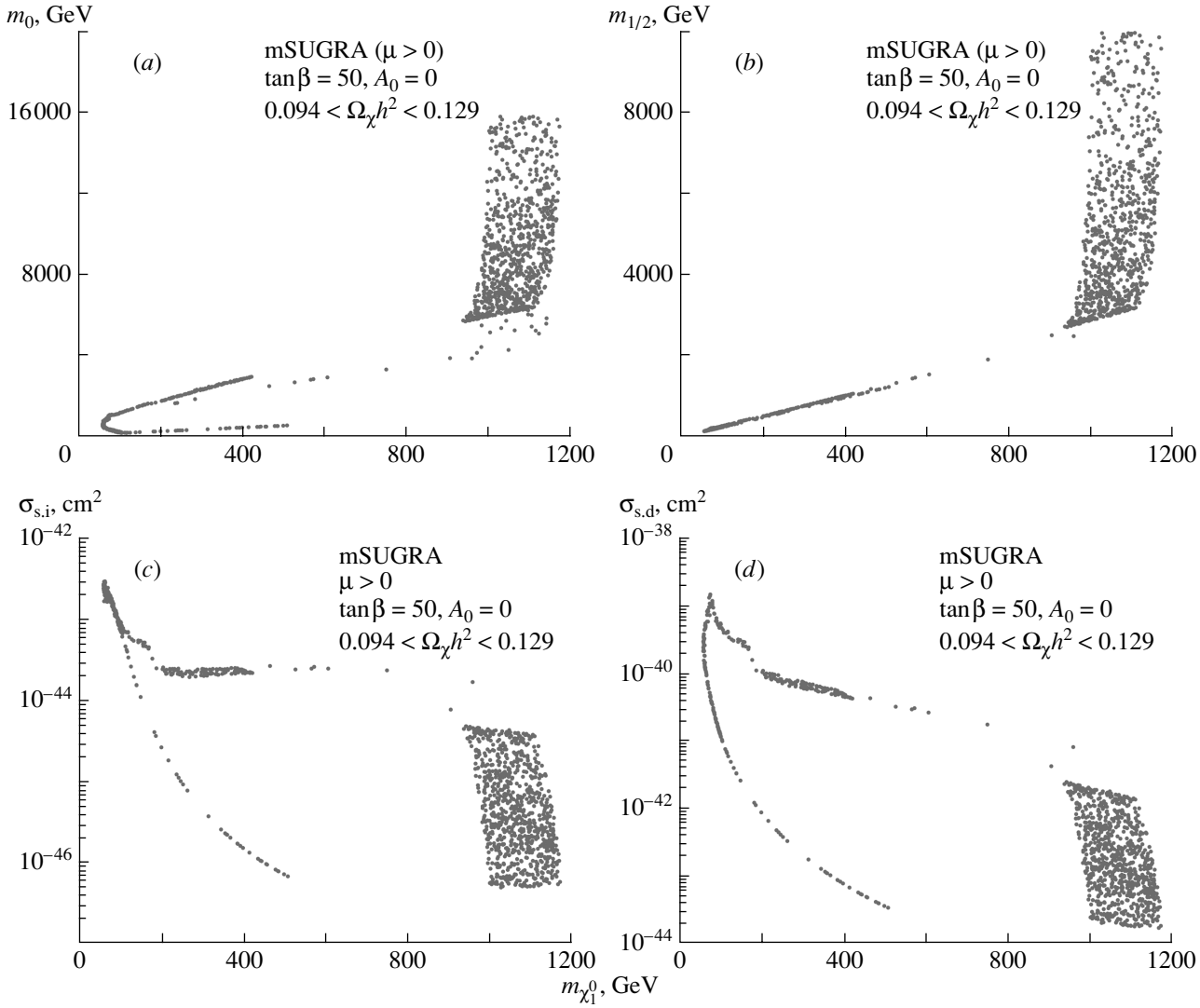

Fig. 4. (*a*) Plot in m_0–$m_{\chi_1^0}$ showing the allowed region consistent with WMAP constraints; (*b*) same as (*a*) except the plot is in m_0–$m_{1/2}$; (*c*) scalar $\sigma_{\chi p}$ cross section as a function of $m_{\chi_1^0}$; (*d*) same as (*c*) except that the plot is for the spin dependent $\sigma_{\chi p}$ cross section. The patches exhibit the inversion region where the neutralino is essentially a higgsino. (Taken from [13].)

tions [43] involving the processes [13]

$$\chi_1^+\chi_1^-, \chi_1^0\chi_2^0 \to u_i\bar{u}_i, d_i\bar{d}_i, W^+W^-, \qquad (3)$$
$$\chi_1^0\chi_1^+, \chi_2^0\chi_1^+ \to u_i\bar{d}_i, \bar{e}_i\nu_i, AW^+, ZW^+, W^+h.$$

Because of coannihilation, relic density constraints can be easily satisfied even though the squark and slepton masses may lie in the several TeV region. Detailed analyses show that, in the HB region, $\sigma_{\chi_1^0 p}$ may still be accessible to dark matter experiment. Thus, observation of dark matter may be the only means of observing SUSY effects if the inversion region of HB is realized in nature. We note in passing that the so called focus point region [12] is a part of the hyperbolic branch and corresponds to low values of $m_{1/2}$. For further discussion see [11, 13, 38, 39].

4. ANALYSIS OF DARK MATTER WITH WMAP CONSTRAINTS

In this section we discuss the implications of the WMAP constraints. We also discuss the implications for the detection of dark matter in dark matter detectors presently in operation [3–6] as well as in those that are planned for the future [7, 8]. We begin with the result of WMAP that gives for CDM [1, 2]

$$\Omega_\chi h^2 = 0.1126^{+0.016}_{-0.018}. \qquad (4)$$

In the theoretical analyses of the relic density, coannihilation [44–51] plays a central role. However, unlike the usual coannihilation phenomena, where the particles that enter in the coannihilation process are the neutralino and the stau, here, the particles that coannihilate are $\chi_1^0, \chi_2^0, \chi_1^\pm$. Specifically, the processes are

listed in Eq. (3). In the inversion region, the neutralino is essentially a Higgsino as opposed to being a Bino, which is what happens over most of the rest of the parameter space of SUGRA models. In Fig. 3, a numerical analysis of the region in the parameter space of m_0–$m_{1/2}$ allowed under the WMAP relic density constraint with a 2σ error corridor is exhibited. One finds that the region consistent with the WMAP relic density constraint can indeed stretch to rather large values in (m_0, $m_{1/2}$), extending into several TeV in each direction. In Fig. 4, a further investigation of the parameter space consistent with the relic density constraints is carried out. Thus, in Fig. 4*a*, an analysis of the parameter space in the m_0 and $m_{\chi_1^0}$ consistent with the relic density constraint is given. Here one finds that $m_{\chi_1^0}$ is sharply limited while m_0 gets large. The vertical patch at $m_{\chi_1^0}$ around a TeV is the inversion region where the neutralino is essentially a Higgsino. A similar phenomenon is visible in Fig. 4*b*. A plot of the neutralino–proton scalar (spin dependent) cross section $\sigma_{\chi p}$ as a function of $m_{\chi_1^0}$ is given in Figs. 4*c*, 4*d*. A comparison with Fig. 1 shows that a significant part of the inversion region will be accessible to future experiments on the direct detection of dark matter.

5. CONCLUSION

In this paper, we have given a brief summary of some of the recent developments in supersymmetric dark matter. We have discussed the constraints of $g_\mu - 2$ and of $B_s^0 \to \mu^+\mu^-$ on dark matter analyses. One of the most stringent constraints arises from the recent observation from WMAP that has measured the relic density for CDM to a high degree of accuracy. We discussed the allowed parameter space in mSUGRA satisfying the WMAP constraints. It was shown that, quite surprisingly, the allowed parameter space is quite large. Specifically, one finds that a very significant region on the hyperbolic branch, with (m_0, $m_{1/2}$) extending in several TeV, still allows the satisfaction of the relic density constraints consistent with WMAP. The consistency with the WMAP data arises due to coannihilation of $\chi_1^0, \chi_2^0, \chi_1^\pm$. Further, one finds that the neutralino–proton cross section falls in a range that may be accessible to dark matter detectors in the future. Thus, if SUSY is realized deep on the hyperbolic branch, then direct observation of sparticles, aside from the light Higgs, may be difficult. However, degeneracy of χ_1^0, χ_2^0, $\chi_1^\pm$ would lead to significant coannihilation and satisfaction of relic density constraints and the direct detection of supersymmetric dark matter may still be possible. Finally, we note that in heterotic string models $\tan\beta$ is a determined quantity under the constraints of radiative breaking of the electroweak symmetry [52] and, thus, dark matter analyses are more constrained in this framework. This constraint will be explored in further work. A similar situation may occur in models based on soft breaking in intersecting D branes [53].

ACKNOWLEDGMENTS

This research was supported in part by NSF grant no. PHY-0139967.

REFERENCES

1. C. L. Bennett *et al.*, Astrophys. J., Suppl. **148**, 1 (2003); astro-ph/0302207.
2. D. N. Spergel *et al.*, Astrophys. J., Suppl. **148**, 175 (2003); astro-ph/0302209.
3. R. Bernabei *et al.*, Riv. Nuovo Cimento **26**, 1 (2003); astro-ph/0307403; R. Belli *et al.*, Phys. Lett. B **480**, 23 (2000); DAMA Collab., Preprint INFN/AE-00/01.
4. R. Abusaidi *et al.*, Phys. Rev. Lett. **84**, 5699 (2000); CDMS Collab., Preprint CWRU-P5-00/UCSB-HEP-00-01; astro-ph/0002471.
5. L. Baudis, A. Dietz, B. Majorovits, *et al.*, Phys. Rev. D **63**, 022001 (2001).
6. A. Benoit *et al.*, Phys. Lett. B **545**, 43 (2002); astro-ph/0206271.
7. H. V. Klapdor-Kleingrothaus *et al.*, MPI-H-V26-1999; hep-ph/9910205; H. V. Klapdor-Kleingrothaus, Nucl. Phys. B (Proc. Suppl.) **110**, 58 (2002); hep-ph/0206250.
8. D. Cline *et al.*, Astropart. Phys. **12**, 373 (2000); D. Cline, astro-ph/0306124.
9. D. R. Smith and N. Weiner, astro-ph/0208403.
10. P. Nath, Phys. At. Nucl. **63**, 1029 (2000); R. Arnowitt, B. Dutta, and B. Hu, hep-ph/0310103; A. B. Lahanas, N. E. Mavromatos, and D. V. Nanopoulos, hep-ph/0308251; J. R. Ellis, astro-ph/0304183; C. Munoz, hep-ph/0309346.
11. K. L. Chan, U. Chattopadhyay, and P. Nath, Phys. Rev. D **58**, 096004 (1998); hep-ph/9710473.
12. J. L. Feng, K. T. Matchev, and T. Moroi, Phys. Rev. D **61**, 075005 (2000); Phys. Rev. Lett. **84**, 2322 (2000); hep-ph/9908309.
13. U. Chattopadhyay, A. Corsetti, and P. Nath, Phys. Rev. D **68**, 035005 (2003); hep-ph/0303201.
14. A. H. Chamseddine, R. Arnowitt, and P. Nath, Phys. Rev. Lett. **49**, 970 (1982); R. Barbieri, S. Ferrara, and C. A. Savoy, Phys. Lett. B **119B**, 343 (1982); L. Hall, J. Lykken, and S. Weinberg, Phys. Rev. D **27**, 2359 (1983); P. Nath, R. Arnowitt, and A. H. Chamseddine, Nucl. Phys. B **227**, 121 (1983).
15. P. Nath, hep-ph/0307123.
16. L. Covi, J. E. Kim, and L. Roszkowski, Phys. Rev. Lett. **82**, 4180 (1999); J. High Energy Phys. **0105**, 033 (2001).

17. P. Nath and R. Arnowitt, Phys. Rev. D **56**, 2820 (1997); E. Accomando, R. Arnowitt, B. Datta, and Y. Santoso, Nucl. Phys. B **585**, 124 (2000).
18. J. Ellis, A. Ferstl, K. A. Olive, and Y. Santoso, Phys. Rev. D **67**, 123502 (2003); hep-ph/0302032.
19. A. Corsetti and P. Nath, Phys. Rev. D **64**, 125010 (2001); hep-ph/0003186; hep-ph/0005234; hep-ph/0011313.
20. A. Birkedal-Hansen and B. D. Nelson, Phys. Rev. D **67**, 095006 (2003); hep-ph/0211071.
21. U. Chattopadhyay and D. P. Roy, Phys. Rev. D **68**, 033010 (2003); hep-ph/0304108.
22. T. C. Yuan, R. Arnowitt, A. H. Chamseddine, and P. Nath, Z. Phys. C **26**, 407 (1984); D. A. Kosower, L. M. Krauss, and N. Sakai, Phys. Lett. B **133B**, 305 (1983).
23. J. L. Lopez, D. V. Nanopoulos, and X. Wang, Phys. Rev. D **49**, 366 (1994).
24. U. Chattopadhyay and P. Nath, Phys. Rev. D **53**, 1648 (1996); hep-ph/9507386.
25. P. Nath and M. Yamaguchi, Phys. Rev. D **60**, 116006 (1999).
26. K. Hagiwara, A. D. Martin, D. Nomura, and T. Teubner, Phys. Lett. B **557**, 69 (2003); hep-ph/0209187.
27. U. Chattopadhyay and P. Nath, Phys. Rev. D **66**, 093001 (2002).
28. H. Baer and J. Ferrandis, Phys. Rev. Lett. **87**, 211803 (2001); hep-ph/0106352; T. Blazek, R. Dermisek, and S. Raby, Phys. Rev. Lett. **88**, 111804 (2002); hep-ph/0107097.
29. T. Ibrahim and P. Nath, Phys. Rev. D **67**, 095003 (2003); hep-ph/0301110.
30. T. Ibrahim and P. Nath, Phys. Rev. D **62**, 015004 (2000); hep-ph/9908443; **61**, 095008 (2000); hep-ph/9907555; T. Ibrahim, U. Chattopadhyay, and P. Nath, Phys. Rev. D **64**, 016010 (2001); hep-ph/0102324.
31. N. Chamoun, C. S. Huang, C. Liu, and X. H. Wu, Nucl. Phys. B **624**, 81 (2002); hep-ph/0110332.
32. U. Chattopadhyay, A. Corsetti, and P. Nath, Phys. Rev. D **66**, 035003 (2002); hep-ph/0201001.
33. U. Chattopadhyay and P. Nath, Phys. Rev. D **65**, 075009 (2002); hep-ph/0110341.
34. S. Komine and M. Yamaguchi, Phys. Rev. D **65**, 075013 (2002); hep-ph/0110032.
35. S. R. Choudhury and N. Gaur, Phys. Lett. B **451**, 86 (1999); K. S. Babu and C. Kolda, Phys. Rev. Lett. **84**, 228 (2000).
36. A. Dedes, H. K. Dreiner, U. Nierste, and P. Richardson, Phys. Rev. Lett. **87**, 251804 (2001); R. Arnowitt, B. Dutta, T. Kamon, and M. Tanaka, Phys. Lett. B **538**, 121 (2002); S. Baek, S. C. Park, and W. Y. Song, Phys. Rev. D **66**, 056004 (2002); hep-ph/0206008; J. K. Mizukoshi, X. Tata, and Y. Wang, Phys. Rev. D **66**, 115003 (2002); hep-ph/0208078; T. Ibrahim and P. Nath, Phys. Rev. D **67**, 016005 (2003); G. L. Kane, C. Kolda, and J. E. Lennon, hep-ph/0310042.
37. R. Arnowitt and P. Nath, Phys. Rev. D **46**, 3981 (1992).
38. J. Ellis, K. A. Olive, Y. Santoso, and V. C. Spanos, Phys. Lett. B **565**, 176 (2003); hep-ph/0303043; H. Baer and C. Balazs, JCAP **0305**, 006 (2003); hep-ph/0303114; A. B. Lahanas and D. V. Nanopoulos, Phys. Lett. B **568**, 55 (2003); hep-ph/0303130.
39. H. Baer, C. Balazs, A. Belyaev, and J. O'Farrill, JCAP **0309**, 007 (2003); hep-ph/0305191; H. Baer, C. Balazs, A. Belyaev, *et al.*, J. High Energy Phys. **0306**, 054 (2003); hep-ph/0304303; J. Ellis, K. A. Olive, Y. Santoso, and V. C. Spanos, hep-ph/0305212.
40. R. Arnowitt and P. Nath, Phys. Rev. Lett. **69**, 725 (1992); P. Nath and R. Arnowitt, Phys. Lett. B **289**, 368 (1992).
41. C. H. Chen, M. Drees, and J. F. Gunion, Phys. Rev. Lett. **76**, 2002 (1996); Phys. Rev. D **55**, 330 (1997); **60**, 039901(E) (1999).
42. J. L. Feng, T. Moroi, L. Randall, *et al.*, Phys. Rev. Lett. **83**, 1731 (1999).
43. J. Edsjo and P. Gondolo, Phys. Rev. D **56**, 1879 (1997); hep-ph/9704361.
44. S. Mizuta and M. Yamaguchi, Phys. Lett. B **298**, 120 (1993); hep-ph/9208251.
45. J. R. Ellis, T. Falk, and K. A. Olive, Phys. Lett. B **444**, 367 (1998); hep-ph/9810360.
46. J. R. Ellis, T. Falk, K. A. Olive, and M. Srednicki, Astropart. Phys. **13**, 181 (2000); **15**, 413(E) (2001); hep-ph/9905481.
47. M. E. Gomez, G. Lazarides, and C. Pallis, Phys. Rev. D **61**, 123512 (2000).
48. R. Arnowitt, B. Dutta, and Y. Santoso, Nucl. Phys. B **606**, 59 (2001); hep-ph/0102181.
49. J. R. Ellis, K. A. Olive, and Y. Santoso, Astropart. Phys. **18**, 395 (2003); hep-ph/0112113.
50. T. Nihei, L. Roszkowski, and R. Ruiz de Austri, J. High Energy Phys. **0207**, 024 (2002); hep-ph/0206266.
51. V. A. Bednyakov, H. V. Klapdor-Kleingrothaus, and V. Gronewold, Phys. Rev. D **66**, 115005 (2002); hep-ph/0208178.
52. P. Nath and T. R. Taylor, Phys. Lett. B **548**, 77 (2002); hep-ph/0209282.
53. B. Kors and P. Nath, hep-th/0309167.

Physics of Atomic Nuclei, Vol. 67, No. 6, 2004, pp. 1195–1197. From Yadernaya Fizika, Vol. 67, No. 6, 2004, pp. 1217–1219.

DARK MATTER

Dark Matter Annihilation in Small-Scale Clumps in the Galactic Halo*

V. S. Berezinsky[1)], V. I. Dokuchaev[**], and Yu. N. Eroshenko

Institute for Nuclear Research, Russian Academy of Sciences, Moscow, Russia

Received November 17, 2003

Abstract—The enhancement of the annihilation signal due to Dark Matter (DM) clumpiness in the Galactic halo, valid for arbitrary DM particles, is described. The mass spectrum of small-scale DM clumps with $M \leq 10^3 M_\odot$ is calculated with tidal destruction of the clumps taken into account within the hierarchical model of clump structure. The mass distribution of the clumps has a cutoff at $M_{\min}$ due to diffusion of DM particles out of a fluctuation and free streaming. In the case of neutralino (considered as a pure bino) being a DM particle, $M_{\min} \sim 10^{-8} M_\odot$. The evolution of the density profile in a DM clump does not result in singularity, because of formation of the core under the influence of tidal interaction. The number density of clumps as a function of their mass, radius, and distance to the Galactic center is presented. © *2004 MAIK "Nauka/Interperiodica".*

1. INTRODUCTION

Both analytic calculations [1, 2] and numerical simulations [3–5] predict the existence of Dark Matter (DM) clumps in the Galactic halo. The density profile in these clumps according to analytic calculations [6–9] and numerical simulations [4, 10] is $\rho(r) \propto r^{-\beta}$. The average density of the DM in a Galactic halo itself also exhibits a similar density profile (relative to a Galactic center) in the both approaches. In the analytic approach of Gurevich and Zybin (see review [9] and references therein), the density profiles are predicted to be universal, with $\beta \approx 1.7$–1.9 for clumps, galaxies, and two-point correlation functions of galaxies. In the numerical simulations, the density profiles can be evaluated only for relatively large scales due to the limited mass resolution.

A central cusp (around the central supermassive black hole) in the Galactic halo and the smaller scale clumps result in the enhancement of the DM annihilation rate and, thus, in the stronger signals in the form of gamma rays, radio emission, positrons, and antiprotons. The gamma ray and radio signal from the central cusp in the Galactic halo was first discussed in [11, 12]. Recently, this problem was examined in [13–17]. The enhancement of the DM annihilation rate due to the clumpiness of the DM halo was first pointed out in [1]. Neutralino annihilation in clumps can result in a very large diffuse gamma-ray flux [18] in the model of the clumpy DM by Gurevich *et al.* [2]. Calculations of the positron and antiproton production in the clumpy DM halo have been performed, e.g., in [13] (see also [19–21]).

The DM clumps may be formed (i) by the growth of the adiabatic or isothermal fluctuations (originated at inflation) during the matter-dominated epoch, (ii) from the density fluctuations in the models with topological defects (cosmic strings and domain walls) [1], and (iii) during the radiation dominating era from the nonlinear isothermal fluctuations (originated by phase transitions in the early Universe) [22] or from the large amplitude adiabatic fluctuations [23].

In the hierarchical theory of large-scale structure formation in the Universe, the first formed objects have some minimal mass $M_{\min}$. This value is crucial for calculation of the DM annihilation rate. The estimates of $M_{\min}$ existing in the literature for neutralino DM are substantially different, from $M_{\min} \sim 10^{-12} M_\odot$ in [24] to $M_{\min} \sim (10^{-7}$–$10^{-6}) M_\odot$ in [25].

2. SMALL-SCALE CLUMPS IN THE GALACTIC HALO

CDM particles at high temperature $T > T_f \sim 0.05 m_\chi$ are in thermodynamical (chemical) equilibrium with cosmic plasma when their number density is determined by temperature. After freezing at $t > t_f$ and $T < T_f$, the DM particles remain for some time in *kinetic* equilibrium with plasma when the temperature of CDM particles T_χ is equal to the temperature of plasma T, but the number density n_χ is determined by freezing concentration and expansion of the Universe. At this stage, the CDM particles are

*This article was submitted by the authors in English.

1)And Laboratori Nazionali del Gran Sasso, INFN, Italy;
e-mail: berezinsky@lngs.infn.it

**e-mail: dokuchaev@inr.npd.ac.ru

not perfectly coupled to the cosmic plasma. Collisions between a CDM particle and fast particles of ambient plasma result in exchange of momenta, and the CDM particle diffuses in the space. Due to diffusion, the DM particles leak from the small-scale fluctuations, and thus, their distribution obtains a cutoff at the minimal mass M_D. When the energy relaxation time for the DM particles $\tau_{\rm rel}$ becomes larger than the Hubble time $H^{-1}(t)$, the DM particles leave the kinetic equilibrium. These conditions determine the time of the kinetic decoupling t_d. At $t \geq t_d$, the CDM particles are moving in the free streaming regime and all the fluctuations on the scale of

$$\lambda_{\rm fs} = a(t_0) \int_{t_d}^{t_0} \frac{v(t')dt'}{a(t')} \qquad (1)$$

and smaller are washed away (here, $a(t)$ is the scaling factor of the expanding Universe and $v(t)$ is the velocity of a DM particle at epoch t). The corresponding minimal mass at epoch t_0, $M_{\rm fs} = (4\pi/3)\rho_\chi(t_0)\lambda_{\rm fs}^3$, is much larger than M_D. The numerical calculations below (for neutralino) show that M_D is close to $M_{\rm min}$ from [24] and $M_{\rm fs}$ is close to $M_{\rm min}$ from [25]. The calculation of the minimal mass $M_{\rm min}$ in the mass spectrum of fluctuations is obviously model dependent. As the DM particle, we shall consider the neutralino χ, for which we take the pure bino state ($\chi = \tilde{B}$). As calculations show, the temperature of kinetic decoupling for a reasonable range of parameters is $T_d \sim 100$ MeV. As a result, we find

$$t_d = 3.5 \times 10^{-5} \left(\frac{m_\chi}{100\ {\rm GeV}}\right)^{-1/2} \times \left(\frac{\tilde{M}}{1\ {\rm TeV}}\right)^{-2} \left(\frac{g_*}{10}\right)^{-3/4} [{\rm s}] \qquad (2)$$

and

$$T_d = 150 \left(\frac{m_\chi}{100\ {\rm GeV}}\right)^{1/4} \left(\frac{\tilde{M}}{1\ {\rm TeV}}\right) \times \left(\frac{g_*}{10}\right)^{1/8} [{\rm MeV}], \qquad (3)$$

where g_* is the number of degrees of freedom. We calculate [26], the diffusion coefficient, using the method given in [27] (§12). The resulting value determines the minimal mass in the density perturbation spectrum due to diffusion of neutralinos from a fluctuation

$$M_D = 4.3 \times 10^{-13} \left(\frac{m_\chi}{100\ {\rm GeV}}\right)^{-15/8} \times \left(\frac{\tilde{M}}{1\ {\rm TeV}}\right)^{-3/2} \left(\frac{g_*}{10}\right)^{-15/16} M_\odot. \qquad (4)$$

After the moment of kinetic decoupling t_d, neutralinos move freely in the expanding Universe background, $a(t)d\mathbf{x} = \mathbf{v}(t)dt$, where $\mathbf{x}$ is the comoving particle coordinates. Free streaming defins the minimal mass

$$M_{\rm min} = 1.5 \times 10^{-8} \left(\frac{m_\chi}{100\ {\rm GeV}}\right)^{-15/8} \times \left(\frac{\tilde{M}}{1\ {\rm TeV}}\right)^{-3/2} \left(\frac{g_*}{10}\right)^{-15/16} M_\odot. \qquad (5)$$

In [9], the relative core radius of the clump is estimated as $x_c = R_c/R \simeq \delta_{\rm eq}^3 \ll 1$ from consideration of the perturbation of the velocity field due to the damped mode of the cosmological density perturbations. Here, $\delta_{\rm eq}$ is an initial density fluctuation value at the end of the radiation dominated epoch. In [18], the core is produced for a spherically symmetric clump by inverse flow caused by annihilation of DM particles. We show [26] that these phenomena are not the main effects and that a much stronger disturbance of the velocity field in the core is produced by tidal forces. As a result, the relative core radius is

$$x_c \simeq \frac{\pi \cdot 2^{5/3} \cdot 3^{13/3}}{5^3} G\rho_{\rm eq} t_{\rm eq}^2 \nu^{-2} f^2(\delta_{\rm eq}) \simeq 0.3\nu^{-2} f^2(\delta_{\rm eq}), \qquad (6)$$

where ν is the height of the peak density in units of dispersion (the peak height): $\nu = \delta_{\rm eq}/\sigma_{\rm eq}(M)$, $\sigma_{\rm eq}(M) \equiv \sigma(t_{\rm eq}, M)$ and function $\delta_{\rm eq} \sim O(1)$. A variance $\sigma_{\rm eq}(M) = \sigma_{(0)}$ in the small-scale range is found in [28] (see also [29]).

We study the growth of fluctuations in the nonlinear regime in the framework of the Press–Schechter theory of hierarchical clustering [30, 31] with the tidal interactions included as the new element [26]. The resulting differential fraction of the mass in the form of clumps, which escape the tidal destruction in the hierarchical objects, is $\xi(n,\nu)d\nu dm/m$ with $\xi(n,\nu) \simeq (2\pi)^{-1/2} e^{-\nu^2/2}(n+3)y(\nu)$. Here, n is an effective perturbation power spectrum index and the function $y(\nu) \sim 0.1$ weakly depends on β. By integrating over ν, we obtain the integral distribution of clumps $\xi_{\rm int} \simeq 0.01(n+3)$. This means that for different n about 0.1–0.5% of clumps survive the stage of tidal destruction in each logarithmic mass interval $\Delta \ln M \sim 1$.

3. ENHANCEMENT OF THE DM ANNIHILATION SIGNAL

We provided the numerical calculations of the enhancement factor η due to DM clumpiness in the Galactic halo for the annihilation signal by taking

into account the distribution of DM clumps over their masses M and radii R and the distribution of clumps in the Galactic halo [26]. This enhancement factor is a function of the minimal clump mass $M_{\min}$ for the clump density profile with index $\beta = 1$ and for the different indices n_p of the primeval perturbation spectrum. Numerically, $\eta = 5$ for $M_{\min} = 2 \times 10^{-8} M_\odot$ and $n_p = 1.0$. It strongly increases at smaller $M_{\min}$ and larger n_p. For example, for $n_p = 1.1$ and $n_p = 1.2$, at the same $M_{\min} = 2 \times 10^{-8} M_\odot$, enhancement becomes tremendously large, $\eta = 130$ and $\eta = 4 \times 10^3$, respectively.

Our approach is based on the hierarchical clustering model in which smaller mass objects are formed earlier than larger ones, i.e., $\sigma_{\rm eq}(M)$ diminishes with increasing M. This condition is satisfied for objects with mass $M > M_{\min} \simeq 2 \times 10^{-8} M_\odot$ only if the primordial power spectrum has the value of the power index $n_p > 0.84$. In this case, the enhancement of the annihilation signal, in fact, is absent, $\eta \simeq 1$ for $n_p < 0.9$.

ACKNOWLEDGMENTS

V.D. and Yu.E. are supported in part by the Russian Foundation for Basic Research, project nos. 03-02-16436-a, 02-02-16762-a, and 04-02-16757.

REFERENCES

1. J. Silk and A. Stebbins, Astrophys. J. **411**, 439 (1993).
2. A. V. Gurevich, K. P. Zybin, and V. A. Sirota, Usp. Fiz. Nauk **167**, 913 (1997) [Phys. Usp. **40**, 869 (1997)].
3. B. Moore *et al.*, Astrophys. J. Lett. **524**, L19 (1999).
4. S. Ghigna *et al.*, Astrophys. J. **544**, 616 (2000).
5. A. Klypin, S. Gottlober, A. V. Kravtsov, and A. M. Khokhlov, Astrophys. J. **516**, 530 (1999).
6. E. Bertschinger, Astrophys. J., Suppl. **58**, 39 (1985).
7. Y. Hoffman and J. Shaham, Astrophys. J. **297**, 16 (1985).
8. B. S. Ryden and J. E. Gunn, Astrophys. J. **318**, 39 (1987).
9. A. V. Gurevich and K. P. Zybin, Usp. Fiz. Nauk **165**, 723 (1995) [Phys. Usp. **38**, 687 (1995)].
10. J. F. Navarro, C. S. Frenk, and S. D. M. White, Astrophys. J. **462**, 563 (1996).
11. V. S. Berezinsky, A. V. Gurevich, and K. P. Zybin, Phys. Lett. B **294**, 221 (1992).
12. V. Berezinsky, A. Bottino, and G. Mignola, Phys. Lett. B **325**, 136 (1994).
13. L. Bergstrom, J. Edsjo, P. Gondolo, and P. Ulio, Phys. Rev. D **59**, 043506 (1999).
14. P. Gondolo and J. Silk, Phys. Rev. Lett. **83**, 1719 (1999).
15. P. Ullio, H. Zhao, and M. Kamionkowski, Phys. Rev. D **64**, 043504 (2001).
16. G. Bertone, G. Sigl, and J. Silk, Mon. Not. R. Astron. Soc. **337**, 98 (2002).
17. D. Merritt, M. Milosavljevic, L. Verde, and R. Jimenez, Phys. Rev. Lett. **88**, 191301 (2002).
18. V. Berezinsky, A. Bottino, and G. Mignola, Phys. Lett. B **391**, 355 (1997).
19. G. Jungman and M. Kaminkowski, Phys. Rev. D **49**, 2316 (1994).
20. A. Bottino, C. Favero, N. Fornengo, and G. Mignola, Astropart. Phys. **3**, 77 (1995).
21. A. Bottino, F. Donato, N. Fornengo, and P. Salati, Phys. Rev. D **58**, 123503 (1998).
22. E. W. Kolb and I. I. Tkachev, Phys. Rev. D **50**, 769 (1994).
23. V. I. Dokuchaev and Yu. N. Eroshenko, Zh. Éksp. Teor. Fiz. **121**, 5 (2002) [JETP **94**, 1 (2002)].
24. K. P. Zybin, M. I. Vysotsky, and A. V. Gurevich, Phys. Lett. A **260**, 262 (1999).
25. D. J. Schwarz, S. Hofmann, and H. Stocker, Phys. Rev. D **64**, 083507 (2001).
26. V. S. Berezinsky, V. I. Dokuchaev, and Yu. N. Eroshenko, Phys. Rev. D **68**, 103003 (2003); astro-ph/0301551.
27. L. D. Landau, E. M. Lifshits, and L. P. Pitaevsky, *Physical Kinetics* (Pergamon Press, Oxford, 1981).
28. E. V. Bugaev and K. V. Konishchev, Phys. Rev. D **65**, 123005 (2002).
29. C. Schmid, D. J. Schwarz, and P. Widerin, Phys. Rev. D **59**, 043517 (1999).
30. W. H. Press and P. Schechter, Astrophys. J. **187**, 425 (1974).
31. C. Lacey and S. Cole, Mon. Not. R. Astron. Soc. **262**, 627 (1993).

Physics of Atomic Nuclei, Vol. 67, No. 6, 2004, pp. 1198–1201. From Yadernaya Fizika, Vol. 67, No. 6, 2004, pp. 1220–1223.

DARK MATTER

Theoretical LSP Detection Rates for ^{71}Ga, ^{73}Ge, and ^{127}I Dark-Matter Detectors*

E. Holmlund, M. Kortelainen, T. S. Kosmas[1)], J. Suhonen[**], **and J. Toivanen**

Department of Physics, University of Jyväskylä, Jyväskylä, Finland

Received November 4, 2003

Abstract—The low-energy structure of the dark-matter detector nuclei ^{71}Ga, ^{73}Ge, and ^{127}I has been studied by using the microscopic quasiparticle–phonon model. The resulting ground states have been used to calculate theoretical predictions for detection rates of the lightest supersymmetric particle (LSP) in experiments studying elastic scattering of an LSP from an atomic nucleus. The highest rate, approximately 0.27 yr^{-1}kg^{-1}, among all the adopted SUSY parameters and renormalization schemes was provided by ^{127}I at the zero limit of the detector energy threshold. © *2004 MAIK "Nauka/Interperiodica".*

1. INTRODUCTION

The open questions of the cosmology and elementary-particle theory are overlapping in the physics of dark matter. It has been concluded, based on a vast amount of astrophysical observations, that the mass of the Universe consists mostly of matter that cannot be seen by detecting electromagnetic radiation.

The dark matter can be divided into baryonic and nonbaryonic components. The nonbaryonic contribution, in turn, consists of so-called hot and cold dark matter, HDM and CDM, respectively. Actually, the dominant dark-matter component is CDM, the constituents of which belong to theories beyond the particle-physics Standard Model.

A very interesting group of CDM candidates are the WIMPs, weakly interacting massive particles, and, in particular, the lightest supersymmetric particle, LSP, resulting from the inclusion of supersymmetry in the Standard Model. LSPs are stable particles on the GeV–TeV scale that only interact via the weak interaction. The possible LSP candidates include sneutrinos, neutralinos, and Higgsino-like and mixed gaugino–Higgsino LSPs.

The nonrelativistic LSPs form a halo enclosing the Milky Way and they should be detectable, for instance, via a neutral-current elastic LSP–nucleus scattering. Because of the Earth's revolution around the Sun, the rate of the recoiling nuclei is assumed to reflect the seasonal changes in the relative velocity of the detector and the halo. The measured signal can be ionization, phonons, or light produced in the target by the recoiled nucleus. The present experiments aiming to detect this process apply targets such as NaI (DAMA [1]) and ^{73}Ge (HDMS [2], EDELWEISS [3]).

A theoretical description of the target nuclei is needed for the interpretation of the LSP–nucleus scattering results. In this work, a microscopic quasiparticle–phonon model (MQPM) [4] has been used for this purpose.

2. THEORETICAL APPROACH

2.1. The MQPM

The quasiparticle–phonon coupling provides a valuable tool for the description of spherical medium-heavy odd-mass nuclei such as ^{71}Ga, ^{73}Ge, and ^{127}I, studied in this work. In the present case, MQPM has been applied to construct the nuclear wave functions needed to calculate the LSP detection rates in the detector nuclei mentioned above. The MQPM has previously been used to predict the energy spectra and transition rates for charge-changing transitions in both spontaneous and neutrino-induced processes [4–7]. As the nucleon–nucleon interaction, a realistic two-body interaction based on a one-boson-exchange potential [8] has been used. The matrix elements have been evaluated by using the G-matrix technique.

In the MQPM, the terms H_{22}, H_{04}, and H_{40} of the BCS-quasiparticle Hamiltonian are diagonalized in the framework of the QRPA to yield the correlated ground state and two-quasiparticle excitations of the even–even reference nucleus. The remaining H_{31} and H_{13} terms are diagonalized by solving the

*This article was submitted by the authors in English.

[1)]Theoretical Physics Division, University of Ioannina, Ioannina, Greece.

[**]e-mail: jouni.suhonen@phys.jyu.fi

Some of the most relevant parameters of the three SUSY-parameter sets adopted in the present work

Solution	SUSY parameters					
	m_χ, GeV	m_h, GeV	m_H, GeV	m_A, GeV	$\tan 2\alpha$	$\tan\beta$
1	126	116.0	345.6	345.0	0.245	10.0
3	102	113.2	326.6	324.0	0.525	5.0
5	124	121.0	567.0	563.0	0.929	2.7

quasiparticle–phonon equations of motion [9] to obtain the amplitudes of the general MQPM excitation of the angular-momentum value j and projection m:

$$\Gamma_i^\dagger(jm) = \sum_n C_n^i a_{njm}^\dagger + \sum_{b,\omega} D_{b\omega}^i [a_b^\dagger Q_\omega^\dagger]_{jm}, \quad (1)$$

where the three-quasiparticle terms are constructed by coupling the BCS quasiparticles $a_b^\dagger$ with the QRPA phonons $Q_\omega^\dagger$ obtained in the QRPA step.

2.2. LSP Detection Rates

The starting point in the LSP detection-rate formalism is the LSP–nucleus scattering cross section:

$$\sigma(v) = \frac{1}{2}\sigma_0 \left(\frac{1}{m_p b}\right)^2 \frac{c^2}{v^2}\sigma_{\mathrm{AVS}}, \quad (2)$$

in which $\sigma_0 = 0.77 \times 10^{-38}$ cm^2, m_p is the proton mass, b is the oscillator-size parameter of the nucleus, and v is the relative velocity of the LSP particle with respect to the detector nucleus. The term containing information about the nucleonic current and nuclear structure, σ_{AVS}, is given in [10]. The vector-current component of σ_{AVS} is omitted in the calculations (leaving σ_{AS}) since it is proportional to the square of the ratio v/c and v is only of the order of 200 km/s.

The detection rate is related to the cross section through

$$R = \frac{dN}{dt} = \frac{\rho(0)}{m_\chi}\frac{m}{Am_p}|v_z|\sigma_{\mathrm{AS}}(v), \quad (3)$$

where A is the mass number, m_χ is the LSP mass, and $\rho(0) = 0.3$ GeV/cm^3 is the local LSP density. In the following, it is convenient to define

$$R_0 = 8.90 \times 10^7 \frac{\sigma_{\mathrm{AS}}}{Am_\chi\,[\mathrm{GeV}]\,(m_p b)^2}[\mathrm{yr}^{-1}\mathrm{kg}^{-1}]. \quad (4)$$

To obtain the average detection rate $\langle R\rangle$, an integral over the LSP-velocity distribution has to be calculated. The folding of the LSP-velocity distribution, assuming the Maxwellian form, results in the final expression

$$\langle R\rangle = 0.543 R_0 m[\mathrm{kg}], \quad (5)$$

where the mass of the detector material, m, is given in units of kg and all the physics of the LSP and nucleus is included in R_0.

The present calculations were performed by using three proposed SUSY-parameter sets. Some of these parameters are listed in the table. The solutions are numbered as 1, 3, and 5 (for 1 and 3, see [11, 12], and, for 5, see [11]).

The renormalization of the interactions on the nucleon level produces some uncertainties. In case of the isoscalar–axial current, the value of the coupling constant can be based on the so-called naive quark model, NQM, or on the experimental data by the European Muon Collaboration [13]. In the present work, both cases were examined. Another issue is how to treat the scalar interaction, where the description of the nucleon substructure plays an important role. The models named as A, B, and C (see [14], for instance) are considered here.

3. RESULTS

The performed MQPM calculations are described in more detail in [6] for ^{127}I, [7] for ^{71}Ga, and [10] for ^{73}Ge. There also the resulting energy spectra are shown and the quasiparticle structure of the low-energy states is discussed.

For the analysis of the ongoing experiments and planning of the future ones, the LSP detection rates have been calculated for ^{71}Ga, ^{73}Ge, and ^{127}I. The nuclear-structure information provided by the MQPM has been used to find the behavior of R_0 of Eq. (4) as a function of the detector energy threshold Q. Four examples of the results are presented graphically in Figs. 1 and 2. Indeed, the calculations were performed in 18 different cases corresponding to different combinations of the adopted SUSY solution and interaction-renormalization schemes.

In Fig. 1 are the results for all three detector nuclei corresponding to the SUSY-parameter set 5 (see table) and NQM. The leftmost graph, corresponding to the scalar-coupling according to model B, shows the highest R_0 value among all the cases considered for ^{127}I at the limit $Q = 0$. The changeover to model C

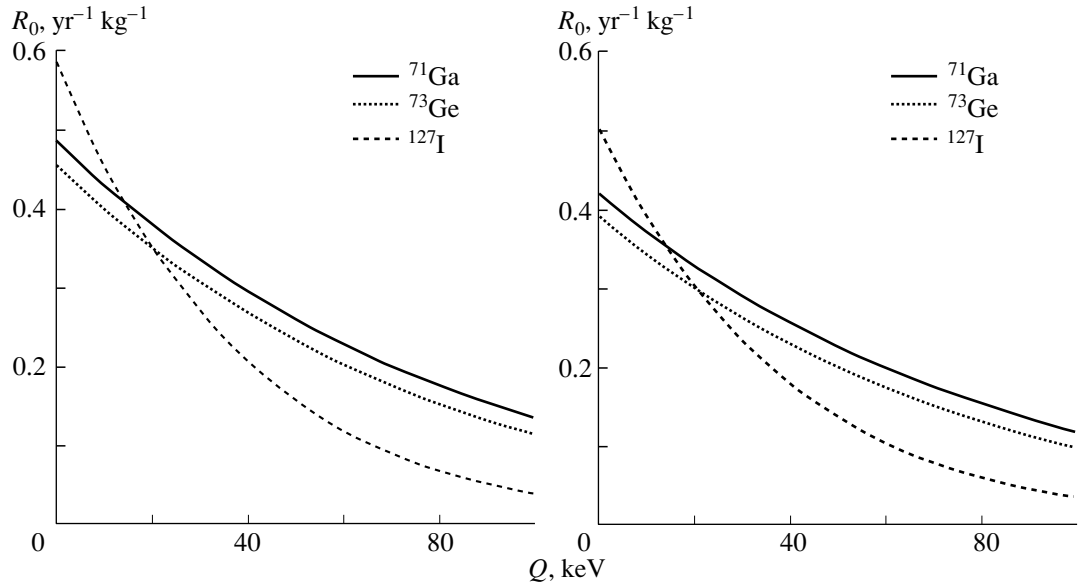

Fig. 1. R_0 as a function of the detector energy threshold Q by applying the SUSY solution 5 and the NQM to renormalize the isoscalar–axial current. The graph on the left-hand side corresponds to model B and the other one to model C.

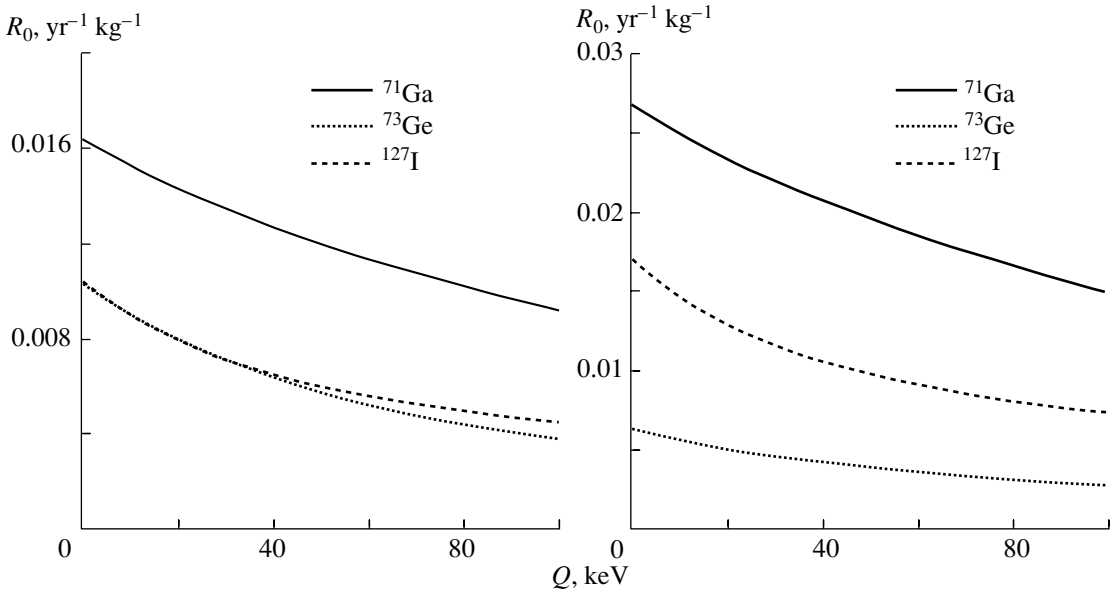

Fig. 2. R_0 as a function of the detector energy threshold Q by applying the SUSY solution 1 and using the model A to describe the internal structure of the nucleons in the case of the scalar interaction. The graph on the left-hand side corresponds to the isoscalar–axialvector current renormalized by using the EMC data and the other one corresponds to the NQM.

does not make a big difference. Generally, the differences between the results obtained by using models B and C were small, whereas the use of model A leads to clearly smaller rates.

The effect of the chosen isoscalar–axial current renormalization, whether owing to the EMC data or the NQM, is demonstrated in Fig. 2, where the EMC result is on the left and the NQM result is on the right. It shows that there are apparent differences but that the overall energy scale remains unchanged if one replaces one renormalization with another. The rates in this figure are the lowest ones found in the present work.

Even though ^{71}Ga, shown by the solid curve, possibly seems, by looking at Figs. 1 and 2, to be the most favorable detector nucleus, ^{127}I turns out to provide the highest rates most often, however, when also the cases not shown here are considered. In particular,

^{127}I outdoes the other nuclei when lowering the energy threshold Q below 15 keV. Furthermore, ^{71}Ga has in every case higher detection rates than ^{73}Ge.

4. CONCLUSIONS

In this work a microscopic quasiparticle–phonon model with realistic interactions, has been applied to describe the low-energy structure of three nuclei suitable for present-day dark-matter experiments. The MQPM calculations have been done for three dark-matter detector candidates: ^{71}Ga, ^{73}Ge, and ^{127}I. These nuclei are applicable for dark-matter detection experiments based on elastic scattering between an atomic nucleus and the lightest supersymmetric particle mediated through a neutral current. The calculations have been performed by adopting different SUSY-parameter sets and various renormalization schemes of scalar and isovector–axial currents. The results are presented as functions of the detector energy threshold and they reveal that, at the low-energy limit of the threshold, the ^{127}I nucleus seems to provide the highest detection rates, i.e., roughly 0.3 yr^{-1} kg^{-1}. A general picture obtained through the calculations suggests that, below the threshold of 15 keV, ^{127}I is the most favorable candidate. Above this limit, ^{71}Ga turned out to be the best nucleus from the LSP-detection point of view.

REFERENCES

1. R. Bernabei *et al.*, Nucl. Phys. B (Proc. Suppl.) **110**, 61 (2002).
2. L. Baudis *et al.*, Phys. Rev. D **63**, 022001 (2001).
3. EDELWEISS Collab., Phys. Lett. B **513**, 15 (2001).
4. J. Toivanen and J. Suhonen, Phys. Rev. C **57**, 1237 (1998).
5. J. Suhonen *et al.*, Nucl. Phys. A **628**, 41 (1998).
6. E. Holmlund and J. Suhonen, Nucl. Phys. A **706**, 335 (2002).
7. E. Holmlund and J. Suhonen, Nucl. Phys. A **714**, 663 (2003).
8. K. Holinde, Phys. Rep. **68**, 121 (1981).
9. D. J. Rowe, Rev. Mod. Phys. **40**, 153 (1968).
10. E. Holmlund *et al.*, Phys. Lett. B (2004) (in press).
11. G. L. Kane *et al.*, Phys. Rev. D **49**, 6173 (1994).
12. J. D. Vergados and T. S. Kosmas, Yad. Fiz. **61**, 1166 (1998) [Phys. At. Nucl. **61**, 1066 (1998)].
13. The European Muon Collab., Nucl. Phys. B **328**, 1 (1989).
14. J. D. Vergados, J. Phys. G **22**, 253 (1996).

Physics of Atomic Nuclei, Vol. 67, No. 6, 2004, pp. 1202–1205. From Yadernaya Fizika, Vol. 67, No. 6, 2004, pp. 1224–1227.

Analysis of the $2\nu\beta\beta$ Decay and Muon-Capture Reactions for the Mass $A = 46$ and $A = 48$ Nuclei Using the Nuclear Shell Model*

M. Kortelainen and J. Suhonen**

Department of Physics, University of Jyväskylä, Jyväskylä, Finland

Received November 4, 2003

Abstract—We discuss the two-neutrino double-beta decays of ^{46}Ca and ^{48}Ca by using the nuclear shell model with well-tested two-body interactions. We also discuss the ordinary muon-capture (OMC) reaction on the final nuclei, ^{46}Ti and ^{48}Ti, of these decays. The OMC leads to the virtual states of the intermediate nuclei, ^{46}Sc and ^{48}Sc, in these double-beta decays. © *2004 MAIK "Nauka/Interperiodica"*.

1. INTRODUCTION

The nuclear double-beta decay is one of the slowest reactions in nature. Therefore, its study is challenging from both the experimental and the theoretical points of view. The two-neutrino mode ($2\nu\beta\beta$) has been observed in several nuclei, whereas the neutrinoless mode ($0\nu\beta\beta$) has not been observed yet. In the theoretical perturbative description, the double-beta-decay transition goes through the states of an intermediate nucleus. In the $2\nu\beta\beta$ mode, the intermediate 1^+ states participate in the process, whereas in the $0\nu\beta\beta$ mode all the intermediate states are active. A reliable description of the structure of these states is essential in theoretical calculations for the double-beta-decay half-life. Unfortunately, only the lowest virtual transition can be probed by electron-capture or β^--decay experiments. However, it has been proposed that many of these virtual transitions to intermediate states could be probed by the ordinary muon-capture (OMC) reaction [1, 2].

In this article, we take ^{46}Ca and ^{48}Ca as examples to study the $2\nu\beta\beta$ decays and the related OMC reactions leading to the intermediate states of the corresponding double-beta decays.

2. THEORY

The $2\nu\beta\beta$ decay proceeds via the 1^+ states of the intermediate double-odd nucleus, and the corresponding expression for the inverse half-life can be factorized as

$$[t_{1/2}^{(2\nu)}(0_i^+ \to 0_f^+)]^{-1} = G_{\rm DGT}^{(2\nu)} |M_{\rm DGT}^{(2\nu)}|^2, \qquad (1)$$

where $G_{\rm DGT}^{(2\nu)}$ is an integral over the phase space of the leptonic variables [3, 4]. The double Gamow–Teller nuclear matrix element $M_{\rm DGT}^{(2\nu)}$, corresponding to the $2\nu\beta\beta$ decay, can be written as

$$M_{\rm DGT}^{(2\nu)} = \frac{\sum_n (0_f^+ || \sum_j \sigma(j)\tau_j^{\mp} || 1_n^+)(1_n^+ || \sum_j \sigma(j)\tau_j^{\mp} || 0_i^+)}{\left(\frac{1}{2}Q_{\beta\beta} + E_n - M_i\right)/m_e + 1}, \qquad (2)$$

where the transition operators are the usual Gamow–Teller operators, $Q_{\beta\beta}$ is the $2\nu\beta\beta$ Q value, E_n is the energy of the nth intermediate state, M_i is the mass of the initial nucleus, and m_e is the rest mass of the electron.

The muon-capture formalism is more involved and can be found, for example, in [5, 6].

The calculations of all the nuclear states of the double-beta-decay processes and muon capture processes were done by using the shell-model code OXBASH [7]. The calculated one-body transition densities were then inputs to the nuclear matrix elements for muon capture and double-beta decay. The interactions used in this work are the FPBP [8] and FPMCC [9]. In the case of ^{48}Ca, the JT dimension of calculation was truncated due to the computational limits. In the truncation, we required minimum particle occupancy in the $f_{7/2}$ orbital to be 2. For the $A = 46$ isobar, 75 lowest 1^+ intermediate states have been calculated, and in the case of the $A = 48$ isobar, 150 lowest 1^+ intermediate states have been taken into account.

3. RESULTS AND DISCUSSION

The results from our double-beta-decay calculations are summarized in Table 1. The cumulative matrix elements can be found in Figs. 1 and 2. From

*This article was submitted by the authors in English.

** e-mail: jouni.suhonen@phys.jyu.fi

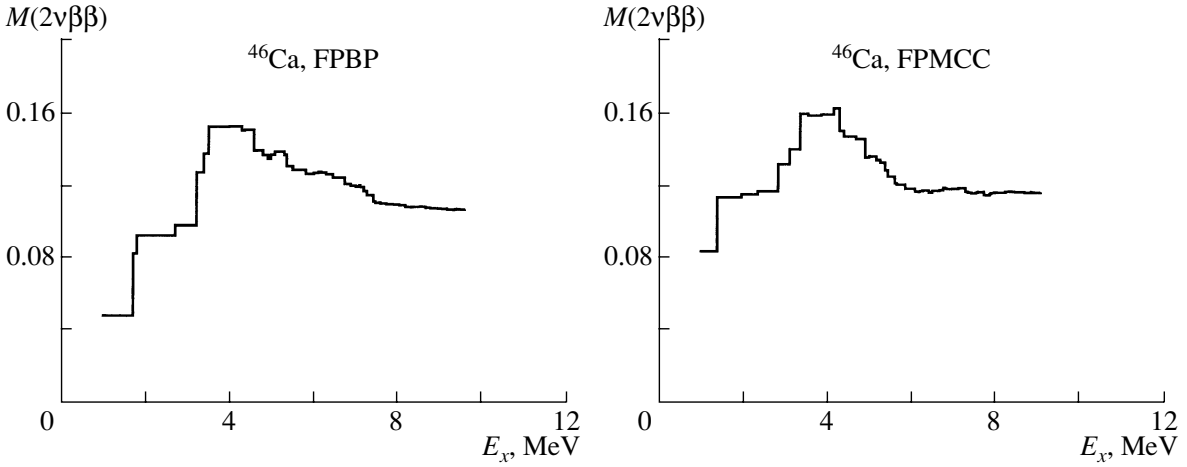

Fig. 1. The matrix element $M^{(2\nu)}_{\mathrm{DGT}}$ summed up to the excitation energy E_x of the intermediate nucleus ^{46}Sc for the transition $^{46}\mathrm{Ca}(0^+_{\mathrm{g.s}}) \to {}^{46}\mathrm{Ti}(0^+_{\mathrm{g.s}})$.

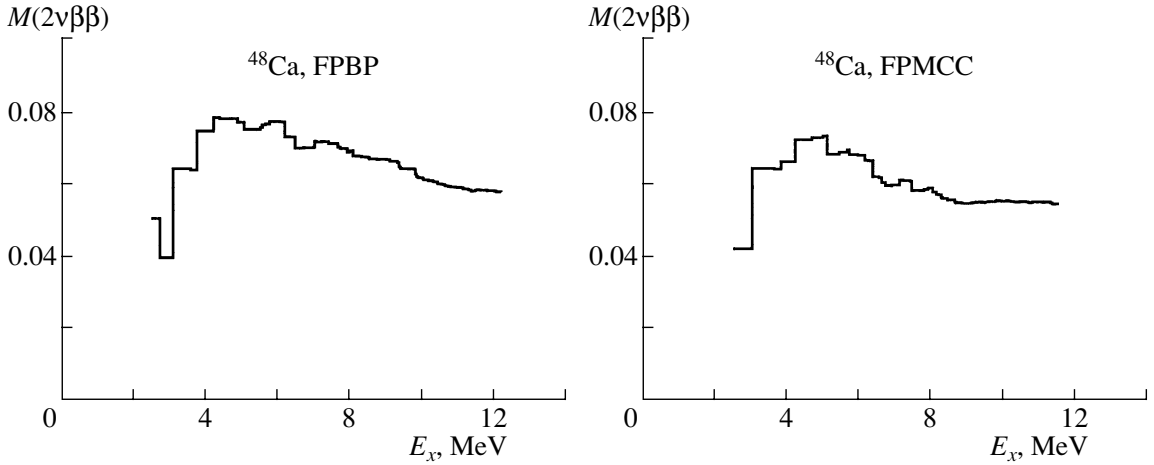

Fig. 2. The matrix element $M^{(2\nu)}_{\mathrm{DGT}}$ summed up to the excitation energy E_x of the intermediate nucleus ^{48}Sc for the transition $^{48}\mathrm{Ca}(0^+_{\mathrm{g.s}}) \to {}^{48}\mathrm{Ti}(0^+_{\mathrm{g.s}})$.

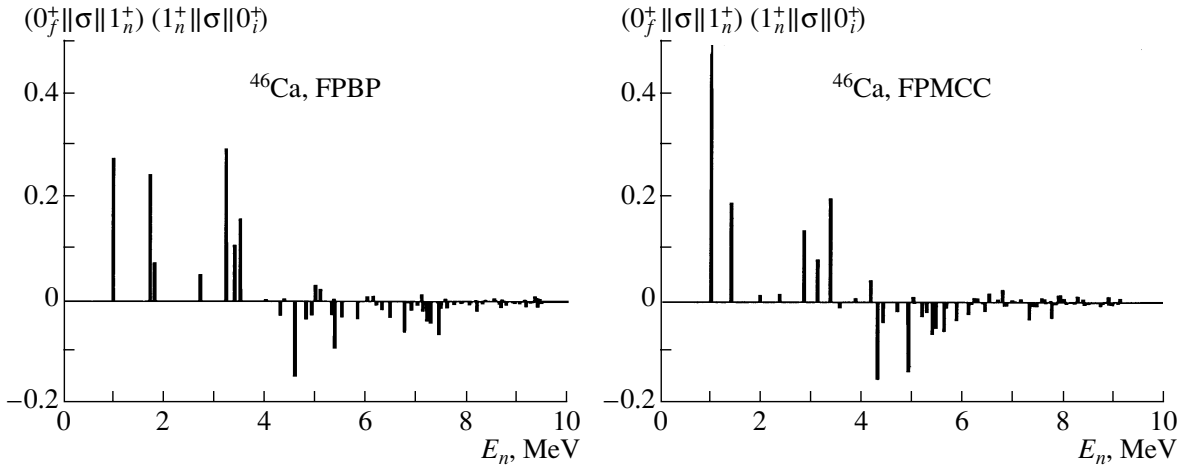

Fig. 3. The matrix elements $(0^+_f||\sigma||1^+_n)(1^+_n||\sigma||0^+_i)$ in the transition $^{46}\mathrm{Ca}(0^+_{\mathrm{g.s}}) \to {}^{46}\mathrm{Ti}(0^+_{\mathrm{g.s}})$.

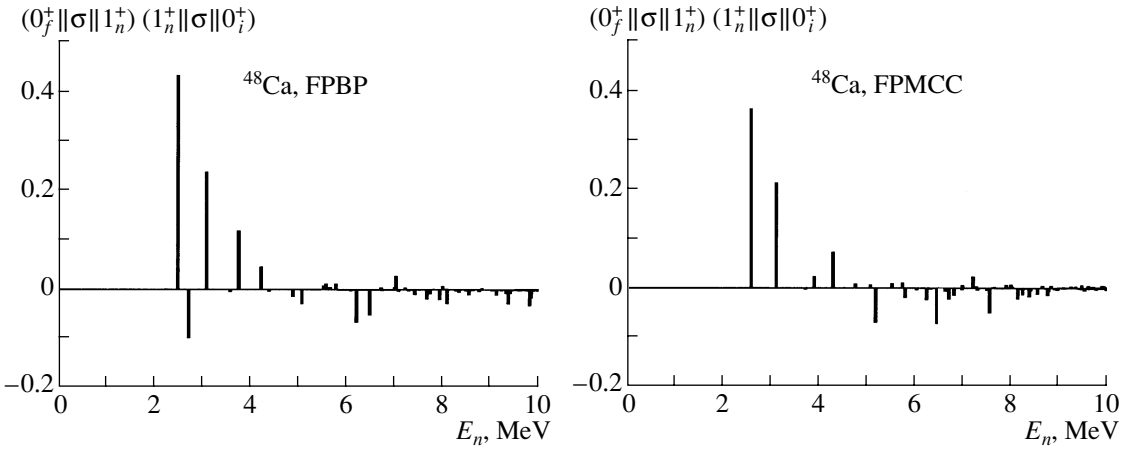

Fig. 4. The matrix elements $(0_f^+||\sigma||1_n^+)(1_n^+||\sigma||0_i^+)$ in the transition $^{48}\mathrm{Ca}(0_{\mathrm{g.s}}^+) \to {}^{48}\mathrm{Ti}(0_{\mathrm{g.s}}^+)$.

the figures, we note that the FPBP and FPMCC interactions give quite similar double Gamow–Teller matrix elements for the discussed nuclei. However, the shapes of the cumulative curves are different. Another notable point is the fact that the biggest contribution for the $2\nu\beta\beta$ matrix elements tends to come from only a few lowest intermediate states. This is, of course, partly explained by the effect of the energy denominator in Eq. (2). However, the product of the two Gamow–Teller matrix elements in Eq. (2) tends to be the biggest for the few lowest intermediate states too. This can be seen in Figs. 3 and 4, where we have plotted the contributions of the double Gamow–Teller matrix elements, without the energy denominator, for each intermediate state. The experimental value for the $2\nu\beta\beta$ half-life of ^{48}Ca is $4.2^{+3.3}_{-1.3} \times 10^{19}$ yr [10].

The calculated ordinary muon-capture rates are presented in Tables 2 and 3. For both considered nuclei, we note that the transition rate is almost independent of the pseudoscalar coupling constant, for both of the interactions. This simplifies the nuclear-structure analysis since then the comparison with the experimental partial OMC rates becomes almost independent of a parameter which has a somewhat uncertain value.

In the case of ^{48}Ti, the two interactions produce quite different muon capture rates, whereas the cumulative sums of Fig. 2 and the intermediate con-

Table 1. Calculated double-beta-decay matrix elements $M_{\mathrm{DGT}}^{(2\nu)}$, the Q values in units of electron rest mass, phase-space factors in units of inverse years, and the corresponding half-lives in units of a year for the studied double-beta-decay transitions (The renormalized value $g_A = -1.0$ has been used in all cases.)

Nuclei	$Q(\beta^-\beta^-)$, m_e	$G_{\mathrm{DGT}}^{(2\nu)}$, yr^{-1}	$M_{\mathrm{DGT}}^{(2\nu)}$	$t_{1/2}$, yr
^{46}Ca, FPBP	1.94	4.8×10^{-23}	0.108	1.7×10^{24}
^{48}Ca, FPBP	8.36	1.6×10^{-17}	0.058	1.8×10^{19}

Table 2. Partial muon-capture rates (in 10^3 s^{-1}) in ^{46}Ti with $g_A = -1.0$

J_f^π (int.)	g_P/g_A			
	−7	0	7	15
1_1^+ (FPBP)	2.875	2.304	2.032	2.086
1_2^+ (FPBP)	15.982	15.448	15.123	15.007
1_3^+ (FPBP)	2.000	1.855	1.780	1.781
1_4^+ (FPBP)	1.894	1.352	1.028	0.927

Table 3. Partial muon-capture rates (in 10^3 s^{-1}) in ^{48}Ti with $g_A = -1.0$ (The minimum number of particles on the $f_{7/2}$ orbital is taken to be 2.)

J_f^π (int.)	g_P/g_A			
	−7	0	7	15
1_1^+ (FPMCC)	33.882	33.598	33.481	33.552
1_2^+ (FPMCC)	2.244	2.170	2.153	2.203
1_3^+ (FPMCC)	1.276	0.983	0.797	0.719
1_4^+ (FPMCC)	9.583	9.477	9.432	9.454
1_1^+ (FPBP)	6.959	6.488	6.258	6.291
1_2^+ (FPBP)	16.953	16.602	16.417	16.411
1_3^+ (FPBP)	13.006	13.013	13.025	13.045
1_4^+ (FPBP)	0.150	0.107	0.076	0.055

tributions of Fig. 4 look very much the same. This sensitivity of the OMC to the two-body interaction used could help in selecting suitable interactions for double-beta-decay calculations.

REFERENCES

1. M. Kortelainen and J. Suhonen, Eur. Phys. Lett. **58**, 666 (2002).
2. M. Kortelainen and J. Suhonen, Nucl. Phys. A **713**, 501 (2003).
3. J. Suhonen and O. Civitarese, Phys. Rep. **300**, 123 (1998).
4. M. Doi, T. Kotani, and E. Takasugi, Prog. Theor. Phys. Suppl. **83**, 1 (1985).
5. M. Morita and A. Fujii, Phys. Rev. **118**, 606 (1960).
6. T. Siiskonen, J. Suhonen, V. A. Kuz'min, and T. V. Tetereva, Nucl. Phys. A **635**, 446 (1998); **651**, 437 (1999).
7. B. A. Brown, A. Etchegoyen, and W. D. M. Rae, The Computer Code OXBASH, MSU–NSCL Report 524 (1988).
8. A. Richter *et al.*, Nucl. Phys. A **523**, 325 (1991).
9. J. B. McGrory, B. H. Wildenthal, and E. C. Halbert, Phys. Rev. C **2**, 186 (1970).
10. V. B. Brudanin *et al.*, Phys. Lett. B **495**, 63 (2000).

Physics of Atomic Nuclei, Vol. 67, No. 6, 2004, pp. 1206–1209. From Yadernaya Fizika, Vol. 67, No. 6, 2004, pp. 1228–1231.

DOUBLE-BETA DECAY AND RARE PROCESSES

Neutrino Masses, Nuclear Matrix Elements, and the $0\nu\beta\beta$ Decay of ^{76}Ge*

O. Civitarese** **and J. Suhonen**[1)]

Departamento de Fisica, UNLP, La Plata, Argentina

Received November 17, 2003

Abstract—Neutrino data, obtained from SNO, SK, CHOOZ, KamLAND, and WMAP, are used to establish the upper limit of $\langle m_\nu \rangle$ relevant for the $0\nu\beta\beta$. The decay of ^{76}Ge is discussed within different light-neutrino mass spectra and with different nuclear matrix elements. © *2004 MAIK "Nauka/Interperiodica".*

1. INTRODUCTION

Our present understanding of the properties of the neutrino has been dramatically advanced by the results of various experiments [1–5]. The experimental evidence has confirmed the existence of neutrino flavor oscillations [6]. In addition to neutrino flavor oscillations and the confirmation of the theoretically predicted possibilities for the mixing and enhancement of the oscillations [7], double-beta-decay experiments can provide information on the nature of the neutrino and about its absolute mass scale [8–10]. This is a unique feature of double-beta decay, which must be consistent with other scale-fixing measurements like the WMAP measurements [5]. As we are going to discuss later on in this work, there turns out to be a gap between the range of mass limits extracted from double-beta-decay studies, 0.4 to 1.3 eV, and those extracted from the other neutrino-related studies, which are on the order of 0.10 to 0.20 eV or even lower. There is a clear discrepancy between both sets of results concerning the observation of neutrinoless double-beta ($0\nu\beta\beta$) decay. This issue has become a hot one due to the recent claim [11] about the positive identification of $0\nu\beta\beta$ decay signals in the decay of ^{76}Ge (see also [12]). In this work, we discuss constraints, set by the oscillation and mass parameters, on the effective neutrino mass relevant for the $0\nu\beta\beta$ decay and compare them with the ones obtained by performing nuclear-structure study.

2. FORMALISM

2.1. Neutrino Data

To calculate effective neutrino properties, like the effective electron-neutrino mass, $\langle m_\nu \rangle$, one needs to know the neutrino-mixing matrix U and the light-neutrino mass spectrum (m_1, m_2, m_3) [8]. Out of the very rich recently published list of articles dealing with analysis of the SNO results, we have selected two representative ones, namely, (a) the results presented in the paper of Bandyopadhyay, Choubey, Goswami, and Kar (BCGK) [13] and (b) the expression of the mixing matrix in terms of the solar-neutrino data and the zeroth-order approximation of the mixing matrix assuming maximum mixing to perform our calculations. The next step consists of the definition of a neutrino mass spectrum. The relative order between the mass eigenvalues, usually referred to in the literature as *mass hierarchy or hierarchical order of the mass eigenvalues*, cannot be fixed only by the measured squared mass differences. In order to estimate the possible range of m_i, we define the relative scales

$$m_1 = f m_2, \qquad m_2 = g m_3 \tag{1}$$

for the so-called normal hierarchy ($m_1 \approx m_2 < m_3$) and

$$m_1 = f m_2, \qquad m_3 = g m_1 \tag{2}$$

for the so-called inverse ($m_1 \approx m_2 > m_3$) and degenerate ($m_3 \approx m_2 \approx m_1$) hierarchies. To these factors we have added the information related to the scale of the mass eigenvalues, which is determined by the extreme value

$$m_0 = \Omega_\nu / 3, \tag{3}$$

where the value of Ω_ν is taken from the WMAP data. The factors f and g are determined in such a way that the resulting masses $m_i(f, g)$ obey the observed mass differences, hereafter, denoted as Δm^2

*This article was submitted by the authors in English.

[1)]Department of Physics, University of Jyväskylä, Jyväskylä, Finland.

**e-mail: civitare@venus.fisica.unlp.edu.ar

Table 1. Calculated effective electron-neutrino masses $\langle m_\nu \rangle_\pm$ (Indicated in the table are the mass spectrum and the adopted mixing matrix. The values are given in eV. The results listed as "extreme" have been obtained by using the extreme upper values of f and g. The adopted values for the mass differences are $\delta m^2_{12} = 7.1 \times 10^{-5}\ \mathrm{eV}^2$, $\delta m^2_{23} = 2.7 \times 10^{-3}\ \mathrm{eV}^2$, and $m_0 = 0.24$ eV. The mixing matrix $U(a)$ is taken from [13], $U(b)$ is calculated by taking the largest values of the solar and atmospheric mixing angles, and $U(c)$ is the maximum-mixing solution.)

Mass spectrum		$\langle m_\nu \rangle$	$U(a)$	$U(b)$	$U(c)$
Normal	$(m_1 = 0)$	$\langle m_\nu \rangle_-$	-0.010	-0.012	-0.019
		$\langle m_\nu \rangle_+$	0.011	0.012	0.019
	(extreme)	$\langle m_\nu \rangle_-$	0.105	0.086	-0.769×10^{-4}
		$\langle m_\nu \rangle_+$	0.231	0.231	0.231
Inverse	$(m_3 = 0)$	$\langle m_\nu \rangle_-$	0.105	0.087	-0.153×10^{-2}
		$\langle m_\nu \rangle_+$	0.234	0.235	0.235
	(extreme)	$\langle m_\nu \rangle_-$	0.108	0.088	-0.749×10^{-4}
		$\langle m_\nu \rangle_+$	0.237	0.237	0.237
Degenerate	(extreme)	$\langle m_\nu \rangle_-$	0.107	0.088	-0.715×10^{-4}
		$\langle m_\nu \rangle_+$	0.237	0.237	0.237

($\Delta m^2_{31} \approx \Delta m^2_{32}$) and δm^2 (Δm^2_{12}). For each set of allowed values of f, g and for each of the hierarchies considered we have calculated m_i. The effective neutrino mass $\langle m_\nu \rangle$, relevant for the $0\nu\beta\beta$ decay, is given by [14]

$$\langle m_\nu \rangle_\pm = \sum_{i=1}^{3} m_i \lambda_i |U_{ei}|^2 = m_1 U_{e1}^2 \pm m_2 U_{e2}^2, \quad (4)$$

since for the adopted best fit $U_{e3} \approx 0$ [13]. We have consistently neglected CP-violating phases, assumed CP conservation, and written $\lambda_i = \pm 1$ for the relative Majorana phases, since the fit of [13] was performed under the assumption of CP conservation. In Table 1 we give, for each of the adopted forms of the mixing matrix U, the range of values of the calculated effective electron-neutrino masses. These values correspond to the limiting values of f and g given in the previous equations. This part of the analysis is, of course, relevant for the present study since it determines exclusion regions for the allowed values of the effective neutrino mass relevant for the $0\nu\beta\beta$ (see, for instance, [6] for a similar approach).

2.2. Nuclear Matrix Elements

The implication of these results for $\langle m_\nu \rangle$ upon the rates of $0\nu\beta\beta$ decay is easily seen if one writes the corresponding half-life $t^{(0\nu)}_{1/2}$ as

$$\left(t^{(0\nu)}_{1/2}\right)^{-1} = \left(\frac{\langle m_\nu \rangle}{m_e}\right)^2 C^{(0\nu)}_{mm}, \quad (5)$$

where the factor $C^{(0\nu)}_{mm}$ is defined as

$$C^{(0\nu)}_{mm} = G^{(0\nu)}_1 \left(M^{(0\nu)}_{\mathrm{GT}}(1 - \chi_{\mathrm{F}})\right)^2 \quad (6)$$

in terms of the nuclear matrix elements, $M^{(0\nu)}_{\mathrm{GT}}(1 - \chi_{\mathrm{F}})$, and the phase-space factors $G^{(0\nu)}_1$ entering the mass term of the transition probability [14]. The standard procedure, applied in the literature to calculate the $0\nu\beta\beta$-decay rate, involves three major components:

(a) The calculation of the spectrum of the intermediate double-odd-mass nucleus with $(A, N \pm 1, Z \mp 1)$ nucleons. The pnQRPA is an approximate diagonalization in the one-particle–one-hole $1p$–$1h$ (or two-quasiparticle) space, and it includes the effects of $2p$–$2h$ ground-state correlations by means of the backward-going amplitudes. Since the calculations are based on a quasiparticle mean field, one forces the breaking of certain symmetries like the particle-number symmetry by the use of the BCS approximation and the isospin symmetry by the use of effective proton and neutron single-particle states. The final results of the pnQRPA calculations will certainly be affected by these symmetry-breaking effects induced by the way in which we handle the nuclear interactions [14].

(b) The calculation of the leptonic phase-space factors, as dictated by the second-order perturbative treatment of the electroweak interaction. At the level of the minimal extension of the Standard Model (SM) Lagrangian (mass sector only), these phase-space factors can be easily calculated. At the level of the

Table 2. Calculated nuclear matrix elements for the case of ^{76}Ge (The adopted value for the lower limit of the half-life is $t_{1/2}^{(0\nu)} = 2.5 \times 10^{25}$ yr. Indicated in the table are the models used to calculate the nuclear matrix elements, which are taken from the literature. The abbreviations stand for the proton–neutron quasiparticle random-phase approximation (pnQRPA), the particle-number-projected pnQRPA (pnQRPA (proj.)), proton–neutron pairing pnQRPA (pnQRPA + pn pairing), the renormalized pnQRPA (RQRPA), the second pnQRPA (SQRPA), the self-consistent renormalized pnQRPA (SCRQRPA), the fully renormalized pnQRPA (full-RQRPA), and the variation after the projection mean-field approach (VAMPIR).)

$C_{mm}^{(0)}$, yr^{-1}	$F_N(\min) \times$ $\times 10^{-12}$	Theory
1.12×10^{-13}	2.80	pnQRPA
6.97×10^{-14}	1.74	pnQRPA
7.51×10^{-14}	1.88	pnQRPA (proj.)
7.33×10^{-14}	1.83	pnQRPA
1.42×10^{-14}	0.35	pnQRPA + + pn pairing
1.18×10^{-13}	2.95	pnQRPA
8.27×10^{-14}	2.07	pnQRPA
2.11×10^{-13}	5.27	RQRPA
6.19×10^{-14}	1.55	RQRPA + q-dep. operators
$(1.8–2.2) \times 10^{-14}$	0.45–0.55	pnQRPA
$(5.5–6.3) \times 10^{-14}$	1.37–1.57	RQRPA
$(2.7–3.2) \times 10^{-15}$	0.07–0.08	SCRQRPA
1.85×10^{-14}	0.46	pnQRPA
1.21×10^{-14}	0.30	RQRPA
3.63×10^{-14}	0.91	full-RQRPA
6.50×10^{-14}	1.62	SQRPA
2.88×10^{-13}	7.20	VAMPIR
1.58×10^{-13}	3.95	Shell Model
1.90×10^{-14}	0.47	Shell Model

two-nucleon mechanism, the value of g_A is currently fixed at $g_A = 1.254$, but, for the medium-heavy and heavy nuclei, an effective value of $g_A = 1.0$ has also been used. In this work we adopt the conservative estimate of $g_A = 1.254$.

(c) The calculation of the matrix elements of the relevant current operators that act upon the nucleons. These operators are also well known and their multipole structures are derived from the expansion of the electroweak current [14]. In the present calculation we have considered the standard type of operators, without introducing momentum dependence.

A compilation of the values of nuclear matrix elements and phase-space factors can be found in [14]. If one compares the extracted upper limits for the neutrino masses from $0\nu\beta\beta$-decay data with the ranges of neutrino masses given in the previous section, it becomes evident that the present generation of $0\nu\beta\beta$ experiments is rather insensitive to the effective neutrino mass coming from the best fit of the solar + atmospheric + reactor data, except for the Heidelberg–Moscow experiment if one takes the range of values ($\langle m_\nu \rangle = 0.11–0.56$ eV) reported in [11]. If one takes the value $\langle m_\nu \rangle \approx 0.24$ eV (the heaviest possible effective mass), which is favored by the inverse and degenerate mass spectra (see Table 1), one sees that it is outside the range of the present upper limits fixed by double-beta-decay experiments, with the possible exception of the decay of ^{76}Ge, which just barely reaches this estimate. To reach the neutrino-mass value resulting from the neutrino data, one definitely needs larger matrix elements than the ones produced thus far by the spherical pnQRPA model and/or longer half-lives than the present measured limits.

2.3. pnQRPA Matrix Elements for ^{76}Ge

Table 2 shows the results of the matrix elements corresponding to the mass sector of the $0\nu\beta\beta$ decay in ^{76}Ge calculated within the family of the pnQRPA-related models [14]. By using the phase-space factors listed in [14], we arrive at the central value for the matrix elements in the pnQRPA, namely,

$$M_{\rm GT}^{(0\nu)}(1-\chi_{\rm F})_{\rm pnQRPA} = 3.65. \qquad (7)$$

The corresponding value for the latest large-scale shell-model calculation is given by

$$M_{\rm GT}^{(0\nu)}(1-\chi_{\rm F})_{\rm shell\ model} = 1.74. \qquad (8)$$

In terms of the effective neutrino mass, using the half-life $t_{1/2}^{(0\nu)} \geq 2.5 \times 10^{25}$ yr, these matrix elements lead to

$$\langle m_\nu \rangle_{\rm pnQRPA} \leq 0.35 \ \ {\rm eV} \qquad (9)$$

for the pnQRPA estimate and

$$\langle m_\nu \rangle_{\rm shell\ model} \leq 0.74 \ \ {\rm eV} \qquad (10)$$

for the shell-model estimate of the matrix element. This means that to go to masses of the order of 0.24 eV, as required by WMAP, one needs larger nuclear matrix elements than the ones given by the pnQRPA or by the available shell-model results. In

fact, to reach the WMAP limit one would need the value

$$M_{\rm GT}^{(0\nu)}(1-\chi_{\rm F})_{\rm exp} \geq 5.36, \qquad (11)$$

which is $\approx\sqrt{2}$ times larger than the reference pnQRPA. The largest matrix element listed in Table 2, coming from the VAMPIR approach, would yield the value $\langle m_\nu\rangle_{\rm VAMPIR} \leq 0.19$ eV, which just touches the value $\langle m_\nu\rangle \leq 0.24$ eV coming from the analysis of the neutrino-related data. However, it is appropriate to point out here that the VAMPIR matrix element is considered unrealistically large, because in the calculations no proton–neutron residual interaction was included.

Finally, our present value

$$M_{\rm GT}^{(0\nu)}(1-\chi_{\rm F})^{\rm present}_{\rm pnQRPA} = 3.33 \qquad (12)$$

is consistent with the central value (7), and it yields an effective neutrino mass

$$\langle m_\nu\rangle^{\rm present}_{\rm pnQRPA} \leq 0.39 \ \ {\rm eV} \qquad (13)$$

if one takes for the half-life the lower limit and

$$\langle m_\nu\rangle^{\rm present}_{\rm pnQRPA} \leq 0.50 \ \ {\rm eV} \qquad (14)$$

if one takes for the half-life the value 1.5×10^{25} yr given by the Heidelberg–Moscow Collaboration [11].

Thus, the issue about the observability of the $0\nu\beta\beta$ decay relies, from the theoretical side, upon the estimates for the effective neutrino mass and upon the estimates of the relevant nuclear matrix elements. While in some cases the differences between the calculated matrix elements are within factors of the order of 3, in some other cases the differences are much larger. This shows one of the essential features of nuclear double-beta decay, namely, that case-by-case theoretical studies are needed instead of a global one [14]. The elucidation of this problem relies on data that may be available in the next generation of double-beta-decay experiments. These future experiments are needed to reach the values of effective neutrino masses extracted from the neutrino-oscillation-related data.

3. CONCLUSIONS

To conclude, in this work we have presented results on the effective neutrino mass, as obtained from the best-fit mass-mixing matrix U determined from the analysis of solar + atmospheric + reactor + satellite data and compared them with the values extracted from neutrinoless double-beta-decay experiments. The value of the effective electron-neutrino mass extracted from the neutrino-related experiments, $\langle m_\nu\rangle \leq 0.24$ eV, does not compare with the central value of $\langle m_\nu\rangle \approx 0.39$ eV, reported in [11]. It does not compare, either, with the values given by the standard pnQRPA model after taking into account the span in the calculated matrix elements. To explain the difference between the above results, we have compiled systematics of the calculated nuclear matrix elements and performed additional pnQRPA calculations. In the case of ^{76}Ge and if one adopts for the half-life the lower limit of 2.5×10^{25} yr, the nuclear matrix elements needed to yield the desired effective neutrino masses are larger than any of the known nuclear matrix elements calculated in the framework of the spherical pnQRPA. This conclusion also holds for the available shell-model results.

ACKNOWLEDGMENTS

This work has been partially supported by the National Research Council (CONICET) of Argentina and by the Academy of Finland under the Finnish Centre of Excellence Programme 2000–2005 (project no. 44875, Nuclear and Condensed Matter Programme at JYFL).

REFERENCES

1. Q. R. Ahmad *et al.* (SNO Collab.), Phys. Rev. Lett. **87**, 071301 (2001); **89**, 011301 (2002); **89**, 011302 (2002).
2. S. Fukuda *et al.* (Super-Kamiokande Collab.), Phys. Rev. Lett. **86**, 5651 (2001).
3. K. Eguchi *et al.* (KamLAND Collab.), Phys. Rev. Lett. **90**, 021802 (2003).
4. M. Appollonio *et al.*, Phys. Lett. B **466**, 415 (1999).
5. C. L. Bennet *et al.*, astro-ph/0302207.
6. S. Pascoli, S. T. Petcov, and W. Rodejohann, hep-ph/0209059; hep-ph/0212113.
7. L. Wolfenstein, Phys. Rev. D **17**, 2369 (1978); S. P. Mikheev and A. Y. Smirnov, Yad. Fiz. **42**, 1441 (1985) [Sov. J. Nucl. Phys. **42**, 913 (1985)].
8. A. Y. Smirnov, Czech. J. Phys. **52**, 439 (2002).
9. H. V. Klapdor-Kleingrothhaus, H. Päs, and A. Y. Smirnov, Phys. Rev. D **63**, 073005 (2001).
10. E. Ma, hep-ph/0303126.
11. H. V. Klapdor-Kleingrothaus, A. Dietz, H. L. Harney, and I. V. Krivosheina, Mod. Phys. Lett. A **16**, 2409 (2001); H. V. Klapdor-Kleingrothaus *et al.*, Part. Nucl. Lett. **110** (1), 57 (2002).
12. C. E. Aalseth *et al.*, hep-ex/0202018; Mod. Phys. Lett. A **17**, 1475 (2002).
13. A. Bandyopadhyay, S. Choubey, S. Goswami, and K. Kar, hep-ph/0110307; Phys. Rev. D **65**, 073031 (2002).
14. J. Suhonen and O. Civitarese, Phys. Rep. **300**, 123 (1998).

Physics of Atomic Nuclei, Vol. 67, No. 6, 2004, pp. 1210–1215. From Yadernaya Fizika, Vol. 67, No. 6, 2004, pp. 1232–1237.

DOUBLE-BETA DECAY AND RARE PROCESSES

Nuclear Deformation and the Double-Beta Decay*

L. Pacearescu[**], **A. Faessler, and F. Šimkovic**[1)]

Institut für Theoretische Physik der Universität Tübingen, Tübingen, Germany

Received November 17, 2003

Abstract—The effect of deformation on the two-neutrino double-beta decay ($2\nu\beta\beta$ decay) for ground-state transition $^{76}\mathrm{Ge} \to {}^{76}\mathrm{Se}$ is studied in the framework of the deformed QRPA with separable Gamow–Teller residual interaction. A new suppression mechanism of the $2\nu\beta\beta$-decay matrix element based on the difference in deformations of the initial and final nuclei is reported. An advantage of this suppression mechanism in comparison with that associated with ground-state correlations is that it allows a simultaneous description of the single-β and the $2\nu\beta\beta$ decay. © *2004 MAIK "Nauka/Interperiodica".*

1. INTRODUCTION

The complexity of the calculation of the double-beta-decay matrix elements consists in the fact that it is a second order process; i.e., in addition to the initial and final nuclear states, knowledge of the complete set of states of the intermediate nucleus is required. In solving this problem, different models and nuclear structure scenarios were applied [1–3].

Double-beta decay can occur in different modes: The neutrinoless mode ($0\nu\beta\beta$ decay) requires violation of the lepton number and probes new physics scenarios beyond the Standard Model (SM) of particle physics [1, 2, 4–6]. The two-neutrino double-beta decay ($2\nu\beta\beta$ decay) mode is a process allowed in the SM; i.e., the half-life of this process is free of unknown parameters of the particle physics side [1–4].

As the half-lives of $2\nu\beta\beta$ decay have already been measured for about ten nuclei, the values of the associated nuclear matrix element can be extracted directly. It provides a cross-check on the reliability of the matrix element calculations.

Since the nuclei undergoing double-beta decay are open shell nuclei, the proton–neutron quasiparticle random phase approximation (pnQRPA) method has been the most employed in the evaluation of the double-beta-decay matrix elements [1, 2]. In addition, this approach has succeeded in reproducing the experimentally observed suppression of the $2\nu\beta\beta$-decay transitions [7–10]. However, a strong sensitivity of the computed matrix elements on an increase in the strength of the particle–particle residual interaction in the 1^+ channel leads to a problem of fixing this parameter [1]. There is an interest in studying the effect of deformation on the double-beta-decay matrix elements within the deformed QRPA [11, 12], which allows a unified description of the $2\nu\beta\beta$ decay in spherical and deformed nuclei. In the first applications, only the particle–hole terms of the Gamow–Teller force were taken into account [11, 12]. It was supposed that the particle–particle terms have a minor effect on the Gamow–Teller strength function. However, from the spherical QRPA calculations, we know that the particle–particle force plays an important role in describing the β^+ and $\beta\beta$ processes [7–10]. Recently, the importance of the particle–particle interaction has been confirmed also in the deformed QRPA treatment of the Gamow–Teller strength distributions [12]. A strong sensitivity of the single-β-decay characteristics to the nuclear shape, RPA ground-state correlations, and pairing correlations were manifested.

The aim of this presentation is to emphasize the new results obtained in our theoretical investigations concerning the effect of nuclear deformation on the matrix element of $2\nu\beta\beta$ decay within the deformed QRPA. Apart from β^- and β^+ distributions, the overlap factors of the single particle wave functions of the initial and final nuclei seem to be very sensitive to deformation and bring a new suppression effect on the matrix element calculations. We present here, as an example, the numerical results for the overlap calculations in four pairs of nuclei which are double-beta-decay candidates and for the $2\nu\beta\beta$ decay of $^{76}\mathrm{Ge}$, which is a prominent transition due to ongoing and planned $\beta\beta$ experiments for this isotope [13].

*This article was submitted by the authors in English.

[1)]Department of Nuclear Physics, Comenius University, Bratislava, Slovakia.

[**]e-mail: Larisa.Pacearescu@uni-tuebingen.de

1063-7788/04/6706-1210$26.00

2. FORMALISM OF THE DEFORMED QRPA

The theoretical approach is based on the deformed pnQRPA with separable proton–neutron residual interaction, which is relevant for the allowed Gamow–Teller transitions [11, 12]. This approach allows for a unified description of the $2\nu\beta\beta$-decay process in deformed and spherical nuclei. The total nuclear Hamiltonian takes the form

$$H = H_0 + H_{\rm int}. \tag{1}$$

H_0 denotes the Hamiltonian for the quasiparticle mean field described by a deformed axially symmetric Woods–Saxon potential [14]

$$H_0 = \sum_{\tau\rho} E_\tau a^\dagger_{\tau\rho_\tau} a_{\tau\rho_\tau} \qquad (\tau = p, n), \tag{2}$$

where E_τ are the quasiparticle energies and $a^\dagger_{\tau\rho_\tau}$ ($a_{\tau\rho_\tau}$) is the quasiparticle creation (annihilation) operator. The $p(n)$ index denotes proton (neutron) quasiparticle states with projection $\Omega_p(\Omega_n)$ of the full angular momentum on the nuclear symmetry axis and parity $\pi_p(\pi_n)$. The index ρ ($\rho = \pm 1$) represents the sign of the angular momentum projection Ω. We note that intrinsic states are twofold degenerate. The states with Ω_τ and $-\Omega_\tau$ have the same energy as a consequence of the time reversal invariance. We shall use notation such that Ω_τ is taken to be positive for states and negative for time-reversed states.

The method includes pairing between like nucleons in the BCS approximation with fixed gap parameters for protons, Δ_p, and neutrons, Δ_n. The residual interaction part $H_{\rm int}$ of the nuclear Hamiltonian in (1) contains two terms associated with particle–hole (ph) and particle–particle (pp) interaction:

$$H_{\rm int} = \chi \sum_{K=0,\pm1} (-1)^K (\beta^-_{1K}\beta^+_{1-K} + \beta^+_{1-K}\beta^-_{1K}) - \kappa \sum_K (-1)^K (P^-_{1K}P^+_{1-K} + P^+_{1-K}P^-_{1K}). \tag{3}$$

The operators β^- and P^- are ph and pp components of the spin–isospin $\tau^+\sigma$ [15]. The ph and pp forces in Eq. (3) are defined to be repulsive and attractive ($\chi, \kappa \geq 0$), respectively, reflecting the general feature of the nucleon–nucleon interaction in the $J^\pi = 1^+$ channel. The intrinsic states are generated by the phonon creation operator

$$Q^{m\dagger}_K = \sum_i [X^m_{i,K} A^\dagger(i,K) - Y^m_{i,K} A(\bar{i},K)], \tag{4}$$

where $A^\dagger_i$ and A_i are the two-quasiparticle creation and annihilation operators:

$$A^\dagger(i,K) = a^\dagger_{p\rho_p} a^\dagger_{n\rho_n}, \quad A^\dagger(\bar{i},K) = \tilde{a}^\dagger_{p\rho_p} \tilde{a}^\dagger_{n\rho_n}, \tag{5}$$

$$A(i,K) = (A^\dagger(i,K))^\dagger.$$

The quasiparticle pairs i and $\bar{i}$ are defined by the selection rules $\Omega_p - \Omega_n = K$ and $\Omega_n - \Omega_p = K$, respectively, and $\pi_p\pi_n = 1$. In the case $K = \pm 1$ ($K = 0$), the sum in (4) includes all bound and quasibound two-quasiparticle spin–projection–flip (nonspin–projection–flip) configurations. We note that the $K = -1$ and $K = 1$ modes are related to each other through time reversal and are degenerate.

The excitation energy ω_k and the amplitudes $X^m_{i,K}$ and $Y^m_{i,K}$ of the phonon $Q^{m\dagger}_K$ are obtained by solving the RPA matrix equation

$$\begin{pmatrix} \mathcal{A}(K) & \mathcal{B}(K) \\ \mathcal{B}(K) & \mathcal{A}(K) \end{pmatrix} \begin{pmatrix} X^m_K \\ Y^m_K \end{pmatrix} = \omega^m_K \begin{pmatrix} 1 & 0 \\ 0 & -1 \end{pmatrix} \begin{pmatrix} X^m_K \\ Y^m_K \end{pmatrix}, \tag{6}$$

where

$$\mathcal{A}_{ij}(K) = \mathcal{E}_i\delta_{ij} + 2\chi[\sigma_K(i)\sigma_K(j) + \bar{\sigma}_K(i)\bar{\sigma}_K(j)] - 2\kappa[\pi_K(i)\pi_K(j) + \bar{\pi}_K(i)\bar{\pi}_K(j)], \tag{7}$$

$$\mathcal{B}_{ij}(K) = 2\chi[\sigma_K(i)\bar{\sigma}_K(j) + \bar{\sigma}_K(i)\sigma_K(j)] + 2\kappa[\pi_K(i)\bar{\pi}_K(j) + \bar{\pi}_K(i)\pi_K(j)]$$

with $\mathcal{E}_i = E_p + E_n$ being the two-quasiparticle excitation energy and

$$\sigma_K(i) = \langle p\rho_p|\tau^+\sigma_K|n\rho_n\rangle u_p v_n, \tag{8}$$

$$\bar{\sigma}_K(i) = \langle p\rho_p|\tau^+\sigma_K|n\rho_n\rangle v_p u_n,$$

$$\pi_K(i) = \langle p\rho_p|\tau^+\sigma_K|n\rho_n\rangle u_p u_n,$$

$$\bar{\pi}_K(i) = \langle p\rho_p|\tau^+\sigma_K|n\rho_n\rangle v_p v_n.$$

An advantage of using separable forces is that the RPA matrix equation reduces to a homogeneous system of only four equations for the four unknown norms N_σ, $N_{\bar{\sigma}}$, N_π, and $N_{\bar{\pi}}$, which is much easier to solve in comparison with the full diagonalization of an RPA matrix of large dimension [15]. The forward and backward amplitudes are written as

$$X^m_{iK} = \frac{2N_\sigma}{\omega^m_K - \mathcal{E}_i}\left[\chi\left(\sigma_K(i) + \bar{\sigma}_K(i)\frac{N_{\bar{\sigma}}}{N_\sigma}\right) - \kappa\left(\pi_K(i)\frac{N_\pi}{N_\sigma} + \bar{\pi}_K(i)\frac{N_{\bar{\sigma}}}{N_\sigma}\right)\right], \tag{9}$$

$$Y^m_{iK} = \frac{-2N_\sigma}{\omega^m_K + \mathcal{E}_i}\left[\chi\left(\bar{\sigma}_K(i) + \sigma_K(i)\frac{N_{\bar{\sigma}}}{N_\sigma}\right) + \kappa\left(\bar{\pi}_K(i)\frac{N_\pi}{N_\sigma} + \pi_K(i)\frac{N_{\bar{\sigma}}}{N_\sigma}\right)\right],$$

where for the norms N_σ, $N_{\bar\sigma}$, N_π, and $N_{\bar\pi}$ we have

$$N_\sigma = \sum_j [\sigma_K(i) X^m_{jK} + \bar\sigma_K(i) Y^m_{jK}], \quad (10)$$

$$N_{\bar\sigma} = \sum_j [\bar\sigma_K(i) X^m_{jK} + \sigma_K(i) Y^m_{jK}],$$

$$N_\pi = \sum_j [\pi_K(i) X^m_{jK} - \bar\pi_K(i) Y^m_{jK}],$$

$$N_{\bar\pi} = \sum_j [\bar\pi_K(i) X^m_{jK} - \pi_K(i) Y^m_{jK}].$$

The normalization factor N_σ is determined from the condition

$$\langle \mathrm{RPA}|[Q^m_K, Q^{m\dagger}_K]|\mathrm{RPA}\rangle = \sum_i (X^m_{iK} X^m_{iK} - Y^m_{iK} Y^m_{iK}) = 1. \quad (11)$$

The β^- and β^+ transition amplitudes from the 0^+ even–even initial nuclear state to a one-phonon state in an odd–odd final nucleus are expressed by

$$\langle 1M(K), m|\hat\beta^-_M|0^+_{\mathrm{g.s}}\rangle = \sum_i [\sigma(i) X^m_{iK} + \bar\sigma(i) Y^m_{iK}], \quad (12)$$

$$\langle 1M(K), m|\hat\beta^+_M|0^+_{\mathrm{g.s}}\rangle = \sum_i [\bar\sigma(i) X^m_{iK} + \sigma(i) Y^m_{iK}].$$

Here, $|0^+_{\mathrm{g.s}}\rangle$ denotes the correlated RPA ground state in the laboratory frame.

The inverse half-life of $2\nu\beta\beta$ decay can be expressed as a product of an accurately known phase-space factor $G^{2\nu}$ and the Gamow–Teller transition matrix element $M^{2\nu}_{\mathrm{GT}}$ in the second order:

$$[T^{2\nu}_{1/2}(0^+_{\mathrm{g.s}} \to 0^+_{\mathrm{g.s}})]^{-1} = G^{2\nu}(g_A)^4 |M^{2\nu}_{\mathrm{GT}}|^2. \quad (13)$$

The contribution from the two successive Fermi transitions is safely neglected as they come from the isospin-mixing effect [16]. Within the deformed QRPA, the double Gamow–Teller matrix element $M^{2\nu}_{\mathrm{GT}}$ for ground-state to ground-state $2\nu\beta\beta$-decay transition takes the form

$$M^{2\nu}_{\mathrm{GT}} = \sum_{m_i m_f} \sum_{K=0,\pm1} \frac{\langle 0^+_f \parallel \beta^- \parallel 1(K), m_f\rangle \langle 1(K), m_f|1(K), m_i\rangle \langle 1(K), m_i \parallel \beta^- \parallel 0^+_i\rangle}{(\omega^{m_f}_K + \omega^{m_i}_K)/2}. \quad (14)$$

The sum extends over all 1^+ states of the intermediate nucleus. The index $i(f)$ indicates that the quasiparticles and the excited states of the nucleus are defined with respect to the initial (final) nuclear ground state $|0^+_i\rangle$ ($|0^+_f\rangle$). The overlap is necessary since these intermediate states are not orthogonal to each other. The two sets of intermediate nuclear states generated from the initial and final ground states are not identical within the considered approximation scheme. Therefore the overlap factor of these states is introduced as follows:

$$\langle 1(K), m_f|1(K), m_i\rangle = \sum_{j_i j_f} [X^{m_i}_{j_f K} X^{m_f}_{j_i K} - Y^{m_i}_{j_f K} Y^{m_f}_{j_i K}] \langle j_f|j_i\rangle \quad (15)$$

with

$$\langle j_f|j_i\rangle = \langle p_f \rho_{p_f}|p_i \rho_{p_i}\rangle \langle n_f \rho_{n_f}|n_i \rho_{n_i}\rangle \times \langle \mathrm{BCS}(^{76}\mathrm{Se})|\mathrm{BCS}(^{76}\mathrm{Ge})\rangle. \quad (16)$$

The overlap factors of the single-particle wave functions of the initial and final nuclei are given explicitly in [15], and the one of the initial and final BCS vacua is given by [17]

$$\langle \mathrm{BCS}(^{76}\mathrm{Se})|\mathrm{BCS}(^{76}\mathrm{Ge})\rangle = \prod_p (u^{(f)}_p u^{(i)}_p + v^{(f)}_p v^{(i)}_p) \prod_n (u^{(f)}_n u^{(i)}_n + v^{(f)}_n v^{(i)}_n). \quad (17)$$

Here, $p(n)$ denotes a pair of proton (neutron) single-particle states of the initial and final nuclei with maximal overlap. In the spherical limit, the value of the BCS overlap factor is about 0.8, and it was commonly neglected in the double-beta-decay calculations [9, 10, 18, 19].

3. CALCULATION AND DISCUSSION

The formalism described in Section 2 is used for the calculation of the $2\nu\beta\beta$-decay ground-state transition $^{76}\mathrm{Ge} \to {}^{76}\mathrm{Se}$. The results are obtained with a deformed, axially symmetric Woods–Saxon potential. The deformation-independent Woods–Saxon parameters (well depth, skin thickness, radius, and spin–orbit constants) are taken from [14]. The deformation parameter can be deduced from the nuclear electric quadrupole laboratory moment or extracted from values based on measured $E2$ probability. However, the available experimental data associated with the above two approaches [20, 21] lead to a different quadrupole deformation for both ^{76}Ge and ^{76}Se. A lack of accurate experimental information on

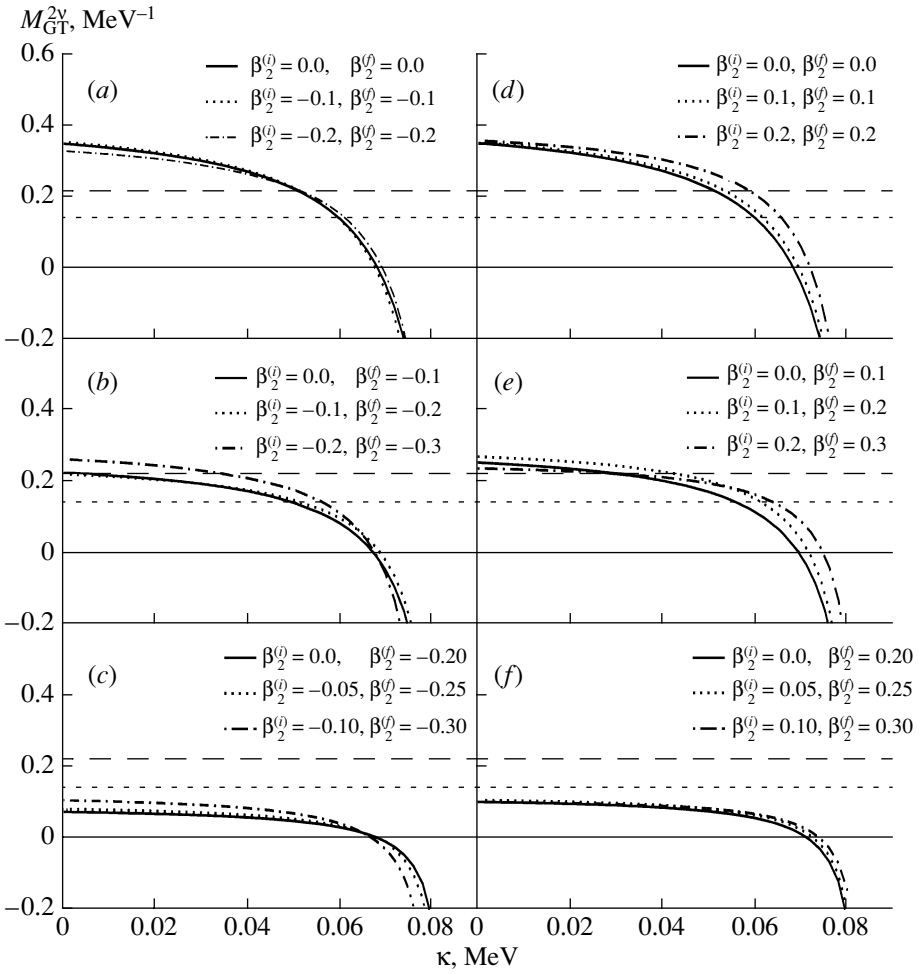

Fig. 1. $2\nu\beta\beta$-Decay matrix element of ^{76}Ge as a function of particle–particle interaction strength κ. In panels (a), (b), and (c) [(d), (e), and (f)], the results corresponding to oblate [prolate] deformation of both initial and final nuclei are presented. Note that, if the deformation of the initial and final nuclei is comparable, there is only a minimal difference between the calculated values of $M^{2\nu}_{\rm GT}$. With increasing difference in deformations of parent and daughter nuclei, the suppression of $M^{2\nu}_{\rm GT}$ is increased in the range $0 \le \kappa \le 0.06$ MeV.

the deformation of ^{76}Ge and ^{76}Se suggests that it is necessary to study the associated $2\nu\beta\beta$-decay matrix element as a function of deformation parameters of both initial and final nuclei.

In the deformed QRPA calculation, we assume truncated model space by considering only single-particle states with the maximal allowed value of the asymptotic quantum number N equal to 5. In contrast to many other microscopic calculations, energies of single-particle levels are not shifted but taken exactly as provided by the deformed Woods–Saxon potential. The BCS equations are solved for protons and neutrons. The proton and neutron pairing gaps are determined phenomenologically to reproduce the odd–even mass differences.

The calculation of the QRPA energies and wave functions requires knowledge of the particle–hole χ and particle–particle κ strengths of the residual interaction. The optimal value of χ is determined by reproducing the systematics of the empirical position of the Gamow–Teller giant resonance in an odd–odd intermediate nucleus as obtained from the (p, n) reactions [22, 23]. The parameter κ can be determined by exploiting the systematics of single-β decay feeding the initial and final nuclei. In [22], the strengths of the particle–hole and particle–particle terms of the separable Gamow–Teller force were fixed as smooth functions of mass number A by reproducing the β-decay properties of nuclei up to $A = 150$ within the spherical pnQRPA model. The recommended values of χ and κ of [22] are as follows:

$$\chi = 5.2/A^{0.7}\ \text{MeV}, \qquad (18)$$
$$\kappa = 0.58/A^{0.7}\ \text{MeV}.$$

In the presented $2\nu\beta\beta$-decay study of the ground-

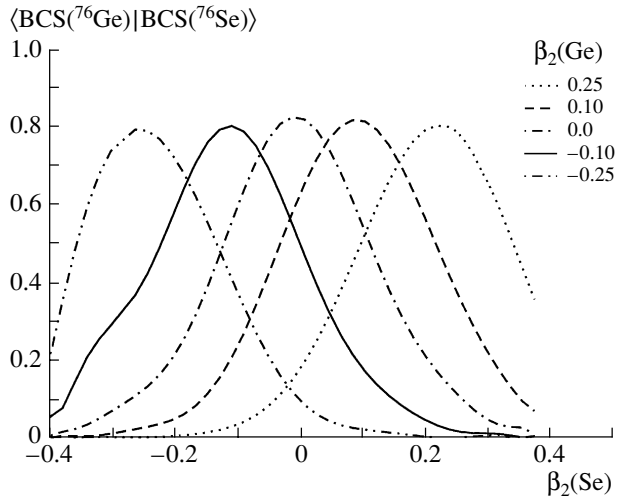

Fig. 2. The overlap factor of the initial and final BCS vacua as a function of the quadrupole deformation parameter β_2 of ^{76}Se. The results are presented for spherical ($\beta_2 = 0.0$), oblate ($\beta_2 = -0.25, -0.10$), and prolate ($\beta_2 = 0.10, 0.25$) deformations of ^{76}Ge.

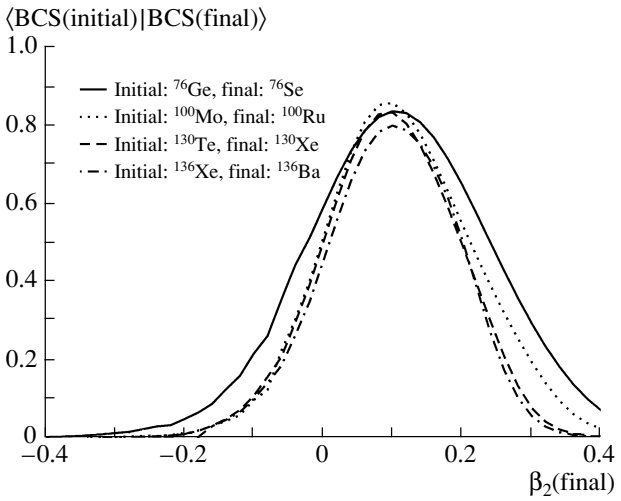

Fig. 3. The overlap factor of the initial and final BCS vacua as function of the quadrupole deformation parameter β_2 of the final nucleus for double-beta decay of ^{76}Ge, ^{100}Mo, ^{130}Te, and ^{136}Xe. The deformation parameter of the initial nucleus is chosen to be $\beta_2(\text{initial}) = 0.1$.

state transition $^{76}\text{Ge} \to {}^{76}\text{Se}$, we use the recommended value for χ ($\chi = 0.25$ MeV) and κ is considered as a free variable.

The QRPA calculations for the $K = 0, \pm 1$ states are performed by following the procedure described in Section 2. The assumption of separable forces simplifies the RPA matrix equation to an algebraic equation. The eigenvalue of the matrix equation is replaced in this way by searching for the poles of the equation, and the wave functions of the eigenstates are calculated accordingly.

The half-life of the $2\nu\beta\beta$ decay of ^{76}Ge is known with high accuracy from the Heidelberg–Moscow experiment, in particular, $T^{2\nu}_{1/2} = [1.55 \pm 0.01(\text{stat.})^{+0.19}_{-0.15}(\text{syst.})] \times 10^{21}$ yr [13]. All existing positive results on the $2\nu\beta\beta$ decay were analyzed by Barabash [7], who suggested considering for the ground state transition $^{76}\text{Ge} \to {}^{76}\text{Se}$ the average value $T^{2\nu}_{1/2} = 1.43^{+0.09}_{-0.07} \times 10^{21}$ yr. By using (13) and knowledge of the kinematical factor $G^{2\nu}$ [$G^{2\nu}(^{76}\text{Ge}) = 1.49 \times 10^{-20}\,\text{yr}^{-1}\text{MeV}^2$] from the $2\nu\beta\beta$-decay half-life of ^{76}Ge, one can deduce the absolute value of the nuclear matrix element $|M^{2\nu-\,\text{exp}}_{\text{GT}}|$ equal to 0.138 MeV^{-1} by assuming $g_A = 1.25$. If the value of the axial coupling constant g_A is considered to be unity, the value of $|M^{2\nu-\,\text{exp}}_{\text{GT}}|$ deduced from the average half-life for $A = 76$ is larger than $0.216\,\text{MeV}^{-1}$.

In Fig. 1, the effect of the deformation on the $2\nu\beta\beta$-decay matrix element $M^{2\nu}_{\text{GT}}$ is analyzed. The results for the $2\nu\beta\beta$-decay matrix element are displayed as a function of the particle–particle strength κ. The curves drawn in panels (a), (b), and (c) [panels (d), (e), and (f)] correspond to the case where both initial and final nuclei are oblate [prolate]. The two horizontal lines represent $M^{2\nu-\,\text{exp}}_{\text{GT}} = 0.138\,\text{MeV}^{-1}(g_A = 1.25)$ and $M^{2\nu-\,\text{exp}}_{\text{GT}} = 0.216\,\text{MeV}^{-1}(g_A = 1.0)$. From Fig. 1, we note that, within the whole range of κ, there is only a minimal difference between values of $M^{2\nu}_{\text{GT}}$ corresponding to the same value of $\Delta\beta_2$, which is defined

$$\Delta\beta_2 = |\beta_2(^{76}\text{Ge}) - \beta_2(^{76}\text{Se})|. \qquad (19)$$

In addition, one finds that, by increasing the value of $\Delta\beta_2$, the suppression of $M^{2\nu}_{\text{GT}}$ becomes stronger within the range $0 \le \kappa \le 0.06$ MeV. This is a new suppression mechanism of the $2\nu\beta\beta$-decay matrix element; namely, $M^{2\nu}_{\text{GT}}$ depends strongly on the difference in deformations of parent and daughter nuclei.

One might ask what is the origin of this suppression. In Fig. 2, this point is clarified by presenting the overlap factor of two BCS vacua for different values of $\beta_2(^{76}\text{Ge})$ as a function of the quadrupole deformation of ^{76}Se. We see that, for a given $\beta_2(^{76}\text{Ge})$, the curve has a maximum for $\beta_2(^{76}\text{Se}) = \beta_2(^{76}\text{Ge})$ and, with increasing difference in deformations of initial and final nuclei, i.e., $\Delta\beta_2$, the value of the BCS overlap factor decreases rapidly. We note that the approximate calculation of $\langle\text{BCS}(^{76}\text{Ge})|\text{BCS}(^{76}\text{Se})\rangle$ is slightly sensitive to the approximations used in the case where one of the nuclei is oblate and the second

prolate. Therefore, we present smoothed curves corresponding to a polynomial function. From Fig. 2, it follows that oblate–prolate (or prolate–oblate) $2\nu\beta\beta$-decay transitions are disfavored in comparison with prolate–prolate or oblate–oblate ones.

The presented suppression mechanism is expected to work also for other $2\nu\beta\beta$-decay transitions. In Fig. 3, we present the BCS overlap factor for the $2\nu\beta\beta$ decay of ^{76}Ge, ^{100}Mo, ^{130}Te, and ^{136}Xe. We see that the behavior of the overlap factor for all considered nuclear systems is qualitatively the same. The maximum of this factor appears for equal quadrupole deformation of the initial and final nuclei. With increasing value of $|\beta_2(\text{initial}) - \beta_2(\text{final})|$, the value of the overlap factor decreases strongly. This fact implies that the deformation of nuclei plays an important role in the calculation of the $2\nu\beta\beta$-decay transitions and should be known with high reliability.

There are two suppression mechanisms of the $2\nu\beta\beta$-decay matrix element. Even long ago, Vogel and Zirnbauer [8] showed that $M^{2\nu}_{\mathrm{GT}}$ is strongly suppressed when a reasonable amount of particle–particle interaction is taken into account, which is achieved close to a collapse of the QRPA solution. In this report, it is manifested that $M^{2\nu}_{\mathrm{GT}}$ depends strongly on the difference in deformations of the initial and final nuclei. A possible criteria to decide which of them is realized can be a requirement for a common description of both single-β and $2\nu\beta\beta$ decay within the same nuclear Hamiltonian.

4. SUMMARY AND CONCLUSIONS

The subject of our interest was the $2\nu\beta\beta$-decay ground-state transition $^{76}\mathrm{Ge} \to {}^{76}\mathrm{Se}$. A detailed study of the corresponding nuclear matrix element within the deformed QRPA with separable spin–isospin interaction in the particle–hole and particle–particle channels was performed. A new mechanism of suppression of the double-beta-decay nuclear matrix elements was found. We showed that the effect of deformation on the $2\nu\beta\beta$-decay matrix element is large for a significant difference in deformations of the parent and daughter nuclei and is not related to the increasing amount of ground-state correlations close to a collapse of the QRPA solution. The origin of this new mechanism is a strong sensitivity of the overlap of the initial and final BCS vacua to the deformations of associated nuclear systems. This factor directly enters the expression for the overlap factor of the intermediate nuclear states generated from the initial and final nuclei via QRPA diagonalization. The study of the BCS overlap factor associated with other double-beta-decay transitions indicates the importance of a new suppression mechanism for the calculation of $2\nu\beta\beta$-decay and $0\nu\beta\beta$-decay matrix elements in general.

ACKNOWLEDGMENTS

This work was supported in part by the Deutsche Forschungsgemeinschaft (436 SLK 17/298), by the "Land Baden–Würtemberg" as a "Landesforschungsschwerpunkt: Low Energy Neutrinos," and by the VEGA Grant Agency of the Slovak Republic under contract no. 1/0249/03.

REFERENCES

1. A. Faessler and F. Šimkovic, J. Phys. G **24**, 2139 (1998).
2. J. Suhonen and O. Civitarese, Phys. Rep. **300**, 2139 (1998).
3. H. Ejiri, Phys. Rep. **338**, 265 (2000).
4. M. Doi, T. Kotani, and E. Takasugi, Prog. Theor. Phys. Suppl. **83**, 1 (1985).
5. S. R. Elliott and P. Vogel, Annu. Rev. Nucl. Part. Sci. **52**, 115 (2002).
6. J. D. Vergados, Phys. Rep. **361**, 1 (2002).
7. A. S. Barabash, Czech. J. Phys. **52**, 567 (2002).
8. P. Vogel and M. R. Zirnbauer, Phys. Rev. Lett. **57**, 3148 (1986).
9. O. Civitarese, A. Faessler, and T. Tomoda, Phys. Lett. B **194**, 11 (1987).
10. K. Muto, E. Bender, and H. V. Klapdor, Z. Phys. A **334**, 177 (1989).
11. J. Krumlinde and P. Möller, Nucl. Phys. A **417**, 447 (1984).
12. P. Sarriguren, E. Moya de Guerra, and A. Escuderos, Nucl. Phys. A **658**, 13 (1999); Phys. Rev. C **64**, 064306 (2001); Nucl. Phys. A **691**, 631 (2001).
13. H. V. Klapdor-Kleingrothaus *et al.*, Eur. Phys. J. A **12**, 147 (2001).
14. Y. Tanaka, Y. Oda, F. Petrovich, and R. K. Sheline, Phys. Lett. B **83B**, 279 (1979).
15. F. Šimkovic, L. Pacearescu, and A. Faessler, hep-th/0308037.
16. W. C. Haxton and G. S. Stephenson, Prog. Part. Nucl. Phys. **12**, 409 (1984).
17. K. Grotz and H. V. Klapdor, Phys. Lett. B **157B**, 242 (1985).
18. J. Suhonen, Phys. Lett. B **477**, 99 (2000).
19. A. Griffiths and P. Vogel, Phys. Rev. C **46**, 181 (1992).
20. S. Balraj, Nucl. Data Sheets **74**, 63 (1995).
21. S. Raman, C. H. Malarkey, W. T. Milner, *et al.*, At. Data Nucl. Data Tables **36**, 1 (1987).
22. H. Homma *et al.*, Phys. Rev. C **54**, 2972 (1996).
23. J. Suhonen, J. Taigel, and A. Faessler, Nucl. Phys. A **486**, 91 (1988).

Physics of Atomic Nuclei, Vol. 67, No. 6, 2004, pp. 1216–1219. From Yadernaya Fizika, Vol. 67, No. 6, 2004, pp. 1238–1241.

DOUBLE-BETA DECAY AND RARE PROCESSES

Double-Beta Decay of ^{150}Nd to the First 0^+ Excited State of ^{150}Sm*

A. S. Barabash**, **F. Hubert**[1)], **Ph. Hubert**[1)], **and V. I. Umatov**

Institute of Theoretical and Experimental Physics, Moscow, Russia

Received November 19, 2003

Abstract—Two-neutrino-double-beta decay of ^{150}Nd to the first 0^+ excited state in ^{150}Sm is investigated with a 400-cm^3 low-background HPGe detector. Data analysis for 11320.5 h shows an excess of events at 333.9 and 406.5 keV. This allows us to estimate the half-life of the investigated process as $[1.4^{+0.4}_{-0.2} \pm 0.3(\text{syst.})] \times 10^{20}$ yr. © *2004 MAIK "Nauka/Interperiodica"*.

1. INTRODUCTION

Neutrinoless double-beta ($0\nu\beta\beta$) decay is allowed if neutrino mixing, involving the electron neutrino ν_e, is present in the weak charged lepton current and the neutrinos with definite mass are Majorana particles (see, e.g., [1]). Strong evidence for neutrino mixing, i.e., for oscillations of the solar electron neutrinos ν_e driven by nonzero neutrino masses and neutrino mixing, have been obtained in solar neutrino experiments (see review [2]): Davis *et al.* (Homestake) experiment and in Kamiokande, SAGE, GALLEX/GNO, and Super-Kamiokande. This evidence has been spectacularly reinforced during the last two years by the data from the SNO solar neutrino and KamLAND reactor antineutrino experiments. These very exciting results have greatly renewed interest in $0\nu\beta\beta$ decay. This process is the most sensitive to the possible Majorana nature of the massive neutrinos. Their detection will give information about the absolute scale of neutrino masses and their type of hierarchy (normal, inverted, and quasi-generated) and under specific conditions of CP violation in the lepton sector (see review [2]).

One of problems in $0\nu\beta\beta$-decay physics is reliable evaluation of nuclear matrix elements, which up to now has an accuracy of a factor of 2–3. In connection with the $0\nu\beta\beta$ decay, the detection of double-beta decay with the emission of two neutrinos ($2\nu\beta\beta$), which is an allowed process of the second order in the Standard Model, enables the experimental determination of nuclear matrix elements involved in the double-beta-decay processes. Accumulation of experimental information for the $2\nu\beta\beta$ processes (transitions to the ground and excited states) promotes better understanding of the nuclear part of double-beta ($\beta\beta$) decay and allows one to check the theoretical schemes for nuclear matrix element calculations for the two neutrino mode as well as for the neutrinoless one.

The $\beta\beta$ decay can proceed through transitions to the ground state as well as to various excited states of the daughter nuclide. Studies of the latter transitions allow one to obtain supplementary information about $\beta\beta$ decay [3]. Because of the smaller transition energies, the probabilities for $\beta\beta$-decay transitions to excited states are substantially suppressed in comparison with transitions to the ground state. However, as it was shown [4], by using low-background HPGe detectors, the $2\nu\beta\beta$ decay to the 0^+_1 level in the daughter nucleus may be detected for such nuclei as ^{100}Mo, ^{96}Zr, and ^{150}Nd. In this case, the energies involved in the $\beta\beta$ transitions are large enough (1903, 2202, and 2627 keV, respectively) and the expected half-lives are of the order of 10^{20}–10^{21} yr. The sensitivity required for detection was only reached for ^{100}Mo, and the transition was detected in the three experiments [5–7] with the half-life lying within $(6–9) \times 10^{20}$ yr (the average value is $(6.8 \pm 1.2) \times 10^{20}$ yr [8]. Recently, additional isotopes ^{82}Se, ^{130}Te, ^{116}Cd, and ^{76}Ge have become of interest for studies of $2\nu\beta\beta$ decay to the 0^+_1 level too (see review [9]).

Theoretical estimates of $2\nu\beta\beta$ decay to a 2^+ excited state have shown that for a few nuclei (^{82}Se, ^{96}Zr, ^{100}Mo, and ^{130}Te) the half-lives can be $\sim 10^{22}$–10^{23} yr [3]. This would mean that detection of such decays is becoming possible using the present and new installations in the near future.

It is very important to note that in the framework of QRPA models the behavior of nuclear matrix elements with g_{pp} parameter is completely different for transitions to the ground and excited (2^+ and 0^+) states [3, 10]. This is why the decay to excited states

*This article was submitted by the authors in English.

[1)]Centre d'Etudes Nucléaires, IN2P3-CNRS et Université de Bordeaux, France.

**e-mail: Alexander.Barabash@itep.ru

Analysis of events in the range of the peaks under study

Peak [keV]	333.9 ± 1.12			406.5 ± 1.12	
Number of events	779			603	
Continuous background [keV]	656.6			484.5	
Isotopes	^{214}Bi	^{227}Th	^{228}Ac	^{214}Bi	^{211}Pb
E_γ [keV]	333.1; 334.78	334.37	332.37	405.74	404.853
Contributions from isotopes	8.8	22.6	5.4	9.7	8.7
Excess of events	86 ± 28			100 ± 25	

may probe different aspects of the calculation method than the decay to the ground states. So, the search for $\beta\beta$ transitions to excited states has its own special interest.

In this article, the results of an experimental investigation of the $\beta\beta$ decay of ^{150}Nd to the first 0^+ excited state in ^{150}Sm are presented. The decay scheme is shown in Fig. 1. A search for $\beta\beta$ transitions of ^{150}Nd to the first 0^+ excited state in ^{150}Sm has been carried out using a germanium detector to look for γ-ray lines corresponding to the decay scheme.

2. EXPERIMENT

The experimental work is performed in the Modane Underground Laboratory (depth of 4800 m w.e.). A 400-cm^3 low-background HPGe detector is being used for investigation of 3046 g of Nd_2O_3 powder placed into a special Marinelli delrin box that has been put on the detector endcap. With taking into account the natural abundance (5.64%), 153 g of ^{150}Nd is exposed. The data collected for 11320.5 h have been used for analysis.

The HPGe detector is surrounded by a passive shield consisting of 2 cm of archeological lead, 10 cm of OFHC copper, and 15 cm of ordinary lead. To reduce the ^{222}Rn gas, which is one of the main sources of the background, special efforts were made to minimize the free space near the detector. In addition, the passive shield was enclosed in an aluminum box flushed with high-purity nitrogen. The cryostat, the endcap, and the critical mechanical components of the HPGe detector are made of very pure Al–Si alloy. Finally, the cryostat has a J-type geometry to shield the crystal from possible radioactive impurities in the dewar.

The electronics consist of currently available spectrometric amplifiers and an 8192-channel ADC. The energy calibration was adjusted to cover the energy range from 50 keV to 3.5 MeV. The energy resolution was 1.9 keV for the 1332-keV line of ^{60}Co. The electronics were stable during the experiment due to the constant conditions in the laboratory (temperature of 23°C, hygrometric degree of 50%). A daily check on the functioning of the apparatus is made.

The detection photopeak efficiencies are equal to 2.33% at 333.9 keV and 2.33% at 406.5 keV. The efficiencies have been computed with the CERN Monte Carlo code GEANT 3.21. Special calibration measurements with radioactive sources and powders containing well-known ^{226}Ra activities confirmed that the accuracy of these efficiencies is about 10%.

The dominate detector backgrounds come from natural ^{40}K, radioactive chains of ^{232}Th and ^{235,238}U, man-made and/or cosmogenic activities of ^{137}Cs, and ^{60}Co. The sample was found to have considerable ^{40}K activity (46.3 mBq/kg). Additionally, long-lived radioactive impurities were observed in the sample but with much weaker activities. In our case, the most important isotopes contributing to the energy ranges of the investigated transition are ^{214}Bi (1.15 mBq/kg), ^{228}Ac (0.93 mBq/kg), ^{227}Ac (0.62 mBq/kg), and their daughters.

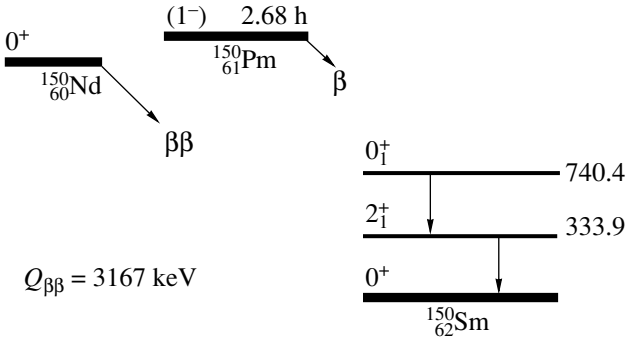

Fig. 1. Decay scheme of ^{150}Nd. Energies of levels are in keV.

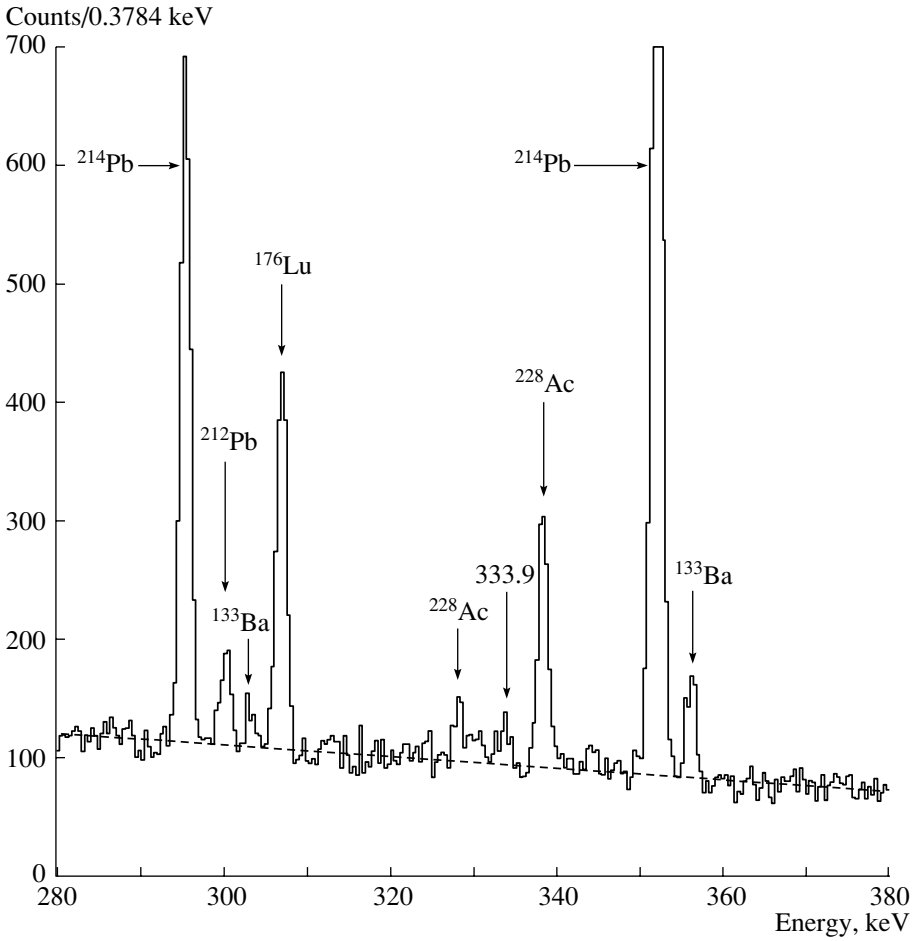

Fig. 2. Energy spectrum in the range of 333.9 keV. Dashed line is the continuous background used in the analysis.

3. ANALYSIS AND RESULTS

Figures 2 and 3 show the energy spectrum in the ranges of interest. As one can see, there is an excess of events above the continuous background at the investigated energies. Isotopes of natural radioactivity (^{211}Pb, ^{214}Bi, ^{227}Th, and ^{228}Ac) found in the spectrum have γ lines near these energies. ^{214}Bi contributes to both investigated ranges through γ rays with energies of 333.31 keV (0.080%) and 334.78 keV (0.034%) for the 333.9-keV peak and 405.74 keV (0.17%) for the 406.5-keV peak. ^{228}Ac touches the 333.9-keV peak range with its γ (332.37 keV, 0.40%). ^{227}Ac exhibits through its daughters, ^{227}Th (334.37 keV, 1.14%) and ^{211}Pb (404.853 keV, 3.78%). There is also the artificial isotope ^{150}Eu ($T_{1/2} = 36.9$ yr) decaying to the same daughter ^{150}Sm with γ rays of 333.9 keV (96%), 406.5 keV (0.14%), 439.4 keV (80%), and 584.3 keV (52.6%). However, its possible exhibition at 439.4 keV is within the standard deviation of the continuous background; therefore, it can be taken into account as a systematic error.

The table presents the results of the analysis for the two peak-energy ranges under study. A peak shape is described as a Gaussian with a standard deviation of ~ 0.56 keV at the energies investigated. For the analysis, a peak range is taken within four standard deviations ($E \pm 2\sigma$), i.e., 0.9545 of a peak area. As one can see, there is an excess of events for each peak under study. If these event excesses are connected with the $2\nu\beta\beta$ decay of ^{150}Nd to the first 0^+ excited state of ^{150}Sm, then, by summing the two peaks, we obtain an effect of 186 ± 38 events, corresponding to a half-life $T_{1/2} = [1.4^{+0.4}_{-0.2} \pm 0.3(\text{syst.})] \times 10^{20}$ yr.

Previous experiments gave only limits on this transition, $>1 \times 10^{20}$ yr [11] and $>1.5 \times 10^{20}$ yr [12]. Taking into account all the errors, our result is not in contradiction with the previous limits.

If one compares our result with the average experimental value [8] of the half-life for the $2\nu\beta\beta$ transition of ^{150}Nd to the ground state, $T_{1/2} = (7.0 \pm 1.7) \times$

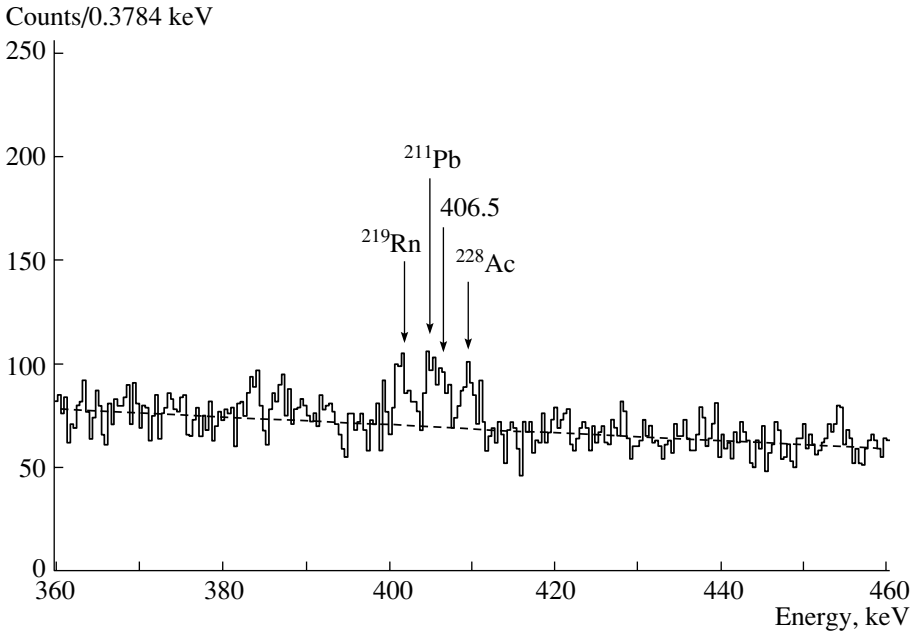

Fig. 3. The same as Fig. 2 but for the range of 406.5 keV.

10^{18} yr, and takes into account the phase-space factors [3], then one can obtain for the nuclear matrix elements the following ratio: $M^{2\nu}_{\text{g.s}} \approx 1.4 M^{2\nu}_{0^+_1}$. As a result, the nuclear matrix element for the transition to the first 0^+ excited level is less a little than one for the transition for the ground state.

ACKNOWLEDGMENTS

The authors would like to thank the Modane Underground Laboratory staff for their technical assistance in running the experiment.

Portions of this work were supported by INTAS grant no. 00-00362.

REFERENCES

1. S. M. Bilenky and S. T. Petcov, Rev. Mod. Phys. **59**, 67 (1987).
2. S. M. Bilenky *et al.*, Phys. Rep. **379**, 69 (2003).
3. J. Suhonen and O. Civitarese, Phys. Rep. **300**, 123 (1998).
4. A. S. Barabash, Pis'ma Zh. Éksp. Teor. Fiz. **51**, 181 (1990) [JETP Lett. **51**, 207 (1990)].
5. A. S. Barabash *et al.*, Phys. Lett. B **345**, 408 (1995).
6. A. S. Barabash *et al.*, Yad. Fiz. **62**, 2211 (1999) [Phys. At. Nucl. **62**, 2039 (1999)].
7. L. De Braeckeleer *et al.*, Phys. At. Nucl. **63**, 1214 (2000).
8. A. S. Barabash, Czech. J. Phys. **52**, 567 (2002).
9. A. S. Barabash, Czech. J. Phys. **50**, 447 (2000).
10. M. Aunola and J. Suhonen, Nucl. Phys. A **602**, 133 (1996).
11. C. Arpesella *et al.*, Nucl. Phys. B (Proc. Suppl.) **70**, 249 (1999).
12. A. A. Klimenko *et al.*, Czech. J. Phys. **52**, 589 (2002).

Physics of Atomic Nuclei, Vol. 67, No. 6, 2004, pp. 1220–1226. From Yadernaya Fizika, Vol. 67, No. 6, 2004, pp. 1242–1248.

The CUORICINO ^{130}Te $\beta\beta$-Decay Experiment and a New Limit on $T^{0\nu}_{1/2}(\beta\beta)$*

C. Arnaboldi, D. R. Artusa[1], F. T. Avignone III[1], M. Balata[2], I. Bandac[1], M. Barucci[3], J. Beeman[4], C. Brofferio, C. Bucci[2], S. Capelli, L. Carbone, S. Cebrian[5], O. Cremonesi, R. J. Creswick[1], A. de Waard[6], H. A. Farach[1], A. Fascilla[7], E. Fiorini, G. Frossati[6], A. Giuliani[7], P. Gorla[5], E. E. Haller[4,8], I. G. Irastorza[5], R. J. McDonald[4], A. Morales[5], E. B. Norman[4], A. Nucciotti, E. Olivieri[3], V. Palmieri[9], E. Pasca[3], M. Pavan, M. Pedretti[7], G. Pessina, S. Pirro, E. Previtali, C. Pobes[5], M. Pyle[2,4], L. Risegari[3], C. Rosenfeld[1], M. Sisti, A. R. Smith[4], L. Torres, and G. Ventura[3]**

(The CUORICINO Collaboration)

Dipartimento di Fisica dell'Università di Milano, Bicocca e Sezione di Milano dell'INFN, Italy

Received November 4, 2003

Abstract—The CUORICINO $\beta\beta$-decay detector is an array of 62 TeO_2 bolometers; 44 are $5 \times 5 \times 5$-cm crystals made with natural tellurium (33.8% ^{130}Te). There are 18, $3 \times 3 \times 6$-cm crystals, 14 of which are made of natural tellurium, 2 are isotopically enriched to 75% in ^{130}Te, and 2 are enriched to 82.3% in ^{128}Te. The total mass of ^{130}Te is ~ 11 kg. The background rate is 0.23 ± 0.04 counts/keV/kg/yr in the energy interval 2480 to 2600 keV. During the cooling process, some of the wires became disconnected and only 32 of the large and 16 of the smaller crystals could be read out. The data presented here come from 29 of the $5 \times 5 \times 5$-cm crystals containing 6.2 kg of ^{130}Te. The new limit on the half-life is $T^{0\nu}_{1/2} \geq 5 \times 10^{23}$ yr, corresponding to an effective Majorana mass of the electron neutrino $\langle m_\nu \rangle$ between 0.42 and 2.05 eV, depending on the nuclear model used to analyze the data. © *2004 MAIK "Nauka/Interperiodica".*

1. THEORETICAL MOTIVATION OF NEUTRINOLESS DOUBLE-BETA EXPERIMENTS

Neutrinoless double-beta decay is an old subject [1]. What is new is the fact that positive observation of neutrino oscillations in atmospheric neutrinos [2] and in solar neutrinos [3] gives new motivation for more sensitive searches. In fact, recently published constraints on the mixing angles of the neutrino-mixing matrix [2, 3] make a strong case that if neutrinos are Majorana particles, there are many scenarios in which next generation $\beta\beta$-decay experiments should be able to observe the phenomenon and measure the effective Majorana mass of the electron neutrino, $|\langle m_\nu \rangle|$, which would provide a measure of the neutrino mass scale, m. One fact is clear: neutrino oscillation experiments can only provide data on the mass differences of the neutrino mass eigenstates. The absolute scale can only be obtained from direct mass measurements, ^{3}H end point measurements for example [4], or in the case of Majorana neutrinos, more sensitively by neutrinoless $\beta\beta$ decay. The time for large, next generation $\beta\beta$-decay experiments has arrived, because if the mass scale is below ~ 0.25 eV, $\beta\beta$ decay may be the only hope for measuring it.

The most sensitive experiments carried out so far have probed the decay $^{76}\mathrm{Ge} \rightarrow \mathrm{Se} + 2\beta^-$ with specially built Ge detectors fabricated from germanium

*This article was submitted by the authors in English.

[1] Department of Physics and Astronomy, University of South Carolina, Columbia, USA.
[2] Laboratori Nazionali del Gran Sasso dell'INFN, Assergi (L'Aquila), Italy.
[3] Dipartimento di Fisica dell'Università di Firenze e Sezione di Firenze dell'INFN, Italy.
[4] Lawrence Berkeley National Laboratory, California, USA.
[5] Laboratorio de Fisica Nuclear y Altas Energías, Universidad de Zaragoza, Spain.
[6] Kamerling Onnes Laboratory, Leiden University, The Netherlands.
[7] Dipartimento di Scienze Chimiche, Fisiche e Matematiche dell'Università dell'Insubria, e Sezione di Milano dell'INFN, Como, Italy.
[8] Department of Material Science and Engineering, University of California, Berkeley, USA.
[9] Laboratori Nazionali di Legnaro, Legnaro (Padova), Italy.
** e-mail: gudkov@asg.sc.edu

isotopically enriched from 7.8 to 86% in ^{76}Ge. The Heidelberg–Moscow Experiment [5] and the International Germanium Experiment (IGEX) [6] have placed lower bounds on the half-life for this process of 1.9×10^{25} yr (90% C.L.) and 1.6×10^{25} yr (90% C.L.), respectively.

2. NEUTRINOLESS DOUBLE-BETA DECAY

The decay rate for the process involving the exchange of a Majorana neutrino can be expressed as follows:

$$(\tau^{0\nu}_{1/2})^{-1} = G^{0\nu}(E_0, Z)|\langle m_\nu\rangle|^2 |M^{0\nu}_{\rm F}|^2 - (g_A/g_V)^2 M^{0\nu}_{\rm GT}|^2. \quad (1)$$

Here, $G^{0\nu}$ is the two-body phase-space factor including coupling constants, $M^{0\nu}_{\rm F}$ and $M^{0\nu}_{\rm GT}$ are the Fermi and Gamow–Teller nuclear matrix elements, respectively, and g_A and g_V are the axial-vector and vector relative weak coupling constants, respectively. The quantity $|\langle m_\nu\rangle|$ is the effective Majorana electron neutrino mass given by:

$$|\langle m_\nu\rangle| = ||U^L_{e1}|^2 m_1 + |U^L_{e2}|^2 m_2 e^{i\phi_2} + |U^L_{e3}|^2 m_3 e^{i\phi_3}|, \quad (2)$$

where $e^{i\phi_2}$ and $e^{i\phi_3}$ are the Majorana CP phases (± 1 for CP conservation), $m_{1,2,3}$ are the mass eigenvalues, and $U^L_{e_{1,2,3}}$ are elements of the first row of the unitary transformation between neutrino mass and flavor eigenstates for left-handed neutrinos.

In this notation, $U^L_{e1} = \cos\theta_3 \cos\theta_2 \equiv c_3 c_2$, $U^L_{e2} = \sin\theta_3 \cos\theta_2 \equiv s_3 c_2$, and $U^L_{e3} = \sin\theta_2 \equiv s_2$. In other notation $\theta_2 = \theta_{13}$ which is very small and $s_2^2 \leq 0.026$. Here we use the notation of Chau and Keung [7]. In the notation of the Particle Data Book: $c_3 = \cos\theta_{12}$, $c_2 = \cos\theta_{13}$, and $c_1 = \cos\theta_{23}$, etc.

The neutrino oscillation data yield values and errors for the mixing angles θ_1, θ_2, and θ_3, and two neutrino mass patterns or hierarchies [8–10]. We use the convention of [9], normal hierarchy $m_1 \leq m_2 \ll m_3$ and $m_1 \ll m_2 \leq m_3$ in the inverted hierarchy. In general, in the normal hierarchy case, for example, we have:

$$|\langle m_\nu\rangle| = |c_3^2 c_2^2 m_1 + s_3^2 c_2^2 e^{i\phi_2} m_2 + s_2^2 e^{i\phi_3} m_3|. \quad (3)$$

With the values and errors (3σ) from the literature, this becomes:

$$|\langle m_\nu\rangle| = |(0.75^{+0.07}_{-0.12})m_1 + (0.25^{+0.12}_{-0.07})e^{i\phi_2} m_2 + (< 0.026)e^{i\phi_3} m_3|. \quad (4)$$

3. NEUTRINO MASS PATTERNS

The measured values of δm^2_s (solar) and $\delta m^2_{\rm AT}$ (atmospheric) motivate the pattern of masses in the two possible hierarchy schemes mentioned above. From the mass hierarchy relations we can write $m_2 = \sqrt{\delta m^2_s + m^2_1}$ and $m_3 = \sqrt{\delta m^2_{\rm AT} + m^2_1}$ in the case of normal hierarchy and $m_2 = \sqrt{\delta m^2_{\rm AT} - \delta m^2_s + m^2_1}$ and $m_3 = \sqrt{\delta m^2_{\rm AT} + m^2_1}$ in the case of inverted hierarchy. From these, we can write Eq. (3), for normal and inverted hierarchy, respectively, in terms of the mixing angles, δm^2_s, $\delta m^2_{\rm AT}$, and CP phases as follows [9, 10]:

$$|\langle m_\nu\rangle| = |c_2^2 c_3^2 m_1 + c_2^2 s_3^2 e^{i\phi_2}\sqrt{\delta m^2_s + m^2_1} + s_2^2 e^{i\phi_3}\sqrt{\delta m^2_{\rm AT} + m^2_1}|, \quad (5)$$

$$|\langle m_\nu\rangle| = |s_2^2 m_1 + c_2^2 c_3^2 e^{i\phi_2}\sqrt{\delta m^2_{\rm AT} - \delta m^2_s + m^2_1} + c_2^2 s_2^2 e^{i\phi_3}\sqrt{\delta m^2_{\rm AT} + m^2_1}|. \quad (6)$$

Numerical values are given in Table 1. These values (Table 1) set the requirements for the sensitivities that a $0\nu\beta\beta$ experiment must reach.

Below we discuss the CUORICINO/CUORE technique designed to reach the levels of interest and give the first results from CUORICINO.

4. DETECTOR PRINCIPLES

CUORICINO is an array of 44 TeO_2 crystals, $5 \times 5 \times 5$ cm with an average mass of 790 g, and 18 TeO_2 crystals, $3 \times 3 \times 6$ cm with an average mass of 330 g. Two of the small crystals are isotopically enriched to 75% in ^{130}Te, and two are isotopically enriched to 82.3% in ^{128}Te. Unfortunately, during the cooling down process, some of the signal wires disconnected, so that only 32 of the large crystals and 16 of the small ones could be read. This gives a total of 30.56 kg of TeO_2 that are functioning effectively as bolometers that can be read out. The data analyzed were from 29 of the 32 readable $5 \times 5 \times 5$-cm crystals.

Tellurium oxide is a dielectric and diamagnetic material. According to the Debye law, the heat capacity of a single crystal at low temperature is proportional to the ratio $(T/T_\Theta)^3$, where T_Θ is the Debye temperature of TeO_2. Thus, providing that the temperature is extremely low, a small energy release in the crystal results in a measurable temperature rise.

Table 1. Central values of the numerical predictions of $|\langle m_\nu \rangle|$ for both hierarchies and CP phase relations (all mass values are given in eV)

Normal hierarchy				Inverted hierarchy			
$e^{i\phi_2} = -1$		$e^{i\phi_2} = +1$		$e^{i\phi_2} = -e^{i\phi_3}$		$e^{i\phi_2} = +e^{i\phi_3}$	
m_1	$\lvert\langle m_\nu \rangle\rvert$	m_1	$\lvert\langle m_\nu \rangle\rvert$	m_1	$\lvert\langle m_\nu \rangle\rvert$	m_1	$\lvert\langle m_\nu \rangle\rvert$
0.02	9.30	0.02	20.4	0.00	26.0	0.00	55.9
0.04	19.1	0.04	40.3	0.02	27.7	0.02	59.0
0.06	28.9	0.06	60.0	0.05	35.3	0.05	74.5
0.08	38.7	0.08	80.0	0.075	44.7	0.075	90.3
0.10	48.5	0.10	100	0.10	55.2	0.10	114
0.20	96.5	0.20	200	0.20	100	0.20	208
0.40	194	0.40	400	0.40	194.5	0.40	404

This temperature change can be recorded with thermal sensors and, in particular, using Neutron Transmutation Doped (NTD) germanium thermistors. These devices were developed and produced at the Lawrence Berkeley National Laboratory (LBNL) and UC Berkeley Department of Material Science [11]. They have been made uniquely uniform in their response and sensitivity by neutron exposure control with neutron absorbing foils accompanying the germanium in the reactor [12].

The TeO_2 crystals are produced by the Shanghai Quinhua Material Company (SQM) in Shanghai, China, which will produce the 750-g TeO_2 crystals for CUORE [13]. A single CUORICINO detector consists of a $5 \times 5 \times 5$-cm single crystal of TeO_2 that acts both as a detector and a source. The detectors are supported by a copper frame. The frame and the dilution refrigerator mixing chamber to which it is thermally connected form the heat sink, while the PTFE (Polytetrafluoroethylene or TEFLON®) standoffs provide the thermal impedance, which delays the cooling of the bolometers. The bolometers operate at ~ 10 mK.

A single Large CUORICINO bolometer is a $5 \times 5 \times 5$-cm single crystal of TeO_2 grown with ultrapure TeO_2 powders and lapped on the surfaces. Crystals of TeO_2 have a tetragonal structure and are grown along the [001] axis. The two axes normal to this axis are crystallographically equivalent, a fact relevant to their use in the search for solar axions [14]. The surface hardness is not the same for all the sides, which complicates the crystal polishing. We have shown that repeated thermal cycling does not damage the crystals, as in the case of crystals of other tellurium compounds or of metallic tellurium. The Debye temperature of the TeO_2 crystals was specially measured for the CUORE project as 232 K [15]. This differs from the previous value of 272 K in the literature [16]. The specific heat of the TeO_2 crystals was found to follow the Debye law down to 60 mK; the heat capacity of the 790-g crystals is 2.3×10^{-9} J/K extrapolated down to 10 mK.

The NTD thermistors are attached by epoxy to the crystal and are operated in the Variable Range Hopping (VRH) conduction regime with a Coulomb gap [17–19]. The most important parameter characterizing the thermal response is the sensitivity A defined as follows:

$$A = \left| \frac{d \log R}{d \log T} \right| = \gamma \left(\frac{T_0}{T} \right)^\gamma. \qquad (7)$$

For the CUORICINO NTD thermistors this parameter ranges between 7 and 10. The resistance behavior follows the relation

$$R = R_0 \exp(T_0/T)^\gamma; \quad \gamma = 1/2. \qquad (8)$$

The VRH regime occurs in Ge when it is "doped" close to the metal-to-insulator transition, which is $\sim 6 \times 10^{16}$ atom/cm^3. This is achieved by thermal neutron radiation in a nuclear reactor, resulting in (n, γ) reactions on ^{70,72,73,74,76}Ge, followed by β^- decay or electron capture. To the first order, this produces (for a natural Ge sample) the following stable isotopes: ^{71}Ga (18%), ^{73}Ge (8.3%), ^{74}Ge (36%), ^{75}As (12%), and ^{77}Se (0.8%). Beta minus and electron capture lead to n and p dopants, respectively. The sensitivity parameter A depends on the neutron irradiation dose. Therefore, each thermistor must be characterized at operating temperatures, similar to that described for Si thermistors by Alessandrello *et al.* [20].

It is very important to optimize the neutron irradiation exposure and to make the exposures as uniform as possible. It is not possible to evaluate the

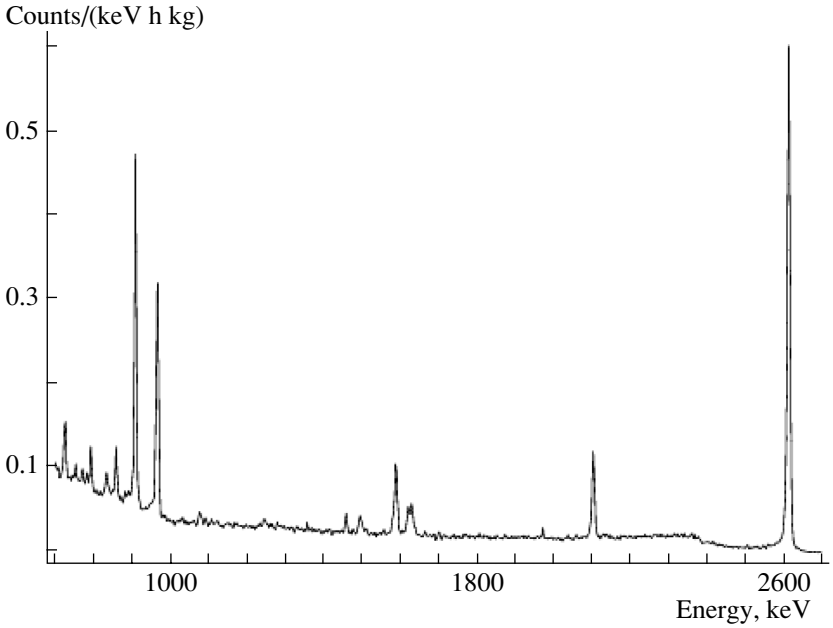

Fig. 1. The sum of calibration spectra of the $5 \times 5 \times 5$-cm detectors taken with a ^{232}Th source.

thermistor material directly from the reactor because of the long half-life of ^{71}Ge (11.43 d). A delay of several months is required to see if the Ge needs more exposure. To circumvent this difficulty, the Ge material is accompanied by foils of metal with long-lived (n, γ) radioactive daughter nuclides. Accordingly, the neutron exposure of the Ge can be determined accurately, and uniformity of exposure is achieved. This technique was developed recently by the LBNL group of the CUORE Collaboration [12]. Following the neutron exposure and radioactive decay period, the NTD germanium is first heat treated to repair the crystal structure then cut into $3 \times 3 \times 1$ mm strips. The thermistors are glued to the TeO_2 crystal by nine spots of Araldit rapid Ciba Geigy epoxy of 0.4 to 0.7 mm in diameter deposited on the crystal surface by an array of pins. The height of each spot is 50 μm. This procedure was found to be reliable and reproducible in the MI–DBD experiment [21]. The heat conductance of the epoxy spots was measured in Milan and the phenomenological relation was found to be $\sim 2.6 \times 10^{-4}\,(T[\mathrm{K}])^3$ watts per degree kelvin per spot.

The stabilization of the response of the bolometers is crucial because of the unavoidable small variations in the temperature of the heat bath that change the detector gain (and consequently deteriorate the energy resolution). This problem is successfully addressed by means of a Joule heater glued onto each crystal. The heater is used to inject a uniform energy into the crystal, the thermal gain is monitored and corrected off-line. The heaters are Si chips with a heavily doped meander structure with a constant resistance between 50 to 100 kΩ. They are manufactured by the ITC–IRST company in Trento, Italy.

The electrical connections are made with two 50-μm diameter gold wires that are ball bonded to metallized surfaces on the thermistor. The gold wires are crimped into a copper tube, which is inserted into a larger one forming the electrical connection, thus avoiding low-temperature solder which contains ^{210}Pb and traces of other radioisotopes. The larger copper tube, $\sim$ 14 mm long and 2 mm in diameter, is glued to the copper frame that supports the crystals. This tube is thermally connected to the frame but electrically insulated.

5. EXPERIMENTAL RESULTS

The detector was run for approximately 865 h with a total of 11 kg of ^{130}Te; however, the data discussed here are from 22.9 kg of TeO_2 collected only with 29 large crystals ($\sim$6.2 kg of ^{130}Te). Accounting for the phase-space factors, computed nuclear matrix elements, and relative isotope abundances, this is as effective in sensitivity to the effective Majorana mass of the electron neutrino as approximately 25 kg of Ge isotopically enriched to 86% ^{76}Ge. A calibration spectrum using a source of ^{232}Th is shown in Fig. 1. It is a sum spectrum of all of the readable $5 \times 5 \times 5$-cm TeO_2 crystals. The mean resolution is FWHM $\simeq$ 7 at 2615 keV. The calibrations are made with a tungsten wire containing ^{232}Th outside the refrigerator but inside the 20 cm thick lead shield.

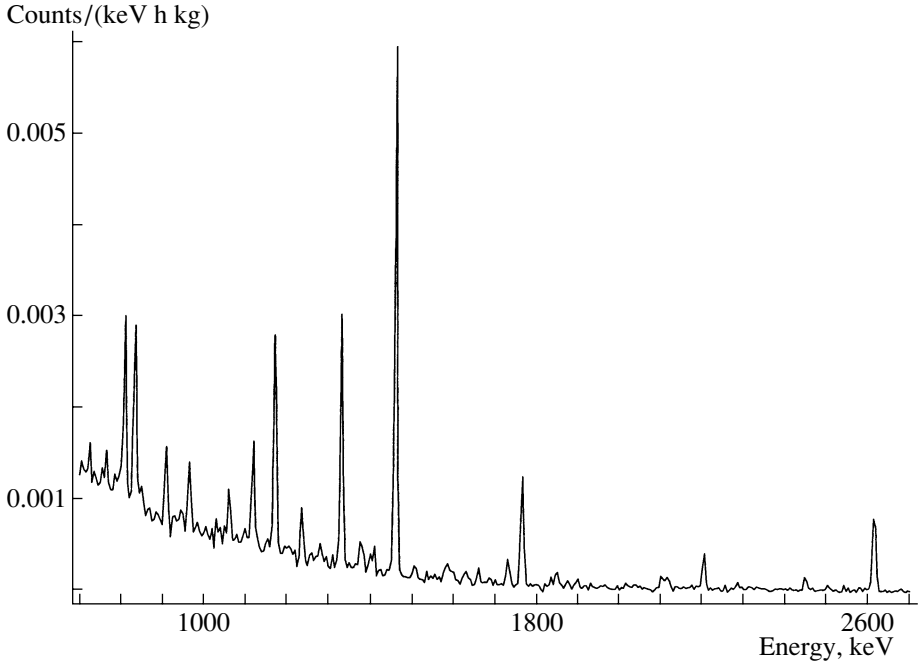

Fig. 2. The sum of background spectra of 29 $5 \times 5 \times 5$-cm detectors taken over the course of the experiment.

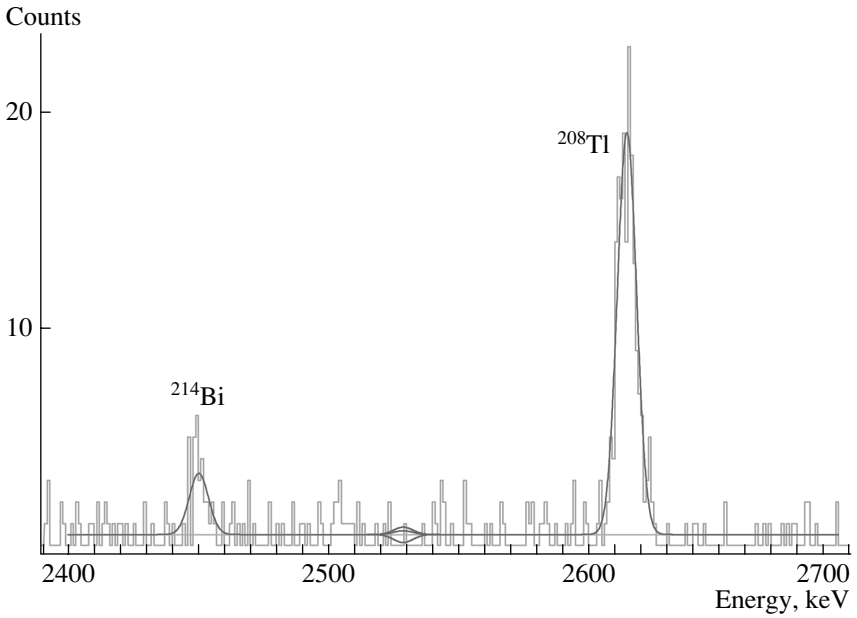

Fig. 3. The portion of the sum spectrum of Fig. 2 in the region of neutrinoless $\beta\beta$ decay.

The spectrum from 19.800 kg × h of live time of 29 of the operating $5 \times 5 \times 5$-cm bolometers is shown in Figs. 2, 3. The data were analyzed as discussed below and the effective Majorana mass of the electron neutrino $\langle m_\nu \rangle$ was evaluated using 15 different nuclear matrix elements [21–36].

The data were analyzed in the usual way using the following expression:

$$T^{0\nu}_{1/2} \geq \frac{(\ln 2) N t \epsilon}{n(\max)}, \qquad (9)$$

where $N = 2.93 \times 10^{25}$ is the total number of ^{130}Te atoms, t is the live counting time in years, ϵ is the detection efficiency, and $n(\max)$ is the maximum number of events in the spectrum that can be attributed

to $0\nu\beta\beta$ decay (to a confidence level of 90%). The counting efficiency ϵ was evaluated by a Monte Carlo computation to be 86.3%. The value of $n(\max) = 3.48$ was obtained from the spectrum by a maximum likelihood analysis. Accordingly,

$$T^{0\nu}_{1/2}(^{130}\mathrm{Te}) > 5.0 \times 10^{23}\ \mathrm{yr}\ (90\%\ \mathrm{C.L.}). \qquad (10)$$

The effective Majorana neutrino mass $|\langle m_\nu\rangle|$ is directly derivable from the measured half-life of the decay as follows:

$$|\langle m_\nu\rangle| = m_e \frac{1}{\sqrt{F_N T^{0\nu}_{1/2}}}\ [\mathrm{eV}], \qquad (11)$$

where $F_N = G^{0\nu}|M^{0\nu}_{\mathrm{F}} - (g_A/g_V)^2 M^{0\nu}_{\mathrm{GT}}|^2$. This quantity is derived from nuclear structure calculations and is model dependent as seen from Table 2. The values of F_N from 15 different calculations are given in Table 2. The result of these analyses is that the upper bound on $|\langle m_\nu\rangle|$ is between 0.42 and 2.05 eV. It can be shown that with the current background rate of 0.20 ± 0.03 counts/keV/kg/yr and the current average energy resolution, the full CUORICINO array can achieve $T^{0\nu}_{1/2} > 3.5 \times 10^{24}$ yr (68% C.L.), corresponding to an upper bound on $|\langle m_\nu\rangle|$ between 0.27 and 0.78 eV. This is similar to the current ^{76}Ge experimental bounds. The values of $F_N(^{130}\mathrm{Te})$ reported in the literature are from very disparate models; however, we have chosen to analyze our data using only the more conventional QRPA models presented in Table 2. The result ranges from $\langle m_\nu\rangle < 0.70-2.06$ eV, depending on the model, to (90% C.L.). If we use the recent theoretical treatment of [36] this half-life corresponds to $\langle m_\nu\rangle = 2.3 \pm 0.2$ eV.

Table 2. Values of the nuclear structure factor $F_N = G^{0\nu}|M^{0\nu}_{\mathrm{F}} - (g_A/g_v)^2 M^{0\nu}_{\mathrm{GT}}|^2$ and the respective values of $|\langle m_\nu\rangle|$ for $T^{0\nu}_{1/2} = 5 \times 10^{23}$ yr (with n–p pairing)*

$F_N(^{130}\mathrm{Te})$, yr^{-1}	$\lvert\langle m_\nu\rangle\rvert$, eV	Ref.	$F_N(^{130}\mathrm{Te})$, yr^{-1}	$\lvert\langle m_\nu\rangle\rvert$, eV	Ref.
1.88×10^{-13}	1.67	[22]	4.84×10^{-13}	1.04	[29]
2.37×10^{-13}	1.48	[23]	5.00×10^{-13}	1.02	[30]
2.43×10^{-13}	1.47	[24]	5.06×10^{-13}	1.02	[31]
2.78×10^{-13}	1.37	[25]	5.33×10^{-13}	1.00	[32]
3.04×10^{-13}	1.31	[26]	5.61×10^{-13}	0.97	[33]
1.24×10^{-13}	2.05*	[26]	7.83×10^{-13}	0.82	[34]
3.96×10^{-13}	1.15	[27]	2.90×10^{-12}	0.42	[35]
4.35×10^{-13}	1.10	[28]			

6. PROSPECTS FOR CUORE

CUORE is a proposed assembly of 25 towers like CUORICINO but with 40 750-g TeO_2 bolometers each. The total mass, 750 kg of TeO_2, would contain 203 kg of ^{130}Te. What do the present results from CUORICINO imply for the success of CUORE?

The early CUORICINO data have already shown us what and where the sources of background are and how to reduce them. We conclude that a reduction in the background by a factor of 20 is quite straightforward. This would allow the full CUORE array to achieve a 5-yr sensitivity of 1.0×10^{26} yr, corresponding to an effective mass between 0.02 and 0.06 eV. Another order of magnitude reduction will present a real challenge, but it is possible. In that case, a 5-yr sensitivity in the effective mass would be as small as 0.015 eV. In the least optimistic scenario above and in the case of inverted hierarchy of the neutrino mass spectrum a null experiment would rule out the Majorana character of neutrinos, whereas a definite observation would confirm that neutrinos are Majorana particles. Only double-beta experiments can achieve this goal. In the more optimistic case, the experiment would be sensitive to a Majorana mass of the lightest neutrino mass eigenvalue of between 0.015 and 0.04 eV in the case of normal hierarchy and again nearly zero in the case of inverted hierarchy. The technology is now proven, and, with adequate funding, there are no show-stoppers. The proposal is to build the CUORE experiment in the Laboratori Nazionale del Gran Sasso (LNGS) in Assergi, Italy, the present site of CUORICINO. CUORE is by far the most cost effective next generation $\beta\beta$-decay experiment proposed that can reach the desired levels of sensitivity.

REFERENCES

1. S. R. Elliot and P. Vogel, hep-ph/0202264; Ann. Rev. Nucl. Part. Sci. **52**, 115 (2002).
2. T. Toshito *et al.* (Super-Kamiokande Collab.), hep-ex/0105023; S. Hatakeyama *et al.*, Phys. Rev. Lett. **81**, 2016 (1998).
3. Q. R. Ahmad *et al.* (SNO Collab.), nucl-ex/0204009; nucl-ex/0204008; Phys. Rev. Lett. **87**, 071301 (2001); S. Fakuda *et al.* (Super-Kamiokande Collab.), hep-ex/0205075; Phys. Lett. B **539**, 179 (2002).
4. A. Osipowicz *et al.* (KATRIN Collab.), hep-ex/0109033; Letter of Intent., 21 Sept. 2001 (in press).
5. H. V. Klapdor-Kleingrothaus *et al.*, Nucl. Phys. (Proc. Suppl.) **100**, 309 (2001); hep-ph/0102276.
6. C. E. Aalseth *et al.*, Phys. Rev. D **65**, 092007 (2002).

7. Ling-Lie Chau and Wai-Yee Keung, Phys. Rev. Lett. **53**, 1802 (1984).
8. M. Apollonio *et al.* (CHOOZ Collab.), Phys. Lett. B **466**, 415 (1999).
9. V. Barger, S. L. Glashow, D. Marfatia, and K. Whisnant, Phys. Lett. B **532**, 15 (2002).
10. S. Pascoli and S. T. Petcov, hep-ph/0205022; Phys. Lett. B **544**, 239 (2002).
11. E. E. Haller *et al.*, in *Proceedings of the 4th International Conference on Neutron Transmutation Doping of Semiconductor Materials,* Nat. Bureau of Standards, Gaithersburg, 1982, Ed. by R. D. Larrabee (Plenum, 1984), p. 21.
12. E. Norman and R. J. McDonald, *Presentation Made to the CUORE Collaboration,* Milan, Italy, 2000, Nucl. Instrum. Methods Phys. Res. (in press).
13. A. Alessandrello *et al.*, Phys. At. Nucl. **66**, 452 (2003); A. Alessandrello *et al.*, Nucl. Phys. B (Proc. Suppl.) **87**, 78 (2000); C. Arnaboldi *et al.*, Nucl. Instrum. Methods Phys. Res. A **15**, 775 (2004).
14. R. J. Creswick *et al.*, Phys. Lett. B **427**, 235 (1998); F. T. Avignone III *et al.*, Phys. Rev. Lett. **81**, 5068 (1998); S. Cebrian *et al.*, Astropart. Phys. **10**, 397 (1999).
15. M. Barucci *et al.*, J. Low Temp. Phys. **123**, 303 (2001).
16. G. K. White, S. J. Collocott, and J. G. Collins, J. Phys.: Condens. Matter **2**, 7715 (1990).
17. A. Giuliani and S. Sanguinetti, Mater. Sci. Eng., R. **11**, 52 (1993).
18. N. F. Mott, Philos. Mag. **19**, 835 (1969).
19. B. I. Shklovskii and A. L. Efros, Zh. Éksp. Teor. Fiz. **60**, 867 (1971) [Sov. Phys. JETP **33**, 468 (1971)].
20. A. Alessandrello *et al.*, J. Phys. D **32**, 3099 (1998).
21. C. Arnaboldi *et al.*, Phys. Lett. B **557**, 167 (2003).
22. F. Simkovič *et al.*, Phys. Rev. C **60**, 055502 (1999).
23. J. Engel and P. Vogel, Phys. Lett. B **225**, 5 (1989).
24. S. Stoica and H. V. Klapdor-Kleingrothaus, Phys. Rev. C **63**, 064304 (2001).
25. A. Faessler and F. Simkovič, J. Phys. G **24**, 2139 (1998).
26. G. Pantis *et al.*, Phys. Rev. C **53**, 695 (1996).
27. P. Vogel *et al.*, Phys. Rev. Lett. **57**, 3148 (1986); Phys. Rev. C **37**, 731 (1988).
28. K. Muto, E. Bender, and H. V. Klapdor, Z. Phys. A **334**, 187 (1989).
29. T. Tomoda, Rep. Prog. Phys. **54**, 53 (1991).
30. O. Civitarese, A. Faessler, and T. Tomoda, Phys. Lett. B **194**, 11 (1987); T. Tomoda and A. Faessler, Phys. Lett. B **199**, 473 (1987); J. Suhonen and O. Civitarese, Phys. Rev. C **49**, 3055 (1994).
31. M. Aunola and J. Suhonen, Nucl. Phys. A **643**, 207 (1998).
32. A. Staudt *et al.*, Europhys. Lett. **13**, 31 (1990).
33. F. Simkovič *et al.*, Phys. Lett. B **393**, 267 (1997).
34. C. Barbero *et al.*, Nucl. Phys. A **650**, 485 (1999).
35. A. Staudt, T. T. S. Kuo, and H. V. Klapdor-Kleingrothaus, Phys. Rev. C **46**, 871 (1992).
36. V. A. Rodin, A. Faessler, F. Simkovič, and P. Vogel, Phys. Rev. C **68**, 044302 (2003).